

Allosteric Potentiation in the α7 and α4β2 Nicotinic Acetylcholine Receptors

Franco Viscarra

St Cross College

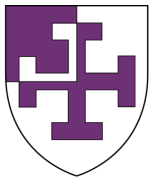

University of Oxford

A thesis submitted in partial fulfilment of the requirements

for the degree of *Doctor of Philosophy*

Supervised by

Professor Isabel Bermudez, Professor Philip C. Biggin

Hilary 2025

I dedicate this Thesis to my parents, who always wanted me to be a Doctor, although maybe not this kind...

Copyright © 2025 by Franco Viscarra
All Rights Reserved

Science knows no country, because knowledge belongs to humanity, and is the torch which illuminates the world.

— Louis Pasteur

Acknowledgements

First and foremost I would like to thank my supervisors Professors Isabel Bermudez and Philip Biggin for their constant support through these four years of hard work. Their guidance was instrumental to my development as a scientist and in carrying out this project. Thank you both for allowing me to explore freely my own ideas and approaches which empowered me to become a more independent thinker. I would also like to thank everyone at SBCB and the third-floor office of the Sinclair building of Brookes University for all the fun times and insightful academic and non-academic discussions. In particular, I would like to thank Dr Afroditi Maria-Zaki, Dr Astrid Brandner, Dr Simon Lichtinger, and Dr Irfan Alibay for their support and training on MD simulations and technical issues. Since science is a collaborative effort, I want to acknowledge Professor Cecilia Bouzat, Dr Juan Facundo Chrestia, Professor John Lopez, Professor Cristiano Bolchi, and Professor Marco Pallavicini for the fructiferous collaborations that made this work possible. Also, I would like to acknowledge funding by ANID Becas Chile.

My experience in Oxford would not have been the same without all the connections I made during my time in this city. Thank you to all my friends who made these four years a memorable experience. Especially to Julian, Andrea, Andres, and Ignacia for making me feel at home in this foreign country and to Ricardo and Daria for all the fun and board games.

Finally, I want to express my gratitude to my family. First, Fernanda, my wife and the love of my life. I don't know if I would have been able to do this without your love and support which allowed me to endure the most stressful times. Lastly, thanks to my parents, Luz and Roberto, and my brother Bastian, who always encouraged my curiosity and supported my crazy dreams of becoming a scientist.

Declaration

I, Franco Viscarra, declare that this thesis is entirely my own work and, except where stated, describes my own research.

Abstract

The human brain is a network of billions of interconnected neurons communicating mainly through chemical synapses. In these synapses, one neuron releases chemical messengers known as neurotransmitters, and the signal is received by a "receptor substance" in the post-synaptic neuron. The nicotinic acetylcholine receptor (nAChR) is one of these "receptive substances", which translates the chemical signal of acetylcholine into an electrical signal through the opening of its ion channel.

nAChRs are ubiquitously expressed throughout the mammalian brain. Therefore, they are involved in a wide array of brain functions and play a role in many neuronal disorders like Alzheimer's disease, Parkinson's disease, schizophrenia, ADHD, depression, and nicotine addiction, making them attractive targets for drug development. Nevertheless, despite their potential, few drugs targeting nAChRs have been successfully developed due to the difficulties of selectively targeting their orthosteric binding site.

Allosteric modulators present themselves as an interesting alternative to orthosteric ligands. Since they bind in sites different from the conserved agonist binding domain, they can achieve high subtype selectivity, even among stoichiometries of the same subtype. Furthermore, positive allosteric modulators (PAMs) enhance the endogenous evoked responses of the receptor instead of replacing them and in some cases can even rescue the receptor from desensitization.

In this thesis allosteric modulators of the two main subtypes of nAChRs in the brain ($\alpha7$ and $\alpha4\beta2$) are investigated using a combination of electrophysiology and molecular dynamics (MD) simulations.

In the first part, Chapter 3, a series of novel ligands for the $\alpha7$ nAChR are presented. They were screened for their function PAMs and the best compound was further studied using MD to determine its binding site.

In the next part, Chapter 4, analogues of NS9283 were studied in the $(\alpha4)_3(\beta2)_2$ nAChR, focusing on their binding to the α4-α4 and the local conformational changes elicited by their activity.

Finally, in Chapter 5, the mechanism of super-agonism of TC-2559 on the $(\alpha4)_2(\beta2)_3$ nAChR was investigated with MD simulations, revealing a new putative allosteric binding site for this receptor present in the β2-β2 interface.

Keywords— Nicotinic Acetylcholine Receptors - Positive Allosteric Modulator - Binding Site Determination - Molecular Dynamics - Voltage-Clamp

List of Publications

The following academic papers were published as part of the research carried out for this thesis.

- **Viscarra, F.**, Chrestia, J. F., Sanchez, Y., Pérez, E. G., Biggin, P. C., Bouzat, C., Bermudez, I., & López, J. J. (**2023**). Side Groups Convert the α7 Nicotinic Receptor Agonist Ether Quinuclidine into a Type I Positive Allosteric Modulator. ACS Chemical Neuroscience, 14(16), 2876–2887.
- Appiani, R.†, **Viscarra, F.**†, Biggin, P. C., Bermudez, I., Giraudo, A., Pallavicini, M., & Bolchi, C. (**2024**). Selective Potentiation of the (α4)3(β2)2 Nicotinic Acetylcholine Receptor Response by NS9283 Analogues. ACS Chemical Neuroscience, 15(7), 1501–1514.
- **Viscarra, F.**, Minguez-Viñas, T., Biggin, P. C., Bermudez, I. (**Manuscript in preparation**). Unorthodox β2-β2 Site Enables the Super-Agonist Profile of TC2559 in the $(\alpha4)_2(\beta2)_3$ Nicotinic Acetylcholine Receptor.

† equal contribution

Conference attendance

- European Biophysical Societies' Association Congress (Stockholm, Sweden, July 2023). Poster presentation.
- Biophysical Society Annual Meeting (Philadelphia, PA, February 2024). Flash talk, Poster presentation.
- Biophysical Society Annual Meeting (Los Angeles, CA, February 2025). Poster presentation.

Table of Contents

List of Figures **xi**

List of Tables **xii**

List of Abbreviations **xiii**

1 Introduction **1**

1.1 Synaptic Transmission and Ligand-gated Ion Channels 1

1.2 Nicotinic Acetylcholine Receptors 2

1.3 nAChR Structure 4

1.3.1 The Extracellular Domain 5

1.3.2 The Transmembrane Domain 7

1.3.3 nAChR Gating Cycle 9

1.3.4 Modulatory Sites in Cys-loop Receptors 10

1.4 nAChR subtypes 12

1.4.1 The $\alpha4\beta2$ Subtype 13

1.4.2 The $\alpha7$ Subtype 15

1.5 Distribution of the $\alpha4\beta2$ and $\alpha7$ nAChRs 16

1.6 Role of the $\alpha4\beta2$ and $\alpha7$ nAChRs in Disease 18

1.6.1 Nicotine Addiction 19

1.6.2 Alzheimer's Disease 20

1.6.3 Parkinson's Disease 22

1.6.4 Attention Deficit Hyperactivity Disorder 23

1.6.5 Schizophrenia 24

1.6.6 Depression 25

1.7 Neuronal nAChR Pharmacology 27

1.7.1 Orthosteric ligands 27
1.7.2 Allosteric ligands 31
1.8 Aims of this Thesis 40

2 Theory and Methods **42**
2.1 Molecular Dynamics Simulations 42
2.1.1 Quantum Mechanics and Molecular Mechanics 43
2.1.2 Force Fields 44
2.1.2.1 Bonded Interactions 45
2.1.2.2 Non-bonded Interactions 46
2.1.3 Algorithms 49
2.1.3.1 Energy Minimization 49
2.1.3.2 Newton's Equation of Motion 50
2.1.3.3 Integration of the Equation of Motion 50
2.1.3.4 Periodic Boundary Conditions and Non-bonded Interactions 52
2.1.3.5 Simulations at Constant Temperature and Pressure . . 55
2.1.4 Enhanced Sampling Techniques 59
2.1.4.1 Replica Exchange with Solute Tempering 59
2.1.4.2 Umbrella Sampling 63
2.1.4.3 Free Energy Estimators 64
2.1.4.4 Metadynamics 66
2.2 Electrophysiology 68
2.2.1 Bioelectricity 69
2.2.2 Two-electrode Voltage Clamp 70
2.2.3 Experimental Setup 71
2.2.3.1 Reagents and Buffers 71
2.2.3.2 Animals 72

2.2.3.3 *Xenopus laevis* Oocytes Preparation. 72
2.2.3.4 cDNA Microinjection 72
2.2.3.5 Electrophysiological recordings 73
2.2.3.6 Concentration Response Curves 76
2.2.3.7 Statistical Analysis 76

3 Functional Characterisation and Binding Site Identification of Novel Positive Allosteric Modulators of the α7 Nicotinic Acetylcholine Receptor 77
3.1 Introduction 77
3.2 Materials and Methods 78
3.2.1 Novel Compounds 78
3.2.2 Single Point Mutation 79
3.2.3 Two-Electrode Voltage-Clamp Recordings 79
3.2.4 Single-Channel Recordings in BOSC 23 Cells 79
3.2.5 Molecular Docking 80
3.2.6 Molecular Dynamics Simulations 81
3.3 Results 83
3.3.1 Functional Screening of Novel Ether-quinuclidine Ligands . . . 83
3.3.2 Binding Site Prediction and Validation 91
3.4 Discussion 96

4 Selective Potentiation of the $(\alpha 4)_3(\beta 2)_2$ Nicotinic Acetylcholine Receptor Response by NS9283 Analogues. 101
4.1 Introduction 101
4.2 Materials and Methods 103
4.2.1 Novel Compounds 103
4.2.2 Two-Electrode Voltage-Clamp Recordings 103
4.2.3 Molecular Dynamics Simulations 104

4.2.3.1 System Preparation 104
4.2.3.2 REST 106
4.2.3.3 Umbrella Sampling Simulations 107
4.3 Results 108
4.3.1 Functional Characterization of NS9283 Analogues 108
4.3.2 Binding Mode Prediction of Selected Analogues 111
4.3.3 The Conformational Change of W181 is Favoured by NS9283 . 118
4.3.4 NS9283 is not Stable in the β2-α4 site 119
4.4 Discussion 120

5 Unorthodox β2-β2 Site Enables the Super-Agonist Profile of 4-(5-ethoxy-3-pyridinyl)-N-methyl-(3E)-3-buten-1-amine (TC-2559) in the $(\alpha4)_2(\beta2)_3$ Nicotinic Acetylcholine Receptor 123
5.1 Introduction 123
5.2 Materials and Methods 124
5.2.1 Molecular Dynamics Simulations 124
5.2.1.1 System Preparation 124
5.2.1.2 REST Simulations 124
5.2.1.3 Funnel Metadynamics 125
5.2.1.4 Two-Electrode Voltage-Clamp Recordings 125
5.2.1.5 Site-Directed Mutagenesis 125
5.3 Results 126
5.3.1 Do all agonists of the HS receptor bind similarly to orthosteric sites? 126
5.3.2 Aspartates at β2 Loop C and Loop F are Critical for TC-2559 Function 128
5.3.3 Displacement of β2 Loop B is Induced by TC-2559 130
5.4 Discussion 132

6 Outlook and Conclusion **139**

6.1 40 Years of nAChR Research 139

6.2 Final Conclusion 142

Bibliography **144**

List of Figures

1.1 Structure of a typical nAChR receptor. 5
1.2 Neurotransmitter binding site of the nAChR. 7
1.3 Transmembrane domain of the nAChR. 8
1.4 Allosteric activation model of a Cys-loop receptor with two binding sites. 10
1.5 Alternative stoichiometries of the $\alpha4\beta2$ subtype. 15
1.6 Desensitisation kinetics of the $\alpha7$ compared to the $\alpha4\beta2$ subtype. 16
1.7 Distribution the $\alpha4\beta2$ and $\alpha7$ subtypes in the brain. 18
1.8 Chemical structures of the orthosteric ligands listed in Table 1.1 31
1.9 Representative macroscopic traces of type I and type II positive allosteric modulators. 34
1.10 Chemical structures of the allosteric ligands listed in Table 1.2 39

2.1 Schematic representation of bonded and non-bonded interactions modelled in a typical force field. 48
2.2 Two-dimensional representation of periodic boundary conditions. 53
2.3 Schematic representation of a replica exchange simulation with four replicas at different temperatures. 63
2.4 Representation of umbrella sampling in an asymmetric double-well potential. 64
2.5 Circuit representation of the TEVC setup with a model membrane. . . . 71
2.6 Schematic representation of cDNA microinjection 73
2.7 Manual and automated electrophysiology setups. 75

3.1 Superimposition of the (+) subunit chain adjacent to each ligand 82
3.2 Functional effects of ether quinuclidine derivatives on $\alpha7$ nAChR expressed heterologously in Xenopus oocytes 84

3.3 Ligands **6**, **8**, and **9** exert effects on human α7 nAChR expressed heterologously in *Xenopus* oocytes 86
3.4 ACh concentration-response curve +/- ligand **6** 88
3.5 Effects of ligand **6** on α7 nAChR at the single-channel level 89
3.6 Concentration-response effects of ligand **6** 91
3.7 Superimposition of blind docking poses of ligand **6** 92
3.8 Ligand **6** binds the transmembrane domain of α7 nAChR 93
3.9 Ligand **6** interaction with residues in the predicted binding site 95

4.1 NS9283 and its Analogues Modified at the Peripheral Rings 104
4.2 Binding poses of ligands on α4-α4 interface 106
4.3 Activity of NS9283 and analogues at α4β2, α5α4β2, and α7 nAChRs . . 109
4.4 Effects of NS9283 and analogues on LS αβ nAChR 111
4.5 Selected conformations for NS9283 112
4.6 Contact analysis of the ligands with the protein side chains 113
4.7 RMSD over time of the 200 ns unbiased simulations 116
4.8 Comparison of the conformation of NS9283 and W182 between constructs 117
4.9 Potential of mean force on the tryptophan χ1 angle 118
4.10 Binding of NS9283 to the β2-α4 interface of the LS α4β2 nAChR 120

5.1 Clustered poses from REST simulations of selected agonists and the antagonist tropisetron at the α4β2 interface. 127
5.2 Free energy landscape of loop C capping from REST simulations. . . . 127
5.3 REST simulations of agonists at the β2-β2 interface. 129
5.4 Concentration-response curves of TC-2559 in the loop C (A) and loop F (B) mutants. 130
5.5 Funnel metadynamics of TC-2559 at the β1-β2 interface. 131
5.6 Principal component analysis of metadynamics simulations. 132

5.7 Clusters from REST simulations superimposed to Cryo-EM structures. 134
5.8 Effect of mutants on the EC_{50} of ACh compared with the wild-type. . . 137
5.9 Salt-bridge interaction between Cys-loop and M2-M3 linker at the β2 subunit. 137

6.1 Hosieine-A is a competitive inhibitor of nAChR subtypes. 140

List of Tables

1.1 Orthosteric ligands of the α4β2 and α7 nAChRs. 32
1.2 Allosteric ligands of the α4β2 and α7 nAChRs. 38

3.1 Restrained residues and their location during the 500ns production run . 82
3.2 Mean Open and Burst Durations of α7 nAChR in the Absence or Presence of Ligand **6** 89

4.1 Average exchange probabilities for each replica exchange simulation . . 107
4.2 Concentration effects of NS9283 and Analogues on LS α4β2 nAChR . . 110
4.3 Cluster distribution from the REST simulations 112

List of Abbreviations

5-HI 5-hydroxyindole.

$5HT_{3A}$ serotonin receptor 3A.

Aβ amiloid-β.

ABT-107 5-(6-[(3R)-1-azabicyclo[2,2,2]oct-3-yloxy]pyridazin-3-yl)-1H-indole.

ACh acetylcholine.

AChBP acetylcholine binding protein.

AD Alzheimer's disease.

ADHD attention deficit hyperactivity disorder.

ANOVA analysis of variance.

AQW051 (3R)-3-[6-(4-methylphenyl)pyridin-3-yl]oxy-1-azabicyclo[2.2.2]octane.

AR-R17779 (3S)-Spiro[1-azabicyclo[2.2.2]octane-3,5'-oxazolidine]-2'-one hydrochloride.

AZD-3480 (E,2S)-N-methyl-5-(5-propan-2-yloxypyridin-3-yl)pent-4-en-2-amine.

BNC375 4-[(1R,3R)-3-[(5-chloro-2-methoxyanilino)methyl]-2,2-dimethylcyclopropyl]benzenesulfonamide.

CBD cannabidiol.

cDNA complementary deoxyribonucleic acid.

CMPI 3-(2-chlorophenyl)-5-(5-methyl-1-(piperidin-4-yl)-1H-pyrrazol-4-yl)isoxazole.

CNS central nervous system.

COM center of mass.

CRC concentration-response curve.

Cryo-EM cryo electron microscopy.

CV collective variable.

Cys-loop cysteine-loop.

dFBr des-Formylflustrabromine.

DMEM Dulbecco's modified eagle medium.

DMSO dimethyl sulfoxide.

EC extracellular.

EC_{100} concentration evoking 100 % of the maximal effect.

EC_{20} concentration evoking 20 % of the maximal effect.

EC_{50} concentration evoking 50 % of the maximal effect.

EVP-6124 (R)-7-chloro-N-quinuclidin-3-yl)benzo[b]thiophene-2-carboxamide.

FBS fetal bovine serum.

FES free energy surface.

FunMetaD funnel metadynamics.

GABA gamma-aminobutyric acid.

GAT107 4-(4-bromophenyl)-3a,4,5,9b-tetrahydro-3H-cyclopenta[c]quinoline-8-sulfonamide.

GFP green fluorescent protein.

GluCl glutamate receptor.

GlyR glicine receptor.

HS high sensitivity.

IC_{50} concentration inhibiting 50 % of the response.

LS low sensitivity.

MBAR multistate Bennett acceptance ratio.

MD molecular dynamics.

MM molecular mechanics.

NAcc nucleus accumbens.

nAChR nicotinic acetylcholine receptor.

NAM negative allosteric modulator.

NS1738 N-(5-Chloro-2-hydroxyphenyl)-N'-[2-chloro-5-(trifluoromethyl)phenyl]urea.

NS9283 3-[3-(3-Pyridinyl)-1,2,4-oxadiazol-5-yl]benzonitrile.

PAM positive allosteric modulator.

PC principal component.

PD Parkinson's disease.

PDB Protein Data Bank.

pLGICs pentameric ligand gated ion channels.

PME particle-mesh Ewald.

PMF potential of mean force.

PNU-120596 N-(5-Chloro-2,4-dimethoxyphenyl)-N'-(5-methyl-3-isoxazolyl)-urea.

POPC 1-palmitoyl-2-oleoyl-sn-glycero-3-phosphocholine.

QM quantum mechanics.

REMD replica exchange molecular dynamics.

REST replica exchange with solute tempering.

RMSD root-mean square deviation.

RO5126946 5-chloro-N-[(1S,3R)-2,2-dimethyl-3-(4-sulfamoyl-phenyl)-cyclopropyl]-2-methoxy-benzamide.

SAM silent allosteric modulator.

SEM standard error of the mean.

SMD steered molecular dynamics.

SOS standard oocyte solution.

TC-2559 4-(5-ethoxy-3-pyridinyl)-N-methyl-(3E)-3-buten-1-amine.

TEVC two-electrode voltage clamp.

TM transmembrane.

TMP Cis-trans-4-(2,3,5,6-tetramethylphenyl)-3a,4,5,9b-tetrahydro-3H-cyclopenta[c]quinoline-8-sulfonamide.

TQS 4-naphthalen-1-yl-3a,4,5,9b-tetrahydro-3H-cyclopenta[c]quinoline-8-sulfonamide.

US umbrella sampling.

VTA ventral tegmental area.

WHAM weighted histogram analysis method.

WT wild-type.

1 | Introduction

1.1 Synaptic Transmission and Ligand-gated Ion Channels

The brain is the most complex organ of the body. It is where all cognitive processes occur and the control centre of all organisms. To understand the function of the brain it is necessary to understand its chemistry. The tightly bound nerve cells communicate with one another mainly through chemical signals that mediate information processing in the brain. These signals consist of molecules known as neurotransmitters, which are released into the synapses where other molecules are waiting for them to receive these signals: the neuronal receptors. The interaction between neurotransmitters and receptors causes changes in the receptor's functional properties, which can translate into an electrical response in the case of ion channels or a metabolic response, for example with G-protein coupled receptors [1].

Ligand-gated ion channels are integral membrane proteins that transduce the binding of an agonist into the opening of the ion-selective pore, enabling passive diffusion of charges [2]. Depending on the ion they allow to pass, the electrical response on the post-synaptic cell will differ. For example, if the gated channels transport Na^+, it will result in depolarization of the cell, inverting the membrane potential and generating a propagation of the signal through voltage-gated Na^+ channels. On the other hand, if the channel is permeable to K^+ or Cl^- the membrane potential of the cell will become more negative, making it hyperpolarized and less responsive to activation [1].

The pentameric ligand gated ion channels (pLGICs) is a superfamily of neuronal receptors with a ubiquitous presence among metazoans that mediate fast synaptic transmission [3]. These receptors are composed of five subunits assembled around a central pore [4,

5]. This superfamily includes the nicotinic acetylcholine receptor (nAChR), serotonin receptor 3A ($5HT_{3A}$), the glicine receptor (GlyR), the gamma-aminobutyric acid (GABA) receptors $GABA_A$ and $GABA_C$, the invertebrate glutamate receptor (GluCl), and the prokaryotic GLIC and ELIC receptors [6]. Members of the family share conserved structural features and functional mechanisms of gating and modulation [7]. In humans, they are important clinical targets for neuronal conditions as they mediate a plethora of physiological processes [2]. They are also relevant as targets for pest control in invertebrates, either for nematode infestations in humans and livestock or crop-damaging insect pests [8]. In this chapter, we will take a look at the structure, function, and pharmacology of one of the members of this superfamily, the nAChR. This family has been extensively studied at the structural level and our current understanding of the pLGIC function is largely based on these findings.

1.2 Nicotinic Acetylcholine Receptors

The nAChRs are a well-known type of ligand-gated ion channel, and they were the first neurotransmitter receptors to be observed. This crucial scientific discovery became a paradigm change in our understanding of the brain and it was achieved through pharmacological research, specifically the study of two poisons from the Americas: Nicotine and Curare.

John Newport Langley introduced the term “receptive substance” in the 1900s when he observed that nicotine provoked contractions in the muscles of fowl, frogs, and toads, which were blocked by the application of curare. From this he concluded that there must be a substance, distinct from the molecule that causes contraction, that combines with nicotine and curare and it can act upon the contracting substance [9]. This receptive substance was none other than the nAChR.

Under the supervision of Langley, Archibald Hill studied the muscle response to varying

concentrations of nicotine [10]. He realized that these responses could be fitted to an exponential function. From this, he determined that the rate-limiting process for the contraction was the binding of nicotine to the "receptive substance" and proposed an early version of the Hill equation (discussed in Section 2.2.3.6), essentially providing the first equation to fit dose-response curves.

Almost 50 years later, del Castillo and Katz [11, 12] compared the mechanism of the hypothetical receptor molecule to an enzyme, like acetylcholinesterase, defining separate "binding" and "gating" steps that involved changes in the configuration of the protein.

The concept of an "ion channel" itself was not completely accepted until the current flowing through this channel was measured. For the nAChR, this was achieved by Katz and Miledi in the 1970s [13, 14] by using the noise analysis method. Later, using the voltage clamp technique Anderson and Stevens [15] showed that the current that flowed through one channel was equal to $5\,\mathrm{pA}$, an amount of current that could only be carried through an aqueous pore.

A breakthrough occurred when the first subunit of the nAChR was cloned in 1982 [16], which allowed the expression of the receptor in oocytes or cell lines, meaning testing the effect of mutations was now possible. The explosion in the molecular biology of the nAChRs, granting knowledge of their gene and amino acid sequences, generated many advances in the structural investigation of the receptor. For example, the determination that every subunit contributes four transmembrane domains [17] and that the M2 transmembrane region lined the ion channel pore [18]. Later, thanks to advances in cryo electron microscopy (Cryo-EM), it was possible to determine the quaternary arrangement of the nAChRs [19] and to resolve the structure of the nAChR, first at a resolution of $9\,\text{Å}$ [20], then at resolutions of $4.6\,\text{Å}$ [21] and $4\,\text{Å}$ [22]. The latter (PDB ID: 2BG9) stood as a significant milestone for several years. Currently, several other structures of the nAChRs in different functional states [23, 24, 25, 26, 27, 28, 29, 30] have been resolved,

some of which are used extensively in this thesis, and have shed light on the mechanisms governing the receptors' function, regulation, and pharmacology.

1.3 nAChR Structure

NAChRs are acetylcholine (ACh) activated neurotransmitter receptors. Unlike the metabotropic muscarinic acetylcholine receptors [31], the nicotinic type is a fast ionotropic cationic channel sensitive to activation by nicotine. As pLGICs nAChRs assemble as pentamers forming a pore in the centre with the neurotransmitter binding sites located at the subunit interfaces (Figure 1.1A). All nicotinic subunits are comprised of a highly conserved extracellular (EC) N-terminal domain of about 200 amino acids, three conserved transmembrane (TM) domains, a cytoplasmic loop of variable size and low conservation, and a fourth TM domain with a short and variable C-terminal sequence (Figure 1.1B). This arrangement is referred to as the 3+1 configuration based on the positions of the TM domains relative to each other [32]. Another trait that is shared among subunits is the existence of a cysteine-loop (Cys-loop) in the EC domain, defined by two cysteines that are separated by 13 amino acids (Figure 1.1B). The nAChR subunits are classified into two main classes: The α subunits, which possess two adjacent cysteines in loop C which are key for ACh binding (Figure 1.1B), and the non-α subunits that do not possess these cysteines [5, 33].

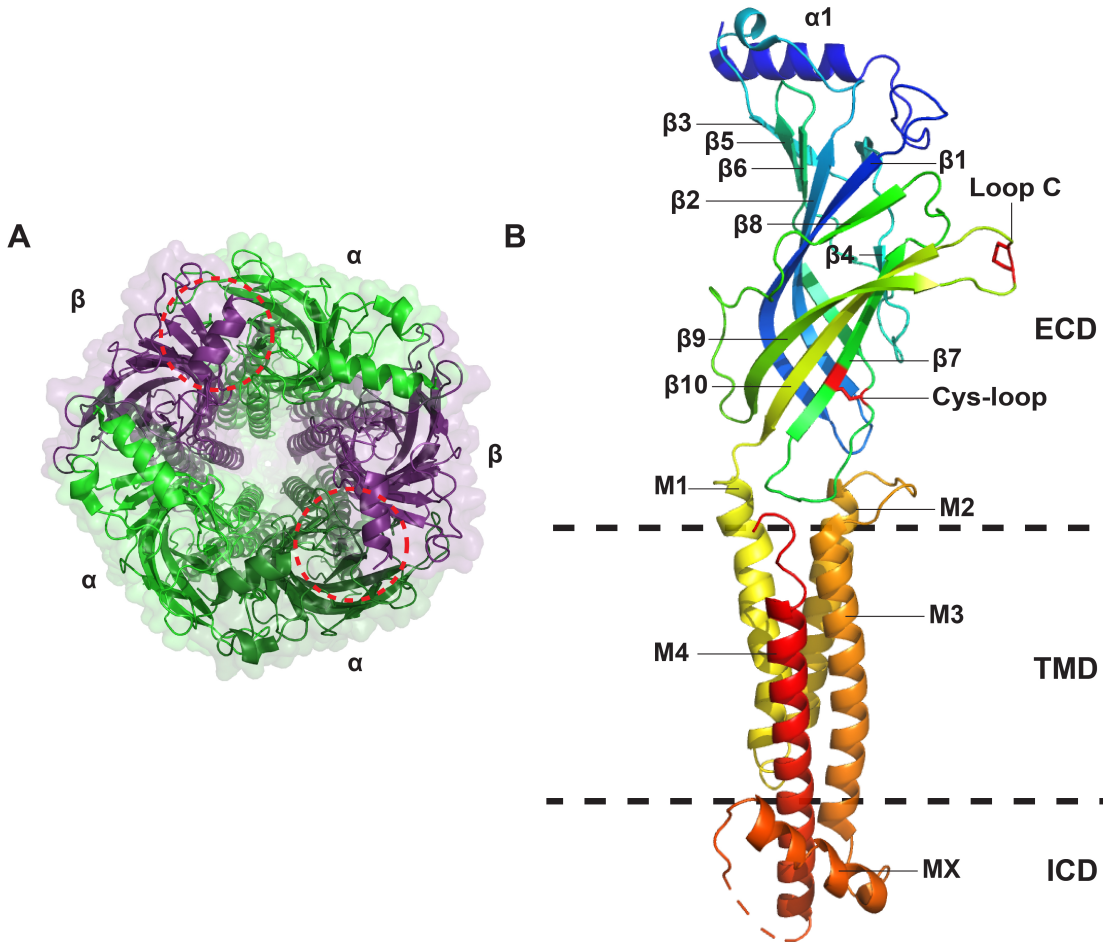

Figure 1.1: Structure of a typical nAChR receptor. (A) Top view of the α4β2 nAChR (PDB ID: 6CNK) [29] showcasing the five subunits that compose it. α subunits are coloured in green, while β subunits are coloured in purple. The red circles indicate the location of the orthosteric binding sites. (B) Side view of an α4 subunit coloured in a rainbow colour scheme with the N-terminal in blue and C-terminal in red. Structural motifs of the subunits are individually labelled with the Cys-loop and loop C cysteines highlighted in red. The dashed black lines represent the cellular membrane.

1.3.1 The Extracellular Domain

The nAChR's EC domain secondary structure is mainly composed of β-strands, which are arranged in a configuration of a β-barrel. This domain also forms the ligand binding site,

which lies at the EC interface between an α and a non-α subunit (except in the homomeric receptors, see Section 1.4.2). The α subunit contributes with the majoritarian or "positive" (+) side of the binding site, where the consecutive cysteines are required, while the minoritarian or "negative" (-) face of the binding site is contributed by the non-α subunit (Figure 1.2A) [32]. Three loops form the binding site from each side of the interface, loops A, B, and C from the (+) face and loops D, E, and F from the (-) side (Figure 2A) [23]. Residues from loops A-E form an aromatic pocket that surrounds the agonist. A tyrosine in loop A and a tryptophan in loop D form the floor of the box, the back is defined by a tryptophan in loop B and a leucine in loop E. The loop B tryptophan is essential in nicotinic receptors since its indole group participates in a cation-π interaction with the positively charged group of the agonist which has been observed to be critical for agonist activity [34]. Two tyrosines in loop C form the front of the pocket. This loop has been shown to change conformation upon agonist binding [35, 36, 30], capping the binding site (Figure 1.2B). This conformational change is necessary for the agonist to induce receptor gating when binding [37, 38]. The top portion of the pocket is formed by a valine and a phenylalanine (α4|β2) [23, 29] or leucine and glutamine (α7) in loop E [36, 30].

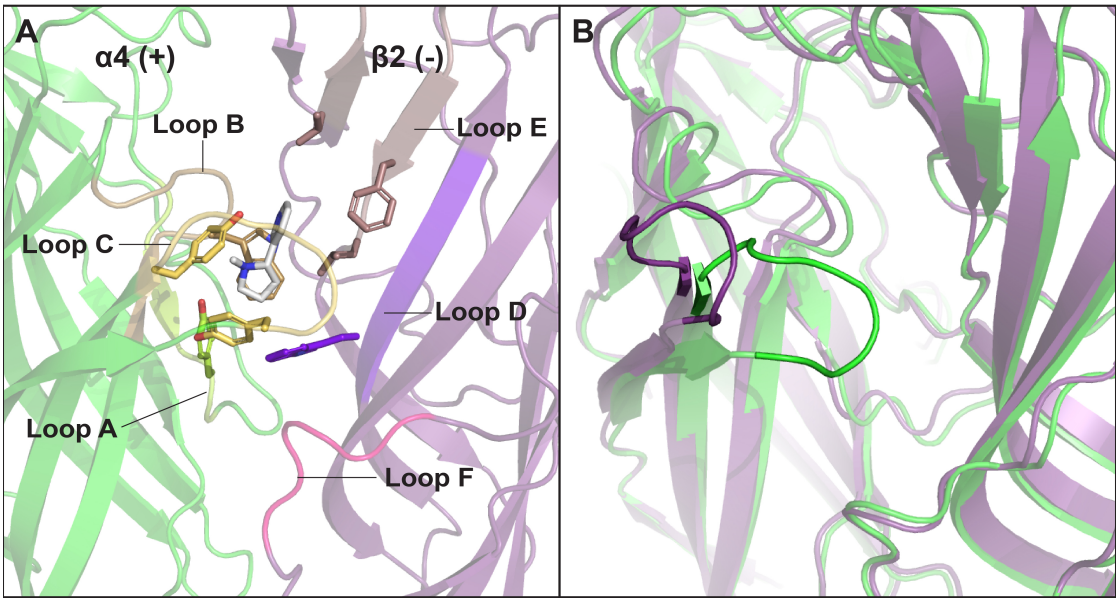

Figure 1.2: Neurotransmitter binding site of the nAChR. (A) α4-β2 interface with nicotine (white) bound (PDB ID: 6CNK) [29]. The amino acids comprising the hydrophobic box are shown in stick representation and the loops are coloured and labelled individually. (B) Loop C of the α7 nAChR [36] in the holo (green) compared to the apo (purple) conformation (PDB ID: 7KOX and 7KOO respectively).

1.3.2 The Transmembrane Domain

The TM domain contains four membrane-spanning α-helices (M1-M4) (Figure 1.1B), which extend beyond the membrane surface, where the ends of M1, M2, and M4 contain polar and/or negatively charged residues [39]. Conversely, the M3 protrudes into the cytoplasm followed by the MX helix that resides in the juxtamembrane region in the intracellular leaflet of the membrane [30, 36]. The M2 helices form the ion permeation path of the channel pore. The residues lining this pore are mostly non-polar, providing a relatively inactive surface for the diffusing ions, but the negatively charged groups at the ends of the helix influence the transport by raising the concentration of cations while lowering the concentration of anions [39]. A highly conserved leucine in position 9' known as the resting gate produces a constriction in the pore when the receptor is in the

closed state (Figure 1.3A) [40, 39]. During the gating of the receptor, this constriction disappears allowing the diffusion of ions through the channel [30, 36]. The movements on the M2 helix during gating are induced by interactions at its intracellular and extracellular ends. At the intracellular end, a salt bridge between a lysine on M2 and an aspartate on M4 coordinates the movement of these two helices (Figure 1.3B) [30]. This aspartate has been reported to be important for subunit assembly both in the α7 nAChR and the $5HT_{3A}$ receptor [41, 42]. Thus, tilting of the M1-M3-M4 bundle during activation pulls M2 outwards through this M2-M4 salt bridge interaction. At the extracellular end, the M2 main chain interacts with a lysine of the β1-β2 loop (Figure 1.3B), fixing it in an open position during activation and desensitization [30].

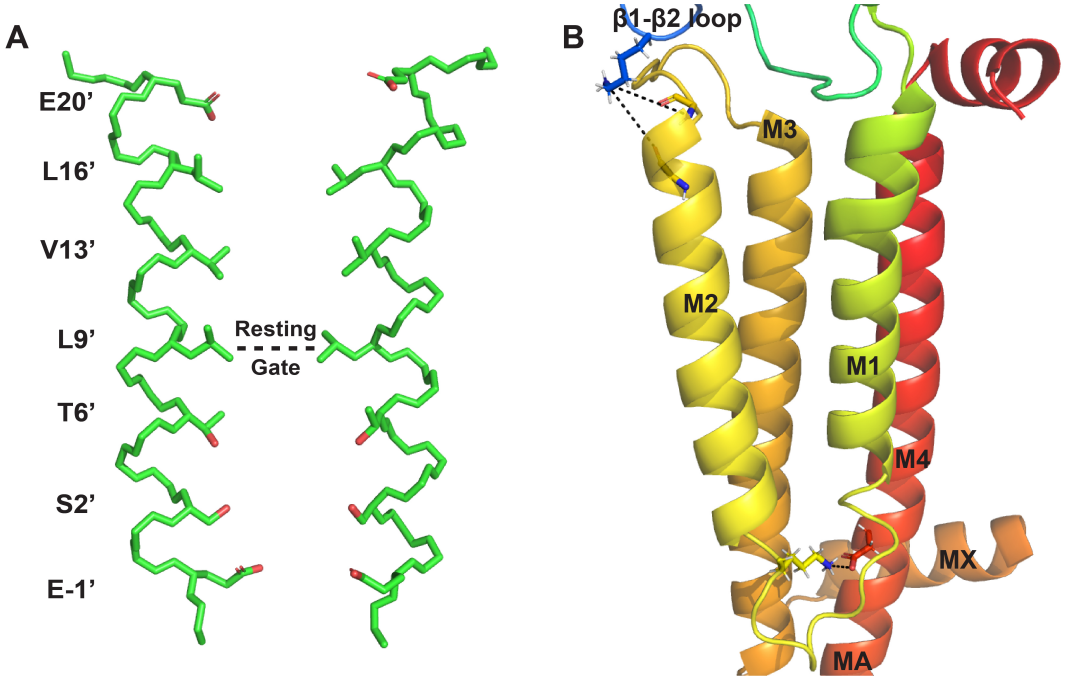

Figure 1.3: Transmembrane domain of the nAChR. (A) Ion permeation pathway of the α7 nAChR (PDB ID 7KOO) [30]. Only two of the five subunits are displayed for clarity. The prime numbering refers to the position of the residue above the cytoplasmic end of the pore. (B) The transmembrane domain of the desensitized α7 nAChR (PDB ID 7KOQ) [30], interactions of M2 with M4 and the β1-β2 loop are displayed as dashed lines.

1.3.3 nAChR Gating Cycle

pLGICs exist in a reversible equilibrium between the resting, activated, and desensitised states where the relative population of these states depends on the pharmacological conditions [43] (Figure 1.4). The binding of an agonist to the EC neurotransmitter binding site stabilises the activated state, increasing the probability of opening the channel [7]. This transition is allosteric since the opening pore is located ~50 Å from the orthosteric binding site [7]. Thus, conformational changes must occur for the binding of the agonist to be transduced into channel gating. These changes begin at the binding site, where the binding of the agonist induces a structural rearrangement, the main feature of which is the capping of loop C [44, 36, 30]. This rearrangement happens in two stages named "catch" and "hold". Catch establishes a low-affinity complex of receptor-ligand, followed by an induced fit, "hold", that increases the agonist affinity and initiates the gating [38]. The hold transition generates a torsional force that gets translated to the TM domain by the coupling region. This flexible region lies at the interface between the EC and TM domains [30]. Here the β1-β2 loop and Cys-loop connect the inner and outer β sheet motions with the TM domain's M2-M3 loop [30] [7]. This concerted movement culminates in the opening of the channel gate, which occurs by a sideway rotation which pulls the tops of the pore lining M2 helices, effectively widening the hydrophobic gate [7]. Finally, after gating the receptor transitions into a desensitized state, this involves uncoupling the motions of the TM and EC domains in the coupling region which allows the TM domain to close while the EC domain remains in the bound conformation [45].

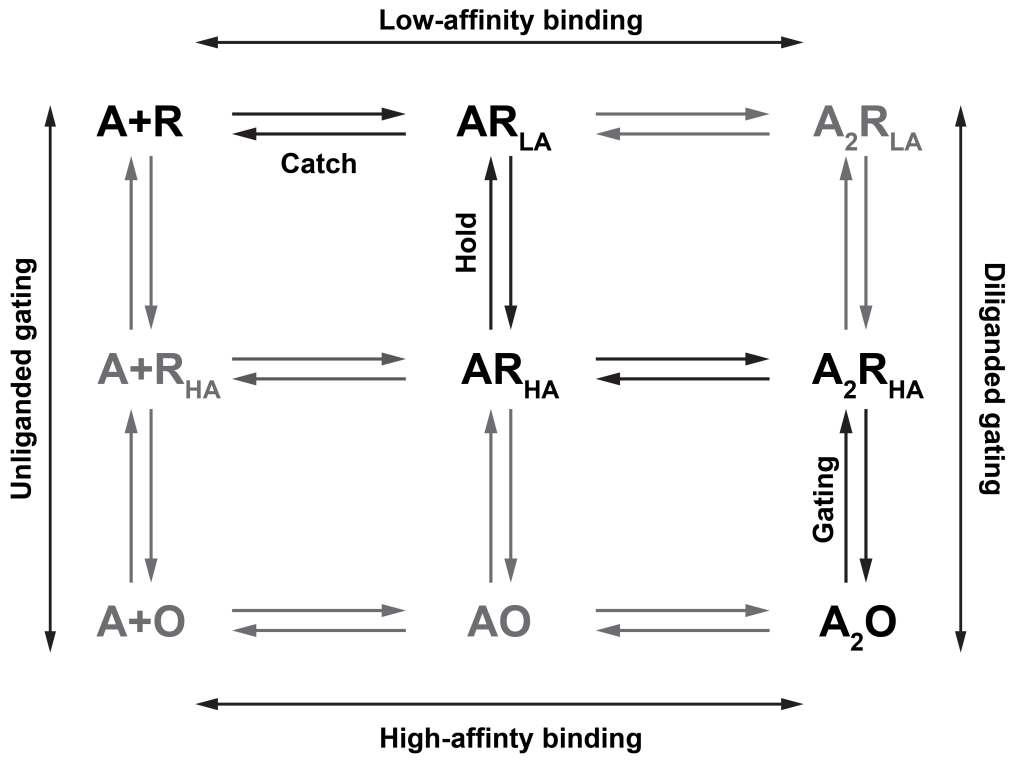

Figure 1.4: Allosteric activation model of a Cys-loop receptor with two binding sites. The model shows the reversible equilibrium of the receptor between the resting (R) and open (O) states, with either a high-affinity (HA) or low-affinity (LA) extracellular domain, and with bound or unbound agonist (A). The black activation pathway indicates the most probable states and transitions, according to the model presented by Plested [46].

1.3.4 Modulatory Sites in Cys-loop Receptors

Due to the conserved nature of the gating cycle among Cys-loop receptors, there is also a certain conservation of binding sites that modulate their activity. Although the locations of these sites are conserved, their structural characteristics are variable among different receptor types and subtypes, making the allosteric modulators highly selective [47]. In Cys-loop receptors, there are allosteric sites located both at the EC domain and the TM

domain. A prime example of the former is the benzodiazepine binding site in the GABA receptor. As with nicotinic receptors, the orthosteric binding site in the EC domain is located at the interface between two subunits, where one specific subunit must provide for the positive face of the site while the other contributes with the complementary side (β and α respectively in the α1β3γ GABA receptor [48] and α and β respectively in the α4β2 nAChR [32]). However, benzodiazepines bind in a site formed with the "reverse" faces of the subunits, namely where the α provides the positive face and the γ provides the negative face [49]. The binding of benzodiazepines to these sites produces a positive modulation of the response by increasing the affinity but not the efficacy of the agonists [49]. An analogous site exists in the nAChRs, where the binding of modulators to the α4-α4 interface of the α4β2 nAChR produces a similar effect to the benzodiazepines in GABA [50]. Allosteric modulators binding to this site are discussed in Section 1.7.2 and Chapter 4. Additionally, mutagenesis experiments have suggested that the non-canonical β(+)-α(-) site of the α3β2 nAChR binds the positive allosteric modulator (PAM) morantel [51]. Another modulator that binds to EC domain sites is Zn^{+2}, which acts as a negative allosteric modulator (NAM) in the GABA receptor, binding to a site lying between the canonical binding site and the membrane interface [52]. Similarly, in the α4β2 nAChR Zn^{+2} binds to the extracellular domain, although it has a dual effect depending on the receptor stoichiometry (more on this in Sections 1.4.1 and 1.7.2), it exerts a positive modulatory effect when binding at the α4-α4 interface and an inhibitory effect when binding to an β(+)-α(-) site [53].

Since the motions of the TM domain are directly implicated in the opening of the ion-conducting pore, it is natural that ligands interacting with this domain will have a direct effect on receptor gating. There are two conserved cavities for allosteric modulation of Cys-loop receptors at the TM domain: an intersubunit cavity, located between the M2-M3 helices of a (+) subunit and the M1-M2 of a (-) subunit and an intrasubunit pocket. Ivermectin potentiates GlyR [54], GluCl receptors [55], GABA receptors [56],

and nAChRs [35] by binding to this conserved PAM site. Moreover, this site is of great importance in the α7 nAChR, as it is the target for most PAM of this subtype (see Section 1.7.2 and Chapter 3). Another type of compound that binds in an intersubunit site is the neurosteroids, which potentiate GABA receptors through a TM site located between the M3 helix of a (+) subunit and the M1-M4 of a (-) subunit [57]. An equivalent site for neurosteroids is present in the GlyR, where they elicit a similar effect [58]. Nevertheless, neurosteroids can also have a NAM effect by binding to a different TM domain site, an intrasubunit pocket between M4 and M3, both in the GABA [57] and the GlyR [59]. In the GlyR, however, this site is also the target of THC (Δ^9-tetrahydrocannabinol), which acts as a PAM [60], suggesting that allosteric binding sites can have dual natures, allowing for different types of modulation depending on the interactions with the ligands.

1.4 nAChR subtypes

Subunit diversity in the nAChR allows for different subtypes arising from assemblies of different combinations of subunits. In the mammalian muscle only five subunits are expressed: α1 and four other non-α subunits, namely β1, δ, γ, and ε. From these subunits two receptors can be constructed: α1β1δγ and α1β1δε, each one of them with a stoichiometric ratio of 2:1:1:1 [32]. On the other hand, mammalian neuronal nAChRs are much more diverse, with seven α subunits, named α2, α3, α4, α5, α6, α7, α9, and α10 (α8 has been purified from avian cells, but has not been found in mammals [61, 62]) and three non-α subunits, named β2, 3, and β4 [32]. Furthermore, neuronal subunits are less restricted than muscle types in their assembly, with at least 14 oligomer combinations observed in mammalian neurons [5, 61]. In the mammalian brain, the α4, β2, and α7 subunits show a widespread distribution (Figure 1.7), with regional expression patterns varying between species. Additionally, in primates, the α2 subunit has a distribution comparable to the α4. The α3, α6, α3, and α4 subunits have a restricted distribution in

the brain (Figure 1.7), according to mRNA distribution data. However, in the neuronal regions where they are expressed, they can constitute the main subpopulation of nAChR [61, 63]. The work in this thesis is focused on the two most expressed subtypes in the brain: the α4β2 and the homomeric α7.

1.4.1 The α4β2 Subtype

The α4β2 nAChR is the predominant nAChR in the mammalian brain, accounting for $90\,\%$ of the high-affinity nAChRs [61, 63], and the main subtype that binds to nicotine. It has been observed that this receptor can assemble in two different stoichiometries: the (α4)2(β2)3 known as high sensitivity (HS) and the (α4)3(β2)2 known as low sensitivity (LS) [29]. As the name implies they are characterised by their sensitivity towards nicotinic ligands [64, 65], with the HS stoichiometry having an ACh concentration evoking 50 $\%$ of the maximal effect (EC_{50}) of $4\,\mu M$ while the LS stoichiometry having an EC_{50} of $88\,\mu M$ [65]. Additionally, the HS stoichiometry has slower desensitisation kinetics [64], lower conductance at the single-channel level [64], and lower Ca^{+2} permeability than the LS [66]. Each stoichiometry contains two α-β interfaces, where the canonical binding site lies, and two β-α interfaces. Additionally, a third interface is unique to each stoichiometry: an α-α interface for the LS and a β-β interface (Figure 1.5). Interfacial free energies calculated from Cryo-EM structures [29] show a higher stability for the assembly of the α-β, followed by β-α, then α-α, and finally β-β as the least favourable. This suggests that, during the quaternary organisation, the more favourable α-β and β-α interfaces assemble first, and then the fifth subunit incorporates to create the unique interface defining the stoichiometry. These observations are consistent with studies showing that the LS multimer is the predominant assembly in the absence of biases when expressed heterologously in *Xenopus laevis* oocytes [64, 65]. However, it is possible to control the stoichiometry of the α4β2 nAChRs in *Xenopus laevis* oocytes by injecting different ratios of subunit cDNA into the cell: a ratio of 1:10 of α4:β2 to favour the

formation of the HS stoichiometry and a ratio of 10:1 of α4:β2 to favour the LS assembly [64, 65]. Additionally, incubating the cells in the presence of nicotine also favours the assembly of the HS multimer [64, 65, 29].

In the LS stoichiometry, the unique α4-α4 interface contains an additional unorthodox binding site. This binding site is capable of binding agonists and it has been shown to increase the maximal probability of activation of agonists and decrease the potency of agonists relative to their potency at the HS stoichiometry, which confer the LS receptor its signature sensitivity [67, 68, 69]. This extra binding site also speeds up receptor desensitization [70]. Additionally, agonist binding to this site increases the gating of the receptor [69, 71, 72] and the maximum efficacy of partial agonists such as cytisine, nicotine, and varenicline [71, 65]. Furthermore, the binding of agonists to this site is necessary to achieve full activation of the receptor, this is evidenced by the low efficacy on the LS stoichiometry of ligands that cannot bind the α4-β4 site. Sazetidine-A is a full agonist of the HS receptor but in the LS receptor evokes less than $20\,\%$ of the ACh response due to its inability to bind the α4-α4 interface [71], but the full agonism is recovered in co-application with a ligand that binds to the α4-α4 site, such as 3-[3-(3-Pyridinyl)-1,2,4-oxadiazol-5-yl]benzonitrile (NS9283) [73]. Thus, this binding site provides an ideal target for developing stoichiometry-selective drugs. Such is the case of the aforementioned NS9283, a positive modulator of the LS stoichiometry that binds exclusively the α4-α4 binding site [74, 75, 76, 50]. This drug is the focus of Chapter 3.



Figure 1.5: Alternative stoichiometries of the α4β2 subtype. The location of the orthosteric and unorthodox binding sites are highlighted with stars.

1.4.2 The α7 Subtype

The α7 nAChR is also abundant in the central nervous system, and it is enriched in regions associated with cognitive functions [77]. Unlike the nicotinic receptors containing α2-6 subunits, which assemble in combination with β subunits, the α7 subtype is constructed in a homopentameric fashion, with the α7 subunit providing both faces of the binding site [36, 30], thus the α7 subtypes contain five identical orthosteric binding sites. Contrary to other neurotransmitter ion channels where the activated state stability increases with the number of binding sites occupied, in the α7 receptor the occupation of only one binding site is sufficient to achieve maximal open-channel lifetime at the single-channel level [78]. Another unique property of the α7 compared to other nicotinic subtypes is its fast desensitisation rate [79]. This can be observed as currents evoked by agonist decay rapidly with continuous agonist application (Figure 1.6). In fact, the desensitisation of the receptor is so fast that in electrophysiological systems the agonist exchange is the limiting factor [80], which means it cannot be properly measured from macroscopic currents recorded in *Xenopus* oocytes, where the drug application is slow. Even in HEK cells, the rates vary if macroscopic currents are recorded from whole-cell or smaller outside-out patches [81]. Because the onset of the desensitisation is too quick, peak amplitude occurs early on the agonist application pulse, even before the solution exchange is complete.

This results in the measured response being lower than the real response evoked by that concentration, making EC_{50} values inaccurate among different experimental setups [79]. Other features that make the α7 receptor unique among the nicotinic subtypes are its low sensitivity to classical agonists like ACh and nicotine, full activation by choline (which acts as a partial agonist of other nAChRs) and its high Ca^{+2} permeability, which results in additional metabotropic effects of the receptor activation [82, 83].

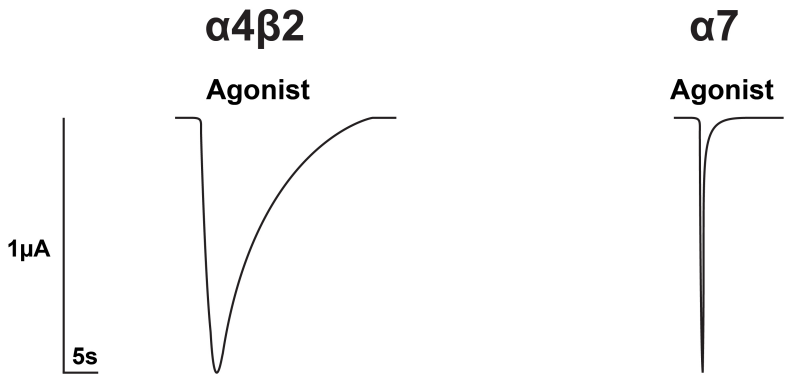

Figure 1.6: Desensitisation kinetics of the α7 compared to the α4β2 subtype. These traces are just schematic and do not necessarily reflect any particular experiment.

1.5 Distribution of the α4β2 and α7 nAChRs

The nAChRs are widely distributed throughout the central and peripheral nervous systems. Also, it has been found that they are expressed in non-neuronal tissue [84, 85]. In the brain, nAChRs are mainly localised presynaptically where they modulate the release of other neurotransmitters like dopamine, glutamate, GABA, serotonin, and noradrenaline [86, 61]. They are also expressed in extrasynaptic sites (axonic and somatodendritic sites) where they regulate neuronal depolarization [87]. Additionally, there are a few observations of synaptic nAChRs mediating cholinergic synaptic transmission in the brain [84].

The $\alpha4\beta2$ subtype is present in the cortex, the striatum, the superior colliculus, the mesencephalon, the hippocampus, and the cerebellum [61, 63] where it contributes to the cognitive function [88]. For example, $\beta2$ knockout mice show attention deficits which can be reverted with selective re-expression of the subunit in the medial prefrontal cortex [89]. The exact distribution of the different stoichiometries of the $\alpha4\beta2$ nAChR in the brain is not entirely clear, although there is evidence that both stoichiometries are expressed natively in the brain [90, 91] with the LS stoichiometry being predominant in the cortex [92, 91].

$\alpha7$ receptors are expressed in neuronal cells in the hippocampus, cortex, and subcortical limbic regions, areas of the brain that relate to learning, memory and cognition [93]. Additionally, they are expressed in non-neuronal cells in the brain, such as astrocytes, microglia, endothelial cells, and macrophages, where they play a role in neuroinflammation, brain immunity and neuroprotection [85, 79].

A summary of the distribution of the $\alpha4\beta2$ and $\alpha7$ subtypes in the brain is illustrated in Figure 1.7.

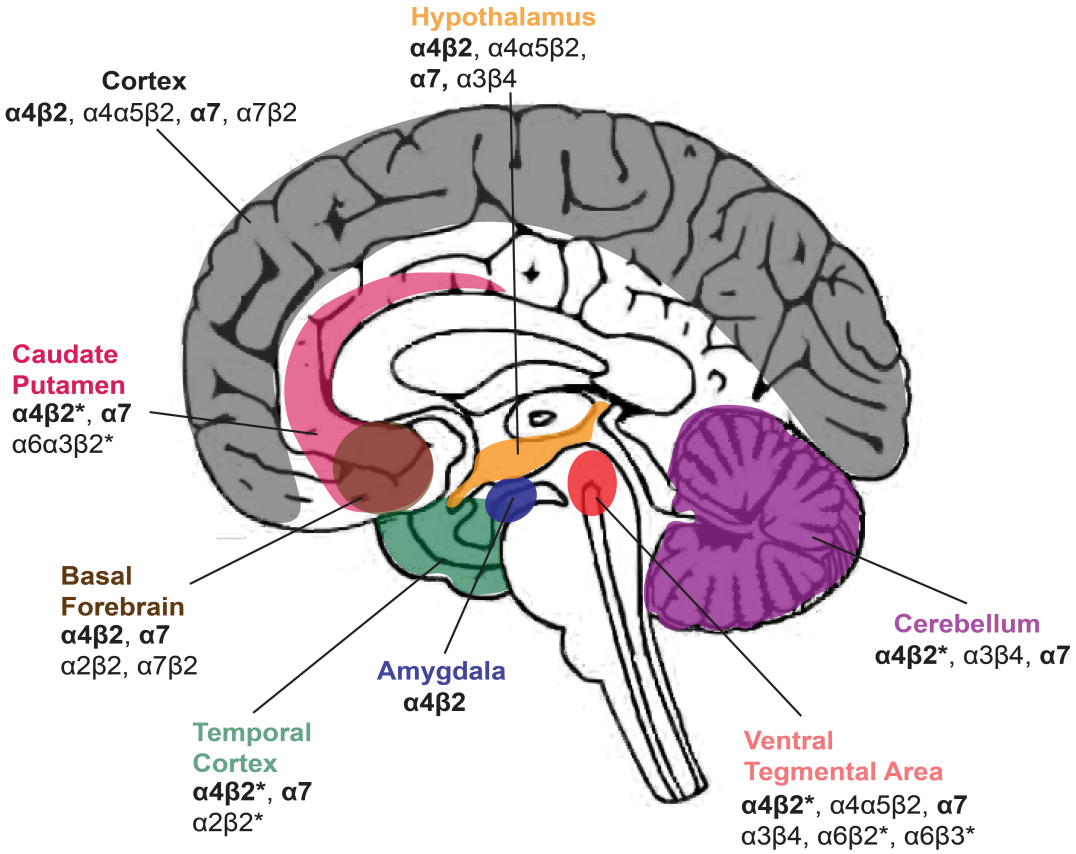

Figure 1.7: Distribution the α4β2 and α7 subtypes in the brain. (Reproduced from Zoli et al [63]).

1.6 Role of the α4β2 and α7 nAChRs in Disease

Because of their ubiquitous distribution and modulatory role in several neuronal circuitries in the brain, nAChRs are involved in the pathophysiology of several neurodegenerative diseases and mood disorders such as Alzheimer's disease (AD), Parkinson's disease (PD), attention deficit hyperactivity disorder (ADHD), schizophrenia, depression, and of course, nicotine addiction [61, 85].

1.6.1 Nicotine Addiction

Tobacco addiction is one of the leading causes of preventable disease worldwide, with more than 7 million deaths each year in the world [94]. The main active compound in tobacco is nicotine, a naturally occurring alkaloid that acts as a non-selective nAChR agonist (see Section 1.7.1). As with all drugs of abuse, nicotine acts at the mesolimbic reward pathway, modulating dopaminergic neurons in the ventral tegmental area (VTA) that project into the nucleus accumbens (NAcc) [95]. Nicotine in the brain can directly activate the dopaminergic neurons in the reward pathway by binding to the high-affinity $\beta 2$ containing receptors (such as the $\alpha 4\beta 2$ subtype) at the presynaptic terminals, producing the release of dopamine in the VTA [96]. $\alpha 4\beta 2$ nAChRs are also expressed in GABAergic neurons in the VTA that inhibit the dopamine neurons, so nicotine produces a simultaneous activation and inhibition of the dopaminergic neurons. Nevertheless, $\alpha 4\beta 2$ nAChRs become desensitised when low nicotine levels are chronically present, reducing the GABAergic drive. On the other hand, glutamatergic activation of the dopamine neurons is enhanced by the activation of pre-synaptic $\alpha 7$ nAChRs, which are less prone to desensitisation by low levels of nicotine due to their lower sensitivity to the drug [97]. This results in a long-lasting excitation of the dopaminergic neurons after nicotine administration. The combination of reduced GABAergic inhibition with increased glutamatergic excitation enhances the activity of the dopaminergic neurons in the mesencephalon. Additionally, VTA dopaminergic neurons projecting into the striatum express nicotinic receptors in their presynaptic terminals, modulating striatal dopamine release [95].

Aside from activating the reward pathway, chronic nicotine administration produces nicotinic receptor upregulation due to persistent receptor desensitization[98]. This occurs because, unlike with the endogenous neurotransmitter ACh, acetylcholinesterase cannot hydrolyse nicotine in the synapse. As mentioned in Section 1.4.1 $\alpha 4\beta 2$ is the

main high-affinity binder of nicotine in the brain, meaning they are upregulated by low, physiologically-relevant nicotine concentrations [95].

Naturally, nicotinic receptors are the primary target for the therapeutic management of tobacco addiction. Approved treatments targeting the nAChR include nicotine-replacement therapy, varenicline, and cytisine [99]. Nicotine replacement therapy includes several alternative means of a slow and sustained administration of nicotine, like gum, nasal spray, oral inhaler, and tablets. They relieve craving symptoms and prevent relapse [100]. Varenicline, a high-affinity partial agonist of the $\alpha4\beta2$ nAChR, was developed by Pfizer in 1997 for smoking cessation therapy. Its structure is derived from the naturally occurring nAChR alkaloid cytisine, which was also tried for smoking cessation [101]. It is highly selective for the $\alpha4\beta2$ over the $\alpha7$, $\alpha3\beta4$, and $\alpha1\beta\gamma\delta$ subtypes, which means it attenuates the reinforcing effect of nicotine exerted over the dopaminergic reward pathway [102]. Varenicline has been demonstrated to be the most effective pharmacotherapy to treat nicotine addiction, while also being safe and tolerable [101]. Finally, cytisine is used for smoking cessation in central and eastern Europe. It has significant efficacy in the treatment of smoking with no serious safety concerns, but shows more adverse effects than nicotine-replacement therapy [103].

1.6.2 Alzheimer's Disease

AD is a neurodegenerative disease and the most common type of dementia, representing about $60\,\%$ to $80\,\%$ of dementia cases. Although the exact causes of AD are still undetermined, several factors have been identified as contributing to the neuronal dysfunction, namely the accumulation of misfolded amiloid-β (Aβ) peptide outside neurons and the accumulation of the protein tau inside neurons [104]. This accumulation leads to an innate immune response producing neuroinflammation [105]. It also produces cell death and interferes with critical processes in neurons, like neuron-neuron communication in

the case of the Aβ peptide and with intracellular transport in the case of the protein tau. This leads to the loss of ACh production and cholinergic neurons in the basal forebrain, leaving brain regions associated with attention and memory deprived of cholinergic innervation in the early stages of AD [85]. It has been observed that Aβ accumulates mainly in regions of the brain enriched with $\alpha4\beta2$ and $\alpha7$ nAChRs, which suggests an explanation for the particular vulnerability of the hippocampus and neocortex to Aβ toxicity [106, 107]. Moreover, the Aβ peptide interacts strongly with the $\alpha4\beta2$ and $\alpha7$ receptors, with a remarkably high affinity for the $\alpha7$ subtype [108]. $\alpha4\beta2$ nAChRs are antagonized by Aβ and lost in early AD [109]. In contrast, the interaction of $\alpha7$ with Aβ results in receptor activation at low concentrations [107] and inhibition at higher concentrations due to prolonged receptor desensitisation [106]. In AD, the aberrant accumulation of Aβ peptide means that the majority of the $\alpha7$ nAChRs are associated with Aβ. Still, upon dissociation, the $\alpha7$ function is recovered [110], suggesting an avenue for therapeutic intervention.

Since cholinergic deficit is one of the hallmarks of early AD, drugs preventing ACh hydrolysis in the synapse (acetylcholinesterase inhibitors) are used as the first line of treatment for AD, improving memory and other cognitive functions throughout the disease [111]. Unfortunately, these drugs do not stop the progression of the disease and they only provide symptomatic relief. As mentioned in Section 1.5 $\alpha4\beta2$ and $\alpha7$ nAChRs are expressed within the basal forebrain cholinergic nuclei (Figure 1.7) and in pre and post-synaptic sites in their projection areas, which are important for the type of cognitive performance affected by AD [85]. Considering this, several agonists and partial agonists targeting $\alpha4\beta2$ and $\alpha7$ nAChRs have been tried as a treatment for AD. Examples are: the $\alpha7$ partial agonist (R)-7-chloro-N-quinuclidin-3-yl)benzo[b]thiophene-2-carboxamide (EVP-6124) [112], varenicline, a partial agonist of the $\alpha4\beta2$ [113], and (E,2S)-N-methyl-5-(5-propan-2-yloxypyridin-3-yl)pent-4-en-2-amine (AZD-3480) a partial agonist of the $\alpha4\beta2$ and the $\alpha2\beta2$ nAChRs [114].

1.6.3 Parkinson's Disease

PD is the second most prevalent neurodegenerative disease after AD. It is characterized by postural instability, bradykinesia, and a general tremor. These motor symptoms result from a degeneration of the nigrostriatal dopaminergic pathway. Additionally, other neurotransmitter systems in the brain are affected, such as the adrenergic, cholinergic, serotonergic, glutamatergic, and GABAergic pathways, but to a lesser degree than the nigrostriatal dopaminergic pathway. The damage in these systems contributes to motor dysfunction but also produces the non-motor symptoms associated with PD, which include cognitive deficit, sleep disturbance, and autonomic function [115].

The striatum receives mainly dopaminergic innervations from the substantial nigra in its dorsal area [116]. About $90\,\%$ of the neuronal population in the striatum is constituted by GABAergic neurons projecting into the rest of the basal ganglia where motor function is regulated [115]. The striatum contains some of the highest levels of ACh in the brain, this comes from a population of large cholinergic interneurons. Even though they represent less than $2\,\%$ of the neurons in the striatum these cells have an ample network of processes [117]. These cholinergic interneurons are tonically active, releasing continuous pulses of ACh under basal conditions [118]. The dopamine afferents manifest a similar tonic activity at rest, but activation of midbrain dopaminergic neuron changes their activity into a burst pattern with a greater release of dopamine in the striatum [119], which is accompanied by inhibition of the cholinergic interneurons. This synchronized reciprocal response relies on nigrostriatal and thalamic inputs to the striatum showcasing the inter-relationship between dopamine and cholinergic systems in the region [115]. Dopaminergic terminals in the striatum contain presynaptic $\alpha4\beta2$ and $\alpha6\beta2$ nAChRs [115]. The dopaminergic neurons that innervate the striatum emerge from mesencephalic projections in the substantia nigra pars compacta [120]. Within the substantia nigra there is also local somatodendritic release of dopamine, which can be modulated by nAChRs

[121] since there is somatodendritic presence of the $\alpha4\beta2$, $\alpha7$ and $\alpha6\beta2$ subtypes [115]. The substantia nigra also contains a population of GABAergic interneurons and afferent neurons that act as a brake for dopaminergic neuronal activation that are modulated by nAChRs, particularly $\alpha4\beta2$ [115].

Epidemiological studies have shown an inverse correlation between smoking and PD. Furthermore, this correlation is dose-dependent, with the incidence of PD decreasing both with smoking duration (years of smoking) and intensity (number of cigarettes per day) [115]. Evidence from Parkinsonian animal models supports the hypothesis that nicotine plays a role in neuroprotection against nigrostriatal damage [122, 123, 124, 125]. This highlights the potential of nicotinic receptors as targets for treating PD. Nevertheless, to date, there are no new nAChR-targeting drugs with prospective or current clinical trials for therapeutic use in PD [126].

1.6.4 Attention Deficit Hyperactivity Disorder

ADHD is the most common neurodevelopmental disorder, affecting about $5\,\%$ of children and $2.5\,\%$ of adults. It is characterized by impaired attention, disorganization, and hyperactivity or impulsivity. This causes significant problems in social, academic, or occupational functioning [127]. One of the main components of ADHD's cognitive dysfunction is a deficit in executive function [128]. This refers to "the ability to maintain an appropriate problem-solving set for the attainment of a future goal" as defined by Welsh and Pennington [129], this involves the capacity to defer a response to a later time, a mental representation of the task, and a strategic plan of action sequences [130].

The underlying pathophysiology of ADHD is not well known, however, available experimental evidence suggests that abnormalities in the frontal and frontostriatal networks and catecholamine dysregulation play a critical role in the disorder [131]. Dopamine and norepinephrine in the subcortical and cortical regions are believed to be the main

modulators of ADHD. In addition, cholinergic dysregulation appears to play a role in the disorder's pathophysiology [127]. Cholinergic pathways that originate in the basal forebrain project into the cerebral cortex, making ACh important for normal cognitive function, this includes processes that are affected in ADHD, such as attention, working memory, and executive function [132]. Furthermore, epidemiological studies have shown a correlation between a higher risk of smoking and the incidence of ADHD [133]. Also, maternal smoking during pregnancy is associated with an increased risk of ADHD in the offspring [134].

Pharmacotherapy for ADHD is often used to treat the disorder, including stimulant medication like methylphenidate and amphetamine and non-stimulants like atomoxetine [135]. Both classes of drugs present several limitations, such as adverse side effects and limited long-term effectiveness [127]. Several nAChR-targeting drugs have been tried for the treatment of ADHD, mainly agonists or partial agonists of the $\alpha 4\beta 2$ subtype, but most failed due to a lack of efficacy when compared to control [127]. A study performed in 2014 showed that AZD-3480, an agonist of the $\alpha 4\beta 2$ nAChR, significantly improved symptoms in adults [136], but no further studies have been published for this drug [127].

1.6.5 Schizophrenia

Schizophrenia is a debilitating mental disorder that affects about $1\,\%$ of the population. This disorder is associated with two types of symptoms, the "positive" type which includes delusions and hallucinations, and the "negative" symptoms which include social withdrawal, poor motivation, and apathy [137]. The main hypothesis of the molecular mechanisms behind schizophrenia points towards changes in dopaminergic function. Imaging studies have shown that presynaptic striatal dopaminergic function is elevated in patients with schizophrenia and correlates directly with the symptoms of psychosis [138]. In line with this, the most used medications for the treatment of schizophrenia are an-

tipsychotics, which act mainly by blocking dopamine D2 receptors [138]. Unfortunately, these drugs produce several unwanted side effects, such as weight gain and metabolic disorders [139]. Moreover, although they block the effect of inappropriate dopamine release, they do not treat the primary upstream neuronal abnormalities at the presynaptic control level [138].

nAChRs, particularly the α7 subtype, have gained some interest as targets for treating schizophrenia. This is due to the epidemiological evidence of a higher incidence of smoking in schizophrenia patients and the observation that exposure to nicotine normalizes sensory deficits produced by schizophrenia [139, 140]. Additionally, genetic analyses show that mutations in the gene that encodes the α7 subunit (CHRNA7) are associated with an increased risk of schizophrenia and that the gene's mRNA is decreased in the prefrontal cortex and hippocampus of schizophrenia patients [141]. Consequently, several agonists and allosteric modulators of the α7 nAChR have been tried for cognitive improvement in schizophrenia, but no drug has made it past the phase III clinical trials. For example, the α7 partial agonist EVP-6124 failed in the clinical trial stage III due to a lack of efficacy and toxicity concerns [139].

1.6.6 Depression

Depression is a debilitating mood disorder that affects about one in five people in any point in their lives, it is characterised by feelings of sadness and helplessness, loss of pleasure and lack of motivation, cognitive deficits, and vegetative symptoms. Despite its far-reaching impact on society, the pathophysiology of depression is not well understood [142]. Thus, the biological processes affected by depression have been underpinned by the pharmacology of drugs used to treat the disorder. The main medications used in antidepressant pharmacotherapy are selective serotonin reuptake inhibitors, which block the serotonin transporter increasing the synaptic concentration of

serotonin. Reduced serotonin receptors in post-mortem brains of depressed patients also support these observations [143]. Dysfunction of other monoamines in the brain, such as norepinephrine and dopamine have also been observed to be involved in depression [143], therefore polypharmacological drugs targeting more than one monoamine transporter in the brain have shown higher efficacy than traditional serotonin reuptake inhibitors [144].

Similarly, the involvement of cholinergic neurotransmission in depression is supported by the effect of cholinergic drugs on depressive symptoms. For example, exposure to anticholinesterase pesticides can induce depression-like symptoms [145, 146]. Additionally, it has been reported that scopolamine, an antagonist of the muscarinic acetylcholine receptors, displays antidepressant properties [147]. Furthermore, there is a well-established relationship between smoking and depression. The prevalence of nicotine dependence in depressive patients ranges from $50\,\%$ to $60\,\%$, much higher than the $25\,\%$ in the general population. Additionally, smoking cessation can lead to the onset of depressive symptoms [148]. Although not recommended as a therapeutic alternative to depression, transdermal nicotine has been shown to improve symptoms of depression, even in nonsmoking patients [149]. Consistently, other nicotinic ligands, such as the antagonists mecamylamine, dihydro-β-erythroidine, and the partial agonist cytisine, have demonstrated antidepressant effects in humans or animal models [150]. This evidence suggests that hyperactivation of the cholinergic system is related to depression, and thus decreasing its activity, either by antagonism or desensitization of the nAChRs, is a valid strategy to treat depressive symptoms [122]. Because of the wide distribution of the $\alpha 4\beta 2$ nAChR in the brain, particularly in areas related to reward and mood (prefrontal cortex, amygdala, hippocampus, VTA, and NAcc), it is the main subtype of interest as a therapeutic target for depression, but no agent has been successfully developed for this purpose yet [150, 151].

1.7 Neuronal nAChR Pharmacology

Neuronal nicotinic receptors exhibit a rich pharmacology of both orthosteric and allosteric ligands. Since this thesis is focused on the $\alpha4\beta2$ and $\alpha7$ subtypes only the compounds that target these receptors will be reviewed in this section.

1.7.1 Orthosteric ligands

Orthosteric ligands are compounds that bind the neurotransmitter binding site present in the extracellular domain of nAChRs (see Section 1.3.1) [152]. Depending on their capacity to elicit gating of the channel these can be divided into agonists, partial agonists, and antagonists. Table 1.1 contains a summary of the ligands reviewed in this section and Figure 1.8 depicts the structure of the ligands.

A common trait among all nAChR agonists is the presence of a protonable amine that carries a positive charge at physiological pH. This charge is necessary to engage in the cation-π interaction that stabilizes the ligand in the aromatic box of the binding site, and this interaction is key for the agonist-induced response as mentioned in Section 1.3.1. Several resolved structures, both from acetylcholine binding protein (AChBP) [153, 44, 154, 155] and nAChRs [23, 30, 36, 29, 28] show agonists with their charged amino groups oriented towards aromatic residues, particularly the tryptophan in loop B (see Figure 1.2. On the other hand, the less conserved residues in the complementary side of the binding site (loops D, E, and F) contribute to ligand selectivity, through hydrogen bond interactions with the main chain of the residues in these loops [156].

Agonists and partial agonists stabilize loop C of the principal subunit in a closed conformation (Figure 1.2B green). Full agonists, such as the endogenous neurotransmitter ACh, can be differentiated from partial agonists by their maximum efficacy (the high concentration asymptote in a concentration-response curve, as constructed in Section

2.2.3.6) when activating the receptors [157]. At a structural level, the efficacy depends on the ligand binding free energy difference between the activated and the open state [38]. Thus, partial agonists have a dual agonist-antagonist action on the receptor, preventing full activation of the receptors at the ensemble level. Nevertheless, it is worth noting that the open state elicited by the partial agonists is the same as the one evoked by full agonists [158]. Antagonists on the other hand stabilize an extended loop C conformation (Figure 1.2B purple) and compete with agonists, preventing their binding [84].

The pharmacological characteristics of ligands are not intrinsic to their structure, instead, they depend on their interactions with the receptor. In the $\alpha4\beta2$ subtype they are different for each receptor stoichiometry [65], this is because of the extra unorthodox $\alpha4$-$\alpha4$ binding site in the LS stoichiometry, as reviewed in Section 1.4.1. On the other hand, the structural difference of the $\alpha7$ nAChR compared to other subtypes [32] confers some unique properties to it, which include a distinct pharmacological profile among nAChRs [79].

ACh is the primary endogenous ligand of all nAChRs. It is a full agonist, and other agonists' efficacy is typically expressed relative to the efficacy of ACh. It is a popular choice to activate nicotinic receptors in electrophysiological experiments, but it has two major limitations that need to be accounted for: It can activate muscarinic acetylcholine receptors if they are present in the system and it is prone to hydrolysis [84].

Choline is both a precursor and a metabolite of ACh. It has no agonist activity on HS $\alpha4\beta2$ nAChRs and has almost no efficacy on the LS stoichiometry with a lower potency than ACh [159], which explains its lack of activity in rat hippocampal neurons [160]. In the $\alpha7$ subtype, it acts as a full agonist, but with even lower potency [160].

Nicotine is the eponymous agonist of the nAChRs, it activates almost all subtypes, except the $\alpha9$ containing receptors [161]. It is the main active compound in tobacco and was used historically to discover and study nAChRs (as briefly reviewed in Section 1.2). It

has a very high affinity for the $\alpha4\beta2$, particularly for the HS stoichiometry. It behaves as a partial agonist of this subtype, with an efficacy of about $30\,\%$ of the ACh response on the HS stoichiometry and about $60\,\%$ on the LS [65]. Similar to the LS receptor, nicotine in the $\alpha7$ subtype behaves as a partial agonist with an efficacy of $70\,\%$ of the ACh response and with a lower affinity compared to the HS receptor [162].

Epibatidine is another classical nAChR agonist, it is a poison originally obtained from the skin of the Amazonian frog *Epidobates tricolor* [84]. This alkaloid is one of the most potent nicotinic agonists, it elicits responses with sub-micromolar EC_{50}s [162]. In the $\alpha4\beta2$ HS stoichiometry it has a maximum efficacy of about $60\,\%$ relative to ACh, while in the LS stoichiometry it elicits a maximum response of close to $200\,\%$ of the ACh one [65]. It behaves as a full agonist of the $\alpha7$ nAChR [162].

Cytisine is a naturally derived tricyclic alkaloid derived from plants of the *Leguminosae* family. It has a high-affinity partial agonist of the $\alpha4\beta2$ subtype, with almost negligible efficacy in HS stoichiometry, but a higher efficacy $(22\,\%)$ in the LS one [65]. In the $\alpha7$ nAChRs it has less potency but elicits a full response [163].

Varenicline is a synthetic alkaloid designed as an aid in smoking cessation using cytisine as a template (see Section 1.6.1). Similar to its parent compound is highly potent in the HS $\alpha4\beta2$, less potent in the LS stoichiometry [156], and even less potent in the $\alpha7$ [164]. Likewise, the efficacy is low in the HS receptor, about $10\,\%$ of the ACh response. It has higher efficacy in the LS multimer eliciting $30\,\%$ of the ACh response [156]. In the $\alpha7$ subtype, it behaves as a full agonist [164].

Although most agonists mentioned have differences in their efficacies and affinities across the $\alpha4\beta2$ stoichiometric, the overall pattern is for most ligands to have higher efficacy and lower affinity for LS and lower efficacy and higher affinity for the HS stoichiometry. However, there are a few ligands that do not conform to this pattern. One of them is sazetidine-A, this highly potent agonist of the $\alpha4\beta2$ receptors has an EC_{50}

in the nanomolar range for both stoichiometries, but it behaves as a full agonist of the HS multimer while eliciting low responses in the LS receptor [73]. Structurally, this occurs due to sazetidine-A being unable to bind the α4-α4 interface, which is necessary to achieve full activation of the LS receptor [71, 73]. Another agonist with such a pattern is TC-2559, a potent agonist that produces similar responses as sazetidine-A in the LS stoichiometry [65, 73] because it also fails to effectively bind the α4-α4 interface [71]. In the HS stoichiometry, however, it elicits a response much higher than the maximum response evoked by ACh, classifying it as a super-agonist [65, 73]. The mechanism behind this so-called super-agonism is not well explained yet and is the focus of Chapter 5.

Tropisetron is an antiemetic owing its effect for its antagonism of the 5-HT_3 receptor [165], likewise, it acts as a weak antagonist of the α4β2 nAChR [166]. In the α7 receptor though, it acts as a potent partial agonist with a relative efficacy of $40\,\%$ [162].

The antagonist selection is not as rich as the partial agonist one for nAChRs, and most of the examples are naturally derived compounds. Probably the most classical nicotinic antagonist is tubocurarine, a poison present in the South American shrub *Chondodendron tomentosum*. It was used, along with nicotine, in early studies to characterize the nicotinic receptors (see Section 1.2). It has a higher affinity for muscle-type nAChRs, but it inhibits neuronal nicotinics with micromolar concentration nonetheless [84].

Dihydro-β-erythroidine is an alkaloid extracted from the seeds of plants from the genus *Erythrina* that blocks α4β2 with a sub-micromolar affinity, and α7 with about 10-50 fold less potency [84].

α-Bungarotoxin is a polypeptide snake toxin from the venom of *Bungarus multicinctus*. It binds the muscle and α7 nicotinic receptors with very high affinity in a quasi-irreversible manner. It is highly selective and it does not interact with heteromeric neuronal nAChR [84].

Methyllycaconitine is an alkaloid obtained from *Delphinium sp.* and it is a potent α7 competitive antagonist. It inhibits the α4β2 nAChR with 3 orders of magnitude less potency, and there is evidence it may bind at the α4-α4 interface [84, 167, 168].

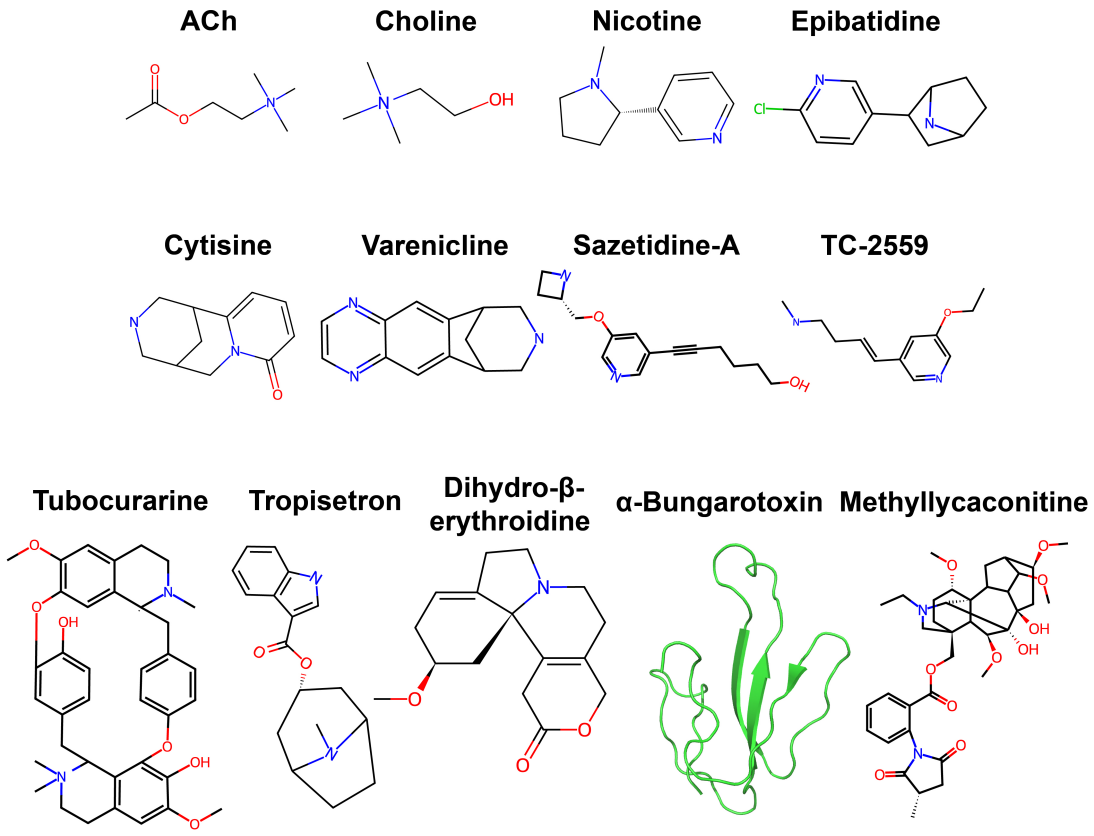

Figure 1.8: Chemical structures of the orthosteric ligands listed in Table 1.1

1.7.2 Allosteric ligands

Allosteric ligands are compounds that interact with binding sites located apart from orthosteric sites, called "allosteric sites". Allosteric modulators do not directly activate the receptor but indirectly affect the activity of agonists. These modulators can be positive,

Table 1.1: Orthosteric ligands of the α4β2 and α7 nAChRs. α4β2 receptor stoichiometric is denoted by (a) and (b) for HS and LS respectively and (ab) for mixed stoichiometry. N.D. refers to a not-determined value. EC_{50} or IC_{50} are reported depending on whether the ligand is an agonist or antagonist respectively. Efficacy is reported relative to the maximum response of ACh.

	α4β2 HS (a) / LS (b)		**α7**		
Ligand	**EC_{50} or IC_{50}**	**I_{max}/I_{ACh}**	**EC_{50} or IC_{50}**	**I_{max}/I_{ACh}**	**Ref**
ACh	4 µM (a) / 88 µM (b)	100 % (ab)	1.6 mM	100 %	[65, 84]
Choline	400 µM (a) / N.D. (b)	3 % (a) / N.D. (b)	1.58 mM	100 %	[159, 160]
Nicotine	1 µM (a) / 34 µM (b)	28 % (a) / 62 % (b)	91 µM	74 %	[65, 162]
Epibatidine	20 nM (a) / 1.3 µM (b)	60 % (a) / 220 % (b)	72 nM	97 %	[65, 162]
Cytisine	N.D. (a) / 12 µM (b)	N.D. (a) / 22 % (b)	14 µM	90 %	[65, 162]
Varenicline	27 nM (a) / 3.6 µM (b)	10 % (a) / 30 % (b)	18 µM	96 %	[156, 164]
Sazetidine-A	10 nM (a) / 23 nM (b)	18 % (a) / 108 % (b)	N.D.	N.D.	[73]
TC-2559	0.64 µM (a) / 3.3 µM (b)	43 % (a) / 330 % (b)	N.D.	N.D.	[73]
Tubocurarine	3.2 µM (ab)	Antagonist	3.1 µM	Antagonist	[169]
Tropisetron	170 µM (ab)	Antagonist	380 nM	Antagonist	[166, 162]
Dihydro-β-erythroidine	110 nM (ab)	Antagonist	20 µM	Antagonist	[169]
α-Bungarotoxin	N.D.	N.D.	50 nM	Antagonist	[162]
Methyllycaconitine	140 nM (a) / 90 nM (b)	Antagonist	25 pM	Antagonist	[167, 168]

negative, silent, or allosteric agonists [170]. PAMs potentiates the effect of agonists without eliciting a receptor response on their own, but by increasing the probability of opening at the single channel level, translating into a higher macroscopic response [171]. On the other hand, NAMs inhibit the receptor's response in a non-competitive manner by decreasing the probability of opening [172]. It is worth noting that NAMs are different from channel blockers, which prevent the transport of ions by occluding the pore instead of modifying the gating dynamics [173]. Silent allosteric modulators (SAMs) are ligands that bind to the allosteric site of a PAM without eliciting the potentiation, thus acting as "competitive antagonists" at the allosteric site [174]. Finally, allosteric agonists are ligands capable of eliciting responses on their own without needing the presence of an agonist, but by binding a site different from the orthosteric binding site [170]. Table 1.2 provides a summary of the allosteric modulators reviewed in this section and Figure 1.10 depicts the structures of the ligands.

Positive allosteric modulation in the α7 nAChRs is classified into two types depending on their macroscopic effects (Figure 1.9). Type I PAMs enhance agonist evoked responses without affecting the desensitization rate of the receptor, which in the α7 subtype is particularly fast (see Section 1.4.2). On the other hand, type II PAMs delay desensitization of the receptor and can rescue desensitized receptors [82].

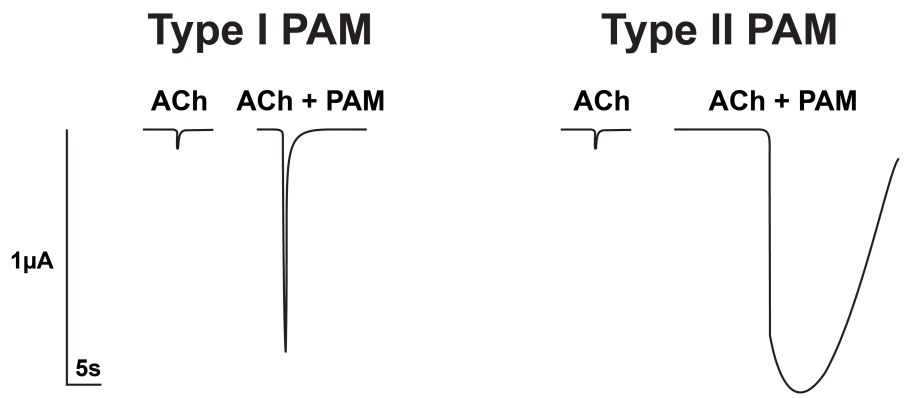

Figure 1.9: Representative macroscopic traces of type I and Type II positive allosteric modulators. These traces are just schematic and do not necessarily reflect any particular experiment.

The first type I α7 PAM ever reported is 5-hydroxyindole (5-HI), it is able to potentiate the response of $60\,\mu\mathrm{M}$ ACh by $1200\,\%$ with an EC_{50} of $2.5\,\mathrm{mM}$ [175]. Another type I PAM is N-(5-Chloro-2-hydroxyphenyl)-N'-[2-chloro-5-(trifluoromethyl)phenyl]urea (NS1738), this compound potentiated the response of $100\,\mu\mathrm{M}$ of ACh to a maximum of $322\,\%$ with an EC_{50} of $3.4\,\mu\mathrm{M}$ in the human α7 receptor and had comparable efficacy and affinity in the rat α7 [176]. Natural products such as the flavonoids genistein, quercetin, and the neoflavonoid 5,7-dihydroxy-4-phenylcoumarin have also demonstrated type I potentiation of $30\,\mu\mathrm{M}$ ACh in the α7 nAChR with EC_{50}s of $9.36\,\mu\mathrm{M}$, $15.39\,\mu\mathrm{M}$, and $9.64\,\mu\mathrm{M}$ respectively [177]. A very interesting PAM of the α7 subtype is 4-[(1R,3R)-3-[(5-chloro-2-methoxyanilino)methyl]-2,2-dimethylcyclopropyl]benzenesulfonamide (BNC375), one stereoisomer behaves as a type I PAM with an EC_{50} of $25\,\mathrm{nM}$ and a maximum potentiation of $650\,\%$, while the other acts as a type II PAM [178]. Finally, ivermectin, an anthelmintic drug used to treat parasite infection, acts as a type I PAM of the α7 receptor in micromolar concentrations, potentiating the response of $100\,\mu\mathrm{M}$ of ACh to a $350\,\%$ [179].

On the side of type II PAMs the prototypical example is N-(5-Chloro-2,4-dimethoxyphenyl)-N'-(5-methyl-3-isoxazolyl)-urea (PNU-120596), the first α7 PAM to reduce drastically receptor desensitization generating a $400\,\%$ enhancement of the agonist response with an EC_{50} of $216\,\mathrm{nM}$ [180]. Another type II PAM is 4-naphthalen-1-yl-3a,4,5,9b-tetrahydro-3H-cyclopenta[c]quinoline-8-sulfonamide (TQS), which has a similar effect to PNU-120596 on agonist activity and receptor desensitization, although with lower potency (EC_{50} of $3.16\,\mu\mathrm{M}$) [181]. 5-chloro-N-[(1S,3R)-2,2-dimethyl-3-(4-sulfamoyl-phenyl)-cyclopropyl]-2-methoxy-benzamide (RO5126946) is another potent type II PAM discovered and characterized by Roche through library screening and it can potentiate ACh evoked responses by $401\,\%$ with an EC_{50} of $60\,\mathrm{nM}$, delaying the desensitization. Although unlike PNU-120596 it cannot recover desensitized receptors [182].

4-(4-bromophenyl)-3a,4,5,9b-tetrahydro-3H-cyclopenta[c]quinoline-8-sulfonamide (GAT107) is a derivative of TQS that has the capacity of evoking α7 currents in the absence of an agonist. It can elicit half of the maximal ACh response at a concentration of $17\,\mu\mathrm{M}$ [183]. Other congeners of TQS with allosteric activity are the enantiomers of Cis-trans-4-(2,3,5,6-tetramethylphenyl)-3a,4,5,9b-tetrahydro-3H-cyclopenta[c]quinoline-8-sulfonamide (TMP). The (+) enantiomer behaves as a weak type II PAM, but its (-) enantiomer antagonizes the gating elicited by GAT107 [184].

Finally, cannabidiol (CBD) is a negative allosteric modulator of the α7 nAChR, which can inhibit the agonist-induced response of ACh $10\,\mu\mathrm{M}$ by more than $90\,\%$ at the micromolar range with an concentration inhibiting 50 % of the response (IC_{50}) of $0.53\,\mu\mathrm{M}$ in single-channel experiments. Aside from the short-term inhibition of the channel opening, it enhances opening time after several minutes of application, having a dual inhibition potentiation effect of single-channel currents [185].

The binding site for both types of PAMs in the α7 nAChR has been reported, first by mutagenesis and later using Cryo-EM. Initial mutagenesis experiments with chimeric

receptors located the binding site of PNU-120596 and NS1738 in the TM domain [186], but site-directed mutagenesis using a quintuple mutant incorrectly suggested that the site was in an intra-subunit cavity [187]. Similar experiments with ivermectin, combined with molecular docking, pointed to a similar intra-subunit cavity. Eventually, a Cryo-EM structure with PNU-120596 bound was resolved [36], which revealed that the binding site of the type II PAM lay in the inter-subunit space of the TM domain. Later studies using Cryo-EM showed that, aside from PNU-120596, TQS, NS1738, ivermectin, and GAT107 bind the same inter-subunit binding site [35]. This suggests that the difference between types I and II PAMs, and even allosteric agonists, is not in the site they bind, but in the nature of the interactions within this binding site.

For the $\alpha4\beta2$ subtype, the first PAM identified was des-Formylflustrabromine (dFBr), one of the alkaloids isolated from the bryozoa *Flustra foliacea*. It has a cognitive enhancer effect in regular and cognitively impaired rats [188]. It potentiates both stoichiometries of the $\alpha4\beta2$ nAChR, but with different potencies, having a higher affinity for LS receptor. The steroid estradiol also potentiates both stoichiometries, with similar affinities but with more efficacy in the HS multimer [150]. The acetylcholinesterase inhibitor, galantamine, has been reported to potentiate the epibatidine evoked currents in $\alpha4\beta2$ receptor, although this was carried in HEK-293 cells without favouring a specific stoichiometry [189].

NS9283 is a positive modulator selective for the HS $\alpha4\beta2$ nAChR. It binds the unorthodox $\alpha4$-$\alpha4$ binding site in the LS stoichiometry [75]. Since NS9283 binds a site that is considered an orthosteric binding site because it is necessary for full activation of the LS $\alpha4\beta2$ receptor, the categorization of this compound as an allosteric ligand is somewhat inaccurate. Still, due to its positive modulatory effect and its inability to elicit responses on its own, it will be considered a PAMs for this thesis. More details about NS9283's effects and pharmacological profile are given in Section 4.1. Another molecule that binds to this site and has a similar profile to NS9283 is 3-(2-chlorophenyl)-5-(5-methyl-

1-(piperidin-4-yl)-1H-pyrrazol-4-yl)isoxazole (CMPI). It binds with more potency to the LS receptor than NS9283 and potentiates the affinity of agonists, but not their efficacy [76].

The divalent cation Zn^{+2} has a dual PAM and NAM activity depending on the stoichiometry and the concentration. In the LS receptor it potentiates the receptor at the micromolar range, but inhibits the response at the near millimolar scale. On the other hand, in the HS stoichiometry, it only inhibits the response of agonists at micromolar concentrations [53]. Finally, the steroid progesterone acts as a NAM of both stoichiometries in the low micromolar range.

Allosteric binding sites in the α4β2 nAChR have been determined by their selectivity towards the different stoichiometries and using mutant receptors, thus the evidence for these sites is less robust than the Cryo-EM structures recently reported in the α7 nAChR. Still, the binding site determined for NS9283 and CMPI is compelling. Their selectivity for the LS stoichiometry points us to the main characteristic of this receptor, the α4-α4. Due to the ability of this site to bind agonists in the EC domain, radioligand binding assays demonstrated that NS9283 competitively displaced [^{3}H]epibatidine [75]. Furthermore, site-directed mutagenesis studies where amino acids of the complementary face of the α4 subunit are changed into their corresponding analogues of the β2 subunits were shown to abolish function for both modulators [75, 50]. The binding site determination is not as straightforward in the case of a non-selective PAM, such as dFBr. Weltzin and Schulte [190] described a series of mutants of the β2 subunit, particularly of its positive face, that suggests it may bind the non-canonical β2(+)-α4(-) interface. Moreover, the effects of the mutants over the activity of dFBr were more acute on the HS receptor, indicating that the β2-β2 interface, unique to this stoichiometry, may also play a role.

Table 1.2: Allosteric ligands of the α4β2 and α7 nAChRs. N.R. refers to a value not reported. EC_{50} or IC_{50} are reported depending on whether the ligand is a PAM or NAM respectively.[a]Depending on the enantiomer it has a type I or type II effect.

Ligand	**EC50/IC50**	**Target**	**Type**	**Ref.**
5-HI	2.5 mM	α7	Type I PAM	[175]
NS1738	3.4 µM	α7	Type I PAM	[176]
BNC375	25 nM	α7	Type I/II PAM[a]	[178]
Genistein	9.36 µM	α7	Type I PAM	[177]
Quercetin	15.39 µM	α7	Type I PAM	[177]
Neoflavonoid	9.64 µM	α7	Type I PAM	[177]
Ivermectin	6.8 µM	α7	Type I PAM	[179]
PNU-120596	216 nM	α7	Type II PAM	[180]
RO5126946	60 nM	α7	Type II PAM	[182]
TQS	3.16 µM	α7	Type II PAM	[181]
(+)TMP	N.R.	α7	Type II PAM	[184]
(-)TMP	N.R.	α7	SAM	[184]
CBD	0.53 µM	α7	NAM	[185]
GAT107	17 µM	α7	Allosteric agonist	[183]
dFBr	50 nM	α4β2	PAM	[150]
dFBr	16 µM	α4β2	PAM	[150]
Zn^{+2}	50 µM	α4β2 LS	PAM	[53]
Zn^{+2}	881 µM	α4β2 LS	NAM	[53]
Zn^{+2}	19 µM	α4β2 HS	NAM	[53]
NS9283	3.4 µM	α4β2 LS	PAM	[75]
CMPI	0.18 µM	α4β2 LS	PAM	[50]
Galantamine	N.R.	α4β2 Mixed	PAM	[189]
Estradiol	18 µM	α4β2 LS	PAM	[150]
Estradiol	18 µM	α4β2 HS	PAM	[150]
Progesterone	7 µM	α4β2 LS	NAM	[150]
Progesterone	11 µM	α4β2 HS	NAM	[150]

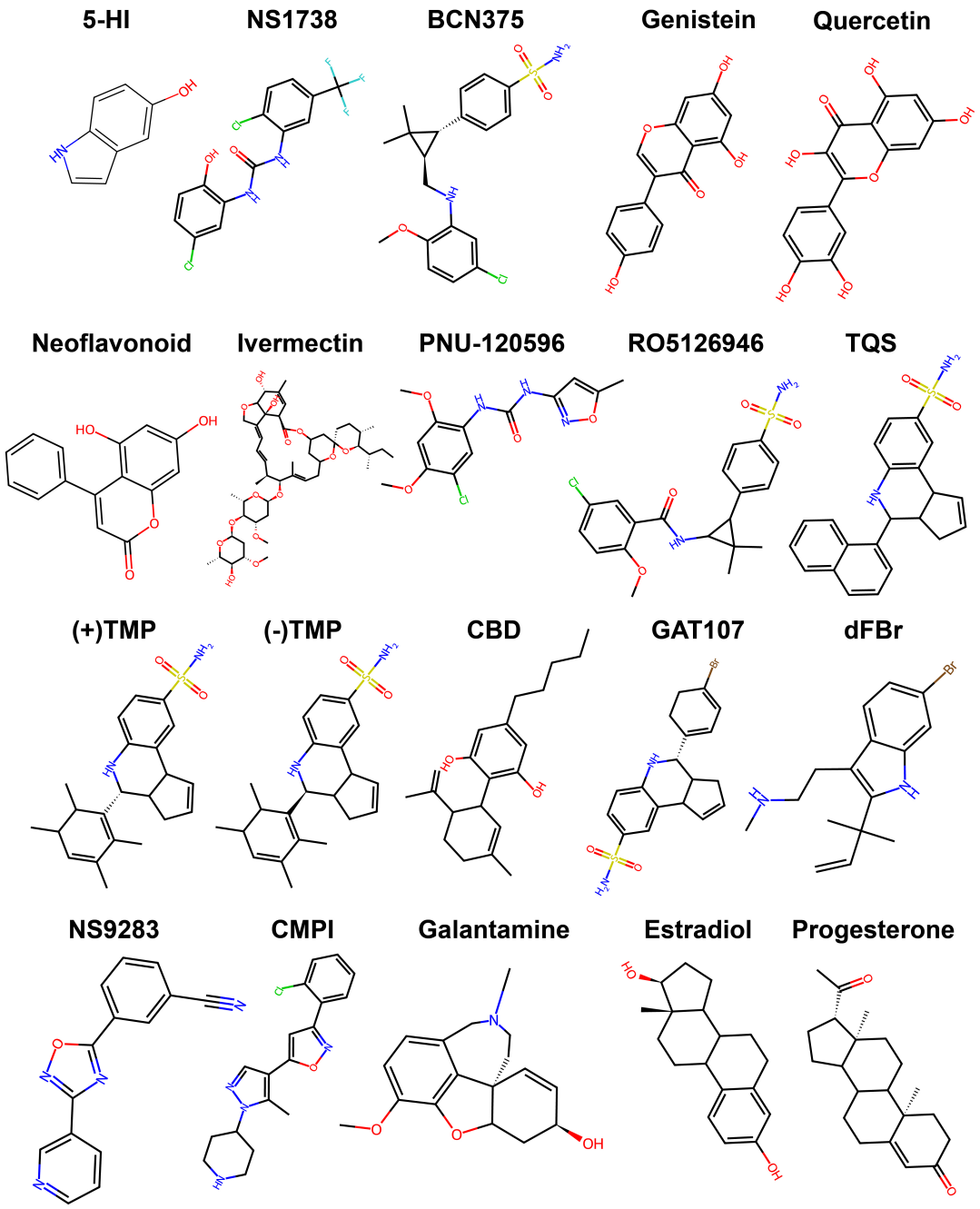

Figure 1.10: Chemical structures of the allosteric ligands listed in Table 1.2

1.8 Aims of this Thesis

Brain nAChRs present themselves as attractive targets for drug discovery because their widespread distribution in the brain makes them key players in many neurological disorders as discussed in Section 1.6. Nevertheless, developing drugs targeting nAChRs orthosteric sites has several difficulties. One of them is that in most of the nicotinic receptor subtypes, prolonged activation of the receptor through the orthosteric site produces desensitization, decreasing the effects elicited by normal ACh binding [191]. Another limitation of orthosteric ligands is the high conservation of the amino acids that compose the binding site across the subtypes, limiting the capability of developing ligands selective enough to target specific diseases that are linked to specific receptor subtype combinations [47]. Allosteric modulators present themselves as an interesting alternative to orthosteric ligands. Since they bind in sites different from the conserved agonist binding domain, they can achieve high subtype selectivity [191], even among stoichiometries of the same subtype [192]. Furthermore, PAMs enhance the endogenous evoked responses of the receptor instead of replacing them [191], and in some cases can even suppress desensitization [193].

To effectively develop ligands that can modulate the activation of receptors it is necessary to have structural insight into their binding sites and binding modes. In this context, the overall goal of this thesis was to characterize the binding mode of allosteric modulators in the $\alpha7$ and $\alpha4\beta2$ nAChRs. The specific objectives were:

- To determine the functional effect, binding site, and binding interactions of novel ether-quinuclidine compounds on the $\alpha7$ nAChR.
- To characterise the structure-activity relationship for NS9283 and a series of congeners by predicting their binding mode in the $\alpha4$-$\alpha4$ interface of the LS $\alpha4\beta2$ nAChR.

- To explore the mechanism behind the super-agonism elicited by the compound TC-2559 on the HS $\alpha4\beta2$ nAChR.

2 | Theory and Methods

2.1 Molecular Dynamics Simulations

Molecular dynamics (MD) is nowadays an essential tool for investigating the function of biomolecules at the atomic level. It can predict the movement of every individual atom in a molecular system as a function of time using classical mechanics, which allows for the estimation of macroscopic equilibrium and non-equilibrium properties that cannot be calculated analytically. This provides a detailed insight into biomolecular processes, such as ligand binding or conformational changes. It can then be combined with experimental methods, as in the work presented in the following chapters, to build a deeper understanding of the key principles contributing to these processes. From the first MD simulations performed in the late 1950s by Alder and Wainwright of an assembly of hard spheres [194], this computational technique has come a long way. The popularity of this technique among scientists has surged in the last decades. In the field of neuroscience, simulations have been widely used to study the behaviour of receptors critical for neuronal signalling and to aid in drug development targeting these receptors [195]. This trend correlates directly with the increased availability of experimentally resolved structures relevant for neuroscience, especially since the recent groundbreaking advances in Cryo-EM for the determination of structures in solution, which earned Jacques Dubochet, Joachim Frank, and Richard Henderson the Nobel Prize in chemistry in 2017 [196]. Furthermore, advances in computer hardware, notably the introduction of GPUs, have made MD simulations of biomolecules, ranging from the hundreds of nanoseconds to the microsecond scale, easily accessible at a moderate expense [197]. Providing a complete review of the mathematical and physical foundations behind the technique is beyond the scope of this chapter, nevertheless, a brief overview of the fundamentals of molecular dynamics will be presented, along with some specific

advanced techniques used in this work, namely replica exchange, umbrella sampling, and metadynamics. The discussion presented in the following sections is based on the exposition by Leach 2001 [198] unless specified.

2.1.1 Quantum Mechanics and Molecular Mechanics

To accurately describe the behaviour of systems at an atomic level, it is necessary to apply quantum mechanics (QM)-based methods. These methods are based on solving the Schrödinger equation, which can be written in an abbreviated, time-independent form:

$$\hat{H}\varphi = E\varphi \tag{2.1}$$

This equation (2.1) pertains to the energy of electrons and nuclei in a molecular system. Here, $\hat{H}$ is the Hamiltonian operator, which corresponds to the sum of the kinetic and potential energy of the system; the latter originates from the electrostatic interactions among the system's particles. φ is the wave function, which characterises the particle's motion and allows us to calculate various of its properties (e.g. expectation values of position, momentum, energy levels, etc.), and E is the particle's energy. Thus, to solve the Schrödinger equation, one must find values of E and functions φ that equate to the wavefunction operated by the Hamiltonian. Solving this equation for simple systems, such as the "particle in a box" or a hydrogen atom with one nucleus and one electron, is analytically possible. Beyond that, getting an exact solution for the Schrödinger equation for a multi-electron system is impossible. To tackle this problem, the Born-Oppenheimer approximation is used [199], in which the motions of the electrons and the nuclei are considered separately. This holds because the mass of the lightest nuclei is about 2000 heavier than the electron, which means that the nuclei can be considered fixed in the timescale of the electronic vibration.

For biomolecular systems in the order of 100,000 atoms, the QM treatment, which considers all electrons in the system, becomes prohibitive in terms of computation time. To overcome this, an alternative to QM is the molecular mechanics (MM) approach, also known as the force field method. In this case, considering the Born-Oppenheimer approximation, the potential energy is calculated for the nuclei alone, and the electrons are regarded as implicit variables of this potential. MM methods, while simplified, can still provide accurate results, even matching those of the QM calculations, but they cannot predict properties that are derived from electronic configuration, such as bond breaking or formation.

2.1.2 Force Fields

Force fields are mathematical functions and parameters that allow us to calculate the potential energy of a molecular system from the spatial coordinates of its particles. Most force fields consist of four components that describe the interactions within the particles of the system: energetic penalties associated with the deviation of bonds and angles from the reference value, a function that describes the energy changes from the bond torsions, and a term that describes the non-bonded interaction between atoms (Figure 2.1). This can be represented by its simplified functional form:

$$U(r_N) = U_{bonds} + U_{angles} + U_{torsions} + U_{non-bonded} \tag{2.2}$$

Where U corresponds to the potential energy as a function of the positions of N particles (r_N), the three left-hand terms correspond to the bonded interactions, and the right-hand term to the non-bonded van der Waals and electrostatic interactions.

2.1.2.1 Bonded Interactions

Bond-stretching: The most elementary approach to model bond stretching is to use a harmonic potential that obeys Hooke's law:

$$U(l) = \frac{k}{2}(l - l_0)^2 \tag{2.3}$$

Here, the energy varies with the square of the difference from the reference bond length l_0. This results in a single global minimum, and deviation from this reference value causes an exponential increment in the energetic penalty (Figure 2.1A).

Angle-bending: The bending of angles is also modelled using Hooke's law as a function of the angle θ (Figure 2.1B):

$$U(\theta) = \frac{k}{2}(\theta - \theta_0)^2 \tag{2.4}$$

Bond-stretching and angle-bending are considered stiff degrees of freedom because you need significant forces to cause deformations from their references. On the other hand, rotations around bonds, or torsions, are hundreds of times less stiff than the vibrational motion of the bond and play a crucial role in the stability of different molecular conformations [200].

Proper torsions: the dihedral angle between the two planes formed by four consecutive bonded atoms are expressed in the form of a cosine series expansion:

$$U(\omega) = \sum_{n=0}^{N} \frac{V_n}{2}[1 + \cos n\omega - \gamma] \tag{2.5}$$

With ω being the dihedral angle. In this equation (2.5), V_n is referred to as the "barrier height", which gives an indication of the relative barriers to rotations, and γ is the phase

factor that determines the minimum value of the torsional energy. n is the multiplicity or number of minimum points in the function. An illustration of examples of torsional potentials for different values of V_n, n, and γ is given in Figure 2.1C. Another type of torsion is the improper type, in which the four atoms are not bonded in a linear sequence. This torsional potential is used to enforce planar geometry in systems where this is necessary, for example, in aromatic rings. To maintain a torsional angle of $0°$ or $180°$ the following form is used (Figure 2.1D):

$$U(\omega) = k(1 - \cos 2\omega) \tag{2.6}$$

2.1.2.2 Non-bonded Interactions

Interactions between atoms that are not covalently bonded, either from different molecules or from the same molecule, do not depend on a specific bonding relationship between atoms and instead propagate through space. These interactions contain a repulsion term, a dispersion term, and a Coulomb term to account for interaction between charged particles.

Different atom types attract electrons with different strengths depending on their electronegativity, giving rise to an unequal distribution of charge across the molecule. This charge distribution is modelled by assigning fractional point charges to the atoms called "partial charges". Then, the electrostatic interaction between two molecules can be calculated by summing the interactions between pairs of point charges using Coulomb's law (Figure 2.1E):

$$U(r) = \sum_{i=1}^{N_A} \sum_{j=1}^{N_B} \frac{q_i q_j}{4\pi\varepsilon_0 r_{ij}} \tag{2.7}$$

N_A and N_B are the numbers of particles in the two molecules, q_i and q_j are the charges

of the particles, and r_{ij} is their displacement vector.

In atoms without a permanent multipole moment, an instantaneous dipole can arise due to fluctuations in the electron clouds; these dipoles can induce a dipole in neighbouring atoms, generating an attractive effect, the London dispersion forces. On the other hand, at very short ranges, atoms experience repulsive forces originating from the Pauli exclusion principle. Both of these effects can be calculated using quantum mechanics, but as mentioned in Section 2.1.1, those calculations are very computationally expensive. The Lennard-Jones 12-6 function is the most widely used potential energy function to model van der Waals interactions. This function can describe both the dispersion and repulsive terms. It takes the following functional form:

$$U(r) = 4\varepsilon[(\frac{\sigma}{r})^{12} - (\frac{\sigma}{r})^{6}] \tag{2.8}$$

In this equation, ε is the well depth, and σ is the collision diameter. Figure 2.1F is a graphical representation of the Lennard-Jones function, where the energy tends to zero when the molecules are far apart, with an energy well as the particles come closer together and a steep energetic penalty when the particles get closer than the collision diameter.

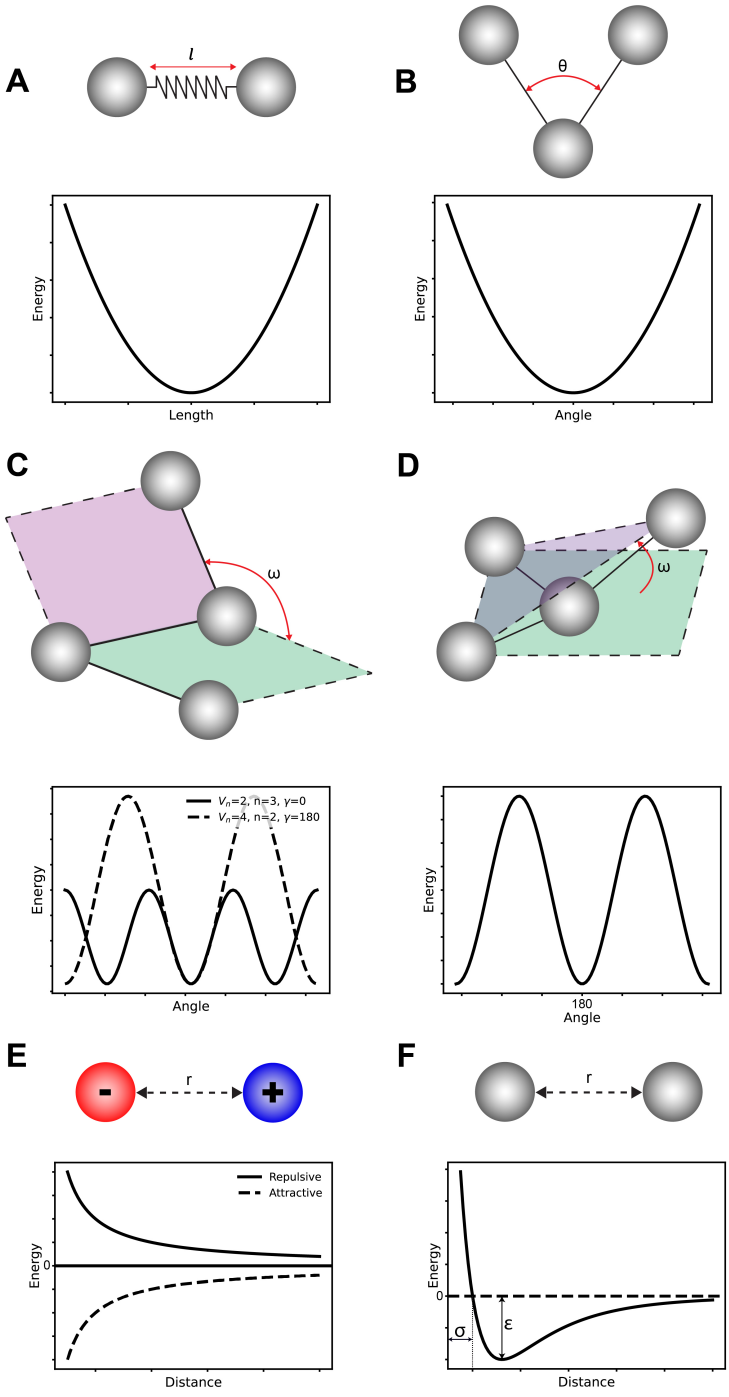

Figure 2.1: Schematic representation of bonded (A: bond stretching, B: angle bending, C: proper torsions, D: improper torsions) and non-bonded (E: Lennard-Jones, F: Coulomb) interactions modelled in a typical force field and the graphical representation of their potential energy function.

2.1.3 Algorithms

2.1.3.1 Energy Minimization

Typically, before beginning an MD simulation, it is necessary to perform an energy minimization to find a stable starting point where all the forces on the atoms are balanced. This is a mathematical optimization problem in which the goal is to find the minimum point in the potential energy surface of the molecule described by the force field. Minimisation algorithms can be classified into two groups: those that use the derivatives of the energy with respect to the coordinates and those which do not. Algorithms that use derivatives are more efficient but require the potential energy function to be differentiable. Since this is the case for molecular mechanics force fields, derivative methods are the most widely used for MD with MM. The simplest of these methods is the steepest descent. In this method, the gradient of the function to be minimized is calculated. Since the gradient of a function gives you the direction that increases the function the most, taking a step in the negative gradient direction will decrease the function [201]. In the case of MM, as described in the GROMACS reference manual [202], in this algorithm, starting from a coordinate vector r_n, the positions in the next steps are calculated by:

$$r_{n+1} = r_n + \frac{F_n}{max(|F_n|)} h_n \tag{2.9}$$

Where h_n is the maximum displacement, F_n is the force (the negative gradient of the potential energy), and $max(|F_n|)$ means the largest scalar force on any atom. At each step, if the energy has decreased, the new positions are accepted, otherwise, they are rejected. Steepest descent is simple and easy to implement, but it is not necessarily the most efficient for convergence to a local minimum. Other, more sophisticated methods, such as conjugate gradient or Newton-Raphson minimization, can fully converge to an energy minimum. Still, steepest descent is robust and fast, meaning it will rapidly

improve a poor conformation. Considering that a perfectly minimized structure is not necessary to start a MD simulation and that it is more important to eliminate high-energy conformations of a molecular structure, steepest descent is the method of choice in this work.

2.1.3.2 Newton's Equation of Motion

In MD simulations the time evolution of a molecular system is generated using Newton's three laws of motion as described in his work "*Philosophiae naturalis principia mathematica*" of 1687: A body continues to move in a straight line at constant velocity unless a force acts on it, force equals the rate of change of momentum, to every action there is an equal and opposite reaction. The trajectory of the particles is then obtained by solving the equation of the second law:

$$\overrightarrow{F} = m\overrightarrow{a} = m\frac{d\overrightarrow{v}}{dt} = m\frac{d^2\overrightarrow{r}}{dt^2} \tag{2.10}$$

This describes the motion of a particle of mass m along the coordinate vector $\overrightarrow{r}$, with $\overrightarrow{v}$ being the particle's velocity vector, $\overrightarrow{a}$ its acceleration vector, and $\overrightarrow{F}$ the force vector on the particle in the coordinate direction. The forces on each particle i are calculated as the negative derivatives of the potential energy as a function of the system coordinates $U(r)$:

$$F_i = -\frac{dU}{dr_i} \tag{2.11}$$

2.1.3.3 Integration of the Equation of Motion

The forces acting on every atom are determined by the interaction between particles, which are governed by the force field, which is pairwise additive. This results in the analytical solution to the equation of motion being unobtainable for a system composed

of more than two atoms. Finite difference methods can be used to generate trajectories in this case. The idea behind this method is that the integration is divided into many small steps, separated in time by a fixed timestep Δt. The total force of each atom at time t is then calculated as a vector sum of its interactions with other atoms. From the calculated force, the acceleration of the particle can be obtained, which, when combined with the positions and velocities at time t, allows the calculation of new positions and velocities at time $t + \Delta t$. In GROMACS, the default integration algorithm is the "leap-frog". This is a method that allows the integration of second-order differential equations of the form:

$$a(x) = \frac{d^2r}{dt^2} \tag{2.12}$$

This can also be expressed in the first-order forms:

$$a = \frac{dv}{dt}; v = \frac{dr}{dt} \tag{2.13}$$

The algorithm then uses the positions of the atoms r at time t and the velocities v at time $t - \frac{1}{2}\Delta t$ to calculate new positions and velocities. Using the velocities staggered by half a time step allows centering the velocity estimation over the full time step, which gives a more accurate average velocity for updating the positions. The new velocities and positions are determined by the following relations using the forces $F(t)$ determined at time t:

$$v(t + \frac{1}{2}\Delta t) = v(t - \frac{1}{2}\Delta t) + \frac{\Delta t}{m}F(t) \tag{2.14}$$

$$r(t + \Delta t) = r(t) + \Delta t v(t + \frac{1}{2}\Delta t) \tag{2.15}$$

Thus, velocities leap over the positions to give their value at $t + \frac{1}{2}\Delta t$, and then the positions leap over the velocities to give their value at $t + \Delta t$, repeating this process iteratively, hence the name "leap-frog". This is the integration algorithm used in all the work carried out throughout this thesis.

2.1.3.4 Periodic Boundary Conditions and Non-bonded Interactions

When using MD simulations to calculate the macroscopic properties of a system, it is necessary to consider boundary effects. In the laboratory, molecules are typically dissolved in bulk solvent, meaning a significant portion of them will not interact with the container's boundaries. In molecular simulation, the small system size means most, if not all, of the molecules will be interacting with the system's boundary, which will cause severe artefacts. To circumvent this issue in simulations with a small number of particles, periodic boundary conditions are used, where the particles are replicated in all directions to generate a periodic array. Figure 2.2 represents a two-dimensional periodic box surrounded by eight nearest neighbours, while in three dimensions, the box would have 26 neighbours. In this configuration, when a particle leaves the box during the simulation, it is replaced by a particle from the periodic image of the opposite side. In such settings, there are no boundaries, which generates artefacts of its own, but are expected to be less severe than the artefacts produced by unnatural boundaries.

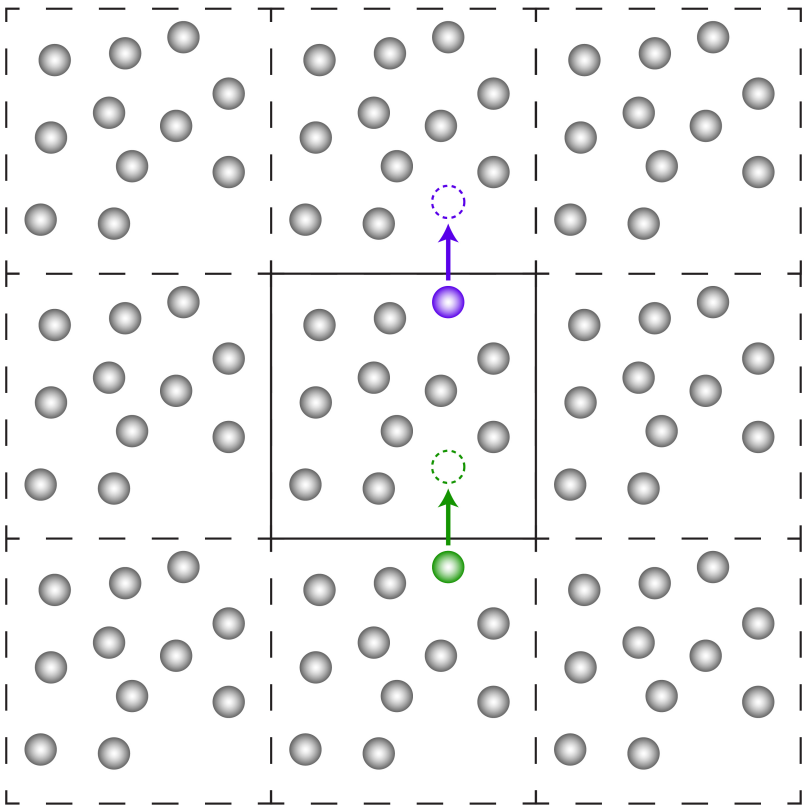

Figure 2.2: Two-dimensional representation of periodic boundary conditions. The original simulation box is surrounded by 8 neighbours. An example particle (purple) leaving the box would be replaced by a particle moving from a periodic image (green) on the exact opposite side.

The most computationally expensive part of a MD simulation is the calculation of the non-bonded energies and forces. The number of bonded interactions scales linearly with the number of particles, but the number of non-bonded interactions that need to be considered in a pairwise additive force field scales by N^2. Theoretically, the non-bonded interactions should be calculated between every pair of atoms in the system. In the case of the Lennard-Jones potential, this is not necessary, as it decays very quickly with a distance dependence of r^{-6} tending to zero. Because of this, a cut-off scheme can be used, where the interaction energy with atoms outside the cut-off distance is set to zero. This includes the particles in the closest periodic image. The use of a cut-off by itself

does not reduce the computational expense significantly since it is still necessary to compute the distance between every atom pair to decide whether they are within the cut-off. Instead, a neighbour list is used, in which all the atoms within the cut-off are stored in an array, together with atoms that are slightly farther away. This neighbour list is updated at regular intervals during the simulations, and between updates, it is used to identify the atoms to be considered for the force calculation.

On the other hand, electrostatic interactions decay at a rate of r^{-1}, so they cannot be disregarded even at longer distances. This means we need to consider the interactions in the original simulation box together with the interaction between the original box and all its periodic images. This can be written as:

$$U = \frac{f}{2} \sum_{n*} \sum_{i=1}^{N} \sum_{j=1}^{N} \frac{q_i q_j}{|r_{ij} + n|} \tag{2.16}$$

Where n is a vector indicating the position of the periodic box, the star indicates that $i = j$ should be omitted when $n = 0$ and $f = \frac{1}{4\pi\varepsilon_0}$. The problem with equation 2.16 is that this summation is very slow to converge. The Ewald sum method [203] converts these summations into two series converging much more rapidly. One of these summations is performed in real space, while the other is performed in reciprocal space. However, the reciprocal part of the sum scales as N^2, making it not useful for larger systems. In GROMACS, the particle-mesh Ewald (PME) method [204] is implemented to compute this sum. In this method, charges are assigned to a grid, and the reciprocal energy term is computed by a fast Fourier transform of the grid. This makes the PME algorithm scale by $Nlog(N)$, which is significantly faster than the Ewald sum method.

2.1.3.5 Simulations at Constant Temperature and Pressure

MD simulations can be carried out with different conditions, called thermodynamic ensembles, that allow us to derive thermodynamic properties. Different ensembles represent systems with varying degrees of separation from the environment. Traditionally, MD simulations are run in the microcanonical or NVE ensemble in which the moles (N), volume (V), and total energy (E) of the system are kept constant. This corresponds to an isolated system that cannot exchange heat or matter with the environment. Generally, in biomolecular simulations, one wants to calculate properties of interest of the system emulating *in vivo* or *in vitro* conditions such as constant temperature or pressure. For the first one, the canonical or NVT ensemble can be used, where the system is in equilibrium with a thermal bath, maintaining a constant temperature. This ensemble is often used in the equilibration phase of an MD simulation to take the system to the desired temperature. For the latter condition, the isothermal-isobaric or NPT ensemble is used. Here, the temperature is kept constant in a similar way as the aforementioned ensemble, but additionally, a barostat maintains a constant pressure. This ensemble is the closest one to the conditions of a laboratory experiment and thus will be utilized in all production simulations throughout this thesis.

Thermostats

Maintaining the temperature constant during the NVT or NPT ensembles requires a thermostat algorithm. The temperature of the system relates to the kinetic energy, which can be calculated as:

$$E_{kinetic} = \frac{1}{2}\sum_{i=1}^{N} m_i v_i = \frac{3}{2} N k_B T \tag{2.17}$$

Where m_i is the mass of the particle i, v_i is the velocity of the particle i, N is the number of particles, k_B is the Boltzmann constant, and T is the temperature of the system. This

means that to conserve the temperature of the system, we need to keep the kinetic energy constant. Considering equation 2.17, a straightforward way to do this is to scale the velocities of the system by multiplying by a factor (λ), with this, if the temperature at time t is $T(t)$, the temperature change can be calculated as follows:

$$\Delta T = \frac{1}{2}\sum_{i=1}^{N}\frac{2}{3}\frac{m_i(\lambda v_i)^2}{Nk_B} - \frac{1}{2}\sum_{i=1}^{N}\frac{2}{3}\frac{m_i v_i^2}{Nk_B} \tag{2.18}$$

$$\Delta T = (\lambda^2 - 1)T(t) \tag{2.19}$$

$$\lambda = \sqrt{\frac{T_{new}}{T(t)}} \tag{2.20}$$

Thus, if we multiply the velocities at each timestep by $\lambda = \sqrt{T_{new}/T(t)}$, we can enforce temperature control on the system. This is the basic idea behind the velocity rescale algorithm, but this is not sufficient to reproduce a canonical ensemble since rescaling the velocities by a precise value at each timestep the kinetic energy will not fluctuate, which does not reproduce the real behaviour of a system in thermodynamical equilibrium. A more sophisticated approach is the one proposed by Berendsen [205], where the system is coupled to a thermal bath that removes or supplies heat to the system as required. With this algorithm, the velocities are also rescaled at each step, but here, the rate of change of the temperature is proportional to the difference in temperature between the bath and the system:

$$\frac{dT(t)}{dt} = \frac{1}{\tau}(T_{bath} - T(t)) \tag{2.21}$$

Where τ is a parameter that determines the strength of the coupling between the system

and the thermal bath. The scaling factor for the Berendsen thermostat is then calculated as follows:

$$\lambda = \sqrt{1 + \frac{dt}{\tau}(\frac{T_{bath}}{T(t)} - 1)} \tag{2.22}$$

When τ is large, then the coupling is weak, and if it is small, the couple will be strong, and when the coupling parameter equals the time step (dt), then this algorithm is equivalent to simple velocity rescaling. This algorithm does not guarantee rigorous sampling of the canonical ensemble but is still useful during equilibrations to bring the system smoothly to the desired temperature. The Bussi-Donadio-Parrinello thermostat [206] is an extension of the Berendsen thermostat, where the target kinetic energy value is stochastically chosen from the canonical equilibrium distribution for the kinetic energy. This allows the simulation to properly sample a rigorous canonical ensemble.

Barostats

To keep the pressure of the system constant, a similar approach to the one taken for the temperature can be used, but instead of rescaling the velocities of the system, we can rescale the volume of the simulation box. The Berendsen barostat [205] is thus based on the same principle of the homonym thermostat, where the system is coupled to a pressure bath by scaling the volume by a factor (λ). Also, the change in pressure is proportional to the difference in pressure between the bath and the system. The scaling factor can then be calculated as follows:

$$\lambda = \sqrt{1 + \frac{\kappa}{\tau}(\frac{P_{bath}}{P(t)} - 1)} \tag{2.23}$$

Where κ denotes the isothermal compressibility of the system. The new positions of the system are then calculated by:

$$r_i^{new} = r_i^{old}\lambda^{1/3} \tag{2.24}$$

This expression can be applied isotropically (scaling factor equal for all directions), semi-isotropically (the scaling factor is the same for x and y but different for z), and anisotropically (the scaling factor is different for all directions). The isotropic pressure scaling is commonly used for biomolecules in solution, while the semi-isotropic is used for proteins in membrane bilayers. Similar to the analogous thermostat, the Berendsen barostat is typically used for equilibration purposes, but it does not sample a valid NPT ensemble. The Andersen barostat [207] can produce a valid NPT ensemble; to do this, it adds an extra degree of freedom to the system, which corresponds to the volume of the box. This degree of freedom represents a piston acting on the box with kinetic energy equal to:

$$E_{kinetic} = \frac{1}{2}Q(\frac{dV}{dt})^2 \tag{2.25}$$

Where Q is the mass of the piston. Also, the potential energy of the piston can be calculated as:

$$U = PV \tag{2.26}$$

Where P is the desired pressure and V is the volume of the system. Low piston mass generates rapid oscillations in the box, while a high mass generates the opposite effect. Then, in the extended pressure-coupling method, the coordinates are scaled by:

$$r_i^{new} = r_i^{old}V^{1/3} \tag{2.27}$$

The Andersen barostat modifies the volume of the simulation box without modifying its shape, so it can only be applied isotropically. The Parrinello-Rahman barostat [208] expands the Andersen barostat, allowing it to change the shape of the box, thus allowing semi-isotropic and anisotropic pressure coupling. In this thesis, this is the barostat algorithm of choice.

2.1.4 Enhanced Sampling Techniques

A molecular dynamics simulation sample from the thermodynamic ensemble that is being used and generates a sequence of points in the phase space. It would be considered ergodic if the simulation trajectory visits all the possible points in the phase space. From an ergodic trajectory, a time average of an observable would be equivalent to an ensemble average, which allows us to derive macroscopic properties from the microscopic states. However, in reality, for a biomolecular system like the ones studied in this work, the phase space is enormous, and the time for the simulation to approach ergodicity can very well be considered infinite, or at least beyond the accessible time scale for computer simulation. Furthermore, many biological interest processes lie in the range of seconds, or even past that, which is not feasible even for the most powerful state-of-the-art high-performance computers [209]. Enhanced sampling techniques accelerate the dynamics of the simulation by introducing biases that allow the system to cross high-energy barriers between metastable states. In this work, two of these enhanced sampling methods were used: replica exchange with solute tempering and umbrella sampling.

2.1.4.1 Replica Exchange with Solute Tempering

Replica exchange molecular dynamics (REMD) is an enhanced sampling method where several copies of the same system are simulated in parallel with different conditions, for example, temperatures, and at a certain frequency, some of their features are exchanged between neighbouring replicas with a probability of acceptance [210]. This allows the

replicas at higher temperatures to overcome energy barriers to explore more of the phase space and then exchange back with the replica at the target temperature. Not every state sampled from a high-temperature replica can be accepted to lower temperatures, otherwise, unrealistic configurations will populate the target replica. First, we will review the original implementation of REMD [211]. Let us consider the probability of configuration X_0 is determined by the Boltzmann distribution at T_0:

$$P_0(X_0) = \frac{e^{\beta_0 E(X_0)}}{Z_0} \tag{2.28}$$

Where β_0 is the inverse temperature $\beta_0 = (k_B T_0)^- 1$ and Z_0 is the partition function, and $E(X_0)$ is the Hamiltonian. Then, the joint probability of a simulation with M replicas having configurations $\{X_0, X_1, X_2, \ldots, X_n\}$ at temperatures $\{T_0, T_1, T_2, \ldots, T_n\}$ is:

$$P_{all} = \prod_{i}^{M} P_i(X_i) \tag{2.29}$$

If we consider a system of four replicas with increasing temperatures (Figure 2.3), where we attempt an exchange between replicas T_0 and T_1, the probability of configuration X_0 at T_0 is exchanged by configuration X_1 at T_1 to be $W(X_0, T_0; X_1, T_1)$ and the probability of configuration X_1 at T_0 is exchanged by configuration X_0 at T_1 to be $W(X_1, T_0; X_0, T_1)$, for a system in thermal equilibrium the detailed balance condition holds:

$$\frac{W(X_0, T_0; X_1, T_1)}{W(X_1, T_0; X_0, T_1)} = \frac{P_{all}(X_1, T_0, X_0, T_1, X_2, T_2, X_3, T_3)}{P_{all}(X_0, T_0, X_1, T_1, X_2, T_2, X_3, T_3)} \tag{2.30}$$

If we substitute equation 2.29 into equation 2.30 we get:

$$\frac{W(X_0, T_0; X_1, T_1)}{W(X_1, T_0; X_0, T_1)} = \frac{P_0(X_0, T_0) P_1(X_1, T_1) P_2(X_2, T_2) P_3(X_3, T_3)}{P_0(X_1, T_0) P_1(X_0, T_1) P_2(X_2, T_2) P_3(X_3, T_3)} \tag{2.31}$$

Cancelling the P_2 and P_3 terms:

$$\frac{W(X_0, T_0; X_1, T_1)}{W(X_1, T_0; X_0, T_1)} = \frac{P_0(X_0, T_0)P_1(X_1, T_1)}{P_0(X_1, T_0)P_1(X_0, T_1)} \tag{2.32}$$

Then, by substituting equation 2.28 into equation 2.32 it becomes:

$$\frac{W(X_0, T_0; X_1, T_1)}{W(X_1, T_0; X_0, T_1)} = \frac{\frac{e^{\beta_0} E(X_0)}{Z_0} \frac{e^{\beta_1} E(X_1)}{Z_1}}{\frac{e^{\beta_0} E(X_1)}{Z_0} \frac{e^{\beta_1} E(X_0)}{Z_1}} \tag{2.33}$$

Cancelling the partition functions and rearranging the terms we get that the exchange probability $e^{-\Delta}$ is equal to:

$$\frac{W(X_0, T_0; X_1, T_1)}{W(X_1, T_0; X_0, T_1)} = e^{-(\beta_0 - \beta_1)(E(X_1) - E(X_0))} = e^{-\Delta} \tag{2.34}$$

To accept an exchange the Metropolis criterion is used:

$$W(X_0, T_0; X_1, T_1) = 1 \quad \text{for} \quad \Delta \leq 0 \tag{2.35}$$

$$W(X_0, T_0; X_1, T_1) = e^{-\Delta} \quad \text{for} \quad \Delta > 0 \tag{2.36}$$

The exchange is always accepted when $\Delta \leq 0$. Δ has two components, one relating to the temperature difference between the replicas and one relating to the potential energy difference. The temperature component $(\beta_0 - \beta_1)$ will always be more than 1, since T_0 is by definition lower than T_1 and therefore β_0 will be bigger than β_1. Considering this, $\Delta \leq 0$ only when the energy of the high-temperature configuration is lower than the energy of the low-temperature configuration $E(X_1) < E(X_0)$. This means that to achieve a good exchange probability, the potential energy distributions of adjacent replicas need

to overlap. This is a problem in bigger systems since the energy of the solvent-solvent interactions and the solvent-protein interactions increase very fast with temperature, requiring many replicas to achieve overlap with higher temperatures, increasing the computational cost. To alleviate this, the Hamiltonian REMD method was introduced, where instead of different temperatures, the replicas have different Hamiltonian, thus weakening the interactions at "higher temperatures". In Hamiltonian replica exchange, the Δ becomes: $\Delta = \beta([E_0(X_1) + E_1(X_0)] - [E_0(X_0) + E_1(X_1)])$. This is the method applied in Chapter 4 and it uses the GROMACS with PLUMED implementation, which allows the selection of the scaled region [212]. Considering equation 2.28, the ensemble probability depends on βE or $\frac{E}{k_B T}$, so doubling the temperature would be completely equivalent to halving the energy. Since the energy is an extensive property, while the temperature is an intensive property, one can select a specific region of the system and specific terms of the Hamiltonian to be “heated”. In the Bussi implementation the system is split between the hot ($\mathscr{H}$) and cold ($\mathscr{C}$) regions, where the Hamiltonian depends on a scaling factor λ according to the following rules: the charge of atoms in the $\mathscr{H}$ region is scaled by $\sqrt{\lambda}$, the ϵ parameter of the Lennard-Jones potential (see equation 2.8) of atoms in the $\mathscr{H}$ region is scaled by λ, the proper dihedral potentials for which the first and fourth atoms are in the $\mathscr{H}$ region is scaled by λ, and the proper dihedral for which either the first or the fourth atom is in the $\mathscr{H}$ region is scaled by $\sqrt{\lambda}$. With these rules the force field terms that contribute to energy barriers are scaled in a way that the interactions between the atoms of the $\mathscr{H}$ region are at an effective temperature T/λ, the interactions between the $\mathscr{H}$ and $\mathscr{C}$ regions are at an effective temperature $T/\sqrt{\lambda}$, and all the interactions inside the $\mathscr{C}$ region are at temperature T. This implementation can reproduce exactly the replica exchange with solute tempering (REST) implementation [213], originally designed to scale the Hamiltonian of just the solute molecule, but with a flexible choice of the solute region, similar to the generalized REST implementation [214]. In this method, the lowest temperature replica (T_0) usually samples the ensemble

of interest, while the sole purpose of the other replicas is to accelerate sampling. However, by using a free energy estimator such as multistate Bennett acceptance ratio (MBAR), it is possible to generate an unbiased free energy surface (FES) by including the samples from higher temperature replicas and calculating their contribution to the free energy at the temperature of interest. This will be discussed in Section 2.1.4.3.

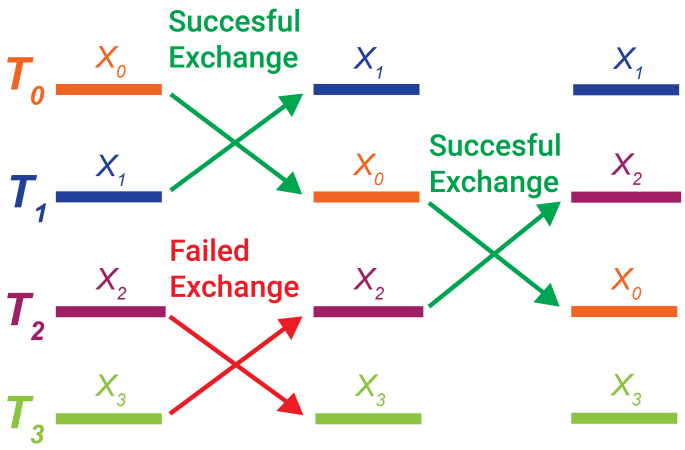

Figure 2.3: Schematic representation of a replica exchange simulation with four replicas at different temperatures. Exchange attempts are represented with arrows; when an exchange is accepted, the neighbouring replicas exchange configurations.

2.1.4.2 Umbrella Sampling

Another widely used enhanced sampling method is the umbrella sampling (US) method [215]. As described by Hénin et al 2022 [216], in this method, sampling is restricted to a small part of the configuration space. This is done over several overlapping windows, which allow proper sampling of regions that would be otherwise unfavourable in conventional MD (Figure 2.4). In the most common case, this is done by imposing a harmonic bias potential $U_i^{bias}(x)$ that keeps the sampling within region i of a chosen coordinate (ξ), which takes the form:

$$U_i^{bias}(x) = \frac{k}{2}|\xi(x) - z_i|^2 \tag{2.37}$$

Then, the unbiased FES of the system along the chosen coordinate can be recovered using a free energy estimator such as weighted histogram analysis method (WHAM), as discussed in Section 2.1.4.3. It is also possible to enhance this method further by combining it with Hamiltonian replica exchange (see Section 2.1.4.1), a method named replica-exchange umbrella sampling (REUS).

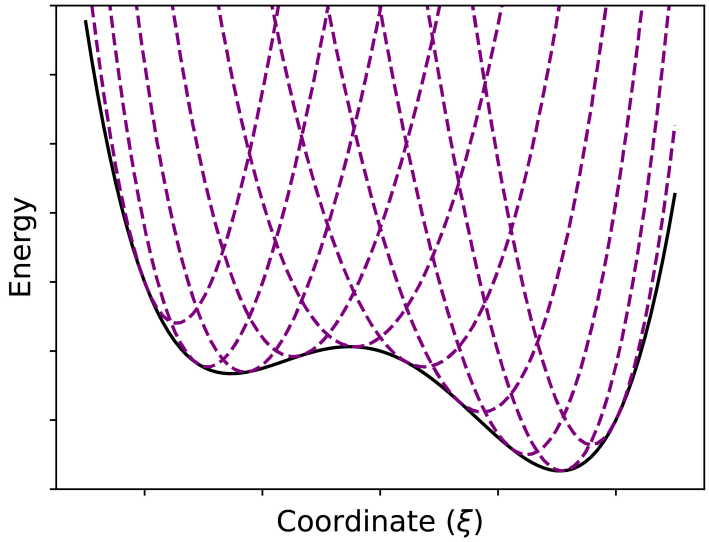

Figure 2.4: Representation of umbrella sampling in an asymmetric double-well potential. The black trace represents the double-well potential with two basins separated by an energy barrier. The purple discontinuous trace represents the biasing potential across 10 umbrella windows, which allows sampling of the FES across the whole reaction coordinate (ξ).

2.1.4.3 Free Energy Estimators

Free energy estimators are mathematical expressions that can compute the FES (or potential of mean force (PMF)[1]) along a collective variable (CV) or the free energy differences between two states. In this work, two of these free energy estimators are

used, WHAM and MBAR, to calculate FES for US and REST, respectively. For WHAM [217], if we consider an US simulation with K windows with restraining potentials and histogram the data into M bins, the unbiased probability distribution of bin i in the kth state is:

$$P_{i,k} = \frac{\sum_{k=1}^{K} n_{k,i} e^{-u_{k,i}}}{\sum_{j=1}^{K} n_k e^{f_j - u_{j,i}}} \tag{2.38}$$

Where $n_{k,i}$ are the counts in each bin from the kth state, $u_{k,i}$ is the energy of the system in the ith bin and kth state, and f_j is the (dimensionless) free energy of the system in the jth state. The free energy can then be calculated by summing :

$$e^{-f_k} = \sum_{m=1}^{M} P_{m,k} \tag{2.39}$$

As we can see, the free energy depends on the probability distribution, while the probability distribution depends on the free energy. Thus, these equations need to be solved self-consistently in an iterative way to reach an optimal estimation of the free energy. In the limit of bins with zero width, the WHAM equations become MBAR. In MBAR [218], if we run simulations at K different thermodynamic states, then the free energy at state i can be calculated as:

$$f_i = -ln \sum_{j=1}^{K} \sum_{n=1}^{N_j} \frac{e^{-u_i(x_{j,n})}}{\sum_{k=1}^{K} N_k e^{f_k - u_k(x_{j,n})}} \tag{2.40}$$

Where N_j is a sum over all samples collected at state j and $u_i(x)$ is the reduced potential energy for state i which is defined as:

[1] Historically, the concept of PMF is very different from FES, but nowadays they are used interchangeably. See the discussion in Hénin et al 2022 [216].

$$u_i(x) = \beta_i(U_i(x) + p_i V(x)) \tag{2.41}$$

In equation 2.40, the free energy at state i depends on the free energy in every of the K states; this leads to a series of K equations that again must be solved iteratively in a self-consistent manner to arrive at a precise free energy estimation.

2.1.4.4 Metadynamics

Metadynamics is an adaptive bias method, where a time-dependent external bias potential is applied over a chosen CV space to counteract the FES. This repulsive potential is composed of a sum of Gaussian kernels that are deposited at the current location in the CV space [219, 220]. In the well-tempered metadynamics scheme [220], the bias potential $U_n^{bias}(x)$ is updated by adding a Gaussian kernel $G(x, x_n)$ at the current CV value x_n:

$$U_n^{bias}(x) = U_{n-1}^{bias}(x) + exp[-\tfrac{1}{\gamma-1}\beta U_{n-1}^{bias}(x_n)]G(x, x_n) \tag{2.42}$$

Where n is the current metadynamics step number (number of deposited Gaussians), $U_0^{bias}(x) = 0$ and the Gaussian kernels are scaled by a factor depending on the so-called bias factor γ. The Gaussian kernels can be defined as:

$$G(x, x_n) = H_0 exp[-\tfrac{1}{2}\sum_{i=1}^{d}\tfrac{(x_i - x_n, i)^2}{\sigma_i^2}] \tag{2.43}$$

With d being the number of CV, σ is the Gaussian width, and H_0 is the height. In between bias potential updates after depositing n Gaussian kernels, the bias potential is calculated by:

$$U_t^{bias}(x) = \sum_{k=1}^{n} exp H_k[-\frac{1}{2}\sum_{i=1}^{d}\frac{(x_i - x_{k,i})^2}{\sigma_i^2}] \tag{2.44}$$

Here $H_k = H_0 exp[-\frac{1}{\gamma-1}\beta U_{k-1}^{bias}(x_k)]$ and is the height of the k-th deposited kernel. In the long run, the value of H_k goes to zero as the scaling factor $exp[-\frac{1}{\gamma-1}\beta U_{k-1}^{bias}(x_k)]$ decreases as $1/k$.

Then, the FES over the chosen CVs can be estimated directly by summing the deposited Gaussians. Additionally, it is possible to obtain a FES over any different CV by reweighting. This can be performed by weighting each configuration x taken at time t with a weighting factor $e^{\beta[U_t^{bias}(x) - c(t)]}$ with c(t) being the logarithm of the ratio of the unbiased and biased partition functions [216].

A variation of the metadynamics methods that can be used to explore the binding of a ligand is the so-called funnel metadynamics (FunMetaD) [221, 222]. This consists of well-tempered metadynamics, as described above, but includes a funnel-shaped restraint potential to limit the space the ligand explores in the unbound state. This allows the simulation to sample several binding and unbinding events, allowing the binding free energy calculation without prior knowledge of the ligand binding mode. A combination of a truncated conical and cylindrical restraint gives the funnel-shaped restraint potential $H_R(x, y, z)$, assuming that the binding site is contained in the range $z_{min} \leq z \leq z_{max}$:

$$H_R(x, y, z) = \begin{cases} H_{\text{cone}}(x, y, z), & z \leq z_{cc} \\ H_{\text{cyl}}(x, y), & z > z_{cc} \end{cases} \tag{2.45}$$

With $z_{cc} > z_{max}$. The truncated conical restraint is defined as:

$$H_{\text{cone}}(x,y,z) = \begin{cases} 1, & \sqrt{x^2+y^2} \leq R(z) \\ 0, & \sqrt{x^2+y^2} > R(z) \end{cases} \tag{2.46}$$

with $R(z) = R_{cyl} + tan(\alpha)(z_{cc} - z)$, R_{cyl} being the radius of the cylinder, and α a factor that modulates the aperture of the cone. The cylindrical part of the restraint is then defined as:

$$H_{\text{cyl}}(x,y,z) = \begin{cases} 1, & \sqrt{x^2+y^2} \leq R(cyl) \\ 0, & \sqrt{x^2+y^2} > R(cyl) \end{cases} \tag{2.47}$$

The application of the funnel-shaped restraint potential produces an entropic penalty to the ligand in the unbound state. This penalty can be calculated analytically and depends on the radius of the cylinder. Then, the absolute binding free energy can be calculated as:

$$\Delta G_b^0 = \Delta G - \tfrac{1}{\beta} ln(\pi R_{cyl}^2 C^0) \tag{2.48}$$

With ΔG as the free energy difference between the bound and unbound states, $\pi R_{cyl}^2 C^0$ is the surface of the cylinder used as a restraint potential, β is the inverse temperature, and C^0 is the standard concentration of $\frac{1}{1660}\text{Å}^{-3}$.

2.2 Electrophysiology

Electrophysiology is the most widely used technique to study the function of the pLGICs. This technique allows real-time recording of the channel's opening and closing at the multi- and single-channel level, enabling the study of gating kinetics and other biophysical properties such as conductance. In this project, the two-electrode voltage clamp (TEVC) technique was used to investigate the function of the nAChRs. This chapter will

present a brief description of the background of the technique and some practical aspects of its use. This section is based on the discussions by Hille 2001 [223] and Rettinger et al 2022 [224] unless otherwise specified.

2.2.1 Bioelectricity

Electrical phenomena arise whenever charges of opposite signs are separated or can move independently. In cells, this is due to asymmetrical ion distributions between the extracellular medium and the cytoplasm and to the ion-selective membrane conductance. This electrochemical gradient across the membrane produces an electrical potential difference known as the membrane potential. If we assume that ion movements are independent, have a constant diffusion coefficient, and that the electrical field in the membrane is constant, the resting potential E can be described by the Goldman-Hodgkin-Katz equation [225, 226]:

$$E = \frac{RT}{F} ln(\frac{P_{Na}[Na^+]_o + P_K[K^+]_o + P_{Cl}[Cl^-]_i}{P_{Na}[Na^+]_i + P_K[K^+]_i + P_{Cl}[Cl^-]_o}) \tag{2.49}$$

R is the gas constant, T is the temperature, and F is the Faraday constant. In equation 2.49, the resting potential is determined by the ion concentrations $[ion]$ and permeabilities $P_{ion} = Da$, where D is the diffusion coefficient and a is the membrane thickness.

The cell membrane is an insulator that separates the internal and external conductive fluid. Due to the extreme thinness of a lipidic bilayer, the cell membrane behaves as an electrical capacitor. Drawing a parallel with electronics, a biological membrane can then be considered as a parallel circuit of a resistor and a capacitor. The opening and closing of ion channels and the action of ion transporters determine the resistance of the membrane. Therefore, due to Ohm's law $R = V/I$, we can study the function of conductive membrane proteins from current-voltage (IV) characteristics.

2.2.2 Two-electrode Voltage Clamp

The voltage clamp technique allows for measuring currents across the cell membrane at a fixed (clamped) membrane potential. This is important because the membrane conductance changes with voltage, which is called rectification. Neuronal nAChRs show inward rectification, meaning that at positive membrane potentials, there is no detectable macroscopic current [227]. Thus, keeping the membrane voltage constant ensures the receptor will respond consistently to stimuli. An idealised voltage clamp setting consists of a voltage source providing the clamp potential, the model membrane, and an amperometer for measuring the membrane current. If we dismiss the resistance of the internal components, the potential drop across the model membrane equals the potential of the battery, $V_M = V_C$. In real life, the connections within the electronic circuits have non-negligible resistances. In particular, the electrode and membrane will act as resistors in series (R_E and R_M respectively), dividing the voltage:

$$V_M = V_C \frac{R_M}{R_M + R_E} \tag{2.50}$$

This means that only a fraction of the clamp potential will reach the membrane, and only in the case where this fraction is close to one ($R_M >> R_E$), the cell voltage will be clamped to the command potential.

In the case of *Xenopus laevis* oocytes, as well as in other large cells with low input resistance, performing voltage clamp with a single electrode is not possible, therefore it is necessary to include another electrode that will independently determine the actual membrane potential (Figure 2.5). Then, the voltage source is adjusted in a way that the membrane potential matches exactly the command potential, even when R_M changes due to the stimuli applied during an experiment (for example, with the gating of an ion channel like the nAChR). Thus, by monitoring the current, one can analyse the changes

in the resistance of the membrane.

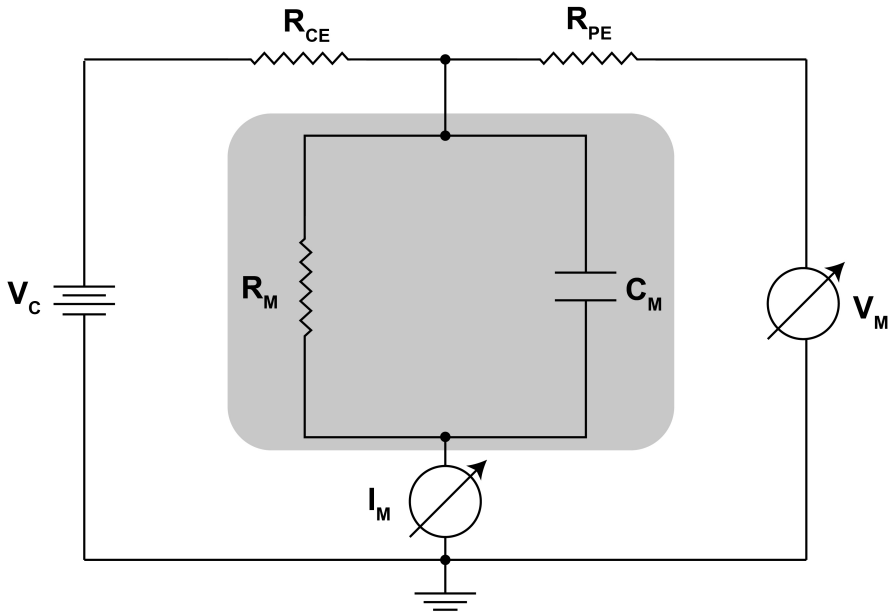

Figure 2.5: Circuit representation of the TEVC setup with a model membrane. The membrane is represented by a resistor and a capacitor in parallel (grey area). The current electrode (CE) clamps the cell and measures the current through the membrane (I_M). The voltage electrode (PE) monitors the membrane voltage (V_M).

2.2.3 Experimental Setup

2.2.3.1 Reagents and Buffers

Standard laboratory reagents used were of analytical grade. ACh, antibiotics, and type I collagenase were purchased from Merck (Sigma-Aldrich, UK). The composition of the buffers used in this work is as follows:

OR2: $82\,\mathrm{mM}$ NaCl, $2\,\mathrm{mM}$ KCl, $2\,\mathrm{mM}$ $MgCl_2$, and $5\,\mathrm{mM}$ HEPES, adjusted to pH 7.6 with NaOH.

OR2 Ca^{+2}: $82\,\mathrm{mM}$ NaCl, $2\,\mathrm{mM}$ KCl, $2\,\mathrm{mM}$ $CaCl_2$, and $5\,\mathrm{mM}$ HEPES, supplemented

with kanamycin $2\,\mu g\,mL^{-1}$, $10\,units/mL$ penicillin, $10\,mg\,mL^{-1}$ streptomycin and $25\,\mu g\,mL^{-1}$ amphotericin B, and $5\,\%$ horse serum, adjusted to pH 7.6 with NaOH.

SOS: $100\,mM$ NaCl, $2\,mM$ KCl, $1.8\,mM$ $CaCl_2$, and $5\,mM$ HEPES, adjusted to pH 7.4 with NaOH

2.2.3.2 Animals

Adult female *Xenopus laevis* toads were purchased from the European Xenopus Resource Centre (Portsmouth, UK) and housed in static tanks filled with dechlorinated water at $17\,^{\circ}C$ under a 12-hour light/dark cycle. Before the surgery, animals were euthanised by immersion in a solution of $5\,\%$ tricaine until non-responsive to the toe pinch reflex and culled by severing of the spinal cord. Ovarian lobes were then removed by two incisions in the abdomen and stored in an ice-cold OR2 buffer for transportation. Only one toad per week was sacrificed.

2.2.3.3 *Xenopus laevis* Oocytes Preparation.

To remove the follicular layer, the ovaries were split into small groups of 5-6 oocytes and incubated for approximately $50\,min$ at room temperature in a solution of $2\,mg\,mL^{-1}$ of type I collagenase. After this time, the solution was replaced with a modified OR2 Ca^{+2} solution to stop the collagenase activity. Only defolliculated oocytes at the maturation stages V and VI were selected for injection and were maintained at $17\,^{\circ}C$ in modified OR2 Ca^{+2}.

2.2.3.4 cDNA Microinjection

Microinjection needles were prepared by pulling Drummond glass capillaries (Sartorius, UK) in one stage using a Narishige PC-10 micropipette puller (Narishige, Japan). Before use, the tip of the needle was broken with a pair of tweezers to achieve a narrow tip of around $3\,mm$ in length and $2\,\mu m$ in diameter. The needle was filled with mineral oil

and loaded in a Nanoject II (Drummond, USA) microinjector. The nAChR cDNA was injected into the oocyte nucleus ($23\,\mathrm{nL}$ of $200\,\mathrm{ng\,nL^{-1}}$ cDNA) as illustrated in Figure 2.6. In the case of the $\alpha4\beta2$ nAChR, the cDNA mixture was prepared in a ratio of 10:1 of $\alpha4$ to $\beta2$ to obtain the LS stoichiometry or a ratio of 1:10 of $\alpha4$ to $\beta2$ to obtain the HS stoichiometry. The injected oocytes were transferred to sterile Petri dishes with OR2 Ca^{2+} and incubated at $17\,^{\circ}\mathrm{C}$ until recording.

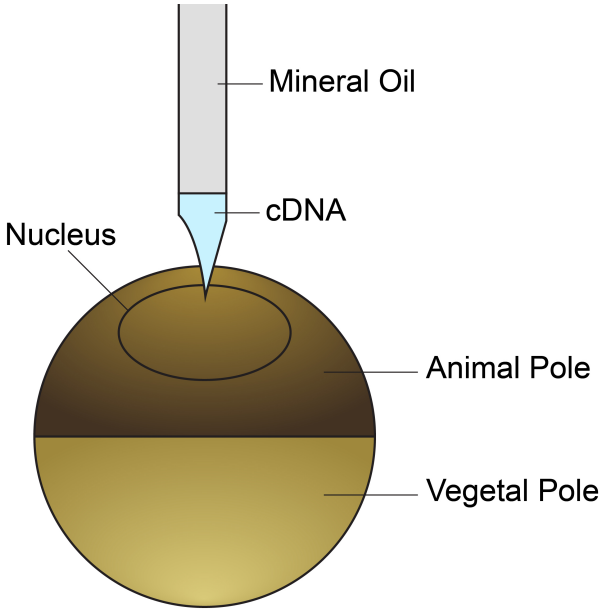

Figure 2.6: Schematic representation of cDNA microinjection. The nucleus of the oocyte is located in the "animal pole" (dark brown).

2.2.3.5 Electrophysiological recordings

Two to four days post-injection, the oocytes were chosen for electrophysiological recording according to their appearance. Only the oocytes with an intact membrane and no signs of degradation were used for electrophysiology, and dead cells were removed daily. Electrodes were made out of borosilicate capillaries (Harvard Apparatus, GC 150 TF) using a Narishige PC-10 micropipette puller to generate a needle with a tip of $1\,\mu\mathrm{m}$

to $2\,\mu\mathrm{m}$ in diameter. The electrodes were filled with a solution of KCl $3\,\mathrm{M}$, and only electrodes with a resistance between $0.1\,\mathrm{M}\Omega$ to $2\,\mathrm{M}\Omega$ were used for recording. The recordings were performed in either a manual or an automated setup (Figure 2.7). For the manual setup, the oocytes were placed in a $30\,\mu\mathrm{L}$ recording chamber (Digitimer Ltd, UK) and constantly perfused with standard oocyte solution (SOS). A gravity-driven perfusion with a rate of $10\,\mathrm{mL\,min^{-1}}$ was used. Manually operated valves were used to add the test compound solutions for $10\,\mathrm{s}$ at a time, allowing $5\,\mathrm{min}$ of washing between applications. Oocytes were impaled by two electrodes connected to an Oocyte Clamp OC-725C (Warner Instruments, USA) and the traces were recorded in a flatbed recorder (Kipp & Zonen, UK). In the automated setup, the HiClamp (Multichannel Systems, Germany) system was used. In this system, the oocytes were loaded into a 96-well plate with $200\,\mu\mathrm{L}$ of SOS. During recording, the oocytes were automatically placed into a recording basket and transferred to a perfusion chamber where it is constantly perfused with SOS. Then, they were impaled with two electrodes connected to the HiClamp amplifier. Compounds were loaded into the system in a flat-bottom 96-well plate with a stirring magnet in each well to keep the compound solution in agitation. Oocytes were then lifted from the washing chamber to the compound plate and submerged in the corresponding test compound for $10\,\mathrm{s}$. Then the recording basket is moved back to the washing chamber for $2\,\mathrm{min}$ before testing the next compound.

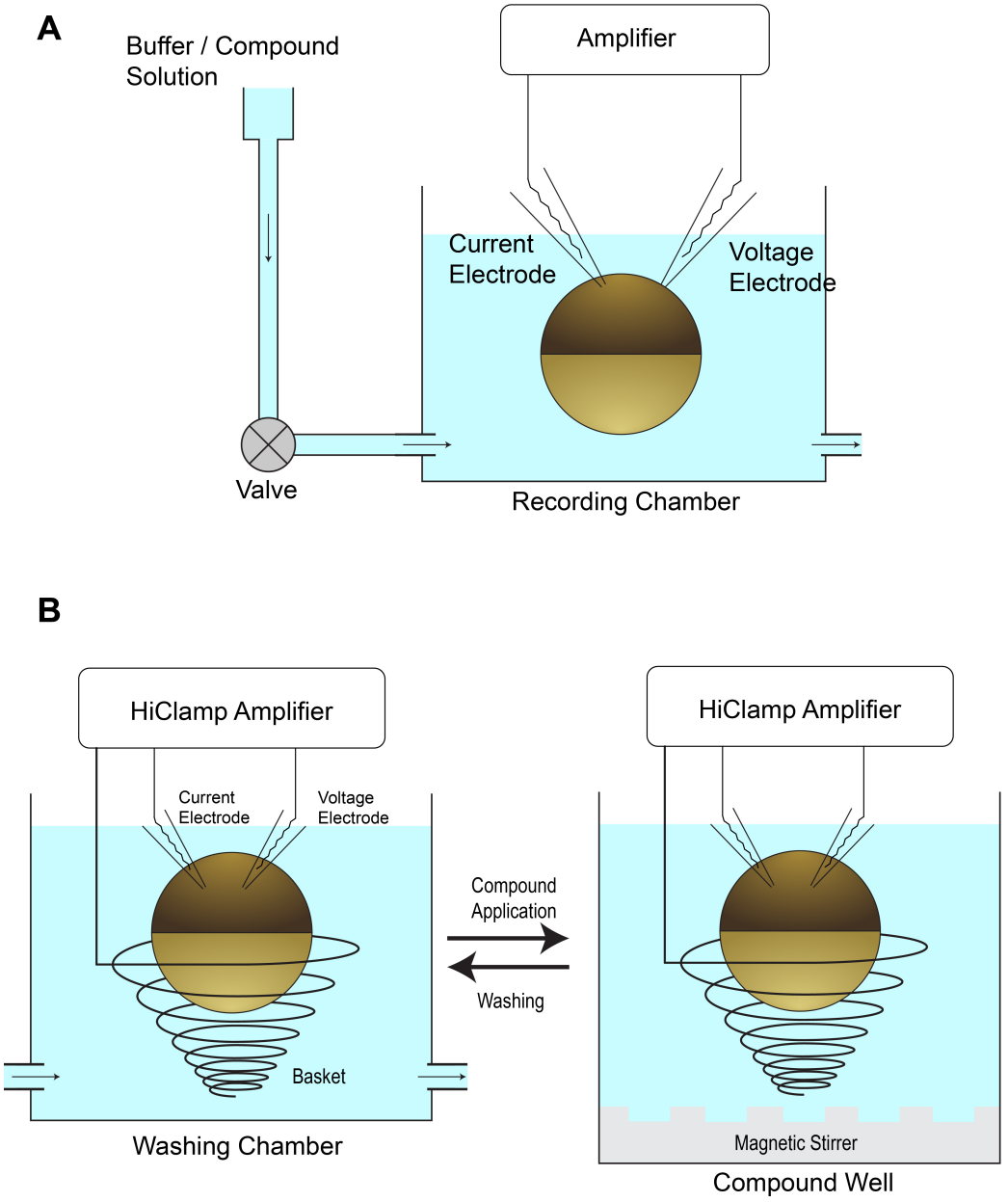

Figure 2.7: Manual (A) and automated (B) electrophysiology setups. In the manual setup, the buffer and/or compound solution are perfused into the recording chamber via gravity and the compound solution application is controlled with a valve. On the other hand, in the automated setup, the oocyte is moved between the compound plate and the washing chamber for compound testing and washing, respectively.

2.2.3.6 Concentration Response Curves

Concentration-response curves (CRCs) were obtained by normalising the induced responses to the control response evoked by a maximum effective ACh concentration ($1\,\mathrm{mM}$) for agonist curves or an concentration evoking 20 $\%$ of the maximal effect (EC_{20}) of ACh ($30\,\mu\mathrm{M}$) for allosteric modulator curves. For the allosteric CRCs the modulator is co-applied with a submaximal concentration of agonist (EC_{20}) to achieve optimal sensitivity to PAM activity [228]. The data was then fitted to the Hill equation using GraphPad Prism 8 (GraphPad, USA):

$$I = \frac{(I_{max})}{(1+10^{(Log_{10}(EC50)-X)})} \tag{2.51}$$

Where I is the normalized response, I_{max} is the maximum normalised response, and X is the base 10 logarithm of the compound concentration in molar. The EC_{50} obtained from fitting this curve is commonly used to compare the function of two compounds, and it is the result of a combination of ligand binding and gating.

2.2.3.7 Statistical Analysis

Every CRC obtained from each oocyte was fitted on its own, and the parameters from each regression were taken as one sample. Data points for relative efficacy and EC_{50} are presented with the mean $\pm$ standard error of the mean (SEM) of a minimum of 5 experiments carried out in at least three batches of oocyte donors. The data were analysed using one-way analysis of variance (ANOVA), followed by a post hoc Dunnett's test and/or a post hoc Bonferroni multiple comparison test to determine the level of significance between the control and target responses. Statistical tests that showed a value of $p < 0.05$ were considered significant. All statistical analyses for CRCs were performed using GraphPad Prism 8.

3 | Functional Characterisation and Binding Site Identification of Novel Positive Allosteric Modulators of the α7 Nicotinic Acetylcholine Receptor

Disclaimer

The research presented in this chapter has been published in ACS Chemical Neuroscience in 2023 [229], see also in the list of publications.

3.1 Introduction

The α7 nAChR is a homomeric subtype of the nicotinic receptors and one of the most abundant in the central nervous system (CNS). It is localised in regions of the brain recognised as important for cognitive function, such as the hippocampus and cortex, as well as the limbic areas, which are involved in addiction [230, 231, 61, 232, 233, 234]. Due to its distribution, the α7 nAChR plays an important role in learning and memory [188, 235]. Additionally, α7 nAChRs are expressed in non-neuronal cells, including lymphocytes, dendritic cells, and macrophages, where they play a role in inflammation and neuroprotection [236, 237, 238, 239].

Because of this widespread distribution and involvement in key brain functions, α7 nAChRs are implicated in diverse diseases such as AD [240, 241], depression [242], pain and inflammation [243], and schizophrenia [141]. Consequently, this makes the α7 receptor an attractive target for the treatment of neuropathic and inflammatory pain [244], cognitive dysfunction in schizophrenia [245, 141] and AD [241], inflammation

[246] and sepsis [247].

Several agonists of the α7 nAChR have been developed as therapeutic drugs for the treatment of AD, schizophrenia, and its associated cognitive deficits [248, 249, 250, 251, 252, 253, 254]. Despite the positive results obtained from preclinical and clinical studies, no α7 nAChR agonist is currently used as a therapy [139, 141].

Most of the a7 nAChR agonists developed for clinical purposes are based on the quinuclidine moiety, a bicyclic amine. This includes spirooxazolidinones like (3S)-Spiro[1-azabicyclo[2.2.2]octane-3,5'-oxazolidine]-2'-one hydrochloride (AR-R17779) [255], ethers like (3R)-3-[6-(4-methylphenyl)pyridin-3-yl]oxy-1-azabicyclo[2.2.2]octane (AQW051) [250] and 5-(6-[(3R)-1-azabicyclo[2,2,2]oct-3-yloxy]pyridazin-3-yl)-1H-indole (ABT-107) [256], and amides like EVP-6124 [257]. Current evidence shows that substituents with hydrophobic properties at position 3 of the quinuclidine scaffold endow the ligands with selectivity for the α7 nAChR and determine the agonist potency and efficacy [258, 259, 260].

In this work, a group of six novel ether quinuclidine compounds with both hydrophobic and hydrophilic side groups, designed as selective agonists, were screened for their abilities to evoke responses in the a7 nAChR. This showed that the properties of the substituent greatly affected the function of the ligands, ranging from retention or abolition of agonism to conversion to an allosteric modulator.

3.2 Materials and Methods

3.2.1 Novel Compounds

Quinuclidine compounds were provided and synthesised by Prof. John Lopez's group from Universidad de Concepción as described in the original paper [229]. The compound structures and numbers are shown in Figure 2.

3.2.2 Single Point Mutation

The mutant M253L α7 subunit was engineered using the Q5 Site-Directed Mutagenesis kit from New England Biolabs (U.K.). The presence of the mutation and the absence of unwanted mutations were confirmed by sequencing the entire cDNA insert (Eurofins, U.K.).

3.2.3 Two-Electrode Voltage-Clamp Recordings

The activity of the test ligands at α7 nAChR was assessed by applying the test ligands on their own or in the presence of EC_{20} ACh ($30\,\mu M$) for α7 nAChR as described in Section 2.2.3.5. CRCs for test ligands and ACh were fitted as described in Section 2.2.3.6.

3.2.4 Single-Channel Recordings in BOSC 23 Cells

Prof. Bouzat and Dr. Chrestia from the Institute of Biochemical Research, Bahia, Argentina, carried out this work, and the methods were directly reproduced from the original paper [229].

Single-channel currents were recorded from BOSC 23 cells co-transfected with α7 subunit cDNA and the chaperone Ric-3 and NACHO cDNA (1:4:1 ratios) by calcium phosphate precipitation [185]. green fluorescent protein (GFP) cDNA was incorporated during the transfection to allow the identification of transfected cells. All transfections were carried out for about $8\,\mathrm{hour}$ to $12\,\mathrm{hour}$ in Dulbecco's modified eagle medium (DMEM) medium supplemented with $10\,\%$ fetal bovine serum (FBS), as previously described [177]. Recordings were obtained in the cell-attached patch-clamp configuration at a holding potential of +$70\,\mathrm{mV}$. The bath and pipet solutions contained $142\,\mathrm{mM}$ KCl, $5.4\,\mathrm{mM}$ NaCl, $1.8\,\mathrm{mM}$ CaCl2, $1.7\,\mathrm{mM}$ MgCl2, and $10\,\mathrm{mM}$ HEPES (pH 7.4). Ligand **6** $0.1\,\mu M$ to $60\,\mu M$ was added to the pipet solution with $10\,\mu M$ ACh. Thus, the single-channel

activity was recorded in the continuous presence of the drugs. The final concentration of dimethyl sulfoxide (DMSO) used to solubilize ligand **6** was lower than $0.1\,\%$ (v/v), which does not affect α7 activation [78, 79]. ACh was solubilized directly in the pipet solution.

Single-channel currents were digitised at $10\,\mu s$ intervals, low-pass filtered at a cutoff frequency of $10\,kHz$ using an Axopatch 200B patch-clamp amplifier (Molecular Devices, CA, USA) and analysed using the program TAC (Bruxton Corporation, Seattle, WA, USA) with the Gaussian digital filter (final cutoff frequency $6.7\,kHz$). Events were detected by the half-amplitude threshold criterion [261]. Open-time histograms were fitted by the sum of exponential functions by maximum likelihood using the program TACFit (Bruxton Corporation, Seattle, WA, USA). Bursts of channel openings were identified as a series of closely separated openings preceded and followed by closings longer than a critical duration (τcrit), which was taken as the point of intersection between closed components as described before [78, 79, 177]. Critical durations were defined by the intersection between the first and second briefest components in the closed-time histogram ($\sim 200\,\mu s$ to $400\,\mu s$). In the presence of ligand **6**, the critical time was defined between the second and the third closed components for bursts ($\sim 1\,ms$ to $5\,ms$). Each series of opening events spaced by durations shorter than τcrit was considered a single burst. Burst duration was determined from the longest duration component of the open time histogram constructed with the imposed τcrit.

3.2.5 Molecular Docking

The α7 nAChR Cryo-EM structure in the open conformation (PDB ID: 7EKT) [36] was retrieved from the Protein Data Bank (PDB) database [262], and the non-protein atoms were removed using Pymol software [263]. The ligand structure was modelled using Avogadro [264]. Polar hydrogens and charges were added to the protein and ligand

structures with the AutoDock Tools suite [265] before docking. Then, blind docking was performed on the receptor, followed by targeted docking on a 15 Å grid box using AutoDock Vina [266]. The resulting poses were clustered by their similarity using the GROMOS algorithm [267].

3.2.6 Molecular Dynamics Simulations

For the simulations, proteins were inserted into a hexagonal 1-palmitoyl-2-oleoyl-sn-glycero-3-phosphocholine (POPC) bilayer membrane using CHARMM-GUI Web server [268] and were parameterized with Amber ff14SB [269] and lipid17 [270] for protein and lipids, respectively. The ligand topology was generated using AmberTools22 [271] with GAFF force field [272]. Finally, the system was solvated with the TIP3P [273] water model and neutralised with $0.15\,\mathrm{mM}$ of NaCl. The system was energy minimised for 5000 steps using the steepest descent algorithm and equilibrated to $310\,\mathrm{K}$ and 1 atm with NVT and NPT ensembles for $1\,\mathrm{ns}$ each with all heavy atoms restrained, allowing the pressure and volume of the system to stabilize respectively. This is followed by a final equilibration step in the NPT ensemble for $90\,\mathrm{ns}$ with the α carbons and the ligand heavy atoms restrained to equilibrate the protein side chains properly. Finally, a molecular dynamics production run was carried out in triplicate for $500\,\mathrm{ns}$. All simulations were run in GROMACS 2021 with the PLUMED library version 2.7.3 [274, 275].

After an initial simulation run, it was observed that the receptor spontaneously collapsed into a closed channel state. To prevent that, conformational restraints were applied to the heavy atoms in the residues that move more than 2 Å between the activated (PDB ID: 7EKT) and desensitised (PDB ID: 7EKP) [36] states (Table 3.1). Ligand conformational analysis was performed by aligning all the ligands in the simulation with the first frame of the first ligand as a reference; to do this, the chain on the positive side of the binding site of each ligand was aligned with the chain next to the reference ligand (Figure

3.1). All the frames from the three replicas and five ligands each were concatenated for further analysis. To select the predominant conformation, the concatenated trajectory was clustered based on the root-mean square deviation (RMSD) of the ligand's heavy atoms between all frames using the GROMOS algorithm [267] with two frames considered as neighbours when the RMSD between them is less than 3 Å. All trajectory analyses and manipulation were performed using the MDAnalysis Python package [276].

Table 3.1: Restrained residues and their location during the 500ns production run.

Helix	Residue
M2	270
MX	326, 328, 329, 330, 331, 333, 334, 335, 336, 338, 339, 341, 312
MA	432, 436, 438, 447, 457

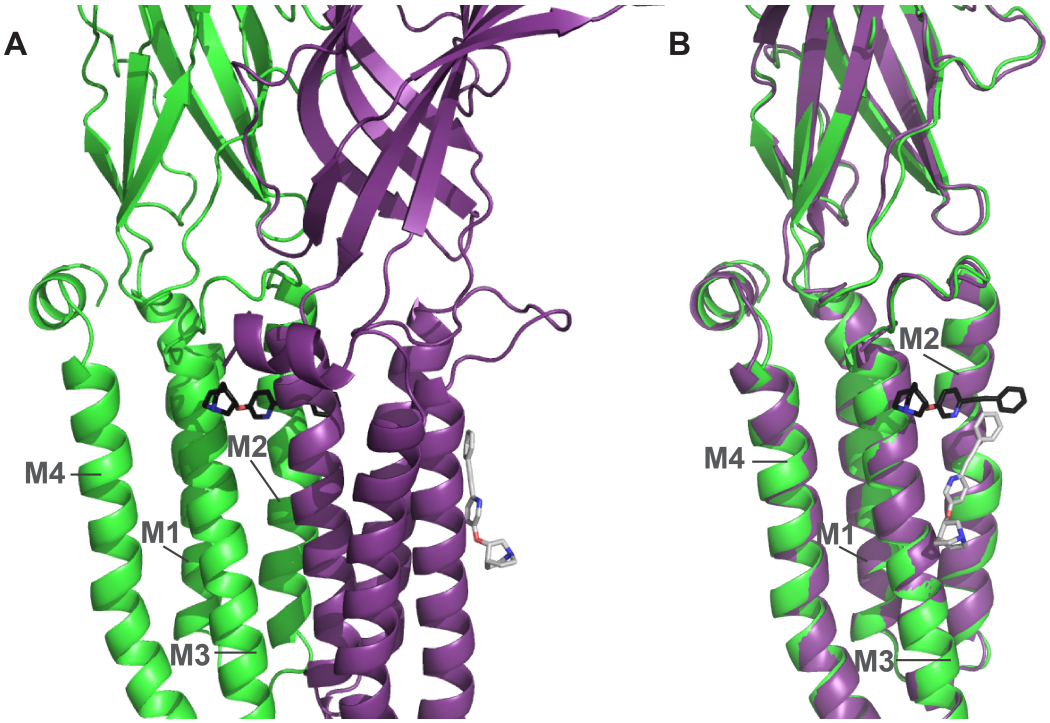

Figure 3.1: Superimposition of the (+) subunit chain adjacent to each ligand. The green chain is the (+) subunit of the first ligand (black) and the purple chain is the (+) subunit of the superimposed ligand (white). (A) Before superimposition. (B) After superimposition.

3.3 Results

3.3.1 Functional Screening of Novel Ether-quinuclidine Ligands

Ether quinuclidines such as AQW051 and ABT-107 activate α7 nAChR with a relative efficacy of about $75\,\%$, compared to the full agonist ACh [250, 256]. Hence, in the first set of functional assays, ligands **4-9** were evaluated for their efficacy in activating macroscopic currents in *Xenopus* oocytes heterologously expressing human α7 nAChR. The ligands were tested over a concentration range between $1\,\mu\mathrm{M}$ to $300\,\mu\mathrm{M}$, and ACh was assayed in parallel as a fully efficacious agonist. Representative current traces obtained by applying $1\,\mathrm{mM}$ ACh or the ligands at $300\,\mu\mathrm{M}$ are shown in Figure 3.2. Ligand **4**, which has a bromine atom at position 5, retained the ability to activate α7 nAChR, although the amplitude of the current responses was approximately only $25\,\%$ of that elicited by $1\,\mathrm{mM}$ ACh, a maximally effective concentration at α7 nAChR. In contrast, ligand **5**, which has the bromine atom in position 6, failed to activate current responses at α7 nAChR. Similar to ligand **5**, ligands **6**, **7**, **8**, and **9** did not display agonism at α7 nAChR.

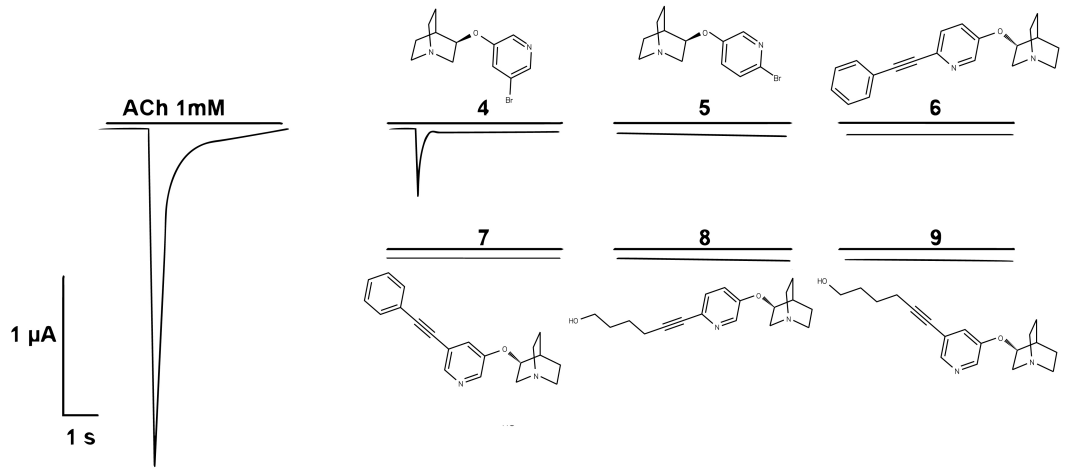

Figure 3.2: Functional effects of ether quinuclidine derivatives on α7 nAChR expressed heterologously in Xenopus oocytes. The traces shown were obtained by $5\,\mathrm{s}$ applications of $1\,\mathrm{mM}$ ACh or $300\,\mu\mathrm{M}$ ligands **4-9** to an oocyte expressing heterologously human α7 nAChR and represent the typical responses found in oocytes expressing human α7 nAChR. The bars above the traces represent the duration of the application of compounds.

Ligands **5-9** may have poor agonist efficacy at α7 nAChR. Partial agonists with very poor efficacy may induce functional inhibition by competing with efficacious agonists for access to the agonist site [277]. Therefore, the ability of ligands **5-9** to inhibit the ACh responses of α7 nAChR was tested. The compounds were assayed at a range of increasing concentrations ($10\,\mathrm{nM}$ to $30\,\mu\mathrm{M}$) for their effects on the amplitude of the current responses generated by an EC_{20} ACh concentration ($30\,\mu\mathrm{M}$). Ligands **5** and **7** did not affect the responses elicited by ACh. This finding, together with their inability to activate α7 nAChR, indicates that ligands **5** and **7** have no selectivity for α7 nAChRs. Unexpectedly, ligands **6**, **8**, and **9** potentiated the currents evoked by ACh with varying efficacy (Figure 3.3A). Concentration-response curves for ligands **6**, **8**, and **9** were generated to assess their potency and efficacy in mediating the potentiation of α7 nAChRs (Figure 3.3B). Ligands **8** and **9** are isomers, with **8** having the hydrophilic group hex-5-yn-1-ol in position 6, whereas **9** has the group in position 5. As shown in Figure

3.3B, ligands **8** and **9** potentiated the responses evoked by ACh EC_{20} with similar potency and efficacy (ligand **8** EC_{50} = $27 \pm 9\,\mu M$; maximal potentiation of EC_{20} ACh responses = $238 \pm 20\,\%$; n = 3; ligand **9**, EC_{50} = $33 \pm 8\,\mu M$, maximal potentiation of EC_{20} ACh responses = $200 \pm 25\,\%$; n = 3). Ligand **6**, which has a hydrophobic phenylacetylene group in position 6 of the pyridine ring, was significantly more potent and efficacious than ligands **8** and **9**, with an estimated EC_{50} for potentiation of $12.60 \pm 3.32\,\mu M$ (n = 8) and a maximal potentiation of EC_{20} ACh responses of $850 \pm 120\,\%$ (n = 8) (n = 6; $p < 0.001$).

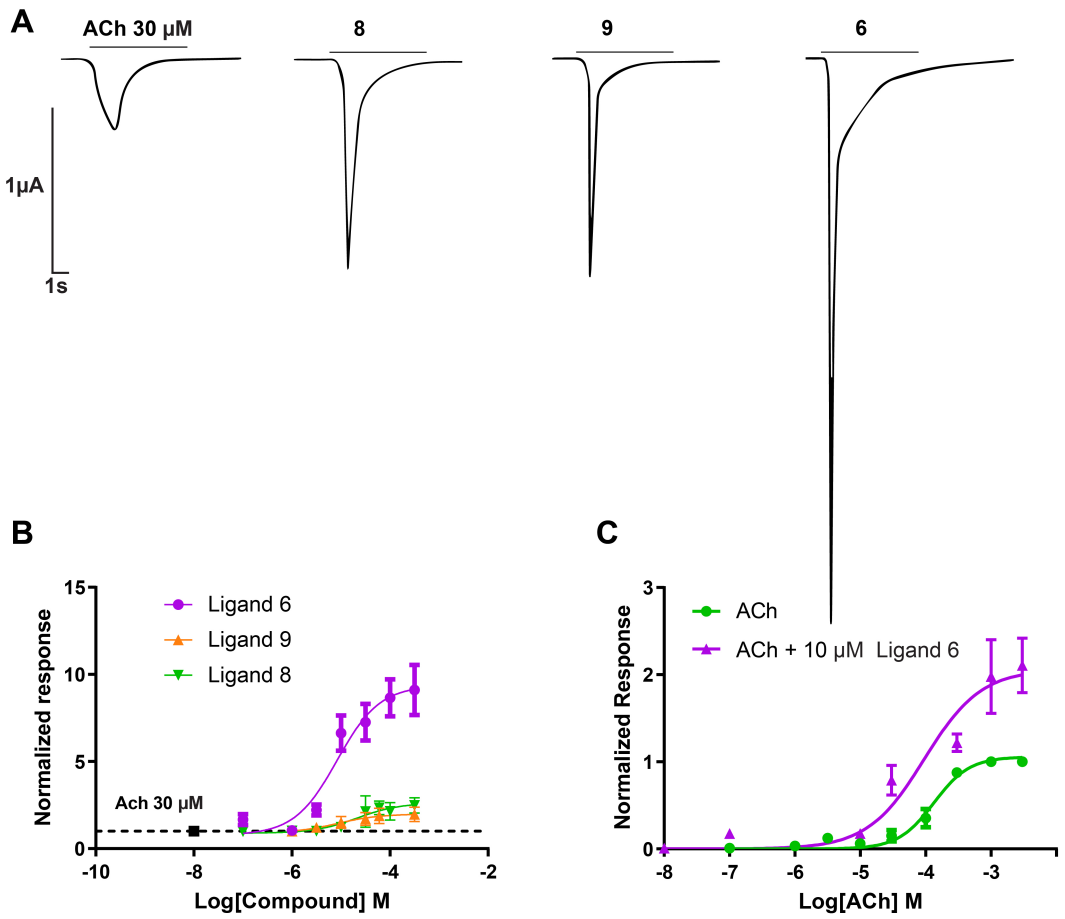

Figure 3.3: Ligands **6**, **8**, and **9** exert effects on human α7 nAChRs expressed heterologously in *Xenopus* oocytes. (A) Representative traces of the macroscopic currents elicited by EC_{20} ACh (30 µM) in the absence or presence of 10 µM ligands **6**, **8**, or **9**. The bar corresponds to the ACh pulse. The currents show that these ligands potentiate EC_{20} ACh responses of human α7 nAChR without noticeably altering the desensitisation rate of the receptors. (B) Agonist concentration-response curves for ligands **6** (blue curve and circles), **8** (green curve and inverted triangles), and **9** (orange curve and triangles). Peak current responses for all three ligands were normalised to the responses elicited by 30 µM ACh (EC_{20} ACh). (Continued on next page)

Figure 3.3: (From previous page) (C) ACh concentration-response curve obtained in the absence (circles) and presence (triangles) of $10\,\mu\mathrm{M}$ ligand **6** (approximately ligand **6** EC_{50} for potentiation). For both curves, data points represent the mean of four to five responses and are normalised to the maximum response elicited by ACh (EC_{100}, $1\,\mathrm{mM}$) in the absence of ligand **6**.

Next, the effect of a fixed concentration of ligand **6** ($10\,\mu\mathrm{M}$, approximately the EC_{50} concentration for potentiation by ligand **6**) on the CRC of ACh at α7 nAChR was determined. As shown in Figure 3.3C, ligand **6** increased the maximal responses of ACh and shifted the curve to the left (control EC_{50} $125 \pm 25\,\mu\mathrm{M}$, n = 5; ACh + ligand **6** EC_{50} $96 \pm 30\,\mu\mathrm{M}$; n = 4; $p < 0.05$). These effects are well-established functional features of α7 nAChR PAMs [193, 181, 176] and are consistent with an allosteric mode of action. Critically, full decay of α7 nAChR currents, with no marked differences in the decay rates, occurred during the duration of the ACh-pulse in the presence of the ligands ($5\,\mathrm{s}$) (Figure 3.3A). This macroscopic profile of potentiation is consistent with ligand **6** (as well as ligands **8** and **9**) being an α7 nAChR type I PAM. PAMs of the α7 nAChR are broadly classified into type I and type II based on their modulation of the macroscopic current responses. Type I PAMs, such as 5-HI, genistein, and NS1738, potentiate the macroscopic current responses with conserved kinetics [278, 177, 175]. In contrast, type II PAMs, such as PNU-120596, not only increase the amplitude of the responses but also slow the decay rate and promote the activation of previously desensitised receptors [78, 181]. Of note, ligand **6** had no effects on the ACh concentration-response curve at α4β2 nAChR, suggesting that its PAM activity is selective for α7 nAChRs (Figure 3.4).

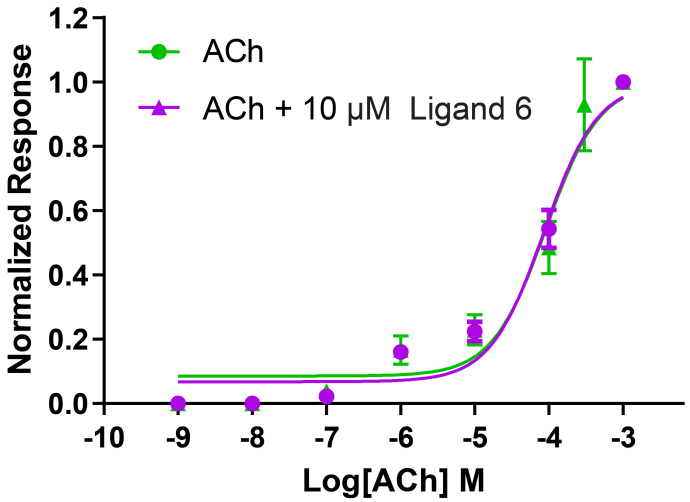

Figure 3.4: ACh concentration-response curve +/- ligand **6**. Ligand **6** does not affect the ACh concentration-response curve of human $\alpha 4\beta 2$ nAChRs expressed heterologously in *Xenopus* oocytes. Current responses were elicited using $10\,\mathrm{s}$ applications of ACh +/- $10\,\mu\mathrm{M}$ ligand **6**.

Single-channel recordings of ligand **6** on the $\alpha 7$ nAChR were performed to gain deeper functional insight into its modulatory function. In the presence of $10\,\mu\mathrm{M}$ ACh, $\alpha 7$ channel activity appears as short and isolated openings, followed by long periods of closed channels, with rare activation events called bursts, which consist of several open events in quick succession [78, 278, 79, 279]. The open and burst durations were determined from the slowest exponential component of each histogram (Figure 3.5, Table 3.2).

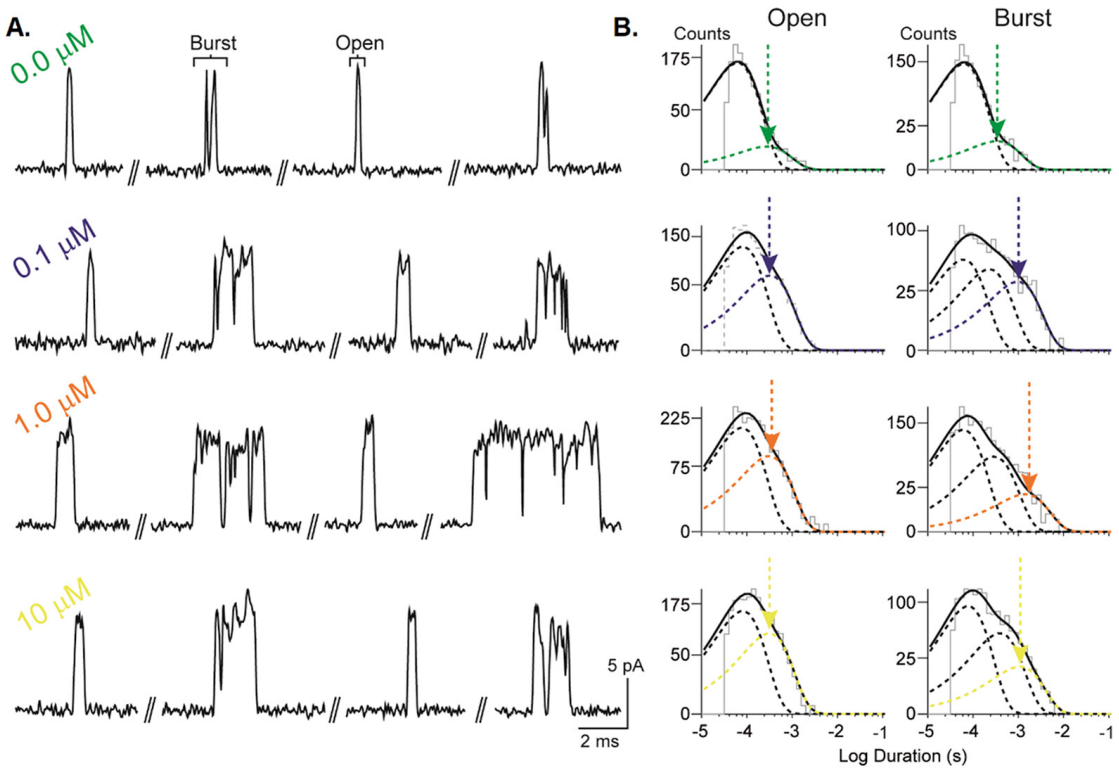

Figure 3.5: Effects of ligand **6** on α7 nAChR at the single-channel level. (A) Typical traces from single-channel recordings of α7 nAChR in the presence of 10 µM ACh alone (0) or combined with ligand **6** at the mentioned concentrations. Channel openings are shown as upward deflections. (B) Representative open and burst duration histograms for each condition. The arrows indicate the mean durations of the slowest components for each compound concentration. Membrane potential: -70 mV. Filter: 9 kHz.

Table 3.2: Mean Open and Burst Durations of α7 nAChR in the Absence or Presence of Ligand **6**. n and N correspond to the number of patches and cell transfections, respectively. Student t-test against the control condition without ligand **6**. ns: $p > 0.05$, **$p < 0.01$, ***$p < 0.001$.

Ligand 6 (µM)	mean open duration (ms)	mean burst duration (ms)	n/N
0	0.31 ± 0.06	0.38 ± 0.08	6/3
0.1	0.29 ± 0.06	0.86 ± 0.17 (**)	4/2
1	0.42 ± 0.10	1.31 ± 0.44 (***)	4/2

Ligand **6**, when co-applied with $10\,\mu M$ ACh at concentrations ranging from $0.1\,\mu M$ to $10\,\mu M$ produced potentiated receptor activations at single-channel level. Notably, burst duration increased significantly with respect to the control (Table 3.2), with a duration of about 4-fold longer than the control at $1\,\mu M$. Increasing the concentration of the modulator beyond $1\,\mu M$ did not yield further potentiation (p = 0.425). On the other hand, the slowest component of the opening events did not show any significant changes in the concentration range tested (Table 3.2).

Interestingly, a further increase in the concentration of ligand **6** to $60\,\mu M$ produced a reduction in channel activity, with recording patches showing such low activity that did not allow for an analysis, which suggests an additional inhibitory effect of the modulator. To determine whether the inhibitory effect could be observed at the macroscopic level, we tested the effects of ligand **6** over a wider concentration range ($10\,nM$ to $5\,mM$). As shown in Figure 3.6, the curve showed that maximal potentiation occurred at $30\,\mu M$ and maintained a steady plateau up to $300\,\mu M$. However, at concentrations higher than $300\,\mu M$, the drug abruptly inhibited the responses, leading to almost complete abolition at $5\,mM$.

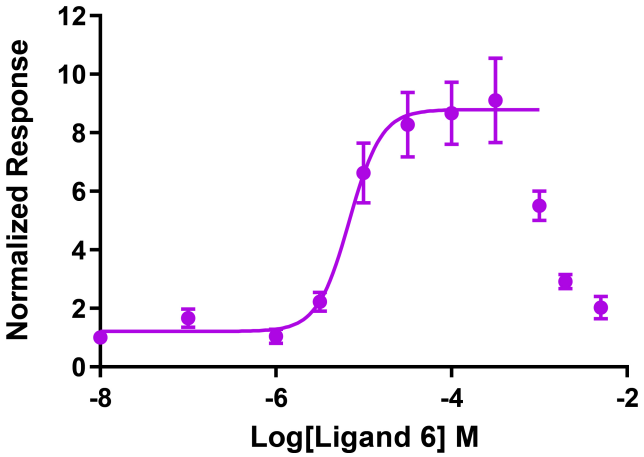

Figure 3.6: Concentration-response effects of ligand **6**. The effects of ligand **6** on the EC_{20} ACh responses of α7 nAChR were determined over a concentration range between $10\,\mathrm{nM}$ and $5\,\mathrm{mM}$. The peak effects of the potentiating effects of ligand **6** were reached at $300\,\mu\mathrm{M}$, after which the application of ligand **6** abruptly inhibited the ACh responses, and almost abolished them at $5\,\mathrm{mM}$. The CRC for ligand **6** was determined as described in Section 2.2.3.6.

3.3.2 Binding Site Prediction and Validation

Blind docking of ligand **6** to α7 nAChR was performed to aid in the identification of the site involved in the effects of ligand **6**. An initial blind docking of ligand **6** revealed a preference of the docking poses for the interface between the transmembrane domains of each chain (Figure 3.7). This site was then selected for targeted docking, and the centroid of the best five clusters was used as a starting point for molecular dynamics ($3 \times 500\,\mathrm{ns}$) simulations. After the simulations, the best conformation was selected by RMSD-based clustering of the ligand's heavy atoms (Figure 3.8). In this conformation, the ligand occupies a binding site in the top portion of the transmembrane domain interface and has several hydrophobic interactions with the M2 and M3 α helices of the (+) side and with M2 and M1 of the (-) side.

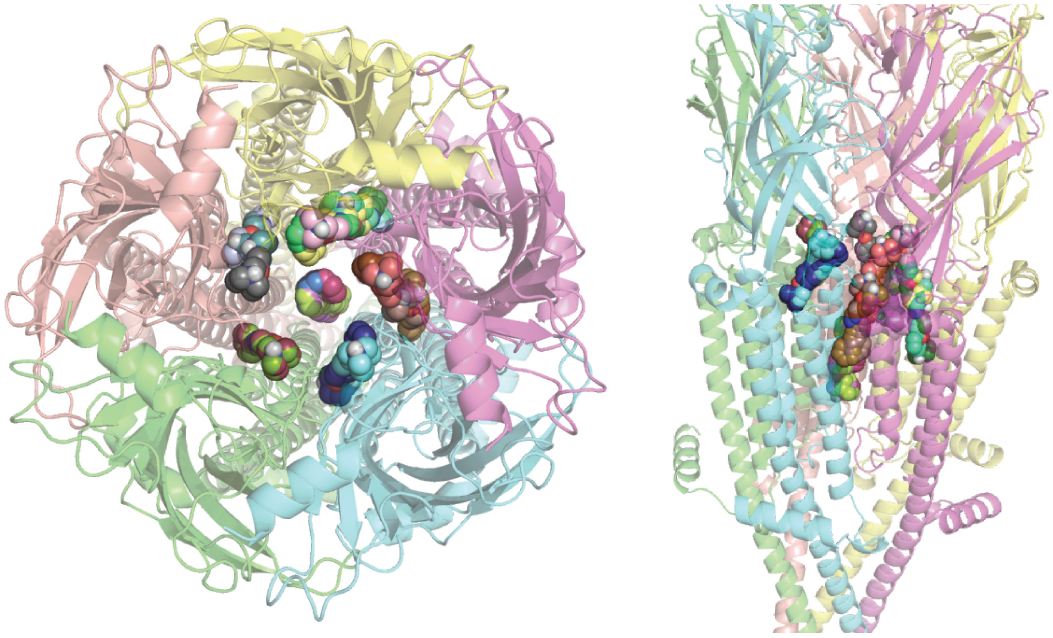

Figure 3.7: Superimposition of blind docking poses of ligand **6**. The poses are as predicted by AutoDock Vina in the α7 nAChR Cryo-EM structure (7EKT).

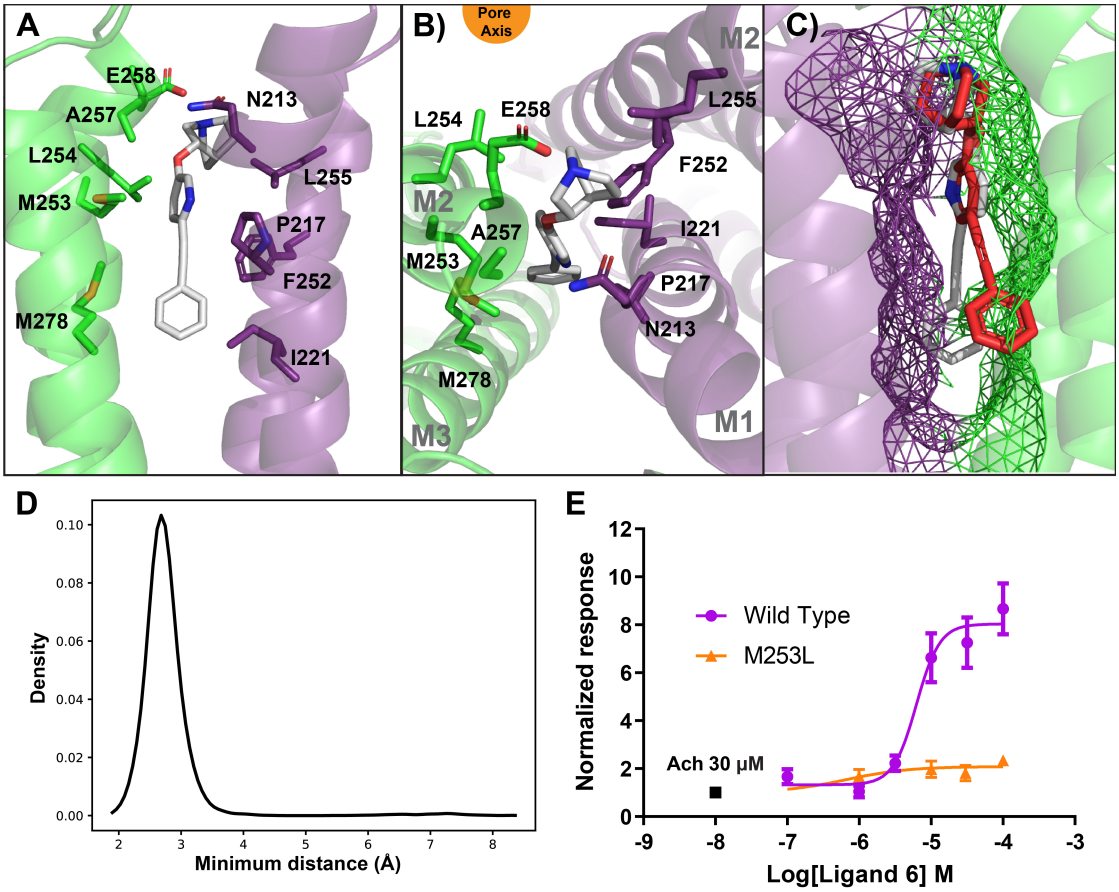

Figure 3.8: Ligand **6** binds the transmembrane domain of α7 nAChR. Binding site pose of ligand **6** (white) in the transmembrane region of α7 nAChR viewed from the side (A) and the top (B). The (+) subunit is in green, and the (-) subunit is in purple. (C) Superimposition of ligand **7** (red) with the selected conformation of ligand 6 (white) in the binding site. The wireframe represents the surface of the binding pocket. (D) Histogram of the minimum distance in angstrom between the side chain of M253 and ligand 6 during the simulation frames in the same cluster of the selected conformation. (E) Mutation of M253 to leucine dramatically reduces the potentiating effects of ligand **6**. The concentration-response curves for WT (purple circles and line) or mutant α7 nAChR (orange triangles and line) were obtained as described in Section 2.2.3.6.

The ligand 3-(pyridin-3-yloxy)quinuclidine moiety in the selected conformation interacts strongly with T250, M253, L254, A257, and E258 in the (+) M2, Y209, L212, N213, L214, P217 from the (-) M1, and F252 and L255 from the (-) M2 during the simulation

(Figure 3.9A). On the other hand, the side group of the ligand interacts with L246, T250, and M253 of the (+) M2, A275, M278 and I279 of the (+) M3, P217, L220, and I221, of the (-) M1, and F252 of the (-) M2 (Figure 3.9B).

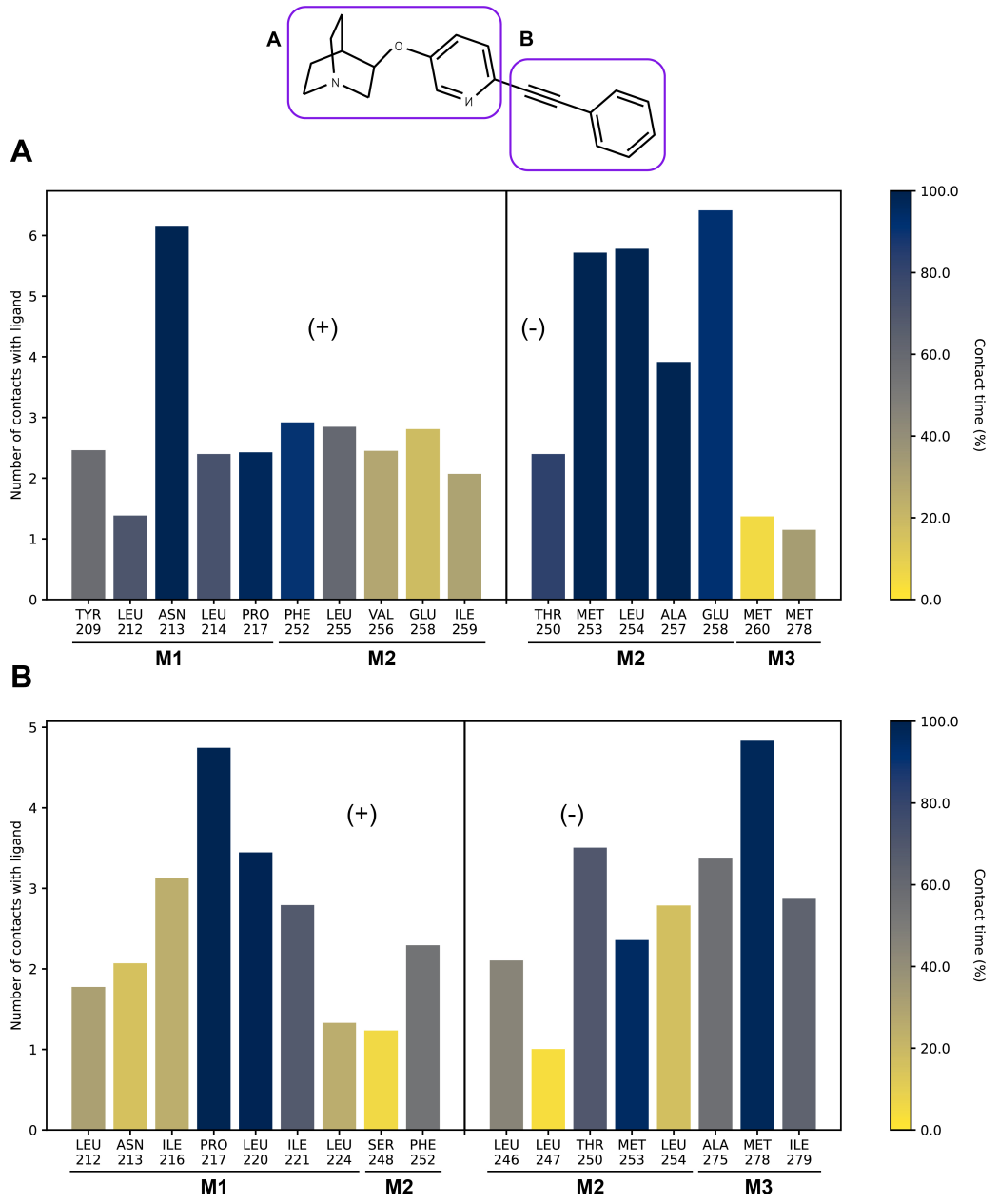

Figure 3.9: Number of contacts and contact time over the simulation for the frames corresponding to the best cluster of the protein transmembrane helices with the ligand 3-(pyridin-3-yloxy)quinuclidine moiety (A) and side group (B).

Demonstrating that residues in the predicted binding site in the transmembrane region of

α7 nAChR are necessary for the potentiating effects of ligand **6** is a pivotal requirement for establishing this compound as an α7-selective type I PAM and would strengthen the conclusion that the residues identified directly interact with ligand **6**. M253, a residue in position 15′ of the transmembrane 2 domain, is predicted to interact with ligand **6**. This residue is unique to the α7 nAChR sequence and has been shown to be essential for α7-selective PAM I [177, 35], PAM II [187, 280, 36, 35], and ivermectin [281]. Furthermore, recent structural insights have shown M253 as a pivotal contributor to the binding site of PAMs PNU-120596 [36, 35], ivermectin [281], and NS1738 [35] on the transmembrane domain of α7 nAChR. The role of M253 on ligand **6** potentiating effects was determined by mutating M253 to leucine, a residue that abolishes α7 PAM activity [179, 187, 280]. As shown in Figure 3.8E, M253L dramatically reduced the ability of ligand **6** to enhance the EC_{20} ACh responses of α7 nAChR. M253L did not affect the ACh potency (WT ACh EC_{50} $125 \pm 25\,\mu M$ (n = 8) vs M253L ACh EC_{50} $120 \pm 14\,\mu M$; n = 5).

3.4 Discussion

Compounds containing the quinuclidine moiety have been used to produce selective agonists of the α7 nAChRs. In this study, a series of novel compounds based on this scaffold were assayed for agonism, with only one of the synthesised molecules showing agonist activity (ligand **4**), while the others failed to elicit currents on their own. Ligands **4** and **5** are isomers, with the only difference between them being the position of the bromine in the pyridine ring, yet their effects on the receptor are completely different. One possible explanation is that the bromine atom at position **6** of the pyridine ring in ligand **5** withdraws electrons by an inductive effect, which makes the nitrogen atom of the pyridine ring less basic and thus less adept at engaging in hydrogen bonding interactions with relevant residues in the agonist binding site. Hydrogen bonding interactions have

been reported for several α7 nAChR agonists containing a pyridine ring (e.g., nicotine [153] and TC-7020 [282]). In the case of ligand **4**, the hydrogen bonding capability of the nitrogen atom of the pyridine is unlikely to be impaired by the bromine atom, as this is located on a carbon far away (position 5 of the pyridine ring) from the nitrogen atom. Allosterically, only ligands **6**, **8** and **9** were able to potentiate the ACh response, with ligand **6** being the most efficacious one. The potency of ligand **6** is comparable to previously reported PAMs of the α7 nAChR such as the flavonoid genistein (EC_{50} = $9.36 \pm 0.81\,\mu M$ [177]) and NS1738 ($12.5 \pm 1.5\,\mu M$ [283]).

In summary, hydrophilic or hydrophobic side groups in 3-(pyridin-3-yloxy)quinuclidine moiety abolish agonism at α7 nAChR. Considering that selectivity and agonist activity are obtained with ether quinuclidines with large hydrophobic substituents (for example, AQW051 [260]), the addition of a relatively bulky hydrophobic side group (phenylacetylene) or a hydrophilic group (hex-5-yn-1-ol) in the pyridine ring may significantly weaken hydrophobic interactions between the hydrophobic motif of the derivatives and the binding site. Interestingly, both types of side groups confer allosteric activity. The hydrophobic group confers potentiating properties only when present in position **6**; the isomer of ligand **6** is **7**, suggesting that the recognition site for this type of potentiator can accommodate only one type of geometric isomer. In contrast, the site that recognizes hex-5-yn-1-ol appears to be able to accommodate both isomers; ligands **8** and **9** potentiated the ACh responses of α7 nAChR with similar potency and efficacy, this may be caused by the higher flexibility of the hex-5-yn-1-ol group, compared to the more rigid phenylacetylene.

Earlier studies have shown that type I and type II PAMs increase the duration of burst events, which can be correlated with the efficacy of the modulator [177]. Thus, depending on the PAM type burst duration can range from several seconds, as with the highly efficacious type II PAM PNU-120596 to a few milliseconds as with type I PAMs 5-HI

and flavonoids [278, 177]. Single-channel recordings revealed that ligand **6** enhances burst duration, as observed for most PAMs. The magnitude of the increase of the burst duration is more similar to that observed in the presence of low-efficacy type I PAM, such as 5-HI, than in the presence of type II PAM, such as PNU-120596. In contrast to what has been reported for other PAM, such as 5-HI [278], flavonoids [177], and phosphonate-functionalized 1,4-disubstituted 1,2,3-triazole compounds [284], ligand **6** did not increase open duration. This may indicate either that it has a very low efficacy to stabilise the open state or that it does not exert any effect on desensitisation, as expected for a type I PAM since desensitisation is the major determinant of α7 nAChR open channel lifetime [78, 81].

On another note, it was observed that ligand **6** produces inhibition of the currents evoked by ACh at higher concentrations, although with a different threshold for macroscopic and single-channel recordings (>$300\,\mu\mathrm{M}$ and >$60\,\mu\mathrm{M}$ respectively). The difference in the concentration at which inhibition is observed between these recordings is likely attributed to the higher sensitivity of the latter technique. However, the data indicates that the inhibitory effect of ligand **6** manifests at concentrations higher than those necessary for potentiation. Furthermore, it is worth noting that the inhibitory concentration, even for single-channel recordings, exceeds the EC_{50} for potentiation ($10\,\mu\mathrm{M}$). The decrease of the potentiation ability at high concentrations has been described for other α7 nAChR PAM, including flavonoids and phosphonate-functionalized 1,2,3-triazoles [284, 177]. Possible mechanisms for this effect may be slow channel blockade, which is in accordance with ligand **6** occluding the ion pore in several of the predicted blind docking poses (Figure 3.7), or a dual positive–negative activity.

Blind docking studies predicted an inter-subunit transmembrane binding site. This is consistent with the site reported for PNU-120596 in α7 nAChR [36, 35], and the binding site of ivermectin in both the *C. elegans* glutamate-gated chloride channel GluClα and α7

nAChR [281, 55]. It is also a similar site to the one reported for type I PAM NS1738 [35], whose activity resembles that of ligand 6. It is worth noting that the Cryo-EM structure for α7 nAChR with NS1738 was reported after the present work was published, thus here it was described for the first time this allosteric site for type I PAM in the α7 nAChR [229].

Using molecular dynamics to refine the binding pose several interactions with the transmembrane helices were observed. Of these interactions, some can be highlighted for their reported importance: N213 and M253 being amino acids previously reported as critical for the function of other allosteric modulators such as NS1738, ivermectin, and PNU-120596 [281, 35, 179, 187, 280, 36], L254 is one of the hydrophobic constriction sites in the receptor pore lining [30], and A257 is one of the amino acids that interact with the β1-β2 loop after it pivots during activation [30]. The importance of the interactions between the protein and the ligand side group is highlighted by the functional results, which showed that smaller substituents, like the bromide in the ligand **5**, fail to potentiate the response, and more polar substituents such as the alcohol group in ligands **8** and **9** have a much weaker allosteric effect. Also, because of the rigidity of the triple bond that connects the phenyl ring with the pyridine ring, changing the position of the substituent in the pyridine ring would cause steric hindrance in the tight transmembrane binding site (Figure 3.8C). Of relevance, except for α7 and α10 subunits, M253 is absent in nAChR subunits. Thus, its absence in α4 and β2 subunits could account for the inability of ligand **6** to potentiate α4β2 nAChRs (Figure 3.3).

To summarize, the purpose of this study was to explore the functional effect of 3-(pyridin-3-yloxy)quinuclidine ethers derivatives on the α7 nAChR. Only ligand **4** showed the ability to activate α7 nAChR, behaving as a partial agonist. While ligands **6**, **8**, and **9** showed the ability to allosterically enhance the ACh-induced current, with **6**, which has a phenylacetylene group in position six with respect to the pyridine ring, being the

most potent and effective potentiator. Single-channel recordings showed that ligand **6** enhances burst durations, a typical effect observed in the presence of α7 nAChR PAMs. This finding together with the observation that ligand **6** potentiates ACh responses with conserved kinetics indicates ligand **6** is a type I PAM. Using computational tools it was predicted that ligand **6** binds in the transmembrane domain of the human α7 nAChR, a site reported for other PAMs, where the phenyl group at position 6 of the pyridine ring of this ligand would be key to the modulatory activity and mutational studies confirmed this prediction.

This work showed that a combination of docking and molecular dynamics can accurately predict the binding site of a novel allosteric drug. Additionally, the binding site predicted was analogous to the site of other type I PAMs that were reported afterwards, but also to the site of type II PAMs, contributing to a body of evidence pointing to these two types of PAM sharing a common binding site in the α7 receptor and leaving the question open as to the exact mechanism that differentiates the two types of PAM.

4 | Selective Potentiation of the $(\alpha4)_3(\beta2)_2$ Nicotinic Acetylcholine Receptor Response by NS9283 Analogues.

Disclaimer

The research presented in this chapter has been published in ACS Chemical Neuroscience in 2024 [285], see also in the list of publications.

4.1 Introduction

The nicotinic receptor subtype assembled from α4 and β2 subunits exists in two stoichiometries in the mammalian brain, the HS $(\alpha4)_2(\beta2)_3$ and the LS $(\alpha4)_3(\beta2)_2$ [65] (Figure 1.5). The LS stoichiometry has a stoichiometry-specific α4-α4 interface, which harbours an operational agonist binding site [68], and it can be exploited to design stoichiometry-selective ligands. The drug NS9283 is one of the most studied compounds for LS α4β2 modulation, it binds at the α4-α4 interface site where it potentiates agonist responses, it does not evoke responses on its own, and shows no modulatory effect on the HS multimer [74, 75, 76, 50]. Furthermore, this allosteric drug is capable of potentiating agonist-induced analgesic effects in nociceptive preclinical pain models without exacerbating the side effects of the analgesic, reducing nicotine self-administration, and improving cognitive performance without exogenous agonists [286, 287, 192, 288].

Early mechanistic studies on NS9283 function revealed that the modulator increases the potency, but not the efficacy of the agonists. It was also observed that it exerts its potentiation mainly by reduction of the macroscopic deactivation rate of the receptor, which corresponds to the decay of the current after removal of the agonist, while having

a minor effect on receptor activation [289]. Additionally, no effect was observed on the desensitisation kinetics, and the modulator is incapable of reactivating desensitised receptors. Furthermore, the modulator reduces the rate of recovery from the desensitised state to the activatable resting state [289].

Structurally, NS9283 has been studied using the *Lymnaea stagnalis* AChBP to obtain a crystal structure of bound NS9283 and constructing a homology model of the α4-α4 interface using the structure as a template. The binding mode observed in that work displays interactions with the complementary face of the binding site, particularly with H142 and W88 [75]. This is consistent with the mutational scan performed, where mutating these residues greatly reduced or completely eliminated the potentiation by NS9283 [75, 290]. Nevertheless, this binding conformation does not explain other mutants of the complementary binding site that also affect potentiation, namely R112, Q150 and T152. Additionally, subsequent mutational analyses done in concatamers showed that substituting the loop B tryptophan in the β2(+)-α4(-) interface significantly diminished the potentiated currents. This suggested that the β2(+)-α4(-) interface contributes to NS9283 potentiation, either by housing an additional binding site for the ligand or by playing a role in the signal transduction for potentiation by NS9283 [291]. The structure-activity relationship of NS9283 has been investigated previously, but only for the development of positive modulators for α4β2α5 nAChR, where the α4-α4 is not present and the derivatives of NS9283 were expected to bind the α5-α4 interface [292]. In this chapter, a series of new NS9283 analogues were screened for the ability to potentiate the response of ACh in the LS α4β2 nAChR. Then, the binding of four selected compounds to the α4-α4 interface was structurally characterised using molecular dynamics simulations.

4.2 Materials and Methods

4.2.1 Novel Compounds

NS9283 analogues were provided and synthesised by Prof. Cristiano Bolchi's group from Università degli Studi di Milano as described in the original paper [285]. The compounds were numbered according to Figure 4.1.

4.2.2 Two-Electrode Voltage-Clamp Recordings

Current responses were recorded using two-electrode voltage-clamp recording at a holding potential of $-60\,\mathrm{mV}$ using an Oocyte Clamp OC-725C amplifier (Warner Instruments, USA) or the automated HiClamp system (Multi Channel Systems, Reutlingen, Germany), as described in Chapter 2 Section 2.2.3.5.

CRCs for potentiation of ACh EC_{20} ($30\,\mu\mathrm{M}$ for LS $\alpha4\beta2$ and $\alpha7$ nAChR and $3\,\mu\mathrm{M}$ for HS $\alpha4\beta2$ and $\alpha5\alpha4\beta2$ nAChR) were obtained according to the procedure described in Section 2.2.3.5 and the regression analysis was performed as described in Section 2.2.3.6.

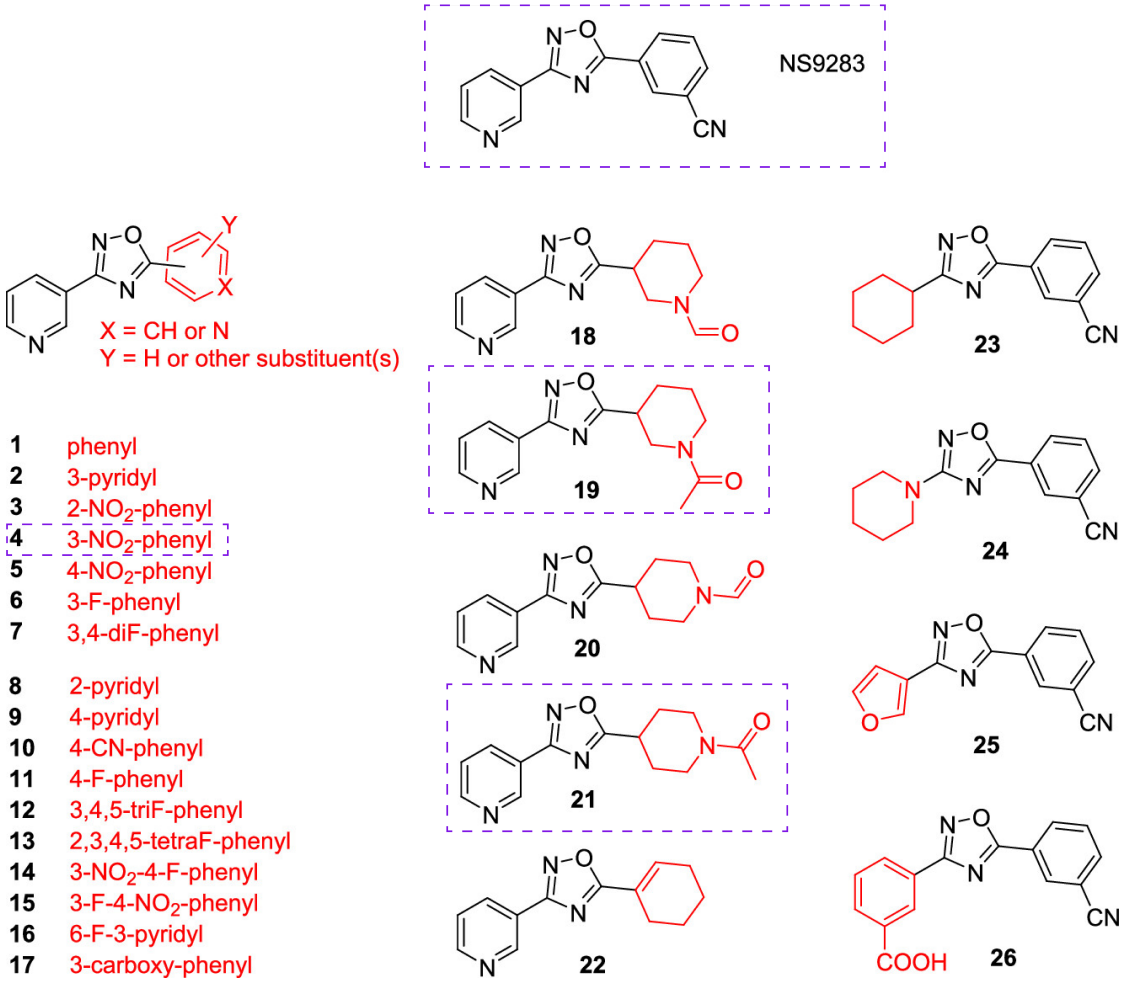

Figure 4.1: Chart describing the structure of NS9283 and its Analogues Modified at the Peripheral Rings. The purple boxes indicate the ligands that were used in the computational studies.

4.2.3 Molecular Dynamics Simulations

4.2.3.1 System Preparation

The α4β2 nAChR in the LS stoichiometry was obtained from the PDB ID: 6CNK [29]. The structure was truncated, and only the extracellular portion of the α4-α4 interface was retained. Harmonic restraints were applied to the five initial and final residues

of each chain to compensate for the absence of the other subunits. Additionally, to validate the truncated construct, two additional simulations were carried out using the full extracellular domain of the protein using the same harmonic restraints with NS9283 occupying the α4-α4 site and nicotine in the α4-β2 site. The coordinates for the ligands NS9283, ligand **4**, ligand **19**, and ligand **21** were prepared with the open-source software RDKit [293] and docked into the α4-α4 interface binding site using AutoDock Vina [266] and the best-ranked poses were used (Figure 4.2). The topology for the ligands was produced with AmberTools22 [271] using the GAFF force field [272]. The best-ranked docking pose was selected for simulations. The protein was parameterized with the Amber99SB force field [294], solvated in a TIP3P water box [273], and neutralised with $0.15\,\mathrm{mM}$ of NaCl. The system was then energy minimized and then equilibrated, first to $310\,\mathrm{K}$ in an NVT ensemble and then to 1 atm in an NPT ensemble, both for $1\,\mathrm{ns}$ to allow the pressure and volume of the system to stabilize. All simulations were run in GROMACS 2021.5 patched with PLUMED version 2.8.0. [274, 275].

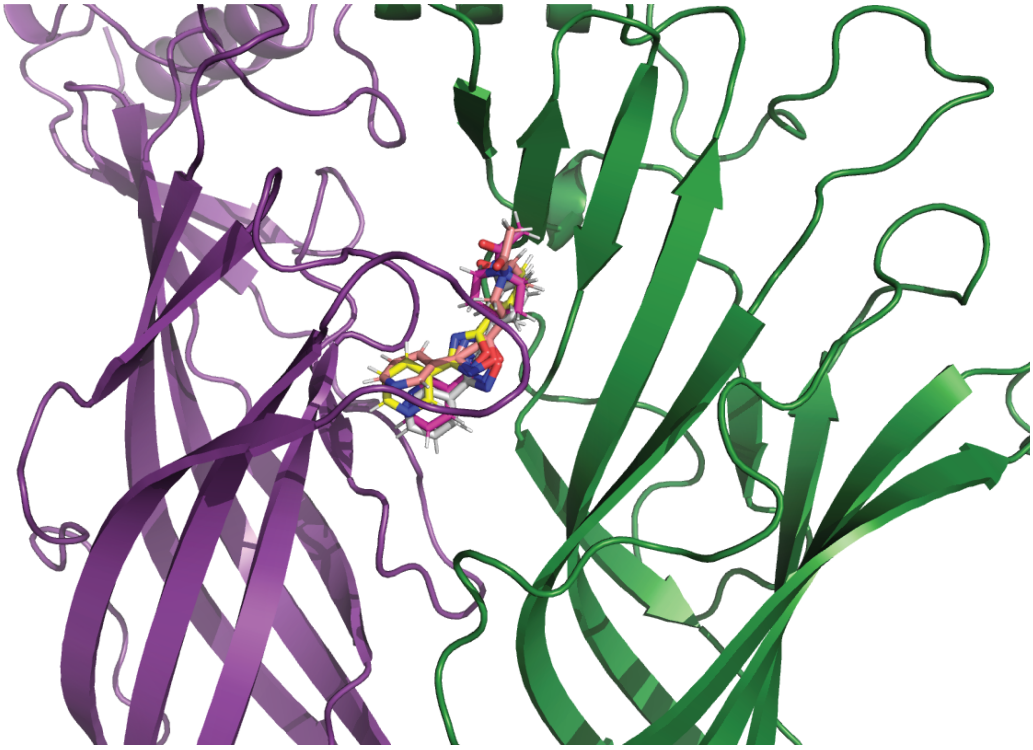

Figure 4.2: **Binding poses of ligands on α4-α4 interface of LS α4β2 nAChRs.** Best ranked binding poses of NS9283 (white) and its **4** (yellow), **19** (pink) and **21** (magenta) derivatives.

4.2.3.2 REST

For the REST simulations (see Section 2.1.4.1), the solute region, the part of the system whose temperature will be scaled, was defined as the ligand and 14 surrounding residues of the binding site (Y126, S181, W182, T183, Y223, C225, C226, and Y230 of the main (+) chain and W88, K90, R112, H142, Q150, and T152 of the complementary (-) chain). To prevent the ligand from dissociating from the binding site at high temperatures, a flat-bottom restraint at 8 Å from the center of mass of the binding site was applied to the ligand. The system was simulated for 200 ns over a temperature range spanning from 310 K to 1000 K, distributed among 16 replicas, with attempted exchanges occurring every 1000 steps. This configuration was enough to provide good mixing between

replicas (Table 4.1). Subsequently, the trajectories at $310\,\mathrm{K}$ were analyzed by clustering the ligand and selected binding site residues to extract representative conformations using the GROMOS algorithm [267]. Then, the selected conformations were used as a starting point for $200\,\mathrm{ns}$ unbiased simulations to assess pose stability and contacts. To recover the free energy landscape of the tryptophan $\chi 1$ angle (the dihedral between N-CA-CB-CG), this collective variable was calculated for every replica and the samples were reweighted using the MBAR estimator (see Section 2.1.4.3). All other analyses were performed using MDAnalysis [276].

Table 4.1: Average exchange probabilities for each replica exchange simulation.

System	Exchange Probability (min-max)
NS9283	30-49%
NS9283 Full Extracellular 1	31-48%
NS9283 Full Extracellular 2	30-48%
Ligand 4	28-48%
Ligand 19	31-50%
Ligand 21	30-50%

4.2.3.3 Umbrella Sampling Simulations

First, to generate a transition path for the US, a $10\,\mathrm{ns}$ steered molecular dynamics (SMD) simulation starting from the equilibrated native structure was run. During the simulation, the heavy atoms of W182 were pulled toward the alternate conformation using a moving restraint on the RMSD of the residue with respect to the NS9283 bound conformation. The restraint was shifted from $0.298\,\mathrm{nm}$ to $0\,\mathrm{nm}$ with a force constant of $5000\,\mathrm{kJ\,mol^{-1}\,nm^{-2}}$. From the resulting trajectory, the frames with the closest tryptophan $\chi 1$ angle to the 20 US restraint centers were selected. Each window of the US was run for $30\,\mathrm{ns}$ with a harmonic restraint, as described on Section 2.4, on the corresponding center and a force constant of $1000\,\mathrm{kJ\,mol^{-1}\,rad^{-2}}$ on the W182 angle. The PMF curve was constructed from the US trajectories using the WHAM algorithm (see Section 2.1.4.3) implemented by Bauer [295].

4.3 Results

4.3.1 Functional Characterization of NS9283 Analogues

Initially, NS9283 and the analogues shown in Figure 4.1 were screened for their ability to potentiate the current responses elicited by the (EC_{20}) of ACh at LS $\alpha4\beta2$, HS $\alpha4\beta2$, $\alpha5\alpha4\beta2$, or $\alpha7$ nAChR expressed heterologously in *Xenopus laevis* oocytes. In these experiments, a single concentration was tested, $30\,\mu M$, a concentration at which NS9283 exerts its maximal potentiation of EC_{20} ACh responses. For control, NS9283 was assayed in parallel as an efficacious and selective PAM of $(\alpha4)_3(\beta2)_2$ nAChR. Neither NS9283 nor its analogues potentiated the responses of EC_{20} ACh at HS $\alpha4\beta2$, $\alpha5\alpha4\beta2$, or $\alpha7$ nAChR (Figure 4.3). In addition, none of the ligands evoked a response on their own.

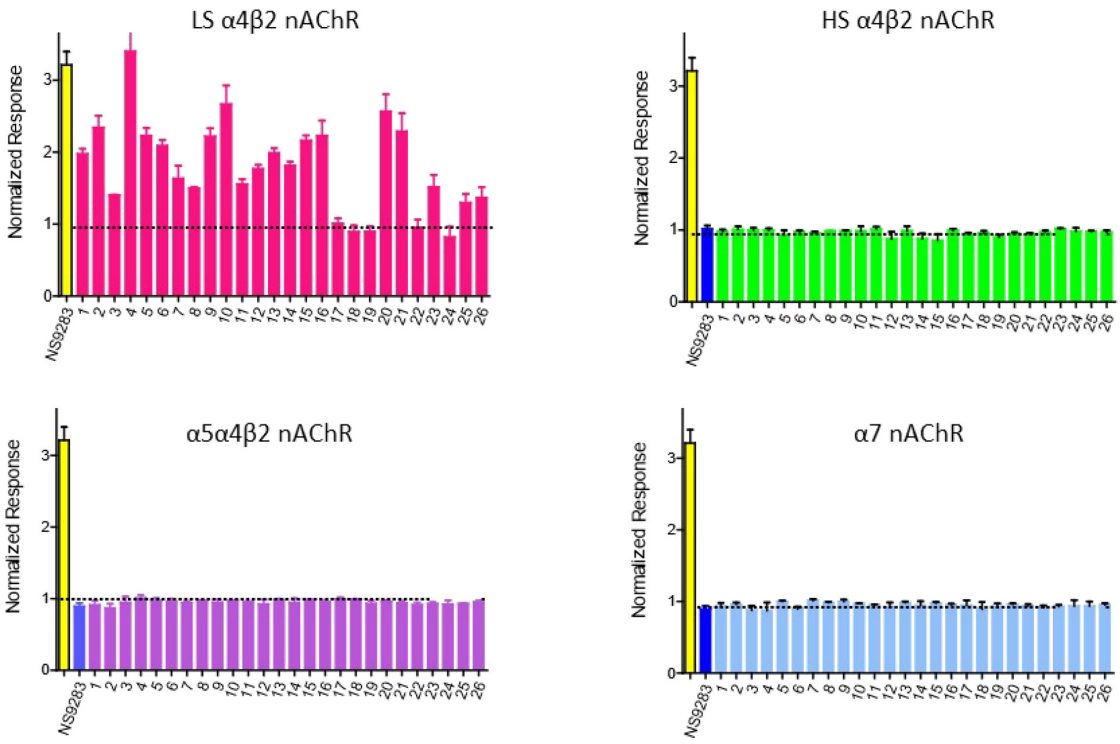

Figure 4.3: Activity of NS9283 and analogues at α4β2, α5α4β2, and α7 nAChRs. Ligands were tested for their effects on the ACh EC_{20} responses of LS α4β2, HS α4β2, α5α4β2, or α7 nAChR expressed heterologously in *Xenopus oocytes* using two-electrode voltage-clamp recording procedures. For comparison purposes, the effects of NS9283 (yellow column) at LS α4β2 nAChR is included on the histograms for LS α4β2, HS α4β2, α5α4β2, and α7 nAChR. All ligands were tested at 30 μM

Of the screened compounds, 10 analogues, all modified at the cyanophenyl portion of NS9283, potentiated the ACh EC_{20} responses of LS α4β2 nAChR with a relative efficacy comparable to that of NS9283 (Figure 4.4). Five of these resulted from the substitution of 3-cyanophenyl with other substituted phenyl residues: 3- or 4-nitrophenyl (**4** and **5**), 3-fluorophenyl (**6**), 4-cyanophenyl (**10**), and 3-fluoro-4-nitrophenyl (**15**); three from replacement with pyridyl residues: 3- or 4-pyridyl (**2** and **9**) and 6-fluoro-3-pyridyl (**16**); and two with N-formyl-4-piperidinyl (**20**) and N-acetyl-4-piperidinyl (**21**). The CRCs of NS9283, seven analogues selected from the above ten (**2**, **4**, **5**, **9**, **10**, **20**, and **21**), and **19** were determined on LS α4β2 nAChR. Their EC_{50} and relative efficacy of potentiation

are reported in Table 4.2. Figure 4.4A shows the CRCs for the analogues tested. For comparison purposes, Table 4.2 and Figure 4.4 show the concentration effects of NS9283 and an analogue that displayed no potentiating activity at LS $\alpha4\beta2$ nAChR (analogue **19**). Representative traces of responses for NS283, **4**, **19**, and **21** are shown in Figure 4.4B.

Table 4.2: Concentration Effects of NS9283 and Analogues on LS $\alpha4\beta2$ nAChR: The concentration effects of the test compounds were determined on ACh responses elicited by an EC_{20} ACh concentration ($30\,\mu M$). The data points were used to generate CRC plots from which EC_{50} and relative efficacy of potentiation were estimated, as described in Section 2.2.3.6. Data for NS9283 and an inactive analogue (**19**) are included for comparison purposes. Statistical analyses were carried out as described in Section 2.2.3.7. Statistical differences between the amplitude of the currents generated by ACh EC_{20} in the absence or presence of ligands are indicated by +. Asterisks indicate that the change in EC_{50} and/or relative efficacy between NS9283 and the analogues is statistically significant (*$p < 0.05$).

Ligand	EC_{50} μM (95% CI)	Efficacy (95% CI)	Efficacy/Efficacy of NS9283
NS9283	3.43 (2.3–4.6)	3.21^{+} (2.8–3.6)	1
2	6.17 (4.1–8.4)	2.25^{+*} (1.9–2.6)	0.44
4	7.67 (5.8–9.5)	3.40^{+*} (2.7–4.1)	1.05
5	6.27 (4.1–8.4)	2.13^{+} (1.8–2.5)	0.67
9	14.48 (6–35)	2.27^{+*} (1.8–2.7)	0.71
10	19.20^{*} (9–28)	3.07^{+} (0.27–5.74)	0.96
19	NA	1.02 (0.97–1.07)	0.32
20	34^{*} (12–56)	3.3^{+} (1.48–5.11)	1.03
21	55^{*} (11–98)	2.58^{+} (1.62–3.53)	0.8

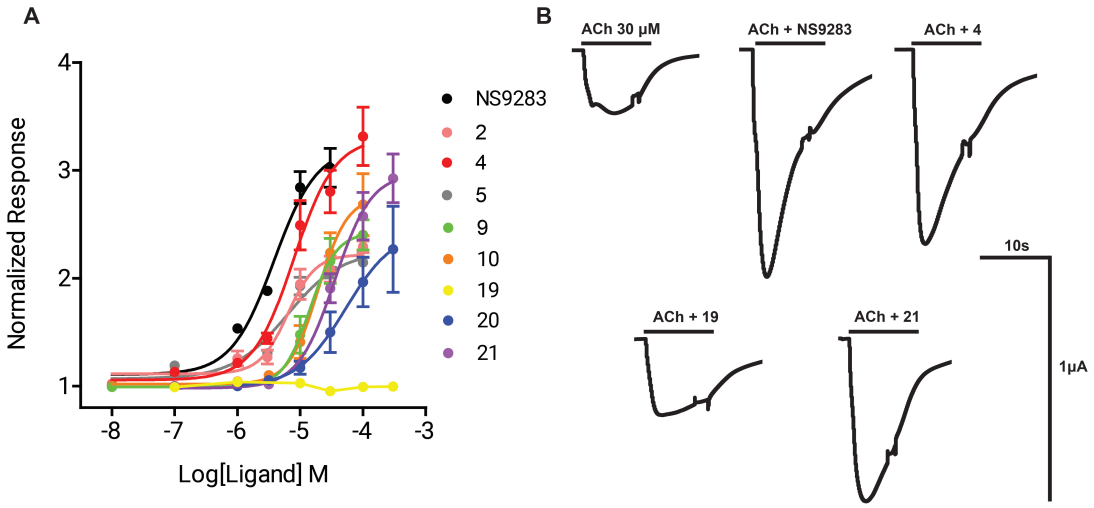

Figure 4.4: Effects of NS9283 and analogues on LS α4β2 nAChR. (A) Concentration-dependent effects of ligands shown in Table 4.2 (NS9283, **2**, **4**, **5**, **9**, **10**, **19**, **20**, and **21**) on the responses of LS α4β2 nAChR to ACh EC_{20} (30 µM). (B) Representative traces of 30 µM ACh-evoked current and 30 µM ACh-evoked currents in the presence of NS9283 or ligands **4**, **21**, and **19**.

4.3.2 Binding Mode Prediction of Selected Analogues

In an attempt to understand how the pattern of substitutions applied to the phenyl and piperidine rings affects the interactions of these compounds with the α4-α4 interface, computational studies focusing on NS9283, its two active analogues, 3-nitrophenyl (**4**) and N-acetyl-4-piperidinyl (**21**), and N-acetyl-3-piperidinyl (**19**), which is an inactive isomer of **21**, were performed.

The cluster densities resulting from the replica exchange simulations show one major cluster for NS9283, ligand **4**, and ligand **19**, and two similarly populated clusters for ligand **21** (Table 4.3). The conformation predicted for NS9283 (Figure 4.5A) shows the ligand mainly interacting with the complementary (-) side of the binding site (Figure 4.6A,B) and remains highly stable in the subsequent unbiased simulation (Figure 4.7A) and the conformation is consistent across the different repeats (Figure 4.8).

Table 4.3: Cluster distribution from the REST simulations.

	NS9283	NS9283 Full Extracel. 1	NS9283 Full Extracel. 2	ligand 4	ligand 19	ligand 21
Cluster #	Fraction of the simulation in the cluster (%)					
1	43.7	51.7	53.8	63	60.6	50.5
2	23.2	15.6	12.2	9.9	18.7	41.8
3	11.2	12.2	6.2	7.2	17.7	2.4
4	6.4	4.6	6.2	4.3	1.1	2.1
Total Clusters	28	28	27	27	17	16

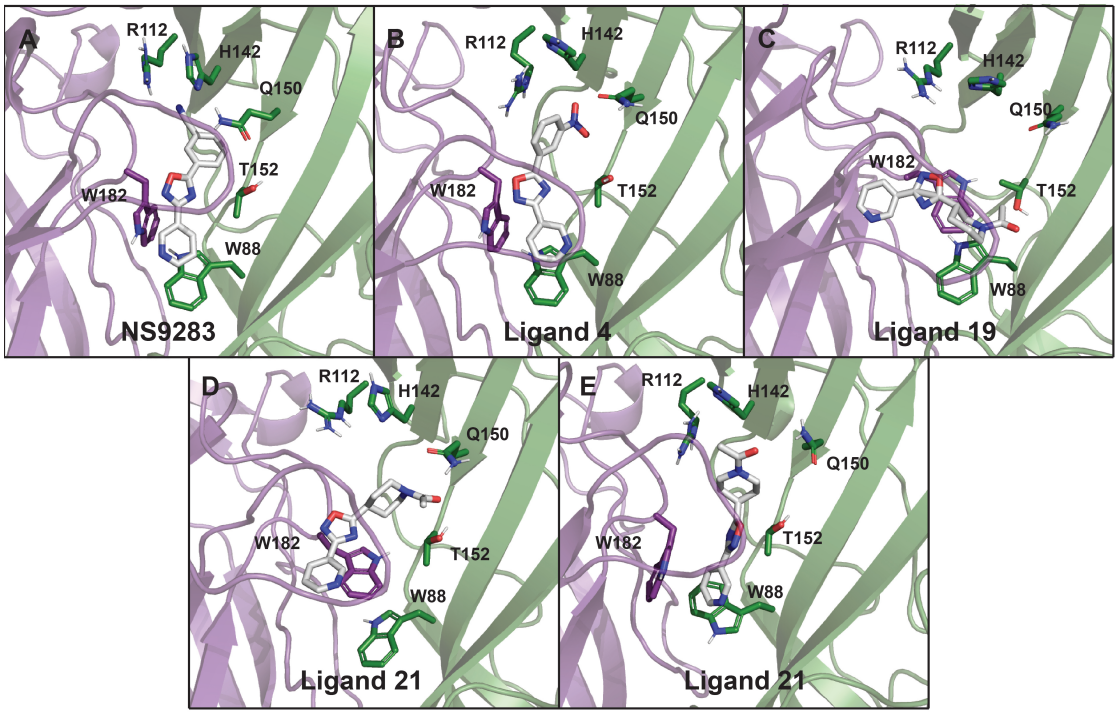

Figure 4.5: Selected conformations for NS9283 (A), ligand **4** (B), ligand **19** (C), and the two clusters of ligands **21** (D, E). The positive α subunit is represented in purple, and the negative α subunit is represented in green.

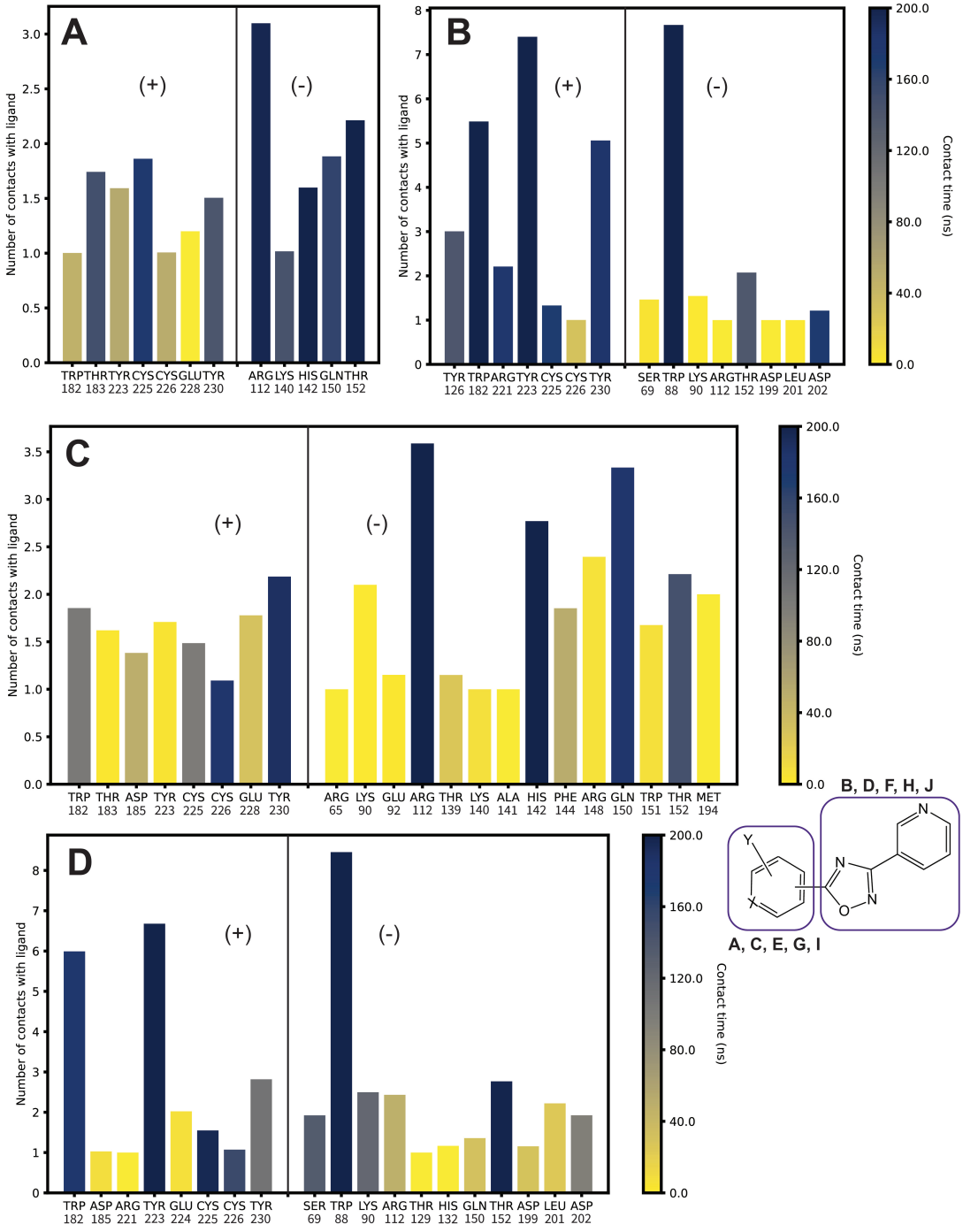

Figure 4.6: Contact analysis of the ligands with the protein side chains for NS9283 (A, B), ligand **4** (C, D). (Continued on next page)

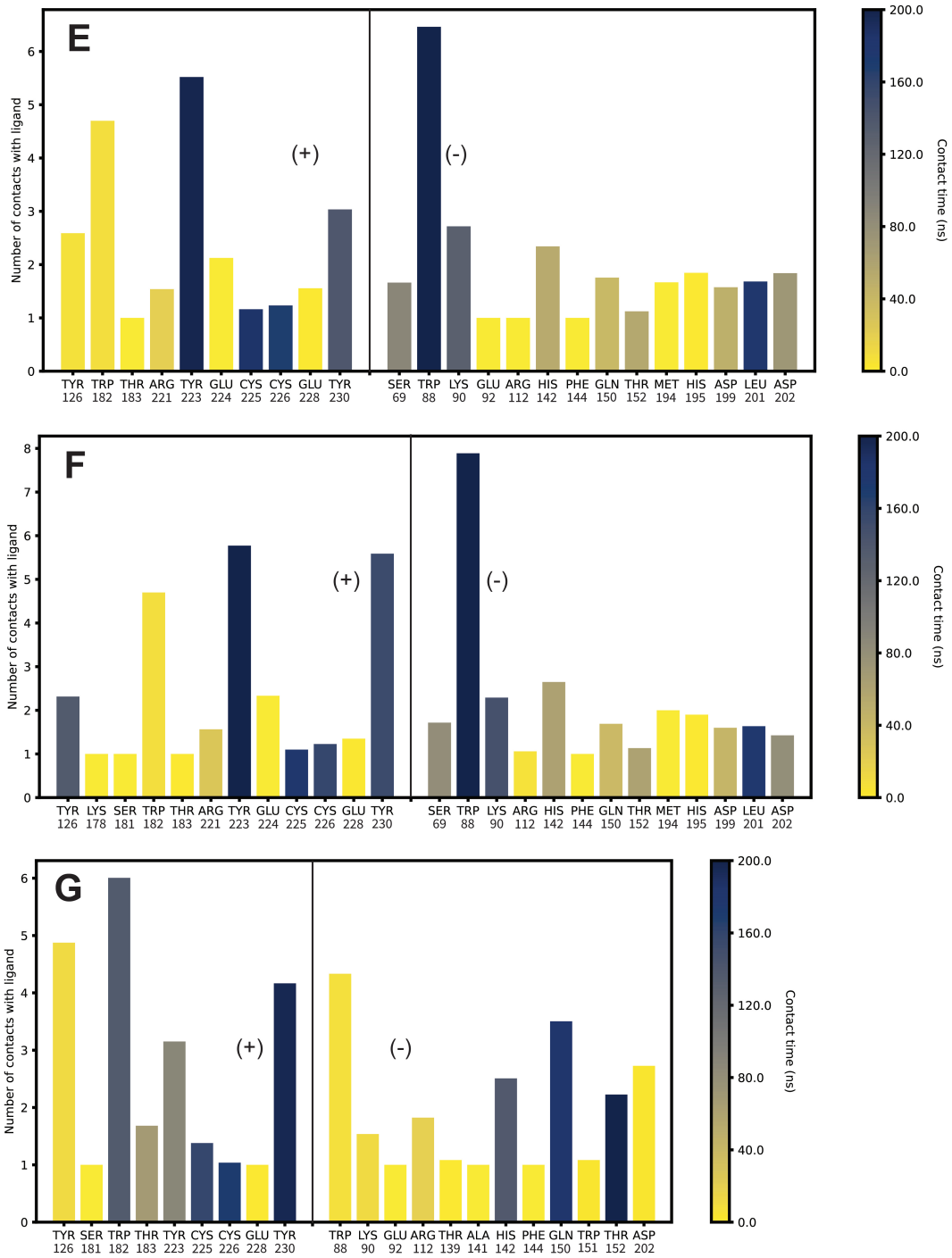

Figure 4.6: (Previous page). Ligand **19** (E, F), ligand **21** cluster 1 (G, H). (Continued on next page)

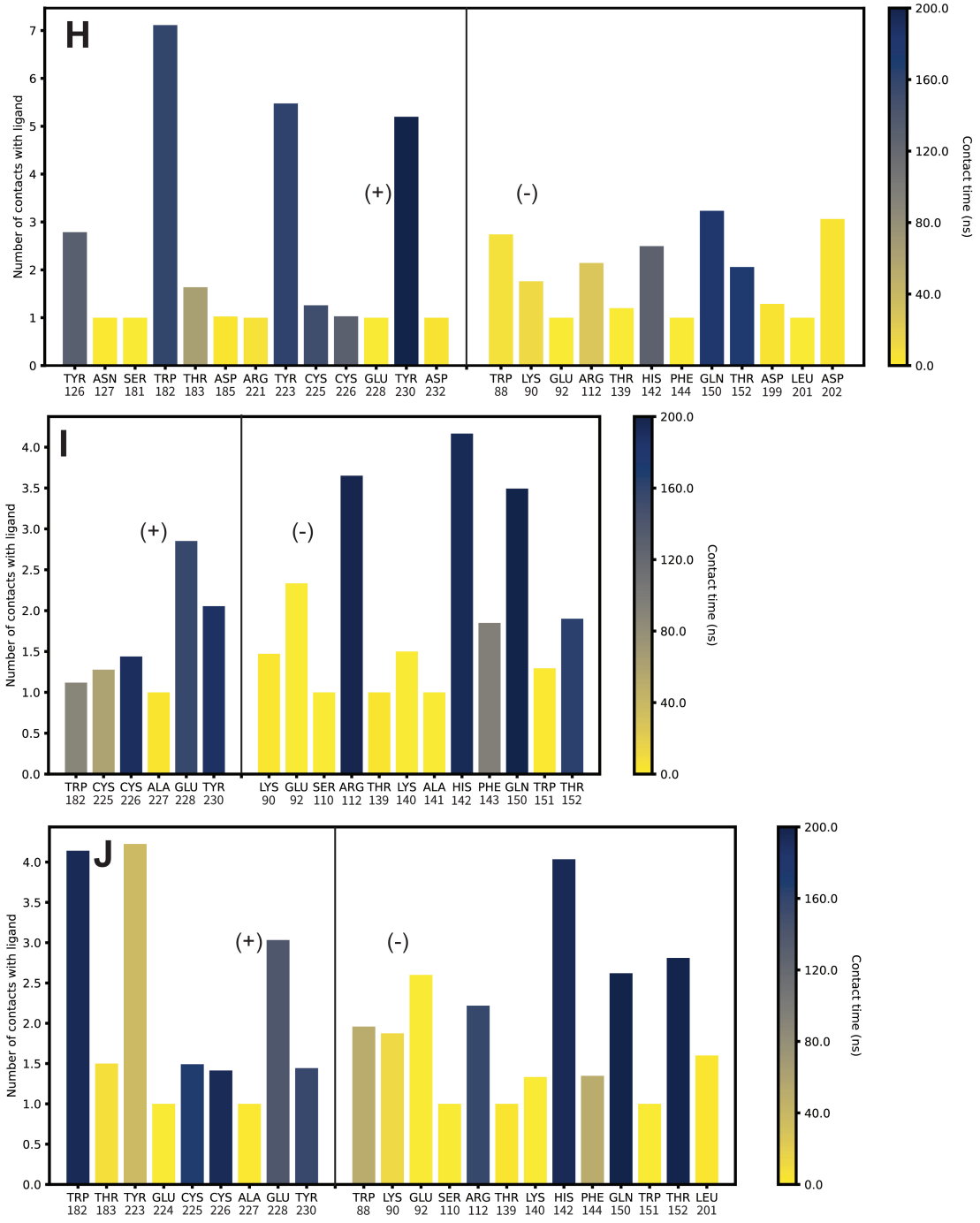

Figure 4.6: (Previous page). Ligand **21** cluster 1 (G, H), and ligand **21** cluster 2 (I, J).

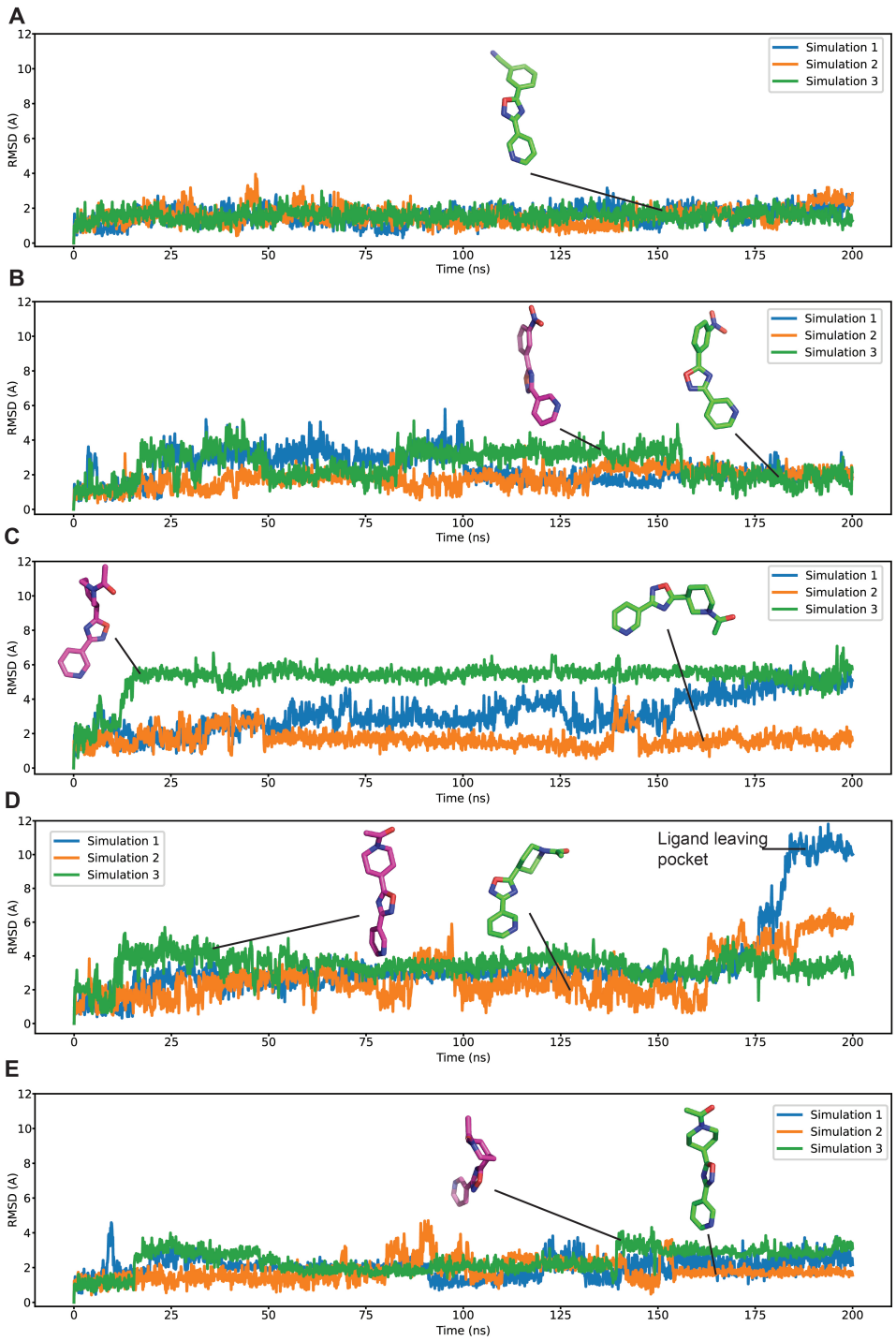

Figure 4.7: RMSD over time of the 200 ns unbiased simulations for NS9283 (A), ligand **4** (B), ligand **19**. (C), ligand **21** cluster 1 (D), and ligand **21** cluster 2 (E). The structures depict the conformations adopted by the ligands at the indicated RMSD values.

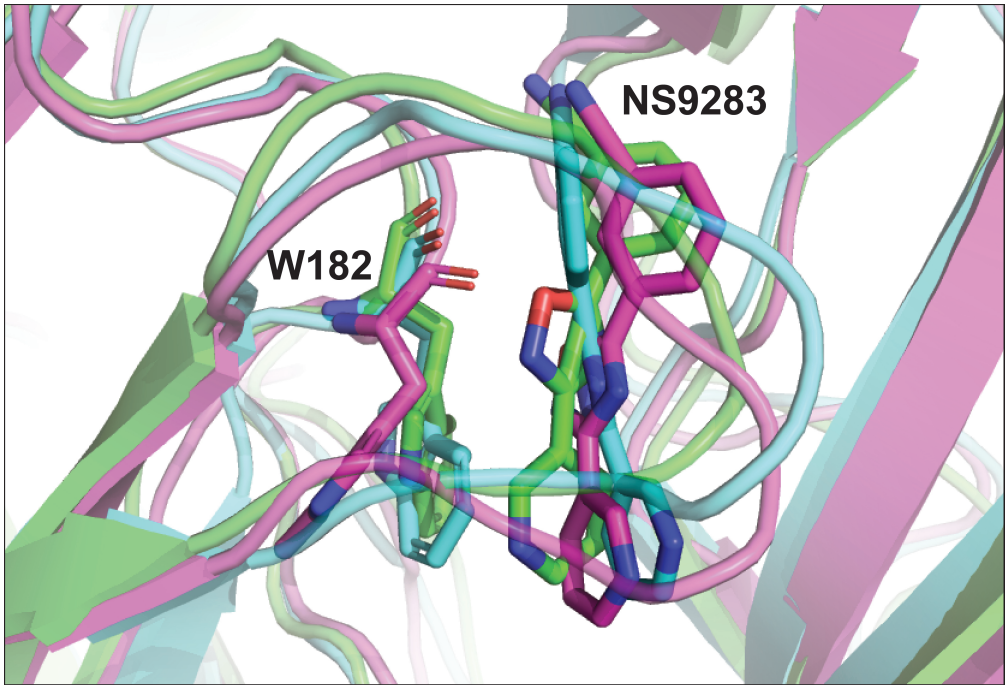

Figure 4.8: Comparison of the conformation of NS9283 and W182 between the original truncated construct (green) and the full extracellular domain constructs (cyan and magenta).

Another striking feature of this binding conformation is the rotameric form of W181, which differs significantly from the native structure (Figure 4.9). In the case of ligand **4**, the conformation is similar to NS9283 (Figure 4.5B) and has a similar contact pattern (Figure 4.6C, D), but it is less stable in the unbiased simulations (Figure 4.7B). This is not surprising as this is the derivative with the closest functional activity to that of NS9283 (Table 4.2). On the other hand, the best pose for ligand **19**, which is inactive, is less stable in the unbiased simulations (Figure 4.7C) and does not resemble the ones from NS9283 or ligand **4** but instead appears oriented in the binding site in a horizontal fashion (Figure 4.5C), lacking both the key interactions present in the former ligands (Figure 4.6E,F) and the conformational change of W181. Finally, since the two clusters obtained for ligand **21** (Figure 4.5D,E) had similar populations 4.3, none of them could be discarded a priori; thus, both were analyzed for stability and contacts. The first conformation resulted in

being less stable than the second (Figure 4.7D,E). Furthermore, the contact pattern of the second pose (Figure 4.6I,J) coincides better with the contacts of NS9283 and contains the alternative rotamer for W181, whereas, in the first cluster, the tryptophan is in its native-like state.

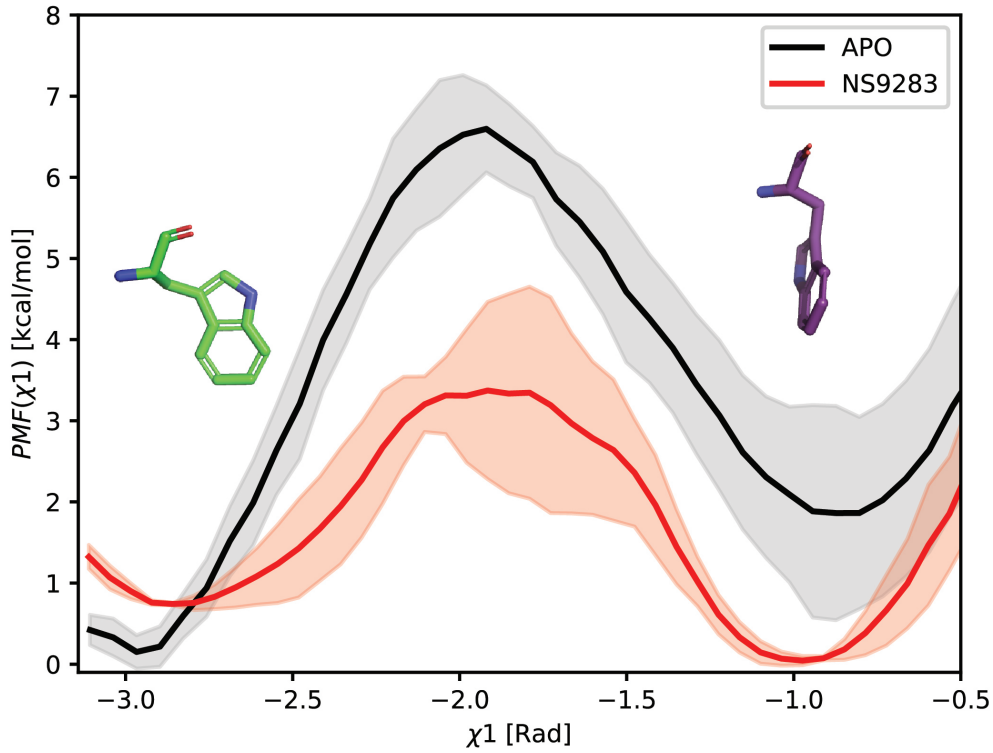

Figure 4.9: Potential of mean force on the tryptophan $\chi 1$ angle with the native (green) and alternative (purple) conformations displayed over their corresponding basin. The PMF in the apo state (black) was calculated from US simulations, while the PMF in the bound state was calculated from REST simulation using the MBAR estimator (red). The shaded region corresponds to the standard deviation between the three replicas.

4.3.3 The Conformational Change of W181 is Favoured by NS9283

To study the energetics of the conformational change and to ensure it is accessible to the protein, the PMF for this transition in the apo state was constructed using umbrella

sampling. The resulting energy surface shows that, even though the native state is much more favourable, the alternative rotameric state is in a local minima basin, separated from the native conformation by a barrier of $6.6\,\mathrm{kcal\,mol^{-1}} \pm 0.54$ (Figure 4.9). For comparison, the PMF for the transition in the presence of NS9283 was obtained from the REST simulations using the MBAR estimator to reweight the samples of higher temperatures to the target temperature ($310\,\mathrm{K}$). In the bound simulations, the energy landscape is inverted, showing the alternative conformation as more favourable and a reduced barrier of $3.4\,\mathrm{kcal\,mol^{-1}} \pm 1.1$.

4.3.4 NS9283 is not Stable in the β2-α4 site

Previous studies on the $(\alpha4)_3(\beta2)_2$ nAChR have proved that mutations at either the principal face of the β2 subunit or the complementary face of the α4 subunit prevent NS9283 potentiation of ACh-elicited single-channel currents, suggesting that the drug targets the β2(+)-α4(-) subunit interface, the α4-α4 agonist site, or both sites. Consistently, microscopic current studies have shown that LS α4β2 nAChR with mutant β2(+)-α4(-) interfaces are not potentiated by NS9283 [291]. To assess the binding of the allosteric modulator in the β2(+)-α4(-) interface, REST simulations were performed using only NS9283 as a ligand. Clustering showed two main conformations for NS9283, neither of which shows strong interactions with the key conserved residues on the complementary face of the β2(+)-α4(-) interface or with the conserved tryptophan (W176) in loop B in the (+) side of the β2(+)-α4(-) interface (Figure 4.10).

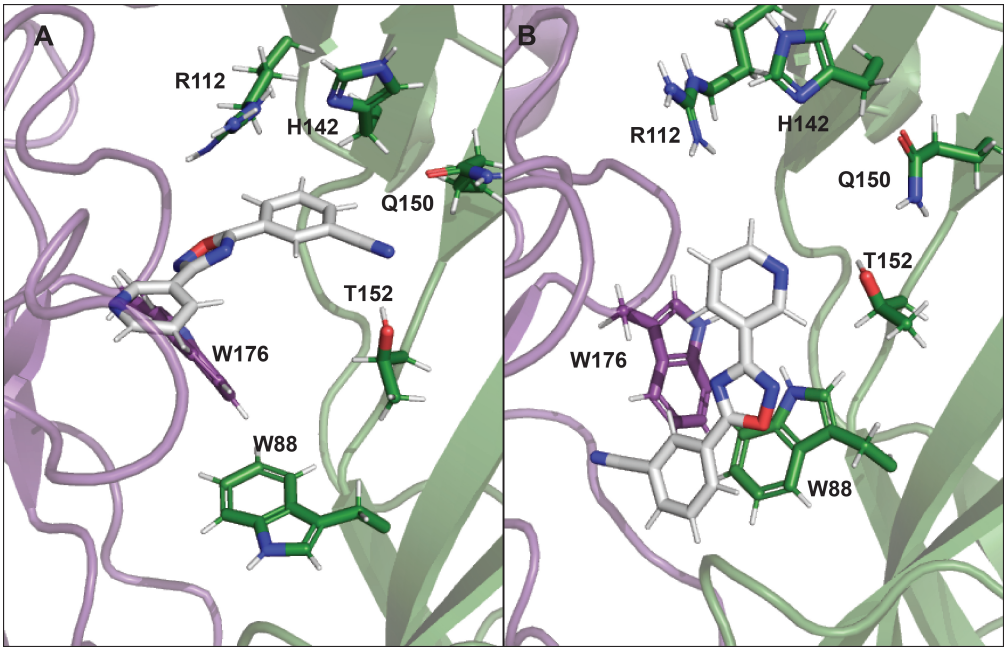

Figure 4.10: Binding of NS9283 to the β2-α4 interface of the LS α4β2 nAChR. First two clusters (A = 40%, B = 32%) resulting from the REST simulations of NS9283 in the β2-α4 interface with the key amino acids of the complementary α subunits and the loop B tryptophan highlighted.

4.4 Discussion

The functional results align with the requirement of the α4-α4 interface for allosteric modulation of nAChR by NS9283 and its analogues [74, 75, 290] and confirmed the validity of this interface to develop uniquely selective LS α4β2 nAChR ligands. Overall, the data is consistent with the critical involvement of a hydrogen bond acceptor correctly positioned at the aromatic ring, as previously suggested for the interaction of 3-cyanophenyl residue with H142 of the complementary α4 side in the homology model of NS9283 binding [75, 50]. Revealingly, shift of the substituents CN, NO2, F, and, to a minor extent, of the pyridyl nitrogen from the 3 to 4 position results in a decrease of ACh potentiation (NS9283 with **10**, **4** with **5**, **6** with **11**, and **2** with **9**) (Figure 4.3),

thus suggesting a similar binding pattern for these compounds driven by the productive interaction of the hydrogen bond accepting atoms in the cycle bound to oxadiazole C(5). Conversely, when replacing 3-cyanophenyl with piperidinyl (compounds **18–21**), the hydrogen bond substituent, formyl or acetyl, has to be shifted from the 3 to 4 position: **20** and **21** show ACh potentiation, **18** and **19** are inactive (Figure 4.3).

Computational experiments predicted strong interactions with the residues W88, R112, H142, Q150, and T152, which have been previously identified as important residues for the potentiating effect of NS9283 [75, 290]. Even though the ligand pose differs significantly from the one previously reported in the literature, it is worth noting that the current work was done using the α4β2 nAChR Cryo-EM structure, which was not available at the time of the previous study. These interactions validate the predicted pose and highlight the importance of the complementary side of the α4-α4 interface to the binding of the ligands.

The strong interactions of NS9283 with the negative face of the α4-α4 site create a gap between both subunits, which combined with the presence of the electron-rich aromatic rings of NS9283 allow for the conformational change of W182 to occur faster and without an energetic penalty. Furthermore, REST simulations suggest that this conformational change is critical for the α4-α4 potentiation elicited by NS9283 and its analogues, but the specific mechanistic significance of this change is still to be determined, although this motion may contribute to the signal transduction from the α4-α4 binding site to either the α4β2 sites or the channel.

An alternative hypothesis for the activity of NS9283 potentiation proposes that this ligand may exert its action via binding the β2(+)-α4(-) interface in addition to the α4-α4 site [291]. The simulations suggest that the binding of NS9283 to the β2(+)-α4(-) subunit interface is not stable, compared to the one at the α4-α4 interface. These observations, together with the findings that alanine substitution of a conserved tryptophan (W176)

in the β2(+) side of β2(+)-α4(-) interfaces in LS α4β2 nAChR abolishes the allosteric effects of NS9283, [291] support the possibility that the β2(+)-α4(-) interface may house components of the transduction machinery of the NS9283 binding site in the α4-α4 interface of the LS α4β2 nAChR.

In conclusion, the work presented in this chapter utilises a series of NS9283 analogues to better understand the potentiation through an unorthodox binding site in the LS α4β2 nAChR. By combining functional evaluation of the potentiation of NS9283 analogues and molecular dynamics of their binding with the α4-α4 site it is shown that the LS selective modulatory activity of NS9283 can be expanded to other 5-yl substituted 3-(3-Pyridinyl)-1,2,4-oxadiazoles bearing either substituted aromatic rings other than benzonitrile or heteroalicyclic rings like in ligands **20** and **21**, as long as a correctly positioned hydrogen bond acceptor on the cyclic substructure bound to C(5) of central oxadiazole is maintained. Moreover, the computational studies show that the ligands endowed with potentiating effects interact similarly with the complementary (-) side, where H142 is critically involved, and, for the first time, the interaction with W182 of the (+) side in a rotameric form significantly differing from the native one is described. These findings, besides providing a rationale for the present activity results, show that NS9283 is a good template for designing new α4-α4 ligands and developing this class of compounds with a focus on their promising therapeutic applications.

5 | Unorthodox β2-β2 Site Enables the Super-Agonist Profile of TC-2559 in the $(\alpha4)_2(\beta2)_3$ Nicotinic Acetylcholine Receptor

Disclaimer

The research presented in this chapter has been presented at the BPS Annual Meeting in 2025 [296], see also in the list of publications.

5.1 Introduction

The orthosteric agonist binding site at the two stoichiometries of the α4β2 nAChR are structurally identical, leading to similar agonist sensitivity, albeit with a range of efficacies [65]. The differences in agonist efficacy can be accounted for partly by the additional agonist site at the α4-α4 subunit interface of the LS receptor. This additional site generally increases the efficacy of agonists [65], with the notable exception of agonists TC-2559 and Sazetidine-A. Neither of these ligands can access the agonist site at the α4-α4 interface of the LS receptor, where they display partial agonism. In contrast, at the HS receptor TC-2559 behaves as a super-agonist (with its maximum response being almost 4-fold greater than ACh) and Sazetidine-A as a full agonist [297, 73, 72, 65].

Since the orthosteric agonist binding sites located at the α4(+)-β2(-) interfaces are structurally identical, they are unlikely to confer receptor stoichiometry-specific functional signatures. However, because the fifth subunit in the α4β2 can be α4 or β2, each α4β2 nAChR stoichiometry has a unique subunit interface, an α4(+)-α4(-) binding interface at the LS receptor and a β2(+)-β2(-) interface at the HS. This suggests that the efficacy

of TC-2559 and Sazetidine-A at the HS receptor may be driven by binding to a β2-β2 interface.

As shown in Chapter 4 the α4-α4 site harbours a modulatory site that seems to be homologous to the benzodiazepine site in the GABAA receptor. Thus, by analogy to the LS and GABAA receptor it is reasonable to suggest that TC-2559 and sazetidine-A may display higher efficacies at the HS by binding to both the orthosteric agonist sites and a region in the β2-β2 interface. Binding to the β2-β2 interface may potentiate the functional effects of the agonists mediated by binding to the orthosteric sites.

In this chapter, computational approaches, mutagenesis, and functional assays were used to explore the view that the β2-β2 site may harbour an allosteric binding site that modifies the efficacy of agonists bound at the orthosteric agonist site of the HS receptor.

5.2 Materials and Methods

5.2.1 Molecular Dynamics Simulations

5.2.1.1 System Preparation

The coordinates for the HS α4β2 nAChR were obtained from the Cryo-EM structure PDB ID: 6CNJ [29]. The interfaces were truncated and prepared for the simulations using the same procedure described in Section 4.2.3.

5.2.1.2 REST Simulations

REST simulations (see Section 2.1.4.1) were run in the α4-β2 and the β2-β2 interface. For the α4-β2 interface the solute region was defined as Y126, W182, T183, Y223, C225, C226 and Y230 of the main (+) chain and W82, V136, F144 and L146 of the complementary (-) chain. In the case of the β2-β2 interface the solute region was defined

as Y120, S175, W176, T177, D217, D218 and Y221 of the main (+) chain and W82, V136, F144 and L146 of the complementary (-) chain. In both cases, the ligand was kept in the binding site using a flat-bottom restraint at 10 and 8 Å from the binding site center of mass (COM) respectively. The system was simulated using the same scheme described in Section 4.2.3.2. Representative conformations from the target temperature replica ($310\,\mathrm{K}$) were extracted by clustering using the GROMOS algorithm [267].

5.2.1.3 Funnel Metadynamics

FunMetaD simulations were run at the β2-β2 interface with the WT, β2 (+) D217A-D218A or β2 (-) D195A-D196A mutants. The funnel was set with the axis between the centre of the binding site and the apex of loop C, with a z_{cc} of 30 Å, an α of 0.5, and a cylinder radius R_{cyl} of 1 Å (see Section 2.1.4.4). The CVs biased by the metadynamics were the position of the ligand COM along the funnel axis (fps.lp) and the distance of the ligand from this axis (fps.ld). These CVs were biased with a Gaussian width of 0.02, and an initial height of $2\,\mathrm{kJ\,mol^{-1}}$. The FES of the FunMetaD simulations over any arbitrary CV was calculated using the reweighting procedure described in Section 2.1.4.4.

5.2.1.4 Two-Electrode Voltage-Clamp Recordings

CRCs of TC-2559 and ACh were constructed as described in Section 2.2.3.6 and the responses were recorded using two-electrode voltage-clamp recording at a holding potential of $-60\,\mathrm{mV}$ as described in Section 2.2.3.5.

5.2.1.5 Site-Directed Mutagenesis

The β2 mutants were produced using the Q5 Site-Directed Mutagenesis kit from New England Biolabs (U.K.). The presence of the mutation and the absence of unwanted mutations were confirmed by sequencing the entire cDNA insert (Eurofins, U.K.).

5.3 Results

5.3.1 Do all agonists of the HS receptor bind similarly to orthosteric sites?

To explore the effect of agonists on the orthosteric binding site of the $\alpha4\beta2$ nAChR, trajectories of the REST simulations of 6 ligands in the $\alpha4$-$\beta2$ interface were analysed to characterise the dynamics of the binding site in the presence of compounds with a range of agonist efficacies. Clustering of the trajectories rendered similar conformations for the tested agonists, with the charged amino group of the agonists interacting with W182 (Figure 5.1). This is the loop B tryptophan that engages in a critical cation-pi interaction with agonists, as described in Section 1.3.1. Loop C capping, a key step in liganded gating of the receptor (see Section 1.3.3), was determined using the distance between the COM of residues in the tip of loop C (residues 223-226) and the COM of the interface. The FES over this CV was calculated with the Boltzmann relation for each ligand. The FES separated the agonists (ACh, epibatidine, nicotine, varenicline, and TC-2559) from the antagonist (tropisetron), with the basins of the agonists lying to the left in a more capped conformation and the basin of tropisetron in a more open one (Figure 5.2 A). In this FES the active state was defined as having a CV value lower than 15.37 Å (the CV value of the starting structure: 6CNJ), and the inactive as having a value higher than 15.37 Å. The free energy difference between the Boltzmann averages of the active and inactive states shows a relationship with the efficacy of the agonist (Figure 5.2 B). Interestingly, TC-2559, a ligand that behaves as a superagonist at HS $\alpha4\beta2$ nAChR, does not comply with this pattern, having a lower free energy difference between states than ACh, a full agonist. This finding supports the view that TC-2559 exerts its super-agonism at the HS receptor through a mechanism that does not involve binding to the orthosteric agonist site.

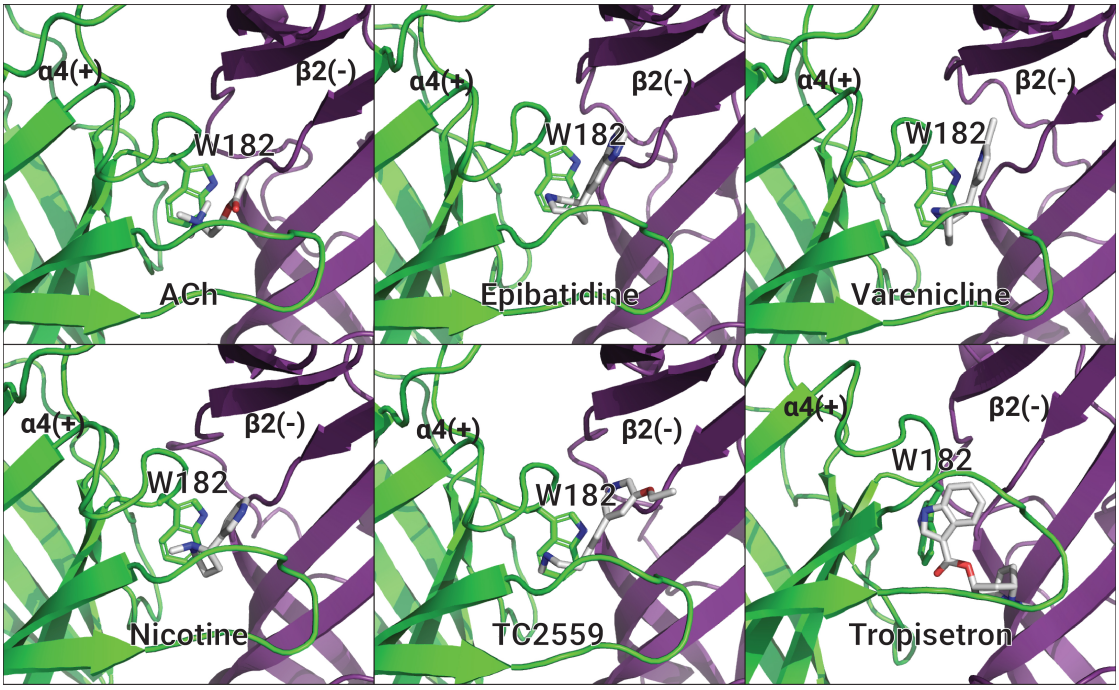

Figure 5.1: Clustered poses from REST simulations of selected agonists and the antagonist tropisetron at the α4β2 interface. The α4 subunit is coloured green, the β2 subunit is coloured purple, and the ligand is coloured in silver. The key W182 is shown in stick representation.

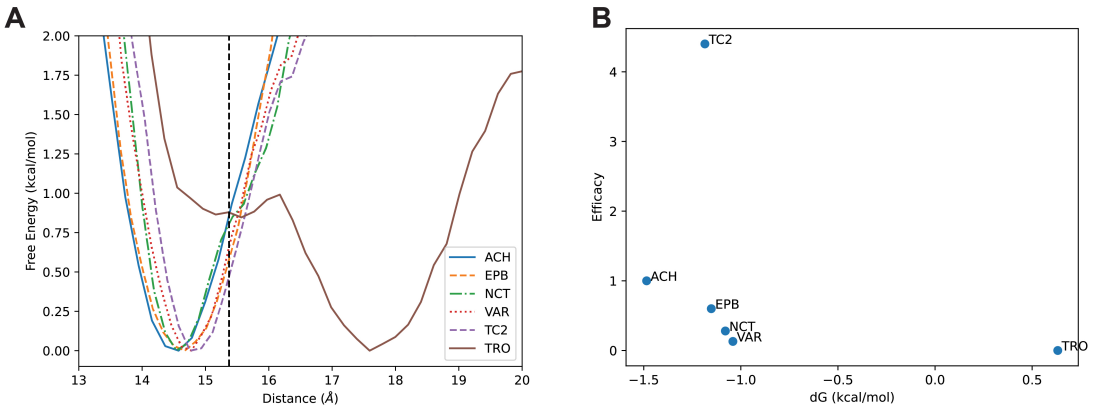

Figure 5.2: Free energy landscape of loop C capping from REST simulations. A. Free energy landscape over the loop C distance to the protein COM. The dashed line represents the value of the Cryo-EM structure (6CNJ). B. Energy difference between the activated and inactive states plotted against the agonist efficacy (assumed 0 for the antagonist).

5.3.2 Aspartates at β2 Loop C and Loop F are Critical for TC-2559 Function

Since the β2-β2 interface is unique to the HS receptor, its potential binding to this subunit interface was explored by performing REST simulations TC-2559 on the β2-β2 interface. These simulations revealed that the charged amine of TC-2559 had strong interactions with the charged oxygen of D195 and D196 of loop F and D217 and D218 of loop C. These interactions are not present for ACh, nicotine, epibatidine or varenicline (Figure 5.3 A). Alanine substitution of these residues demonstrated that altering these residues greatly diminished the efficacy and potency of TC-2559 without affecting the ACh response (Figure 5.4 A and B). Modification of D217A significantly reduced the efficacy of TC-2559 (2.8 ± 0.8) but kept its super-agonist profile. D218A produced a more dramatic decrease in efficacy (1.5 ± 0.3), similar to the effect of the double mutant (1.1 ± 0.4) (Figure 5.4 C). In the case of the loop F aspartates, both mutations eliminated the super-agonism (D195A efficacy: 0.93 ± 0.2; D196A efficacy: 1.1 ± 0.5) with the double mutant rendering TC-2559 into a partial agonist (0.52 ± 0.1) (Figure 5.4 C). On the other hand, the mutants significantly decreased the affinity of TC-2559, except for D217A (Figure 5.4 D).

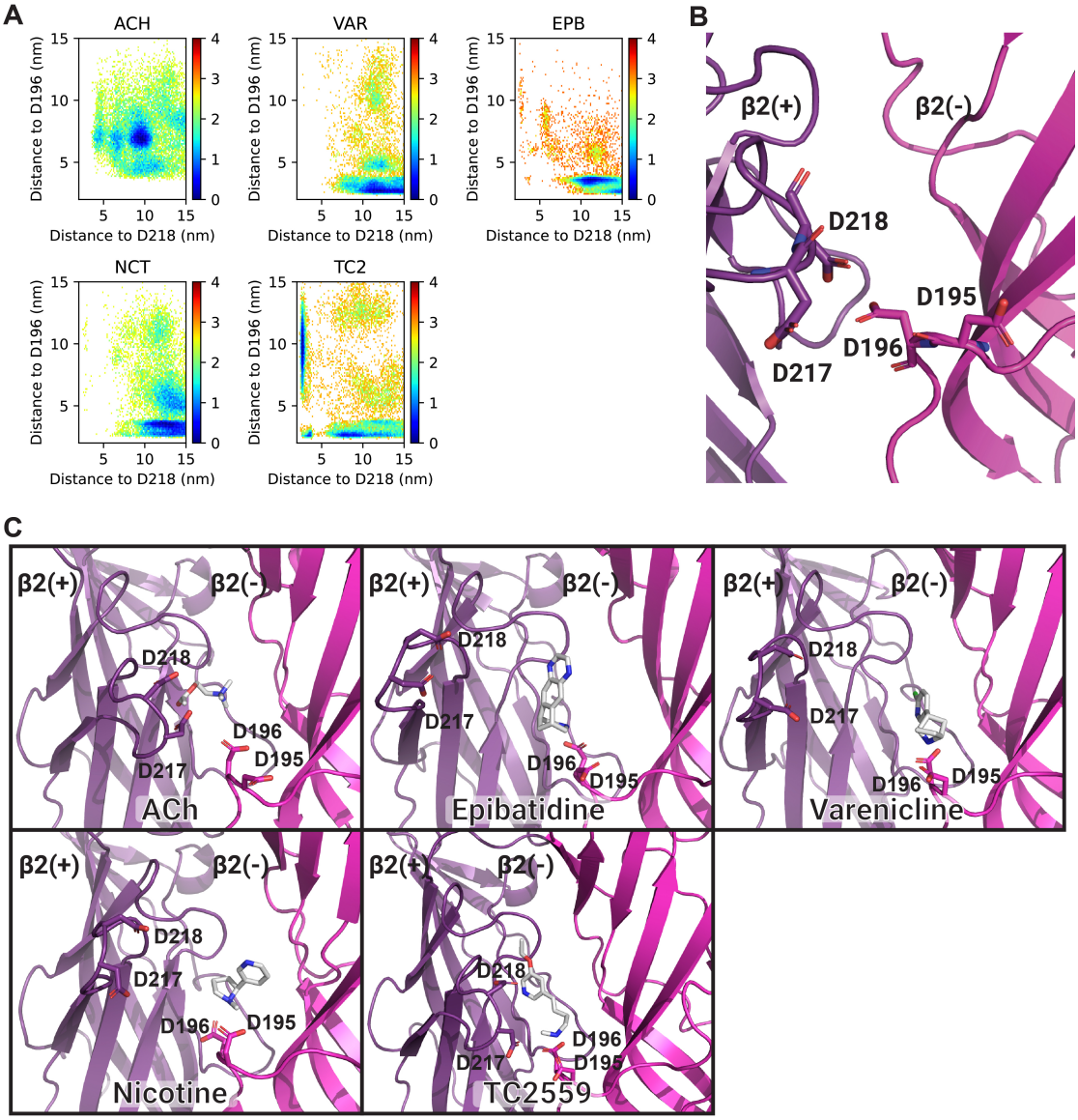

Figure 5.3: REST simulations of agonists at the β2-β2 interface. A. 2-dimensional FES for the interaction of the charged amino group of every agonist with the charged oxygen of D196 and D218. B. Aspartates in the β2(+) (purple)/β2(-) (magenta) interface. C. Clustered conformations obtained from REST simulations. The β2(+) interface is coloured purple, the β2(-) is magenta, and the ligand is coloured grey. The key aspartates and the ligand are shown in stick representation.

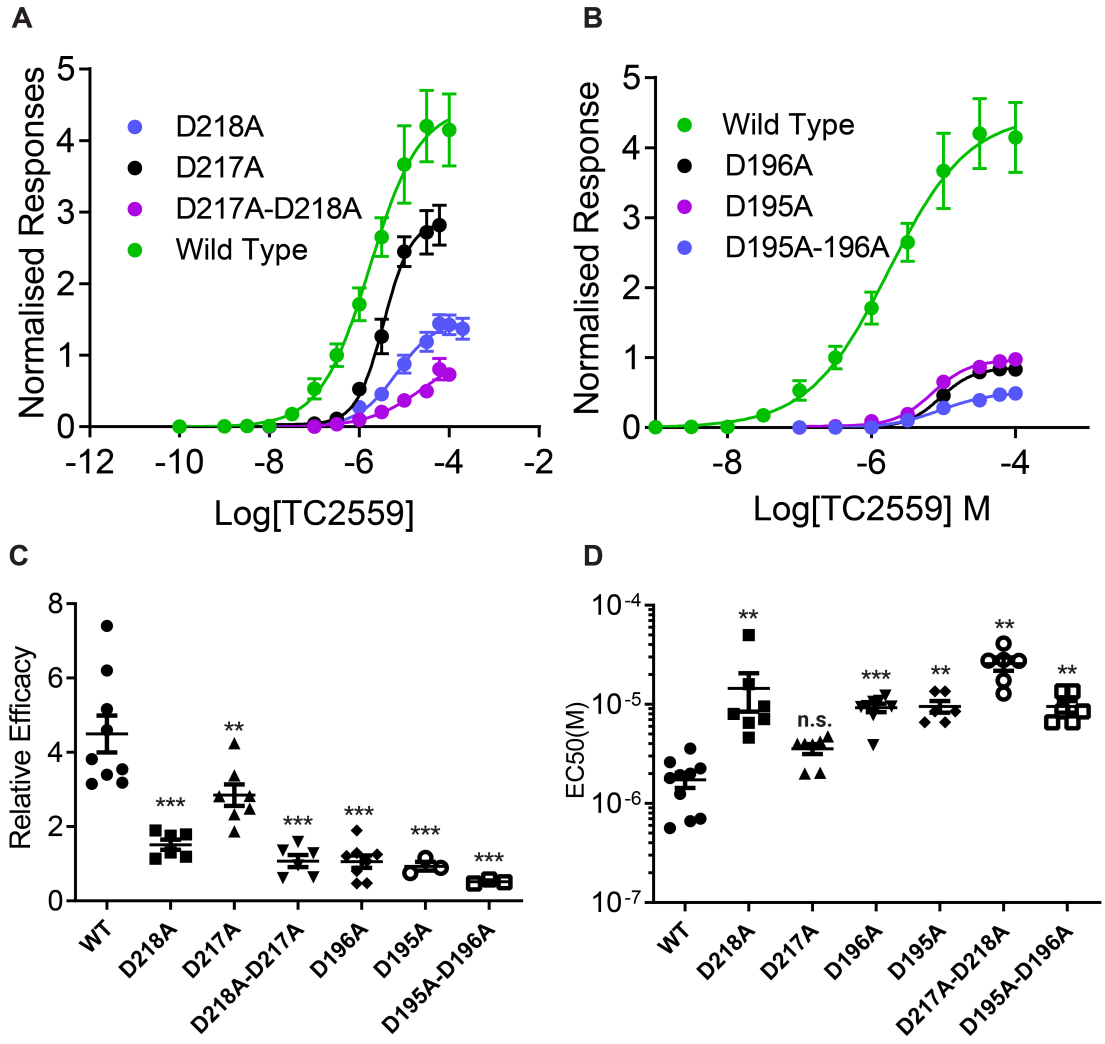

Figure 5.4: Concentration-response curves of TC-2559 in the loop C (A) and loop F (B) mutants. C. Efficacy of TC-2559 on each mutant compared against the wild-type. D. Affinity of TC-2559 on each mutant compared against the wild-type. Statistical significance was tested using a one-way ANOVA with multiple comparison tests: ** = $p < 0.01$; *** = $p < 0.001$; n.s. = not significant.

5.3.3 Displacement of β2 Loop B is Induced by TC-2559

Using FunMetaD simulations, further analysis of TC-2559's binding at this site was performed. The ligand was simulated in the β2-β2 WT, D217A-D218A, and D195A-

D196A receptors for a total of 25 µs each. From the metadynamics simulations, no significant difference in the binding free energy of the WT compared with the mutants was observed. Nevertheless, the FES of ligand binding showed a shift in the binding mode of TC-2559 with the low energy basins located in different sections of the interface when the aspartates are mutated (Figure 5.5 A). Representative structures extracted from clustering the basins show that upon binding TC-2559 establishes simultaneous interactions with loops B and F, causing significant loop B displacement (Figure 5.5 B).

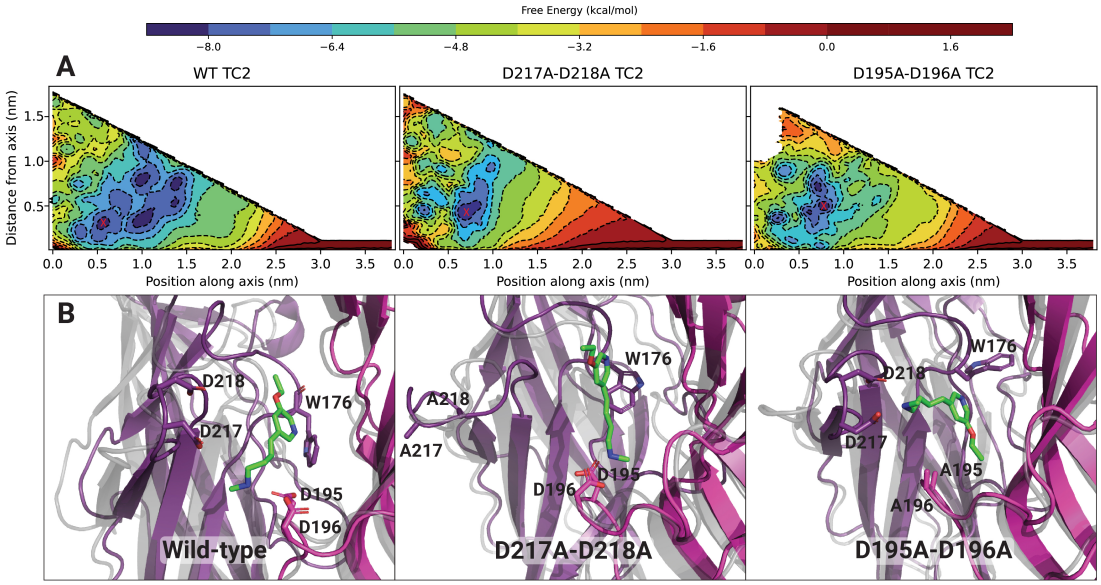

Figure 5.5: Funnel metadynamics of TC-2559 at the β1-β2 interface. A. Free energy landscape of the ligand COM along the funnel coordinates (position along the funnel axis and distance from the funnel axis) for the wild-type and mutants. The minimum energy basins are highlighted with a red X. B. Representative structures of each basin are obtained through RMSD-based clustering of the trajectory frames in each basin. The β2(+) subunit is coloured in purple, while the β2(-) subunit is coloured in magenta. The Cryo-EM structure (6CNJ) is superimposed in grey. Residues W176, D195, D196, D217, and D218 are shown in stick representation. TC-2559 is coloured green.

To characterise this conformational change, the principal components (PCs) of the loop B alpha carbons (residues 174-182) between the frames of the bound basin from the WT

simulation and an apo simulation of the β2-β2 WT interface (10 replicas of 500 ns each) were calculated (Figure 5.6 A). The FES was projected over the first PC (Figure 5.6 B) for the WT and mutant receptors. The WT simulation in the presence of TC-2559 has a minimum energy at a PC value of -5.7, while the apo simulation is most stable at -4.7. In the mutant simulations, D217A-D218A elicited a lesser deviation from the apo state, with a minimum energy state in the -5.2, and D195A-D196A did not induce a deviation towards a WT-like state with a global minimum at -4.5.

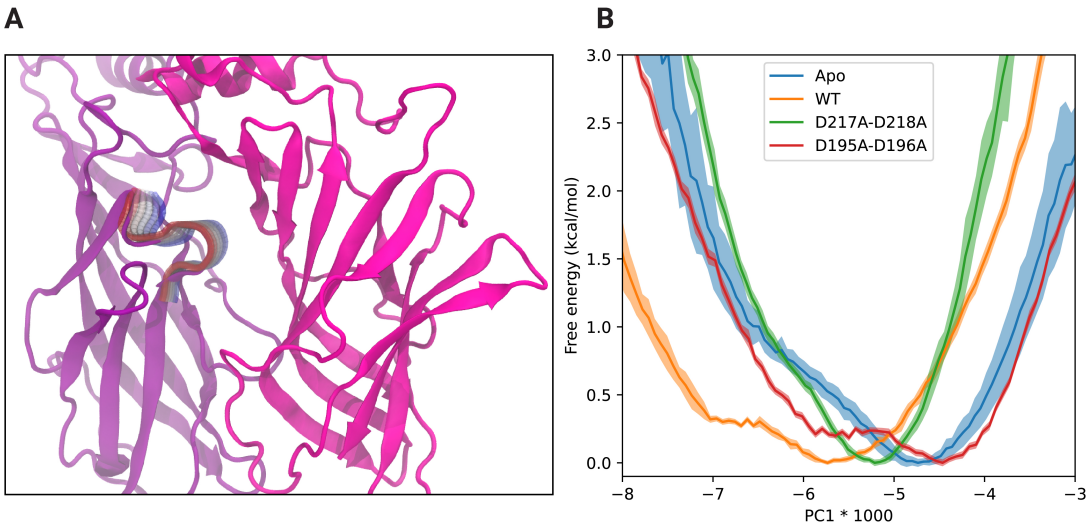

Figure 5.6: Principal component analysis of metadynamics simulations. A. Schematic representation of the motion described by PC 1 at the β2-β2 interface. The β2(+) subunit is coloured in purple, while the β2(-) subunit is coloured in magenta. The alpha carbons included in the calculation are coloured on a scale from red to blue, going from the apo-like to the bound-like conformations. B. FES of PC1 for the apo and TC-2559 with WT, D217A-D218A, and D195A-D196A receptors. The shaded areas represent the standard deviation calculated with 1000 bootstraps.

5.4 Discussion

The agonist conformations obtained from MD simulations performed at the α4-β2 interface concur with previous observations reported in the literature, validating the REST

technique in these conditions. First, the binding mode of both nicotine and ACh aligns closely with the binding poses of these ligands in Cryo-EM structures of the $\alpha4\beta2$ nAChR [29, 28] (Figure 5.7). Moreover, displacement of loop C has been well established as a conformational change occurring upon agonist binding. Early studies have shown that agonists, but not competitive antagonists, protect the binding site of nAChRs against reduction from dithiothreitol in *Torpedo californica* electric membrane, suggesting a "closing" conformational change in the binding site upon agonist binding [298]. Later, crystal structures of AChBP from *Aplysia californica* display loop C capping in the presence of epibatidine, while in the apo and methyllycaconitine-bound structures, the loop C appears in a more open fashion [44]. More recent structures resolved from Cys-loop receptors, such as the GluCl [55] and the $\alpha7$ nAChR [36, 30], also show this conformational change in the presence of activating agonists. Additionally, loop C truncation eliminates ACh activation of nAChRs, although it does not affect unliganded gating [37]. Allosteric gating models, such as the one presented in Figure 1.4, postulate that a transition between low-affinity and high-affinity binding domain conformations (the latter characterised by the capping of loop C) is a favourable step in agonist-induced gating [46]. Furthermore, the efficacy of a ligand is related to the binding energy of the ligand to these two states [38]. Thus, theoretically, it is possible to estimate the efficacy of a ligand by calculating the difference between the absolute binding free energy of the ligand to the protein in each conformation [299] or, alternatively, by calculating the free energy difference between the states in the presence of the ligand. This work uses these ideas to relate loop C's displacement from REST simulations in the presence of different ligands to their relative efficacy. However, this comes with limitations: since it is necessary to apply a flat-bottom restraint potential on the ligand to avoid dissociation at high-temperature replicas [300], this may affect the ligand's ability to induce conformational changes, adding unknown biases to the free energy landscape. Nevertheless, the free energy difference between the capped and uncapped conformations in the REST

simulations show a direct relationship with ligand efficacy, with the antagonist stabilising a non-capped conformation. It would be expected for a compound like TC-2559, whose efficacy surpasses that of ACh, that it would stabilise an activated-like conformation even further than the endogenous neurotransmitter. Calculations show this is not the case, and simulations with TC-2559 show a behaviour similar to the partial agonists studied here (Figure 5.2). Therefore, our evidence suggests that TC-2559 does not exert its signature super-agonism through binding at the orthosteric binding site. This, taken together with the stoichiometric selectiveness of this effect, we propose an additional binding site at the β2-β2, which is unique to the HS receptor.

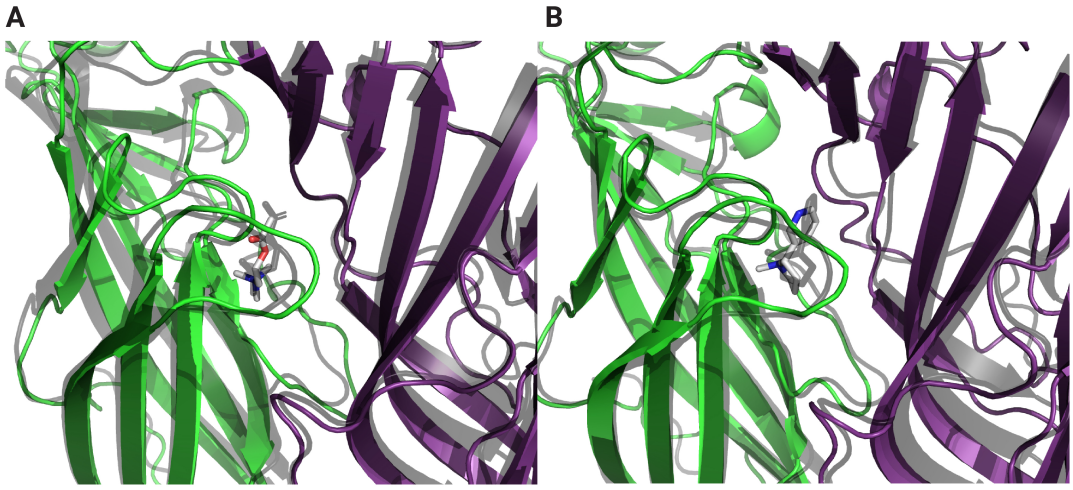

Figure 5.7: Clusters from REST simulations superimposed to Cryo-EM structures. A. Best cluster superimposed with one of the α4-β2 interfaces with nicotine bound of 6CNJ [29]. B. Best cluster superimposed with one of the α4-β2 interfaces with ACh bound of 8ST4 [28]. The coordinates derived from REST simulations are coloured in green (α4), purple (β2), and grey (ligand). The coordinates from the Cryo-EM structures are coloured in transparent black.

In the LS stoichiometry of the α4β2 receptor, binding of ligands to the unorthodox α4-α4 binding site enhances the probability of opening of the receptor, allowing partial agonists, such as cytisine and varenicline [65, 71], to display higher efficacy than at the HS receptor. Furthermore, epibatidine, a partial agonist at the HS stoichiometry, evokes a

response even higher than ACh's in the LS multimer [65]. Additionally, this site can bind positive modulators like NS9283 and CMPI [75, 50], although these modulators enhance the affinity of orthosteric ligands rather than their efficacy. On the HS stoichiometry, binding the β2-β2 site could generate a similar effect. However, it is not a straightforward comparison, since the α4-α4 site is formed by a positive α4 subunit, which contains the conserved structural motifs that bind to agonists and translates this binding to gating, namely a longer loop C and an electron-rich aromatic box (as described in Section 1.3). This makes the binding of an agonist to this site necessary for full activation of the receptor [68, 71]. On the other hand, binding sites containing a positive β2 subunit cannot bind traditional agonists, due to the presence of R175 (whose equivalent amino acid in the α4 subunit is a glycine), which is oriented with its positive charge at the base of the binding site. This arginine compensates the electron-rich π pocket, like a positively charged agonist would, sandwiched between loop C's tyrosine and loop A's tyrosine [23]. This reorganisation also produces a change in loop B's tryptophan, which in the Cryo-EM structure appears oriented away from the binding site [23, 29]. REST simulations of TC-2559 in this binding site confirm these observations by suggesting that TC-2559's positively charged amino group interacts with negatively charged aspartates in loop C and loop F of the β2 subunit, rather than with the aromatic box as in the orthosteric binding site. The importance of these aspartates is confirmed by alanine substitution of these amino acids, which significantly affects both the affinity and efficacy of TC-2559. It is worth noting that although loop C's aspartates are unique to the non-canonical β2-β2 and β2-α4 interfaces, the loop F's aspartates are also present in the orthosteric α4-β2 site. Still, the current evidence suggests that at the orthosteric binding site of Cys-loop receptors, this loop plays a role in ligand accommodation and selectivity rather than receptor activation [301, 6], therefore its alteration should not produce a noticeable effect on ligand efficacy, yet the mutants of loop F's aspartates produces a significant decrease in TC-2559's efficacy (Figure 5.4 C). Additionally, the

substitution of loop F's aspartates does not affect the pharmacology of ACh (Figure 5.8). Metadynamics simulations of TC-2559 in the β2-β2 binding site also highlighted the importance of these aspartates, suggesting that they are key for determining TC-2559's binding mode and the conformational changes induced by this ligand. Notably, a displacement of loop B is induced upon binding of TC-2559 to this site. This loop contains the key conserved tryptophan analogous to the one that engages in cation-π interactions with agonists at the α4 subunit of the orthosteric binding site. Furthermore, Cryo-EM structures from the $5HT_{3A}$ receptor and the α7 nAChR have shown a displaced loop B in the agonist-bound structures compared to the apo [36, 302]. Loop B is directly connected to the coupling's region Cys-loop through the β7 sheet (Figure 1.1 B), which links the motions of loop B with the transmembrane domain. Moreover, unique to the β2 subunit, there is a salt-bridge connecting K160 of the Cys-loop (a threonine in the α4 sequence) to D293 in the M2-M3 linker (a valine in the α4) (Figure 5.9). This provides for a putative allosteric communication pathway between the motions induced by TC-2559's binding and a displacement of the pore lining the M2 helix, which could result in further stabilisation of the open state and the observed super-agonism at a macroscopic level. Additionally, computational studies have highlighted the role of β2's loop F in allosteric communication between the extracellular and transmembrane domains upon nicotine binding [303].

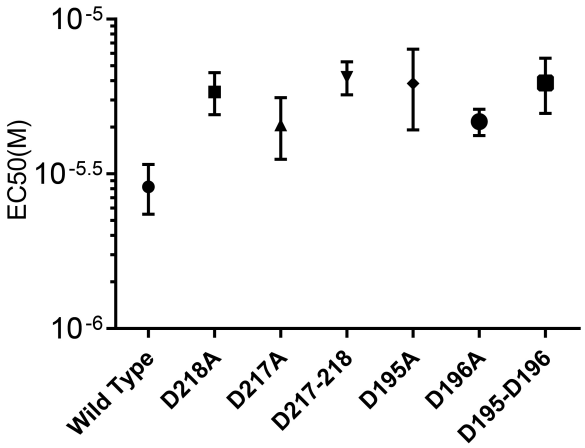

Figure 5.8: Effect of mutants on the EC_{50} of ACh compared with the wild-type. One-way ANOVA with multiple comparisons showed no significant difference between the mutants and the wild-type.

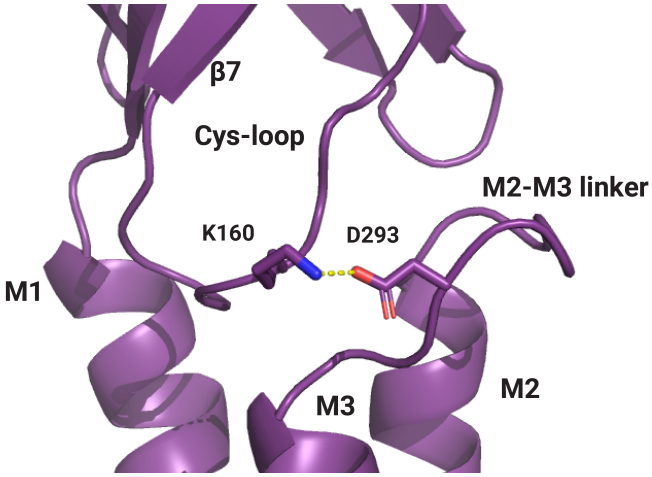

Figure 5.9: Salt-bridge interaction between Cys-loop and M2-M3 linker at the β2 subunit. K160 and D293 are shown in stick representation. The interaction is represented by the dashed line.

Another parallelism with a similar binding site is the benzodiazepine site in GABAA receptors. This binding site lies at the interface between the positive face of an α subunit and the negative face of a γ subunit [304]. In GABAA receptors, the α subunit

normally contributes to the negative face of the orthosteric binding site, while the γ subunit does not contribute to an orthosteric binding site [305]. Thus, this site can be considered partially analogous to the β2-β2 site as it contains a non-orthosteric positive face. Mutational studies in the GABAA receptor have revealed residues that are relevant for benzodiazepine binding. In the α subunit, amino acids of loops C [306] and B [307, 308] are critical for benzodiazepine function, affecting both their affinity and efficacy. On the other hand, in the γ subunit, mutations along loop F significantly reduce the efficacy of benzodiazepine potentiation, with one mutant (D192A) completely abolishing diazepam potentiation [309], which lies in a position analogous to D196 in β's loop F.

In summary, this work presents a combination of computational and experimental evidence that supports the hypothesis of TC-2559 exerting its super-agonist effect at the HS α4β2 nAChR through binding at an additional allosteric binding site. On the one hand, computational calculations at the orthosteric binding site show that TC-2559's binding mode aligns with that of classical partial agonists. On the other hand, investigation of TC-2559's binding at the β2-β2 site revealed key residues whose modification alters the ligand's behaviour in both experimental and computational tests. Moreover, analogy with other modulators of Cys-loop receptors supports the possibility of positive modulation at a non-canonical extracellular binding site, mediated by the key structural motifs identified in this study. This binding site provides a target for the development of novel PAMs selective for the HS stoichiometry of the α4β2 nAChR, which have not yet been reported. Finally, although a putative allosteric mechanism has been proposed, more studies are required to confirm the validity of these conjectures.

6 | Outlook and Conclusion

6.1 40 Years of nAChR Research

More than 40 years have passed since the first nAChR subunit cDNA was cloned in 1982 [16]. This advancement made possible the recombinant expression and manipulation of the receptor, allowing a detailed study of its function. Nevertheless, early determination of the nAChRs proved elusive due to the challenges in crystallising the protein for X-ray crystallography [310], mainly due to the difficulty of obtaining sufficient amounts of properly folded proteins [311].

The discovery of the water-soluble nAChR homologs, AChBP [312], provided a surrogate for studying the neurotransmitter-binding domain of nAChRs at an atomic resolution. This allowed for the identification of the key components of agonist recognition and the conformational changes that occur upon agonist and antagonist binding in the EC domain of Cys-loop receptors [44, 154, 313] (reviewed in Section 1.3.1).

Although insightful, the study of AChBP has its limitations when it comes to investigating nAChRs (or any Cys-loop receptor for that matter). The most obvious one is that this protein is missing a TM domain, which prevents the study of the structural rearrangements that translate binding to gating. Additionally, it was observed that AChBP crystalised in apo conditions did not exhibit a resting-like conformation (such as the ones obtained by crystalising in the presence of neurotoxins) due to the lack of a complementary TM domain [310]. This suggests that the presence of a TM domain influences the conformations of the EC domain, meaning that one has to be careful to draw functional conclusions from AChBP structures.

As an example, Parker et al [314] labelled the natural product hosieine-A as an agonist of nAChRs, based on crystal structures obtained in complex with *Aplysia californica*

AChBP. However, our functional data shows that hosieine-A, in fact, behaves as a competitive antagonist of the α4β2 and α3α4 nAChRs instead (Figure 6.1). Also, the results featured in Chapter 4.2.3.2 show that the binding mode predicted for NS9283 using MD with the Cryo-EM structure of the α4β nAChR fits better with the experimental evidence that the binding mode determined by Olsen et al [75] by co-crystallisation with AChBP.

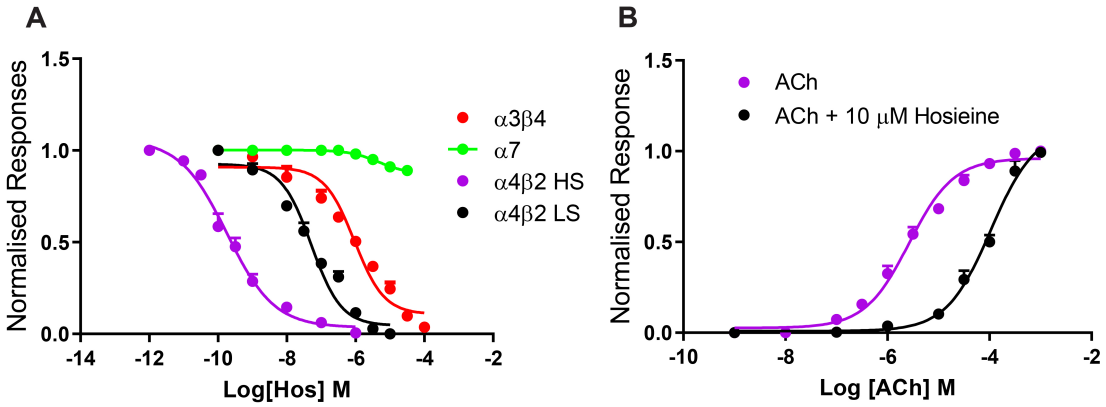

Figure 6.1: Hosieine-A is a competitive inhibitor of nAChR subtypes. A. Concentration-response curves of competitive inhibition of nAChR subtypes by hosieine-A. B. Concentration-response curves of ACh with and without 10 μM of hosieine-A.

On the other hand, Nigel Unwin and colleagues have extensively used Cryo-EM to study the structure of nAChRs in *Torpedo marmorata*'s electric organ. This work resulted in the 4 Å resolution structure of the nAChR pore [39], which was later refined using the AChBP crystal [22]. This contributed to the elucidation of the conformational changes that lead to receptor gating while providing insight into the structure of the channel pore.

More advancements in the illumination of the structure of Cys-loop receptors came with the discovery of the prokaryotic pLGICs [315, 316]. Among these, GLIC and ELIC are cation-selective channels gated by primary amines and are readily expressed in *E. coli* at sufficient levels for biochemical characterization, making them excellent models for the

study of pLGIC function [310].

Following the success of prokaryotic pLGICs the crystal structures of eukaryotic pLGICs were solved by X-ray crystallography, with the first one being the [**C. elegans**] GluCl [55]. More recently, due to groundbreaking advances in Cryo-EM several structures of eukaryotic pLGICs have been resolved, with over 27 structures of nAChRs available in the PDB database to date [317], featuring a range of subtypes, states, and pharmacological conditions.

Despite all these advancements through the decades, no novel nAChR-targeting drug has been approved since varenicline in 2006 [318] (see Section 1.6). This is due to the highly conserved nature of the orthosteric binding site, which makes the production of subtype-selective agonists quite challenging. Additionally, although we have structures of the nAChRs and other Cys-loop receptors in several conformational states, the annotation and functional relevance of Cryo-EM solved structures is not always trivial. Also, Cryo-EM structures present static snapshots of the protein, usually in non-native mediums such as detergents and nanodiscs, that can impact the structural state obtained [319]. Additionally, electrophysiological and fluorometry experiments have shown that the motions of the subunits of Cys-loop receptors during the gating cycle are asymmetric [320, 321], something that is not straightforward to resolve with Cryo-EM. However, recent approaches are being applied to reconstruct asymmetric conformational states of Cys-loop receptors [322].

Thus, there is still a gap to be filled in this field to enable the successful rational design of novel drugs targeting nAChRs and other Cys-loop receptors. Understanding the gating cycle and how it is modulated by the binding of drugs, orthosteric and allosteric, is crucial to successfully predicting the effect of ligands. Computational simulations of molecular models, such as MD, are an exceptional tool to bridge the gap between the structural snapshots obtained by Cryo-EM and the receptor pharmacology recorded

through functional experiments.

6.2 Final Conclusion

In this thesis, the pharmacology of PAMs of the α7 and the α4β2 nAChRs was explored through MD and TEVC, to gain insight into the structural components of positive allosteric modulation. First, novel type I allosteric modulators targeting the α7 subtype were assessed, screening their function to establish a structure-activity relationship and predicting its binding site to investigate and rationalize its function. The predicted binding site overlapped significantly with the reported binding site of other PAMs, such as type II PAM PNU-120596, suggesting that the difference between type I and type II α PAMs does not depend on the binding site of the allosteric modulator.

Next, analogues of a known PAM of the LS α4β2, NS9283, were screened for their function. MD simulations were later used to characterize their interactions and the dynamics induced by the active analogues when compared to the inactive one, to gain insight into the key motions associated with potentiation at the α4-α4 site. This work confirmed the importance of certain structural motifs for ligands to potentiate the LS α4β2 receptor through the α4-α4 site. Additionally, it provided a more consistent binding mode that explains the nature of the interactions with key amino acids previously reported and suggests a conformational change induced by active PAMs at this site.

Finally, the function of TC2559, a super-agonist of the HS α4β2, was investigated computationally to unravel the mechanisms behind its high efficacy. Computational calculations suggested a distinct mechanism for the efficacy of TC2559 compared to other agonists, which was attributed to binding to an additional binding site in the β2-β2 interface. This was validated by mutating key residues of this interface and rationalized using metadynamics simulations. This work suggests for the first time that the β2β2 site of the HS α4β2 nAChR is a positive modulatory site, responsible for the super-agonist

response of TC2559 and proposing a putative mechanism for potentiation through this binding site.

In summary, this thesis addresses key gaps in the understanding of the molecular pharmacology of allosteric modulation in the nAChRs by a synergistic approach integrating data from electrophysiological recordings and MD simulations. The results presented in this work refine our comprehension of ligand-receptor interactions in the nAChRs and highlight the potential of computational modelling to inform wet-lab experiments and predict the behaviour of ion channels. Finally, this research provides the scientific community with deeper knowledge and practical tools to define the role of nAChR subtypes in cholinergic signalling in the brain, which should stimulate the development of novel nAChR-based therapies for neurological and psychiatric disorders.

Bibliography

1. Kandel E. Principles of Neural Science, Fifth Edition. McGraw-Hill's AccessMedicine. McGraw-Hill Education, 2013
2. Howard RJ. Elephants in the Dark: Insights and Incongruities in Pentameric Ligand-gated Ion Channel Models. Journal of Molecular Biology. Ion channels : Intersection of Structure, Function, and Pharmacology 2021 Aug 20; 433:167128. DOI: 10.1016/j.jmb.2021.167128
3. Jaiteh M, Taly A, and Hénin J. Evolution of Pentameric Ligand-Gated Ion Channels: Pro-Loop Receptors. PLOS ONE. 2016 Mar 17; 11. Publisher: Public Library of Science:e0151934. DOI: 10.1371/journal.pone.0151934
4. Sine SM and Engel AG. Recent advances in Cys-loop receptor structure and function. Nature. 2006 Mar; 440. Publisher: Nature Publishing Group:448–55. DOI: 10.1038/nature04708
5. Corringer PJ, Novère NL, and Changeux JP. Nicotinic Receptors at the Amino Acid Level. Annual Review of Pharmacology and Toxicology. 2000 Apr; 40:431–58. DOI: 10.1146/annurev.pharmtox.40.1.431
6. Nys M, Kesters D, and Ulens C. Structural insights into Cys-loop receptor function and ligand recognition. Biochemical Pharmacology. 2013 Oct 15; 86:1042–53. DOI: 10.1016/j.bcp.2013.07.001
7. Miller PS and Smart TG. Binding, activation and modulation of Cys-loop receptors. Trends in Pharmacological Sciences. 2010 Apr 1; 31. Publisher: Elsevier:161–74. DOI: 10.1016/j.tips.2009.12.005
8. Jones AK and Sattelle DB. Diversity of Insect Nicotinic Acetylcholine Receptor Subunits. *Insect Nicotinic Acetylcholine Receptors*. Ed. by Thany SH. New York, NY: Springer, 2010 :25–43. DOI: 10.1007/978-1-4419-6445-8_3

9. Langley JN. On the contraction of muscle, chiefly in relation to the presence of "receptive" substances. The Journal of Physiology. 1907 Dec 31; 36:347–84
10. Hill AV. The mode of action of nicotine and curari, determined by the form of the contraction curve and the method of temperature coefficients. The Journal of Physiology. 1909 Dec 23; 39:361–73
11. Castillo JD and Katz B. Interaction at end-plate receptors between different choline derivatives. Proceedings of the Royal Society of London Series B - Biological Sciences. 1957 Jan; 146. Publisher: Royal Society:369–81. DOI: 10.1098/rspb.1957.0018
12. Castillo JD and Katz B. A study of curare action with an electrical micro-method. Proceedings of the Royal Society of London Series B - Biological Sciences. 1957 Jan; 146. Publisher: Royal Society:339–56. DOI: 10.1098/rspb.1957.0015
13. Katz B and Miledi R. Membrane noise produced by acetylcholine. Nature. 1970 Jun 6; 226:962–3. DOI: 10.1038/226962a0
14. Katz B and Miledi R. The statistical nature of the acetycholine potential and its molecular components. The Journal of Physiology. 1972 Aug; 224:665–99. DOI: 10.1113/jphysiol.1972.sp009918
15. Anderson CR and Stevens CF. Voltage clamp analysis of acetylcholine produced end-plate current fluctuations at frog neuromuscular junction. The Journal of Physiology. 1973 Dec; 235:655–91. DOI: 10.1113/jphysiol.1973.sp010410
16. Noda M, Takahashi H, Tanabe T, Toyosato M, Furutani Y, Hirose T, Asai M, Inayama S, Miyata T, and Numa S. Primary structure of alpha-subunit precursor of Torpedo californica acetylcholine receptor deduced from cDNA sequence. Nature. 1982 Oct 28; 299:793–7. DOI: 10.1038/299793a0

17. Claudio T, Ballivet M, Patrick J, and Heinemann S. Nucleotide and deduced amino acid sequences of Torpedo californica acetylcholine receptor gamma subunit. Proceedings of the National Academy of Sciences of the United States of America. 1983 Feb; 80:1111–5

18. Imoto K, Methfessel C, Sakmann B, Mishina M, Mori Y, Konno T, Fukuda K, Kurasaki M, Bujo H, and Fujita Y. Location of a delta-subunit region determining ion transport through the acetylcholine receptor channel. Nature. 1986 Dec 18; 324:670–4. DOI: 10.1038/324670a0

19. Unwin N, Toyoshima C, and Kubalek E. Arrangement of the acetylcholine receptor subunits in the resting and desensitized states, determined by cryoelectron microscopy of crystallized Torpedo postsynaptic membranes. The Journal of Cell Biology. 1988 Sep; 107:1123–38. DOI: 10.1083/jcb.107.3.1123

20. Unwin N. Nicotinic Acetylcholine Receptor an 9 Å Resolution. Journal of Molecular Biology. 1993 Feb 20; 229:1101–24. DOI: 10.1006/jmbi.1993.1107

21. Miyazawa A, Fujiyoshi Y, Stowell M, and Unwin N. Nicotinic acetylcholine receptor at 4.6 Å resolution: transverse tunnels in the channel1. Journal of Molecular Biology. 1999 May 14; 288:765–86. DOI: 10.1006/jmbi.1999.2721

22. Unwin N. Refined Structure of the Nicotinic Acetylcholine Receptor at 4 Å Resolution. Journal of Molecular Biology. 2005 Mar 4; 346:967–89. DOI: 10.1016/j.jmb.2004.12.031

23. Morales-Perez CL, Noviello CM, and Hibbs RE. X-ray structure of the human α4β2 nicotinic receptor. Nature. 2016 Oct; 538. Publisher: Nature Publishing Group:411–5. DOI: 10.1038/nature19785

24. Gharpure A, Teng J, Zhuang Y, Noviello CM, Walsh RM, Cabuco R, Howard RJ, Zaveri NT, Lindahl E, and Hibbs RE. Agonist Selectivity and Ion Permeation in the α3β4 Ganglionic Nicotinic Receptor. Neuron. 2019 Nov 6; 104. Publisher: Elsevier:501–511.e6. DOI: 10.1016/j.neuron.2019.07.030

25. Rahman MM, Basta T, Teng J, Lee M, Worrell BT, Stowell MHB, and Hibbs RE. Structural mechanism of muscle nicotinic receptor desensitization and block by curare. Nature Structural & Molecular Biology. 2022 Apr; 29. Publisher: Nature Publishing Group:386–94. DOI: 10.1038/s41594-022-00737-3

26. Rahman MM, Teng J, Worrell BT, Noviello CM, Lee M, Karlin A, Stowell MHB, and Hibbs RE. Structure of the Native Muscle-type Nicotinic Receptor and Inhibition by Snake Venom Toxins. Neuron. 2020 Jun 17; 106. Publisher: Elsevier:952–962.e5. DOI: 10.1016/j.neuron.2020.03.012

27. Goswami U, Rahman MM, Teng J, and Hibbs RE. Structural interplay of anesthetics and paralytics on muscle nicotinic receptors. Nature Communications. 2023 Jun 1; 14. Publisher: Nature Publishing Group:3169. DOI: 10.1038/s41467-023-38827-5

28. Mazzaferro S, Kang G, Natarajan K, Hibbs RE, and Sine SM. Structural bases for stoichiometry-selective calcium potentiation of a neuronal nicotinic receptor. British Journal of Pharmacology. 2024; 181. _eprint: https://onlinelibrary.wiley.com/doi/pdf/10.1111/bph 92. DOI: 10.1111/bph.16321

29. Walsh RM, Roh SH, Gharpure A, Morales-Perez CL, Teng J, and Hibbs RE. Structural principles of distinct assemblies of the human α4β2 nicotinic receptor. Nature. 2018 May; 557. Publisher: Nature Publishing Group:261–5. DOI: 10.1038/s41586-018-0081-7

30. Noviello CM, Gharpure A, Mukhtasimova N, Cabuco R, Baxter L, Borek D, Sine SM, and Hibbs RE. Structure and gating mechanism of the α7 nicotinic acetylcholine receptor. Cell. 2021; 184. Publisher: Elsevier:2121–34

31. Eglen RM. Muscarinic Receptor Subtype Pharmacology and Physiology. *Progress in Medicinal Chemistry*. Ed. by King FD and Lawton G. Vol. 43. Elsevier, 2005 Jan 1:105–36. DOI: 10.1016/S0079-6468(05)43004-0

32. Albuquerque EX, Pereira EFR, Alkondon M, and Rogers SW. Mammalian Nicotinic Acetylcholine Receptors: From Structure to Function. Physiological Reviews. 2009 Jan; 89. Publisher: American Physiological Society:73–120. DOI: 10.1152/physrev.00015.2008

33. Lukas RJ, Changeux JP, Le Novère N, Albuquerque EX, Balfour DJ, Berg DK, Bertrand D, Chiappinelli VA, Clarke PB, Collins AC, Dani JA, Grady SR, Kellar KJ, Lindstrom JM, Marks MJ, Quik M, Taylor PW, and Wonnacott S. International Union of Pharmacology. XX. Current status of the nomenclature for nicotinic acetylcholine receptors and their subunits. Pharmacological Reviews. 1999 Jun; 51:397–401

34. Xiu X, Puskar NL, Shanata JAP, Lester HA, and Dougherty DA. Nicotine Binding to Brain Receptors Requires a Strong Cation-π Interaction. Nature. 2009 Mar 26; 458:534–7. DOI: 10.1038/nature07768

35. Burke SM, Avstrikova M, Noviello CM, Mukhtasimova N, Changeux JP, Thakur GA, Sine SM, Cecchini M, and Hibbs RE. Structural mechanisms of α7 nicotinic receptor allosteric modulation and activation. Cell. 2024 Feb 29; 187. Publisher: Elsevier:1160–1176.e21. DOI: 10.1016/j.cell.2024.01.032

36. Zhao Y, Liu S, Zhou Y, Zhang M, Chen H, Eric Xu H, Sun D, Liu L, and Tian C. Structural basis of human α7 nicotinic acetylcholine receptor activation. Cell Research. 2021 Jun; 31:713–6. DOI: 10.1038/s41422-021-00509-6

37. Purohit P, Gupta S, Jadey S, and Auerbach A. Functional anatomy of an allosteric protein. Nature Communications. 2013 Dec 19; 4. Publisher: Nature Publishing Group:2984. DOI: 10.1038/ncomms3984

38. Indurthi DC and Auerbach A. Agonist efficiency links binding and gating in a nicotinic receptor. eLife. 2023 Jul 3; 12. Ed. by Csanády L, Swartz KJ, Csanády L, and Plested AJ. Publisher: eLife Sciences Publications, Ltd:e86496. DOI: 10.7554/eLife.86496

39. Miyazawa A, Fujiyoshi Y, and Unwin N. Structure and gating mechanism of the acetylcholine receptor pore. Nature. 2003 Jun; 423. Publisher: Nature Publishing Group:949–55. DOI: 10.1038/nature01748

40. Labarca C, Nowak MW, Zhang H, Tang L, Deshpande P, and Lester HA. Channel gating governed symmetrically by conserved leucine residues in the M2 domain of nicotinic receptors. Nature. 1995 Aug; 376. Publisher: Nature Publishing Group:514–6. DOI: 10.1038/376514a0

41. Mesoy S, Jeffreys J, and Lummis SCR. Characterization of Residues in the 5-HT3 Receptor M4 Region That Contribute to Function. ACS chemical neuroscience. 2019 Jul 17; 10:3167–72. DOI: 10.1021/acschemneuro.8b00603

42. Costa Couto AR da, Price KL, Mesoy S, Capes E, and Lummis SCR. The M4 Helix Is Involved in α7 nACh Receptor Function. ACS Chemical Neuroscience. 2020 May 20; 11. Publisher: American Chemical Society:1406–12. DOI: 10.1021/acschemneuro.0c00027

43. Chang Yc, Wu W, Zhang Jl, and Huang Y. Allosteric activation mechanism of the cys-loop receptors. Acta Pharmacologica Sinica. 2009 Jun; 30. Publisher: Nature Publishing Group:663–72. DOI: 10.1038/aps.2009.51

44. Hansen SB, Sulzenbacher G, Huxford T, Marchot P, Taylor P, and Bourne Y. Structures of Aplysia AChBP complexes with nicotinic agonists and antagonists reveal distinctive binding interfaces and conformations. The EMBO Journal. 2005 Oct 19; 24:3635–46. DOI: 10.1038/sj.emboj.7600828

45. Zhang J, Xue F, Liu Y, Yang H, and Wang X. The Structural Mechanism of the Cys-Loop Receptor Desensitization. Molecular Neurobiology. 2013 Aug 1; 48:97–108. DOI: 10.1007/s12035-013-8420-z

46. Plested AJ. Don't Flip Out: AChRs are Primed to Catch and Hold Your Attention. Biophysical Journal. 2014 Jul 1; 107:8–9. DOI: 10.1016/j.bpj.2014.05.021

47. Mitra S, Khatri SN, Maulik M, Bult-Ito A, and Schulte M. Allosterism of Nicotinic Acetylcholine Receptors: Therapeutic Potential for Neuroinflammation Underlying Brain Trauma and Degenerative Disorders. International Journal of Molecular Sciences. 2020 Jan; 21. Number: 14 Publisher: Multidisciplinary Digital Publishing Institute:4918. DOI: 10.3390/ijms21144918

48. Smart TG and Stephenson FA. A half century of -aminobutyric acid. Brain and Neuroscience Advances. 2019 Jan 1; 3. Publisher: SAGE Publications Ltd STM:2398212819858249. DOI: 10.1177/2398212819858249

49. Goldschen-Ohm MP. Benzodiazepine Modulation of GABAA Receptors: A Mechanistic Perspective. Biomolecules. 2022 Dec; 12. Number: 12 Publisher: Multidisciplinary Digital Publishing Institute:1784. DOI: 10.3390/biom12121784

50. Wang ZJ, Deba F, Mohamed TS, Chiara DC, Ramos K, and Hamouda AK. Unraveling amino acid residues critical for allosteric potentiation of (α4)3(β2)2-type nicotinic acetylcholine receptor responses. Journal of Biological Chemistry. 2017 Jun; 292:9988–10001. DOI: 10.1074/jbc.M116.771246

51. Seo S, Henry JT, Lewis AH, Wang N, and Levandoski MM. The Positive Allosteric Modulator Morantel Binds at Noncanonical Subunit Interfaces of Neuronal Nicotinic Acetylcholine Receptors. Journal of Neuroscience. 2009 Jul 8; 29. Publisher: Society for Neuroscience Section: Articles:8734–42. DOI: 10.1523/JNEUROSCI.1859-09.2009

52. Hosie AM, Dunne EL, Harvey RJ, and Smart TG. Zinc-mediated inhibition of GABAA receptors: discrete binding sites underlie subtype specificity. Nature Neuroscience. 2003 Apr; 6. Publisher: Nature Publishing Group:362–9. DOI: 10.1038/nn1030

53. Moroni M, Vijayan R, Carbone A, Zwart R, Biggin PC, and Bermudez I. Non-Agonist-Binding Subunit Interfaces Confer Distinct Functional Signatures to the Alternate Stoichiometries of the α4β2 Nicotinic Receptor: An α4–α4 Interface

Is Required for Zn2+ Potentiation. The Journal of Neuroscience. 2008 Jul 2; 28:6884. DOI: 10.1523/JNEUROSCI.1228-08.2008

54. Huang X, Chen H, and Shaffer PL. Crystal Structures of Human GlyRα3 Bound to Ivermectin. Structure. 2017 Jun 6; 25:945–950.e2. DOI: 10.1016/j.str.2017.04.007

55. Hibbs RE and Gouaux E. Principles of activation and permeation in an anion-selective Cys-loop receptor. Nature. 2011; 474. Publisher: Nature Publishing Group UK London:54–60

56. Estrada A and Lynch J. Functional characterization of ivermectin binding sites in α1β22L GABA(A) receptors. Frontiers in Molecular Neuroscience. 2015 Sep 25; 8. Publisher: Frontiers. DOI: 10.3389/fnmol.2015.00055

57. Mortensen M, Bright DP, Fagotti J, Dorovykh V, Cerna B, and Smart TG. Forty Years Searching for Neurosteroid Binding Sites on GABAA Receptors. Neuroscience. 2024 Jun 7. DOI: 10.1016/j.neuroscience.2024.06.002

58. Weir CJ, Ling ATY, Belelli D, Wildsmith JaW, Peters JA, and Lambert JJ. The interaction of anaesthetic steroids with recombinant glycine and GABAA receptors†. British Journal of Anaesthesia. 2004 May 1; 92. Publisher: Elsevier:704–11. DOI: 10.1093/bja/aeh125

59. Maksay G, Laube B, and Betz H. Subunit-specific modulation of glycine receptors by neurosteroids. Neuropharmacology. 2001 Sep 1; 41:369–76. DOI: 10.1016/S0028-3908(01)00071-5

60. Kumar A, Kindig K, Rao S, Zaki AM, Basak S, Sansom MSP, Biggin PC, and Chakrapani S. Structural basis for cannabinoid-induced potentiation of alpha1-glycine receptors in lipid nanodiscs. Nature Communications. 2022 Aug 18; 13:4862. DOI: 10.1038/s41467-022-32594-5

61. Gotti C, Zoli M, and Clementi F. Brain nicotinic acetylcholine receptors: native subtypes and their relevance. Trends in Pharmacological Sciences. 2006 Sep 1; 27:482–91. DOI: 10.1016/j.tips.2006.07.004

62. Gerzanich V, Anand R, and Lindstrom J. Homomers of alpha 8 and alpha 7 subunits of nicotinic receptors exhibit similar channel but contrasting binding site properties. Molecular Pharmacology. 1994 Feb 1; 45. Publisher: American Society for Pharmacology and Experimental Therapeutics:212–20

63. Zoli M, Pistillo F, and Gotti C. Diversity of native nicotinic receptor subtypes in mammalian brain. Neuropharmacology. 2015 Sep; 96(Pt B):302–11. DOI: 10.1016/j.neuropharm.2014.11.003

64. Nelson ME, Kuryatov A, Choi CH, Zhou Y, and Lindstrom J. Alternate stoichiometries of alpha4beta2 nicotinic acetylcholine receptors. Molecular Pharmacology. 2003 Feb; 63:332–41. DOI: 10.1124/mol.63.2.332

65. Moroni M, Zwart R, Sher E, Cassels BK, and Bermudez I. $\alpha 4\beta 2$ Nicotinic Receptors with High and Low Acetylcholine Sensitivity: Pharmacology, Stoichiometry, and Sensitivity to Long-Term Exposure to Nicotine. Molecular Pharmacology. 2006 Aug; 70:755–68. DOI: 10.1124/mol.106.023044

66. Tapia L, Kuryatov A, and Lindstrom J. Ca2+ permeability of the (alpha4)3(beta2)2 stoichiometry greatly exceeds that of (alpha4)2(beta2)3 human acetylcholine receptors. Molecular Pharmacology. 2007 Mar; 71:769–76. DOI: 10.1124/mol.106.030445

67. Wang J, Kuryatov A, Sriram A, Jin Z, Kamenecka TM, Kenny PJ, and Lindstrom J. An Accessory Agonist Binding Site Promotes Activation of $\alpha 4\beta 2$* Nicotinic Acetylcholine Receptors. The Journal of Biological Chemistry. 2015 Apr 13; 290:13907. DOI: 10.1074/jbc.M115.646786

68. Mazzaferro S, Benallegue N, Carbone A, Gasparri F, Vijayan R, Biggin PC, Moroni M, and Bermudez I. Additional Acetylcholine (ACh) Binding Site at

α4/α4 Interface of (α4β2)2α4 Nicotinic Receptor Influences Agonist Sensitivity. Journal of Biological Chemistry. 2011 Sep; 286:31043–54. DOI: 10.1074/jbc.M111.262014

69. Harpsøe K, Ahring PK, Christensen JK, Jensen ML, Peters D, and Balle T. Unraveling the High- and Low-Sensitivity Agonist Responses of Nicotinic Acetylcholine Receptors. The Journal of Neuroscience. 2011 Jul 27; 31:10759. DOI: 10.1523/JNEUROSCI.1509-11.2011

70. Benallegue N, Mazzaferro S, Alcaino C, and Bermudez I. The additional ACh binding site at the α4(+)/α4(-) interface of the (α4β2)2α4 nicotinic ACh receptor contributes to desensitization. British Journal of Pharmacology. 2013 Sep; 170:304–16. DOI: 10.1111/bph.12268

71. Mazzaferro S, Gasparri F, New K, Alcaino C, Faundez M, Vasquez PI, Vijayan R, Biggin PC, and Bermudez I. Non-equivalent Ligand Selectivity of Agonist Sites in (α4β2)2α4 Nicotinic Acetylcholine Receptors: A KEY DETERMINANT OF AGONIST EFFICACY *. Journal of Biological Chemistry. 2014 Aug 1; 289. Publisher: Elsevier:21795–806. DOI: 10.1074/jbc.M114.555136

72. New K, Del Villar SG, Mazzaferro S, Alcaino C, and Bermudez I. The fifth subunit of the (α4β2)2β2 nicotinic ACh receptor modulates maximal ACh responses. British Journal of Pharmacology. 2018; 175. _eprint: https://onlinelibrary.wiley.com/doi/pdf/10.1111/bph 37. DOI: 10.1111/bph.13905

73. Indurthi DC, Lewis TM, Ahring PK, Balle T, Chebib M, and Absalom NL. Ligand Binding at the α4-α4 Agonist-Binding Site of the α4β2 nAChR Triggers Receptor Activation through a Pre-Activated Conformational State. PLOS ONE. 2016 Aug 23; 11. Publisher: Public Library of Science:e0161154. DOI: 10.1371/journal.pone.0161154

74. Malysz J, Dyhring T, Ahring P, Olsen G, Peters D, Gronlien J, Wetterstrand C, Ween H, Haakerud M, Thorin-Hagene K, Andersen E, Anderson D, Hu M,

Kroeger P, Lee CH, Gopalakrishnan M, and Timmermann D. In vitro pharmacological profile of a novel α4β2 positive allosteric modulator NS9283 (A-969933). Biochemical Pharmacology. 2009 Oct; 78:919–20. DOI: 10.1016/j.bcp.2009.06.080

75. Olsen JA, Ahring PK, Kastrup JS, Gajhede M, and Balle T. Structural and Functional Studies of the Modulator NS9283 Reveal Agonist-like Mechanism of Action at α4β2 Nicotinic Acetylcholine Receptors. Journal of Biological Chemistry. 2014 Sep; 289:24911–21. DOI: 10.1074/jbc.M114.568097
76. Wang J and Lindstrom J. Orthosteric and allosteric potentiation of heteromeric neuronal nicotinic acetylcholine receptors. British Journal of Pharmacology. 2018 Jun; 175:1805–21. DOI: 10.1111/bph.13745
77. Lendvai B, Kassai F, Szájli Á, and Némethy Z. α7 Nicotinic acetylcholine receptors and their role in cognition. Brain Research Bulletin. Extrasynaptic ionotropic receptors 2013 Apr 1; 93:86–96. DOI: 10.1016/j.brainresbull.2012.11.003
78. Andersen N, Corradi J, Sine SM, and Bouzat C. Stoichiometry for activation of neuronal α7 nicotinic receptors. Proceedings of the National Academy of Sciences of the United States of America. 2013 Dec 17; 110:20819–24. DOI: 10.1073/pnas.1315775110
79. Bouzat C, Lasala M, Nielsen BE, Corradi J, and Esandi MdC. Molecular function of α7 nicotinic receptors as drug targets. The Journal of Physiology. 2018; 596. _eprint: https://onlinelibrary.wiley.com/doi/pdf/10.1113/JP275101:1847–61. DOI: 10.1113/JP275101
80. Pesti K, Szabo AK, Mike A, and Vizi ES. Kinetic properties and open probability of α7 nicotinic acetylcholine receptors. Neuropharmacology. 2014 Jun; 81:101–15. DOI: 10.1016/j.neuropharm.2014.01.034

81. Bouzat C, Bartos M, Corradi J, and Sine SM. The interface between extracellular and transmembrane domains of homomeric Cys-loop receptors governs open-channel lifetime and rate of desensitization. The Journal of Neuroscience: The Official Journal of the Society for Neuroscience. 2008 Jul 30; 28:7808–19. DOI: 10.1523/JNEUROSCI.0448-08.2008

82. Corradi J and Bouzat C. Understanding the Bases of Function and Modulation of α 7 Nicotinic Receptors: Implications for Drug Discovery. Molecular Pharmacology. 2016 Sep; 90:288–99. DOI: 10.1124/mol.116.104240

83. Kabbani N and Nichols RA. Beyond the Channel: Metabotropic Signaling by Nicotinic Receptors. Trends in Pharmacological Sciences. 2018 Apr 1; 39. Publisher: Elsevier:354–66. DOI: 10.1016/j.tips.2018.01.002

84. Wonnacott S. Nicotinic ACh Receptors. Tocris Bioscience Scientific Review Series. 2015

85. Dineley KT, Pandya AA, and Yakel JL. Nicotinic ACh receptors as therapeutic targets in CNS disorders. Trends in Pharmacological Sciences. 2015 Feb 1; 36:96–108. DOI: 10.1016/j.tips.2014.12.002

86. Wonnacott S. Presynaptic nicotinic ACh receptors. Trends in Neurosciences. 1997 Feb 1; 20. Publisher: Elsevier:92–8. DOI: 10.1016/S0166-2236(96)10073-4

87. Zoli M, Pucci S, Vilella A, and Gotti C. Neuronal and Extraneuronal Nicotinic Acetylcholine Receptors. Current Neuropharmacology. 2018 May; 16:338. DOI: 10.2174/1570159X15666170912110450

88. Levin ED, McClernon FJ, and Rezvani AH. Nicotinic effects on cognitive function: behavioral characterization, pharmacological specification, and anatomic localization. Psychopharmacology. 2006 Feb 1; 184:523–39. DOI: 10.1007/s00213-005-0164-7

89. Guillem K, Bloem B, Poorthuis RB, Loos M, Smit AB, Maskos U, Spijker S, and Mansvelder HD. Nicotinic Acetylcholine Receptor β2 Subunits in the Medial Prefrontal Cortex Control Attention. Science. 2011 Aug 12; 333. Publisher: American Association for the Advancement of Science:888–91. DOI: 10.1126/science.1207079

90. Marks MJ, Whiteaker P, and Collins AC. Deletion of the α7, β2, or β4 Nicotinic Receptor Subunit Genes Identifies Highly Expressed Subtypes with Relatively Low Affinity for [3H]Epibatidine. Molecular Pharmacology. 2006 Sep 1; 70. Publisher: American Society for Pharmacology and Experimental Therapeutics Section: Article:947–59. DOI: 10.1124/mol.106.025338

91. Gotti C, Moretti M, Meinerz NM, Clementi F, Gaimarri A, Collins AC, and Marks MJ. Partial Deletion of the Nicotinic Cholinergic Receptor α4 or β2 Subunit Genes Changes the Acetylcholine Sensitivity of Receptor-Mediated 86Rb+ Efflux in Cortex and Thalamus and Alters Relative Expression of α4 and β2 Subunits. Molecular Pharmacology. 2008 Jun 1; 73. Publisher: American Society for Pharmacology and Experimental Therapeutics Section: Article:1796–807. DOI: 10.1124/mol.108.045203

92. DeDominicis KE, Sahibzada N, Olson TT, Xiao Y, Wolfe BB, Kellar KJ, and Yasuda RP. The (α4)3(β2)2 Stoichiometry of the Nicotinic Acetylcholine Receptor Predominates in the Rat Motor Cortex. Molecular Pharmacology. 2017 Sep 1; 92. Publisher: American Society for Pharmacology and Experimental Therapeutics Section: Article:327–37. DOI: 10.1124/mol.116.106880

93. D. Levin E. α7-Nicotinic Receptors and Cognition. Current Drug Targets. 2012 May 1; 13:602–6. DOI: 10.2174/138945012800398937

94. Gowing LR, Ali RL, Allsop S, Marsden J, Turf EE, West R, and Witton J. Global statistics on addictive behaviours: 2014 status report. Addiction. 2015; 110.

_eprint: https://onlinelibrary.wiley.com/doi/pdf/10.1111/add.12899:904–19. DOI: 10.1111/add.12899

95. Wittenberg RE, Wolfman SL, De Biasi M, and Dani JA. Nicotinic acetylcholine receptors and nicotine addiction: A brief introduction. Neuropharmacology. 2020 Oct 15; 177:108256. DOI: 10.1016/j.neuropharm.2020.108256

96. Mao D, Gallagher K, and McGehee DS. Nicotine Potentiation of Excitatory Inputs to Ventral Tegmental Area Dopamine Neurons. Journal of Neuroscience. 2011 May 4; 31. Publisher: Society for Neuroscience Section: Articles:6710–20. DOI: 10.1523/JNEUROSCI.5671-10.2011

97. Pidoplichko VI, Noguchi J, Areola OO, Liang Y, Peterson J, Zhang T, and Dani JA. Nicotinic Cholinergic Synaptic Mechanisms in the Ventral Tegmental Area Contribute to Nicotine Addiction. Learning & Memory. 2004 Jan 1; 11. Company: Cold Spring Harbor Laboratory Press Distributor: Cold Spring Harbor Laboratory Press Institution: Cold Spring Harbor Laboratory Press Label: Cold Spring Harbor Laboratory Press Publisher: Cold Spring Harbor Lab:60–9. DOI: 10.1101/lm.70004

98. Lester RA, ed. Nicotinic Receptors. Vol. 26. The Receptors. New York, NY: Springer New York, 2014. DOI: 10.1007/978-1-4939-1167-7

99. Selby P and Zawertailo L. Tobacco Addiction. New England Journal of Medicine. 2022 Jul 27; 387. Publisher: Massachusetts Medical Society:345–54. DOI: 10.1056/NEJMcp2032393

100. Wadgave U and Nagesh L. Nicotine Replacement Therapy: An Overview. International Journal of Health Sciences. 2016 Jul; 10:425

101. Jordan CJ and Xi ZX. Discovery and development of varenicline for smoking cessation. Expert Opinion on Drug Discovery. 2018 Jul 3; 13. Publisher: Taylor & Francis:671–83. DOI: 10.1080/17460441.2018.1458090

102. Coe JW, Brooks PR, Vetelino MG, Wirtz MC, Arnold EP, Huang J, Sands SB, Davis TI, Lebel LA, Fox CB, Shrikhande A, Heym JH, Schaeffer E, Rollema H, Lu Y, Mansbach RS, Chambers LK, Rovetti CC, Schulz DW, Tingley FD, and O'Neill BT. Varenicline: an alpha4beta2 nicotinic receptor partial agonist for smoking cessation. Journal of Medicinal Chemistry. 2005 May 19; 48:3474–7. DOI: 10.1021/jm050069n

103. Tutka P, Vinnikov D, Courtney RJ, and Benowitz NL. Cytisine for nicotine addiction treatment: a review of pharmacology, therapeutics and an update of clinical trial evidence for smoking cessation. Addiction. 2019; 114. _eprint: https://onlinelibrary.wiley.com/doi/pdf/10.1111/add.14721:1951–69. DOI: 10.1111/add.14721

104. Association A. 2011 Alzheimer's disease facts and figures. Alzheimer's & Dementia. 2011; 7. _eprint: https://onlinelibrary.wiley.com/doi/pdf/10.1016/j.jalz.2011.02.004:208–44. DOI: 10.1016/j.jalz.2011.02.004

105. Heneka MT, Carson MJ, Khoury JE, Landreth GE, Brosseron F, Feinstein DL, Jacobs AH, Wyss-Coray T, Vitorica J, Ransohoff RM, Herrup K, Frautschy SA, Finsen B, Brown GC, Verkhratsky A, Yamanaka K, Koistinaho J, Latz E, Halle A, Petzold GC, Town T, Morgan D, Shinohara ML, Perry VH, Holmes C, Bazan NG, Brooks DJ, Hunot S, Joseph B, Deigendesch N, Garaschuk O, Boddeke E, Dinarello CA, Breitner JC, Cole GM, Golenbock DT, and Kummer MP. Neuroinflammation in Alzheimer's disease. The Lancet Neurology. 2015 Apr 1; 14. Publisher: Elsevier:388–405. DOI: 10.1016/S1474-4422(15)70016-5

106. Parri HR, Hernandez CM, and Dineley KT. Research update: Alpha7 nicotinic acetylcholine receptor mechanisms in Alzheimer's disease. Biochemical Pharmacology. 2011 Oct 15; 82:931–42. DOI: 10.1016/j.bcp.2011.06.039

107. Dineley KT. Beta-amyloid peptide – nicotinic acetylcholine receptor interaction: the two faces of health and disease. Frontiers in Bioscience-Landmark. 2007 Sep 1; 12. Number: 13 Publisher: IMR Press:5030–8. DOI: 10.2741/2445

108. Wang HY, Lee DHS, Davis CB, and Shank RP. Amyloid Peptide Aβ1-42 Binds Selectively and with Picomolar Affinity to α7 Nicotinic Acetylcholine Receptors. Journal of Neurochemistry. 2000; 75. _eprint: https://onlinelibrary.wiley.com/doi/pdf/10.1046/j.1471-4159.2000.0751155.x:1155–61. DOI: 10.1046/j.1471-4159.2000.0751155.x

109. Liu Q, Huang Y, Xue F, Simard A, DeChon J, Li G, Zhang J, Lucero L, Wang M, Sierks M, Hu G, Chang Y, Lukas RJ, and Wu J. A Novel Nicotinic Acetylcholine Receptor Subtype in Basal Forebrain Cholinergic Neurons with High Sensitivity to Amyloid Peptides. Journal of Neuroscience. 2009 Jan 28; 29. Publisher: Society for Neuroscience Section: Articles:918–29. DOI: 10.1523/JNEUROSCI.3952-08.2009

110. Wang HY, Stucky A, Liu J, Shen C, Trocme-Thibierge C, and Morain P. Dissociating β-Amyloid from α7 Nicotinic Acetylcholine Receptor by a Novel Therapeutic Agent, S 24795, Normalizes α7 Nicotinic Acetylcholine and NMDA Receptor Function in Alzheimer's Disease Brain. Journal of Neuroscience. 2009 Sep 2; 29. Publisher: Society for Neuroscience Section: Articles:10961–73. DOI: 10.1523/JNEUROSCI.6088-08.2009

111. Marucci G, Buccioni M, Ben DD, Lambertucci C, Volpini R, and Amenta F. Efficacy of acetylcholinesterase inhibitors in Alzheimer's disease. Neuropharmacology. 2021 Jun 1; 190:108352. DOI: 10.1016/j.neuropharm.2020.108352

112. Deardorff WJ, Shobassy A, and Grossberg GT. Safety and clinical effects of EVP-6124 in subjects with Alzheimer's disease currently or previously receiving

an acetylcholinesterase inhibitor medication. Expert Review of Neurotherapeutics. 2015 Jan; 15:7–17. DOI: 10.1586/14737175.2015.995639

113. Kim SY, Choi SH, Rollema H, Schwam EM, McRae T, Dubrava S, and Jacobsen J. Phase II Crossover Trial of Varenicline in Mild-to-Moderate Alzheimer's Disease. Dementia and Geriatric Cognitive Disorders. 2013 Nov 14; 37:232–45. DOI: 10.1159/000355373

114. Schneider LS, Mangialasche F, Andreasen N, Feldman H, Giacobini E, Jones R, Mantua V, Mecocci P, Pani L, Winblad B, and Kivipelto M. Clinical trials and late-stage drug development for Alzheimer's disease: an appraisal from 1984 to 2014. Journal of Internal Medicine. 2014; 275. _eprint: https://onlinelibrary.wiley.com/doi/pdf/10.1111/j 83. DOI: 10.1111/joim.12191

115. Quik M and Wonnacott S. α6β2* and α4β2* Nicotinic Acetylcholine Receptors As Drug Targets for Parkinson's Disease. Pharmacological Reviews. 2011 Dec 1; 63. Ed. by Sharp BM. Publisher: American Society for Pharmacology and Experimental Therapeutics Section: Review Article:938–66. DOI: 10.1124/pr.110.003269

116. Björklund A and Dunnett SB. Dopamine neuron systems in the brain: an update. Trends in Neurosciences. 2007 May; 30:194–202. DOI: 10.1016/j.tins.2007.03.006

117. Wilson CJ and Groves PM. Fine structure and synaptic connections of the common spiny neuron of the rat neostriatum: a study employing intracellular inject of horseradish peroxidase. The Journal of Comparative Neurology. 1980 Dec 1; 194:599–615. DOI: 10.1002/cne.901940308

118. Wilson CJ, Chang HT, and Kitai ST. Firing patterns and synaptic potentials of identified giant aspiny interneurons in the rat neostriatum. The Journal of Neuroscience: The Official Journal of the Society for Neuroscience. 1990 Feb; 10:508–19. DOI: 10.1523/JNEUROSCI.10-02-00508.1990

119. Goto Y, Otani S, and Grace AA. The Yin and Yang of Dopamine Release: A New Perspective. Neuropharmacology. 2007 Jul 19; 53:583. DOI: 10.1016/j.neuropharm.2007.07.007

120. Kreitzer AC and Malenka RC. Striatal plasticity and basal ganglia circuit function. Neuron. 2008 Nov 26; 60:543–54. DOI: 10.1016/j.neuron.2008.11.005

121. Rahman S, Zhang J, and Corrigall WA. Local perfusion of nicotine differentially modulates somatodendritic dopamine release in the rat ventral tegmental area after nicotine preexposure. Neurochemical Research. 2004 Sep; 29:1687–93. DOI: 10.1023/b:nere.0000035803.64724.17

122. Picciotto MR, Addy NA, Mineur YS, and Brunzell DH. It is not "either/or": Activation and desensitization of nicotinic acetylcholine receptors both contribute to behaviors related to nicotine addiction and mood. Progress in Neurobiology. 2008 Apr 1; 84:329–42. DOI: 10.1016/j.pneurobio.2007.12.005

123. Bencherif M. Neuronal nicotinic receptors as novel targets for inflammation and neuroprotection: mechanistic considerations and clinical relevance. Acta Pharmacologica Sinica. 2009 Jun; 30. Publisher: Nature Publishing Group:702–14. DOI: 10.1038/aps.2009.37

124. Belluardo N, Mudò G, Blum M, and Fuxe K. Central nicotinic receptors, neurotrophic factors and neuroprotection. Behavioural Brain Research. 2000 Aug; 113:21–34. DOI: 10.1016/s0166-4328(00)00197-2

125. Meshul CK, Kamel D, Moore C, Kay TS, and Krentz L. Nicotine alters striatal glutamate function and decreases the apomorphine-induced contralateral rotations in 6-OHDA-lesioned rats. Experimental Neurology. 2002 May; 175:257–74. DOI: 10.1006/exnr.2002.7900

126. Zhang Cl, Han Qw, Chen Nh, and Yuan Yh. Research on developing drugs for Parkinson's disease. Brain Research Bulletin. 2021 Mar 1; 168:100–9. DOI: 10.1016/j.brainresbull.2020.12.017

127. Pozzi M, Bertella S, Gatti E, Peeters GGAM, Carnovale C, Zambrano S, and Nobile M. Emerging drugs for the treatment of attention-deficit hyperactivity disorder (ADHD). Expert Opinion on Emerging Drugs. 2020 Oct 1; 25. Publisher: Taylor & Francis _eprint: https://doi.org/10.1080/14728214.2020.1820481:395–407. DOI: 10.1080/14728214.2020.1820481

128. Denckla MB. Executive function, the overlap zone between attention deficit hyperactivity disorder and learning disabilities. International Pediatrics. 1989; 4. Publisher: Miami Children's Hospital Medical Journal Inc.:155–60

129. Welsh MC and Pennington BF. Assessing frontal lobe functioning in children: Views from developmental psychology. Developmental Neuropsychology. 1988; 4. Publisher: Routledge _eprint: https://doi.org/10.1080/87565648809540405:199–230. DOI: 10.1080/87565648809540405

130. Pennington BF and Ozonoff S. Executive Functions and Developmental Psychopathology. Journal of Child Psychology and Psychiatry. 1996; 37. _eprint: https://onlinelibrary.wiley.com/doi/pdf/10.1111/j.1469-7610.1996.tb01380.x:51–87. DOI: 10.1111/j.1469-7610.1996.tb01380.x

131. Wilens TE and Decker MW. Neuronal nicotinic receptor agonists for the treatment of attention-deficit/hyperactivity disorder: focus on cognition. Biochemical Pharmacology. 2007 Oct 15; 74:1212–23. DOI: 10.1016/j.bcp.2007.07.002

132. Cummings JL. Cholinesterase inhibitors: A new class of psychotropic compounds. The American Journal of Psychiatry. 2000 Jan; 157:4–15. DOI: 10.1176/ajp.157.1.4

133. Kollins SH, McClernon FJ, and Fuemmeler BF. Association between smoking and attention-deficit/hyperactivity disorder symptoms in a population-based sample

of young adults. Archives of General Psychiatry. 2005 Oct; 62:1142–7. DOI: 10.1001/archpsyc.62.10.1142

134. Milberger S, Biederman J, Faraone SV, Chen L, and Jones J. Is maternal smoking during pregnancy a risk factor for attention deficit hyperactivity disorder in children? The American Journal of Psychiatry. 1996 Sep; 153:1138–42. DOI: 10.1176/ajp.153.9.1138

135. Posner J, Polanczyk GV, and Sonuga-Barke E. Attention-deficit hyperactivity disorder. Lancet (London, England). 2020 Feb 8; 395:450–62. DOI: 10.1016/S0140-6736(19)33004-1

136. Potter AS, Dunbar G, Mazzulla E, Hosford D, and Newhouse PA. AZD3480, a novel nicotinic receptor agonist, for the treatment of attention-deficit/hyperactivity disorder in adults. Biological Psychiatry. 2014 Feb 1; 75:207–14. DOI: 10.1016/j.biopsych.2013.06.002

137. Sawa A and Snyder SH. Schizophrenia: Diverse Approaches to a Complex Disease. Science. 2002 Apr 26. Publisher: American Association for the Advancement of Science. DOI: 10.1126/science.1070532

138. Howes OD and Kapur S. The Dopamine Hypothesis of Schizophrenia: Version III—The Final Common Pathway. Schizophrenia Bulletin. 2009 Mar 26; 35:549. DOI: 10.1093/schbul/sbp006

139. Antonio-Tolentino K and Hopkins CR. Selective α7 nicotinic receptor agonists and positive allosteric modulators for the treatment of schizophrenia–a review. Expert Opinion on Investigational Drugs. 2020; 29. Publisher: Taylor & Francis:603–10

140. Koukouli F, Rooy M, Tziotis D, Sailor KA, O'Neill HC, Levenga J, Witte M, Nilges M, Changeux JP, Hoeffer CA, Stitzel JA, Gutkin BS, DiGregorio DA, and Maskos U. Nicotine reverses hypofrontality in animal models of addiction and schizophrenia. Nature Medicine. 2017 Mar; 23:347–54. DOI: 10.1038/nm.4274

141. Tregellas JR and Wylie KP. Alpha7 Nicotinic Receptors as Therapeutic Targets in Schizophrenia. Nicotine & Tobacco Research. 2018 Aug 23; 21:349. DOI: 10.1093/ntr/nty034

142. Pizzagalli DA and Roberts AC. Prefrontal cortex and depression. Neuropsychopharmacology. 2022 Jan; 47. Publisher: Nature Publishing Group:225–46. DOI: 10.1038/s41386-021-01101-7

143. Saveanu RV and Nemeroff CB. Etiology of Depression: Genetic and Environmental Factors. Psychiatric Clinics. 2012 Mar 1; 35. Publisher: Elsevier:51–71. DOI: 10.1016/j.psc.2011.12.001

144. Subbaiah MAM. Triple Reuptake Inhibitors as Potential Therapeutics for Depression and Other Disorders: Design Paradigm and Developmental Challenges. Journal of Medicinal Chemistry. 2018 Mar 22; 61. Publisher: American Chemical Society:2133–65. DOI: 10.1021/acs.jmedchem.6b01827

145. Suarez-Lopez JR, Hood N, Suárez-Torres J, Gahagan S, Gunnar MR, and López-Paredes D. Associations of acetylcholinesterase activity with depression and anxiety symptoms among adolescents growing up near pesticide spray sites. International Journal of Hygiene and Environmental Health. 2019 Aug 1; 222:981–90. DOI: 10.1016/j.ijheh.2019.06.001

146. Bazylewicz-Walczak B, Majczakowa W, and Szymczak M. Behavioral effects of occupational exposure to organophosphorous pesticides in female greenhouse planting workers. Neurotoxicology. 1999 Oct 1; 20:819–26

147. Furey ML and Drevets WC. Antidepressant Efficacy of the Antimuscarinic Drug Scopolamine: A Randomized, Placebo-Controlled Clinical Trial. Archives of General Psychiatry. 2006 Oct 1; 63:1121–9. DOI: 10.1001/archpsyc.63.10.1121

148. Mineur YS and Picciotto MR. Nicotine receptors and depression: revisiting and revising the cholinergic hypothesis. Trends in Pharmacological Sciences. 2010 Dec 1; 31:580–6. DOI: 10.1016/j.tips.2010.09.004

149. Salín-Pascual RJ, Rosas M, Jimenez-Genchi A, Rivera-Meza BL, and Delgado-Parra V. Antidepressant effect of transdermal nicotine patches in nonsmoking patients with major depression. The Journal of clinical psychiatry. 1996 Sep 1; 57:387–9

150. Mantione E, Micheloni S, Alcaino C, New K, Mazzaferro S, and Bermudez I. Allosteric Modulators Of α4β2 Nicotinic Acetylcholine Receptors: A New Direction For Antidepressant Drug Discovery. Future Medicinal Chemistry. 2012 Nov 1; 4. Publisher: Taylor & Francis _eprint: https://doi.org/10.4155/fmc.12.172:2217–30. DOI: 10.4155/fmc.12.172

151. Terry AV, Jones K, and Bertrand D. Nicotinic acetylcholine receptors in neurological and psychiatric diseases. Pharmacological Research. 2023 May 1; 191:106764. DOI: 10.1016/j.phrs.2023.106764

152. Bouzat C. New insights into the structural bases of activation of Cys-loop receptors. Journal of Physiology, Paris. 2012 Jan; 106:23–33. DOI: 10.1016/j.jphysparis.2011.09.012

153. Celie PH, Rossum-Fikkert SE van, Dijk WJ van, Brejc K, Smit AB, and Sixma TK. Nicotine and carbamylcholine binding to nicotinic acetylcholine receptors as studied in AChBP crystal structures. Neuron. 2004; 41. Publisher: Elsevier:907–14

154. Brejc K, Dijk WJ van, Klaassen RV, Schuurmans M, Oost J van der, Smit AB, and Sixma TK. Crystal structure of an ACh-binding protein reveals the ligand-binding domain of nicotinic receptors. Nature. 2001 May; 411. Publisher: Nature Publishing Group:269–76. DOI: 10.1038/35077011

155. Zhang HK, Eaton JB, Yu LF, Nys M, Mazzolari A, Elk R van, Smit AB, Alexandrov V, Hanania T, Sabath E, Fedolak A, Brunner D, Lukas RJ, Vistoli G, Ulens C, and Kozikowski AP. Insights into the Structural Determinants Required for High-Affinity Binding of Chiral Cyclopropane-Containing Ligands to α4β2-Nicotinic Acetylcholine Receptors: An Integrated Approach to Behaviorally Active Nicotinic Ligands. Journal of Medicinal Chemistry. 2012 Sep 27; 55. Publisher: American Chemical Society:8028–37. DOI: 10.1021/jm3008739

156. Tavares XDS, Blum AP, Nakamura DT, Puskar NL, Shanata JAP, Lester HA, and Dougherty DA. Variations in Binding Among Several Agonists at Two Stoichiometries of the Neuronal, α4β2 Nicotinic Receptor. Journal of the American Chemical Society. 2012 Jul 18; 134. Publisher: American Chemical Society:11474–80. DOI: 10.1021/ja3011379

157. Hurst R, Rollema H, and Bertrand D. Nicotinic acetylcholine receptors: From basic science to therapeutics. Pharmacology & Therapeutics. 2013 Jan 1; 137:22–54. DOI: 10.1016/j.pharmthera.2012.08.012

158. Lape R, Colquhoun D, and Sivilotti LG. On the nature of partial agonism in the nicotinic receptor superfamily. Nature. 2008 Aug; 454. Publisher: Nature Publishing Group:722–7. DOI: 10.1038/nature07139

159. Bizimana L. Pharmacological Evaluation of Choline on α4β2 Neuronal Nicotinic Acetylcholine Receptors. PhD thesis. 2015 Mar 31

160. Alkondon M, Pereira EFR, Cartes WS, Maelicke A, and Albuquerque EX. Choline is a Selective Agonist of α7 Nicotinic Acetylcholine Receptors in the Rat Brain Neurons. European Journal of Neuroscience. 1997; 9. _eprint: https://onlinelibrary.wiley.com/doi/9568.1997.tb01702.x:2734–42. DOI: 10.1111/j.1460-9568.1997.tb01702.x

161. Verbitsky M, Rothlin CV, Katz E, and Elgoyhen AB. Mixed nicotinic-muscarinic properties of the α9 nicotinic cholinergic receptor. Neuropharmacology. 2000;

39. Publisher: Elsevier Limited:2515–24. DOI: 10.1016/S0028-3908(00)00124-6

162. Jensen AA, Frølund B, Liljefors T, and Krogsgaard-Larsen P. Neuronal Nicotinic Acetylcholine Receptors: Structural Revelations, Target Identifications, and Therapeutic Inspirations. Journal of Medicinal Chemistry. 2005 Jul 1; 48. Publisher: American Chemical Society:4705–45. DOI: 10.1021/jm040219e

163. Rouden J, Lasne MC, Blanchet J, and Baudoux J. ()-Cytisine and Derivatives: Synthesis, Reactivity, and Applications. Chemical Reviews. 2014 Jan 8; 114. Publisher: American Chemical Society:712–78. DOI: 10.1021/cr400307e

164. Mihalak KB, Carroll FI, and Luetje CW. Varenicline Is a Partial Agonist at α4β2 and a Full Agonist at α7 Neuronal Nicotinic Receptors. Molecular Pharmacology. 2006 Sep 1; 70. Publisher: American Society for Pharmacology and Experimental Therapeutics Section: Accelerated Communication:801–5. DOI: 10.1124/mol.106.025130

165. Bruijn KM de. Tropisetron. Drugs. 1992 Jun 1; 43:11–22. DOI: 10.2165/00003495-199200433-00005

166. Papke RL, Porter Papke JK, and Rose GM. Activity of α7-selective agonists at nicotinic and serotonin 5HT3 receptors expressed in *Xenopus* oocytes. Bioorganic & Medicinal Chemistry Letters. Neuronal Nicotinic Receptors and Ligands (Special Section pp 1821-1900) 2004 Apr 19; 14:1849–53. DOI: 10.1016/j.bmcl.2003.09.104

167. Gallagher R, Qudah T, Balle T, Chebib M, and McLeod MD. Novel methyllycaconitine analogues selective for the α4β2 over α7 nicotinic acetylcholine receptors. Bioorganic & Medicinal Chemistry. 2021 Dec 1; 51:116516. DOI: 10.1016/j.bmc.2021.116516

168. Palma E, Bertrand S, Binzoni T, and Bertrand D. Neuronal nicotinic alpha 7 receptor expressed in Xenopus oocytes presents five putative binding sites for methylly-

caconitine. The Journal of Physiology. 1996; 491. _eprint: https://onlinelibrary.wiley.com/doi/pdf/
61. DOI: 10.1113/jphysiol.1996.sp021203

169. Chavez-Noriega LE, Crona JH, Washburn MS, Urrutia A, Elliott KJ, and Johnson EC. Pharmacological Characterization of Recombinant Human Neuronal Nicotinic Acetylcholine Receptors hα2β2, hα2β4, hα3β2, hα3β4, hα4β2, hα4β4 and hα7 Expressed in Xenopus Oocytes. Journal of Pharmacology and Experimental Therapeutics. 1997 Jan 1; 280. Publisher: American Society for Pharmacology and Experimental Therapeutics Section: CELLULAR AND MOLECULAR PHARMACOLOGY:346–56

170. Manetti D, Dei S, Arias HR, Braconi L, Gabellini A, Teodori E, and Romanelli MN. Recent Advances in the Discovery of Nicotinic Acetylcholine Receptor Allosteric Modulators. Molecules. 2023 Jan; 28. Number: 3 Publisher: Multidisciplinary Digital Publishing Institute:1270. DOI: 10.3390/molecules28031270

171. Duret G, Van Renterghem C, Weng Y, Prevost M, Moraga-Cid G, Huon C, Sonner JM, and Corringer PJ. Functional prokaryotic-eukaryotic chimera from the pentameric ligand-gated ion channel family. Proceedings of the National Academy of Sciences of the United States of America. 2011 Jul 19; 108:12143–8. DOI: 10.1073/pnas.1104494108

172. Moaddel R, Abdrakhmanova G, Kozak J, Jozwiak K, Toll L, Jimenez L, Rosenberg A, Tran T, Xiao Y, Zarate CA, and Wainer IW. Sub-anesthetic concentrations of (*R*,*S*)-ketamine metabolites inhibit acetylcholine-evoked currents in α7 nicotinic acetylcholine receptors. European Journal of Pharmacology. 2013 Jan 5; 698:228–34. DOI: 10.1016/j.ejphar.2012.11.023

173. Buisson B and Bertrand D. Allosteric modulation of neuronal nicotinic acetylcholine receptors. Journal of Physiology-Paris. 1998 Apr 1; 92:89–100. DOI: 10.1016/S0928-4257(98)80144-7

174. Noblin DJ, Bertekap RL, Burford NT, Hendricson A, Zhang L, Knox R, Banks M, O'Connell J, and Alt A. Development of a High-Throughput Calcium Flux Assay for Identification of All Ligand Types Including Positive, Negative, and Silent Allosteric Modulators for G Protein-Coupled Receptors. ASSAY and Drug Development Technologies. 2012 Oct; 10. Publisher: Mary Ann Liebert, Inc., publishers:457–67. DOI: 10.1089/adt.2011.443

175. Zwart R, De Filippi G, Broad L, McPhie G, Pearson K, Baldwinson T, and Sher E. 5-Hydroxyindole potentiates human α7 nicotinic receptor-mediated responses and enhances acetylcholine-induced glutamate release in cerebellar slices. Neuropharmacology. 2002; 43. Publisher: Elsevier:374–84

176. Timmermann DB, Grønlien JH, Kohlhaas KL, Nielsen EØ, Dam E, Jørgensen TD, Ahring PK, Peters D, Holst D, Chrsitensen JK, et al. An allosteric modulator of the α7 nicotinic acetylcholine receptor possessing cognition-enhancing properties in vivo. Journal of Pharmacology and Experimental Therapeutics. 2007; 323. Publisher: ASPET:294–307

177. Nielsen BE, Bermudez I, and Bouzat C. Flavonoids as positive allosteric modulators of α7 nicotinic receptors. Neuropharmacology. 2019 Dec 1; 160:107794. DOI: 10.1016/j.neuropharm.2019.107794

178. Harvey AJ, Avery TD, Schaeffer L, Joseph C, Huff BC, Singh R, Morice C, Giethlen B, Grishin AA, Coles CJ, Kolesik P, Wagner S, Andriambeloson E, Huyard B, Poiraud E, Paul D, and O'Connor SM. Discovery of BNC375, a Potent, Selective, and Orally Available Type I Positive Allosteric Modulator of α7 nAChRs. ACS Medicinal Chemistry Letters. 2019 May 9; 10. Publisher: American Chemical Society:754–60. DOI: 10.1021/acsmedchemlett.9b00001

179. Collins T and Millar NS. Nicotinic acetylcholine receptor transmembrane mutations convert ivermectin from a positive to a negative allosteric modulator. Molecular pharmacology. 2010; 78. Publisher: ASPET:198–204

180. Hurst RS, Hajós M, Raggenbass M, Wall TM, Higdon NR, Lawson JA, Rutherford-Root KL, Berkenpas MB, Hoffmann WE, Piotrowski DW, Groppi VE, Allaman G, Ogier R, Bertrand S, Bertrand D, and Arneric SP. A Novel Positive Allosteric Modulator of the α7 Neuronal Nicotinic Acetylcholine Receptor: In Vitro and In Vivo Characterization. Journal of Neuroscience. 2005 Apr 27; 25. Publisher: Society for Neuroscience Section: Cellular/Molecular:4396–405. DOI: 10.1523/JNEUROSCI.5269-04.2005

181. Grønlien JH, Håkerud M, Ween H, Thorin-Hagene K, Briggs CA, Gopalakrishnan M, and Malysz J. Distinct profiles of α7 nAChR positive allosteric modulation revealed by structurally diverse chemotypes. Molecular pharmacology. 2007; 72. Publisher: ASPET:715–24

182. Sahdeo S, Wallace T, Hirakawa R, Knoflach F, Bertrand D, Maag H, Misner D, Tombaugh GC, Santarelli L, Brameld K, Milla ME, and Button DC. Characterization of RO5126946, a Novel α_7 Nicotinic Acetylcholine Receptor–Positive Allosteric Modulator. Journal of Pharmacology and Experimental Therapeutics. 2014 Aug; 350:455–68. DOI: 10.1124/jpet.113.210963

183. Gill JK, Savolainen M, Young GT, Zwart R, Sher E, and Millar NS. Agonist activation of α7 nicotinic acetylcholine receptors via an allosteric transmembrane site. Proceedings of the National Academy of Sciences. 2011 Apr 5; 108. Publisher: Proceedings of the National Academy of Sciences:5867–72. DOI: 10.1073/pnas.1017975108

184. Papke RL, Garai S, Stokes C, Horenstein NA, Zimmerman AD, Abboud KA, and Thakur GA. Differing Activity Profiles of the Stereoisomers of 2,3,5,6TMP-TQS, a Putative Silent Allosteric Modulator of α7 nAChR. Molecular Pharmacology.

2020 Oct 1; 98. Publisher: American Society for Pharmacology and Experimental Therapeutics Section: Article:292–302. DOI: 10.1124/mol.120.119958

185. Chrestia JF, Esandi MdC, and Bouzat C. Cannabidiol as a modulator of α7 nicotinic receptors. Cellular and Molecular Life Sciences. 2022; 79. Publisher: Springer:564

186. Bertrand D, Bertrand S, Cassar S, Gubbins E, Li J, and Gopalakrishnan M. Positive Allosteric Modulation of the α7 Nicotinic Acetylcholine Receptor: Ligand Interactions with Distinct Binding Sites and Evidence for a Prominent Role of the M2-M3 Segment. Molecular Pharmacology. 2008 Nov 1; 74. Publisher: American Society for Pharmacology and Experimental Therapeutics Section: Article:1407–16. DOI: 10.1124/mol.107.042820

187. daCosta CJB, Free CR, Corradi J, Bouzat C, and Sine SM. Single-Channel and Structural Foundations of Neuronal α7 Acetylcholine Receptor Potentiation. Journal of Neuroscience. 2011 Sep 28; 31. Publisher: Society for Neuroscience Section: Articles:13870–9. DOI: 10.1523/JNEUROSCI.2652-11.2011

188. Nikiforuk A, Kos T, Potasiewicz A, and Popik P. Positive allosteric modulation of alpha 7 nicotinic acetylcholine receptors enhances recognition memory and cognitive flexibility in rats. European Neuropsychopharmacology. 2015 Aug 1; 25:1300–13. DOI: 10.1016/j.euroneuro.2015.04.018

189. Samochocki M, Höffle A, Fehrenbacher A, Jostock R, Ludwig J, Christner C, Radina M, Zerlin M, Ullmer C, Pereira EFR, Lübbert H, Albuquerque EX, and Maelicke A. Galantamine Is an Allosterically Potentiating Ligand of Neuronal Nicotinic but Not of Muscarinic Acetylcholine Receptors. Journal of Pharmacology and Experimental Therapeutics. 2003 Jun 1; 305. Publisher: American Society for Pharmacology and Experimental Therapeutics Section: NEUROPHARMACOLOGY:1024–36. DOI: 10.1124/jpet.102.045773

190. Weltzin MM and Schulte MK. Desformylflustrabromine Modulates α4β2 Neuronal Nicotinic Acetylcholine Receptor High- and Low-Sensitivity Isoforms at Allosteric Clefts Containing the β2 Subunit. The Journal of Pharmacology and Experimental Therapeutics. 2015 Aug; 354:184. DOI: 10.1124/jpet.115.223933

191. Williams DK, Wang J, and Papke RL. Positive allosteric modulators as an approach to nicotinic acetylcholine receptor-targeted therapeutics: Advantages and limitations. Biochemical Pharmacology. Nicotinic Acetylcholine Receptors as Therapeutic Targets: Emerging Frontiers in Basic Research and Clinical Science (Satellite to the 2011 Meeting of the Society for Neuroscience) 2011 Oct 15; 82:915–30. DOI: 10.1016/j.bcp.2011.05.001

192. Timmermann D, Sandager-Nielsen K, Dyhring T, Smith M, Jacobsen AM, Nielsen E, Grunnet M, Christensen J, Peters D, Kohlhaas K, Olsen G, and Ahring P. Augmentation of cognitive function by NS9283, a stoichiometry-dependent positive allosteric modulator of α2- and α4-containing nicotinic acetylcholine receptors. British Journal of Pharmacology. 2012 Sep; 167:164–82. DOI: 10.1111/j.1476-5381.2012.01989.x

193. Bertrand D and Gopalakrishnan M. Allosteric modulation of nicotinic acetylcholine receptors. Biochemical pharmacology. 2007; 74. Publisher: Elsevier:1155–63

194. Alder BJ and Wainwright TE. Studies in Molecular Dynamics. I. General Method. The Journal of Chemical Physics. 1959 Aug 1; 31:459–66. DOI: 10.1063/1.1730376

195. Hollingsworth SA and Dror RO. Molecular Dynamics Simulation for All. Neuron. 2018 Sep 19; 99. Publisher: Elsevier:1129–43. DOI: 10.1016/j.neuron.2018.08.011

196. The Nobel Prize in Chemistry 2017. NobelPrize.org

197. Salomon-Ferrer R, Götz AW, Poole D, Le Grand S, and Walker RC. Routine Microsecond Molecular Dynamics Simulations with AMBER on GPUs. 2. Explicit Solvent Particle Mesh Ewald. Journal of Chemical Theory and Computation. 2013 Sep 10; 9:3878–88. DOI: 10.1021/ct400314y

198. Leach AR. Molecular Modelling: Principles and Applications. Pearson Education, 2001. 788 pp.

199. Born M and Oppenheimer R. Zur Quantentheorie der Molekeln. Annalen der Physik. 1927; 389. _eprint: https://onlinelibrary.wiley.com/doi/pdf/10.1002/andp.19273892002:457–84. DOI: 10.1002/andp.19273892002

200. González M. Force fields and molecular dynamics simulations. École thématique de la Société Française de la Neutronique. 2011; 12:169–200. DOI: 10.1051/sfn/201112009

201. Wang X. Method of Steepest Descent and its Applications. 2008. Available from: https://sces.phys.utk.edu/~moreo/mm08/XuWangP571.pdf

202. Abraham M, Alekseenko A, Bergh C, Blau C, Briand E, Doijade M, Fleischmann S, Gapsys V, Garg G, Gorelov S, Gouaillardet G, Gray A, Irrgang ME, Jalalypour F, Jordan J, Junghans C, Kanduri P, Keller S, Kutzner C, Lemkul JA, Lundborg M, Merz P, Miletić V, Morozov D, Páll S, Schulz R, Shirts M, Shvetsov A, Soproni B, Spoel Dvd, Turner P, Uphoff C, Villa A, Wingbermühle S, Zhmurov A, Bauer P, Hess B, and Lindahl E. GROMACS 2023.2 Manual. 2023 Jul 12. Publisher: Zenodo. DOI: 10.5281/zenodo.8134388

203. Ewald PP. Die Berechnung optischer und elektrostatischer Gitterpotentiale. Annalen der Physik. 1921; 369. _eprint: https://onlinelibrary.wiley.com/doi/pdf/10.1002/andp.19213690304:87. DOI: 10.1002/andp.19213690304

204. Darden T, York D, and Pedersen L. Particle mesh Ewald: An N·log(N) method for Ewald sums in large systems. The Journal of Chemical Physics. 1993; 98.

Publisher: American Institute of Physics Publising LLC:10089–92. DOI: 10.1063/1.464397

205. Berendsen HJC, Postma JPM, Gunsteren WF van, DiNola A, and Haak JR. Molecular dynamics with coupling to an external bath. The Journal of Chemical Physics. 1984 Oct 15; 81:3684–90. DOI: 10.1063/1.448118

206. Bussi G, Donadio D, and Parrinello M. Canonical sampling through velocity rescaling. The Journal of Chemical Physics. 2007 Jan 3; 126:014101. DOI: 10.1063/1.2408420

207. Andersen HC. Molecular dynamics simulations at constant pressure and/or temperature. The Journal of Chemical Physics. 1980 Feb 15; 72:2384–93. DOI: 10.1063/1.439486

208. Parrinello M and Rahman A. Polymorphic transitions in single crystals: A new molecular dynamics method. Journal of Applied physics. 1981; 52. Publisher: American Institute of Physics:7182–90

209. Shaw DE, Adams PJ, Azaria A, Bank JA, Batson B, Bell A, Bergdorf M, Bhatt J, Butts JA, Correia T, Dirks RM, Dror RO, Eastwood MP, Edwards B, Even A, Feldmann P, Fenn M, Fenton CH, Forte A, Gagliardo J, Gill G, Gorlatova M, Greskamp B, Grossman J, Gullingsrud J, Harper A, Hasenplaugh W, Heily M, Heshmat BC, Hunt J, Ierardi DJ, Iserovich L, Jackson BL, Johnson NP, Kirk MM, Klepeis JL, Kuskin JS, Mackenzie KM, Mader RJ, McGowen R, McLaughlin A, Moraes MA, Nasr MH, Nociolo LJ, O'Donnell L, Parker A, Peticolas JL, Pocina G, Predescu C, Quan T, Salmon JK, Schwink C, Shim KS, Siddique N, Spengler J, Szalay T, Tabladillo R, Tartler R, Taube AG, Theobald M, Towles B, Vick W, Wang SC, Wazlowski M, Weingarten MJ, Williams JM, and Yuh KA. Anton 3: twenty microseconds of molecular dynamics simulation before lunch. *Proceedings of the International Conference for High Performance Computing, Networking, Storage and Analysis*. SC '21: The International Conference for High

Performance Computing, Networking, Storage and Analysis. St. Louis Missouri: ACM, 2021 Nov 14:1–11. DOI: 10.1145/3458817.3487397

210. Peng C, Wu L, Xu Z, and Zhu W. Replica Exchange Molecular Dynamics. Progress in Chemistry. 2022 Feb 20; 34. Number: 2:384–96. DOI: 10.7536/PC201226

211. Sugita Y and Okamoto Y. Replica-exchange molecular dynamics method for protein folding. Chemical Physics Letters. 1999 Nov 26; 314:141–51. DOI: 10.1016/S0009-2614(99)01123-9

212. Bussi G. Hamiltonian replica exchange in GROMACS: a flexible implementation. Molecular Physics. 2014 Feb 16; 112. Publisher: Taylor & Francis _eprint: https://doi.org/10.1080/00268976.2013.824126:379–84. DOI: 10.1080/00268976.2013.824126

213. Wang L, Friesner RA, and Berne B. Replica Exchange with Solute Scaling: A more efficient version of Replica Exchange with Solute Tempering (REST2). The journal of physical chemistry B. 2011 Aug 4; 115:9431–8. DOI: 10.1021/jp204407d

214. Jung J, Kobayashi C, and Sugita Y. Acceleration of generalized replica exchange with solute tempering simulations of large biological systems on massively parallel supercomputer. Journal of Computational Chemistry. 2023; 44. _eprint: https://onlinelibrary.wiley.com/doi/pdf/10.1002/jcc.27124:1740–9. DOI: 10.1002/jcc.27124

215. Roux B. The calculation of the potential of mean force using computer simulations. Computer Physics Communications. 1995 Sep 2; 91:275–82. DOI: 10.1016/0010-4655(95)00053-I

216. Hénin J, Lelièvre T, Shirts MR, Valsson O, and Delemotte L. Enhanced sampling methods for molecular dynamics simulations. Living Journal of Computational

Molecular Science. 2022; 4. DOI: 10.33011/livecoms.4.1.1583. arXiv: 2202.04164[cond-mat,physics:physics]

217. Kumar S, Rosenberg JM, Bouzida D, Swendsen RH, and Kollman PA. Multidimensional free-energy calculations using the weighted histogram analysis method. Journal of Computational Chemistry. 1995; 16. _eprint: https://onlinelibrary.wiley.com/doi/pdf/10 50. DOI: 10.1002/jcc.540161104

218. Shirts MR and Chodera JD. Statistically optimal analysis of samples from multiple equilibrium states. The Journal of Chemical Physics. 2008 Sep 28; 129:124105. DOI: 10.1063/1.2978177

219. Laio A and Parrinello M. Escaping free-energy minima. Proceedings of the National Academy of Sciences. 2002 Oct; 99. Publisher: Proceedings of the National Academy of Sciences:12562–6. DOI: 10.1073/pnas.202427399

220. Barducci A, Bussi G, and Parrinello M. Well-Tempered Metadynamics: A Smoothly Converging and Tunable Free-Energy Method. Physical Review Letters. 2008 Jan 18; 100. Publisher: American Physical Society:020603. DOI: 10.1103/PhysRevLett.100.020603

221. Raniolo S and Limongelli V. Ligand binding free-energy calculations with funnel metadynamics. Nature Protocols. 2020 Sep; 15. Publisher: Nature Publishing Group:2837–66. DOI: 10.1038/s41596-020-0342-4

222. Limongelli V, Bonomi M, and Parrinello M. Funnel metadynamics as accurate binding free-energy method. Proceedings of the National Academy of Sciences. 2013 Apr 16; 110. Publisher: Proceedings of the National Academy of Sciences:6358–63. DOI: 10.1073/pnas.1303186110

223. Hille B. Ionic Channels of Excitable Membranes. Sinauer, 2001

224. Rettinger J, Schwarz S, and Schwarz W. Electrophysiology: Basics, Methods, Modern Approaches and Applications. Cham: Springer International Publishing, 2022. DOI: 10.1007/978-3-030-86482-8

225. Hodgkin AL and Katz B. The effect of sodium ions on the electrical activity of the giant axon of the squid. The Journal of Physiology. 1949 Mar 1; 108:37–77

226. Goldman DE. POTENTIAL, IMPEDANCE, AND RECTIFICATION IN MEMBRANES. The Journal of General Physiology. 1943 Sep 20; 27:37–60. DOI: 10.1085/jgp.27.1.37

227. Haghighi AP. MECHANISM OF INWARD RECTIFICATION OF NEURONAL NICOTININC ACETYCHOLINE RECEPTORS. Doctoral Thesis. Montreal, Quebec, Canada: McGill University', 1999

228. Kenakin TP. Chapter 8 - Allosteric modulation. *A Pharmacology Primer (Sixth Edition)*. Ed. by Kenakin TP. Academic Press, 2022 Jan 1:233–67. DOI: 10.1016/B978-0-323-99289-3.00002-6

229. Viscarra F, Chrestia JF, Sanchez Y, Pérez EG, Biggin PC, Bouzat C, Bermudez I, and López JJ. Side Groups Convert the α7 Nicotinic Receptor Agonist Ether Quinuclidine into a Type I Positive Allosteric Modulator. ACS Chemical Neuroscience. 2023 Aug 16; 14. Publisher: American Chemical Society:2876–87. DOI: 10.1021/acschemneuro.3c00225

230. Agulhon C, Abitbol M, Bertrand D, and Malafosse A. Localization of mRNA for CHRNA7 in human fetal brain. Neuroreport. 1999 Aug 2; 10:2223–7

231. Clarke PB, Schwartz RD, Paul SM, Pert CB, and Pert A. Nicotinic binding in rat brain: autoradiographic comparison of [3H]acetylcholine, [3H]nicotine, and [125I]-alpha-bungarotoxin. Journal of Neuroscience. 1985 May 1; 5. Publisher: Society for Neuroscience Section: Articles:1307–15. DOI: 10.1523/JNEUROSCI.05-05-01307.1985

232. Gu Z, Lamb PW, and Yakel JL. Cholinergic Coordination of Presynaptic and Postsynaptic Activity Induces Timing-Dependent Hippocampal Synaptic Plasticity. Journal of Neuroscience. 2012 Sep 5; 32. Publisher: Society for Neuroscience Section: Articles:12337–48. DOI: 10.1523/JNEUROSCI.2129-12.2012

233. Séguéla P, Wadiche J, Dineley-Miller K, Dani JA, and Patrick JW. Molecular cloning, functional properties, and distribution of rat brain alpha 7: a nicotinic cation channel highly permeable to calcium. Journal of Neuroscience. 1993; 13. Publisher: Soc Neuroscience:596–604

234. Tribollet E, Bertrand D, Marguerat A, and Raggenbass M. Comparative distribution of nicotinic receptor subtypes during development, adulthood and aging: an autoradiographic study in the rat brain. Neuroscience. 2004 Jan 1; 124:405–20. DOI: 10.1016/j.neuroscience.2003.09.028

235. Wallace TL and Porter RH. Targeting the nicotinic alpha7 acetylcholine receptor to enhance cognition in disease. Biochemical pharmacology. 2011; 82. Publisher: Elsevier:891–903

236. Gahring LC, Enioutina EY, Myers EJ, Spangrude GJ, Efimova OV, Kelley TW, Tvrdik P, Capecchi MR, and Rogers SW. Nicotinic receptor alpha7 expression identifies a novel hematopoietic progenitor lineage. PLoS One. 2013; 8. Publisher: Public Library of Science San Francisco, USA:e57481

237. Olofsson PS, Rosas-Ballina M, Levine YA, and Tracey KJ. Rethinking inflammation: neural circuits in the regulation of immunity. Immunological reviews. 2012; 248. Publisher: Wiley Online Library:188–204

238. Wessler I and Kirkpatrick C. Acetylcholine beyond neurons: the non-neuronal cholinergic system in humans. British journal of pharmacology. 2008; 154. Publisher: Wiley Online Library:1558–71

239. Zanetti SR, Ziblat A, Torres NI, Zwirner NW, and Bouzat C. Expression and functional role of α7 nicotinic receptor in human cytokine-stimulated natural killer (NK) cells. Journal of Biological Chemistry. 2016; 291. Publisher: ASBMB:16541–52

240. Gu Z and Yakel JL. Timing-dependent septal cholinergic induction of dynamic hippocampal synaptic plasticity. Neuron. 2011; 71. Publisher: Elsevier:155–65

241. Hoskin JL, Al-Hasan Y, and Sabbagh MN. Nicotinic acetylcholine receptor agonists for the treatment of Alzheimer's dementia: an update. Nicotine and Tobacco Research. 2019; 21. Publisher: Oxford University Press US:370–6

242. Mineur YS, Mose TN, Blakeman S, and Picciotto MR. Hippocampal α7 nicotinic ACh receptors contribute to modulation of depression-like behaviour in C57BL/6J mice. British journal of pharmacology. 2018; 175. Publisher: Wiley Online Library:1903–14

243. Liu Q, Liu C, Jiang L, Li M, Long T, He W, Qin G, Chen L, and Zhou J. α7 Nicotinic acetylcholine receptor-mediated anti-inflammatory effect in a chronic migraine rat model via the attenuation of glial cell activation. Journal of pain research. 2018. Publisher: Taylor & Francis:1129–40

244. Hone AJ and McIntosh JM. Nicotinic acetylcholine receptors in neuropathic and inflammatory pain. FEBS letters. 2018; 592. Publisher: Wiley Online Library:1045–62

245. Beinat C, Banister SD, Herrera M, Law V, and Kassiou M. The therapeutic potential of α 7 nicotinic acetylcholine receptor (α 7 nAChR) agonists for the treatment of the cognitive deficits associated with schizophrenia. CNS drugs. 2015; 29. Publisher: Springer:529–42

246. Rosas-Ballina M, Goldstein RS, Gallowitsch-Puerta M, Yang L, Valdés-Ferrer SI, Patel NB, Chavan S, Al-Abed Y, Yang H, and Tracey KJ. The selective α7 agonist GTS-21 attenuates cytokine production in human whole blood and human monocytes activated by ligands for TLR2, TLR3, TLR4, TLR9, and RAGE. Molecular Medicine. 2009; 15. Publisher: Springer:195–202

247. Pavlov VA, Ochani M, Yang LH, Gallowitsch-Puerta M, Ochani K, Lin X, Levi J, Parrish WR, Rosas-Ballina M, Czura CJ, et al. Selective α7-nicotinic acetylcholine receptor agonist GTS-21 improves survival in murine endotoxemia and severe sepsis. Critical care medicine. 2007; 35. Publisher: LWW:1139–44

248. Bertrand D, Lee CHL, Flood D, Marger F, and Donnelly-Roberts D. Therapeutic potential of α7 nicotinic acetylcholine receptors. Pharmacological Reviews. 2015; 67. Publisher: ASPET:1025–73

249. Bitner R, Anderson D, Drescher K, Kohlhaas K, Gronlien H, Hu M, Li J, Markosyan S, Marsh K, Mohler E, et al. P4–310: Preclinical characterization of a selective alpha-7 neuronal nicotinic acetylcholine receptor agonist ABT-126: A novel therapeutic agent for the treatment of cognitive impairment in Alzheimer's disease and schizophrenia. Alzheimer's & Dementia. 2013; 9. Publisher: Wiley Online Library:P817–P818

250. Feuerbach D, Pezous N, Weiss M, Shakeri-Nejad K, Lingenhoehl K, Hoyer D, Hurth K, Bilbe G, Pryce CR, McAllister K, et al. AQW 051, a novel, potent and selective α 7 nicotinic ACh receptor partial agonist: pharmacological characterization and phase I evaluation. British journal of pharmacology. 2015; 172. Publisher: Wiley Online Library:1292–304

251. Lieberman JA, Dunbar G, Segreti AC, Girgis RR, Seoane F, Beaver JS, Duan N, and Hosford DA. A randomized exploratory trial of an alpha-7 nicotinic receptor agonist (TC-5619) for cognitive enhancement in schizophrenia. Neuropsychopharmacology. 2013; 38. Publisher: Nature Publishing Group:968–75

252. Preskorn SH, Gawryl M, Dgetluck N, Palfreyman M, Bauer LO, and Hilt DC. Normalizing effects of EVP-6124, an alpha-7 nicotinic partial agonist, on event-related potentials and cognition: a proof of concept, randomized trial in patients with schizophrenia. Journal of Psychiatric Practice®. 2014; 20. Publisher: LWW:12–24

253. Olincy A, Harris JG, Johnson LL, Pender V, Kongs S, Allensworth D, Ellis J, Zerbe GO, Leonard S, Stevens KE, et al. Proof-of-concept trial of an α7 nicotinic agonist in schizophrenia. Archives of general psychiatry. 2006; 63. Publisher: American Medical Association:630–8

254. Tregellas JR, Tanabe J, Rojas DC, Shatti S, Olincy A, Johnson L, Martin LF, Soti F, Kem WR, Leonard S, et al. Effects of an alpha 7-nicotinic agonist on default network activity in schizophrenia. Biological psychiatry. 2011; 69. Publisher: Elsevier:7–11

255. Levin ED, Bettegowda C, Blosser J, and Gordon J. AR-R 17779, an α7 nicotinic agonist, improves learning and memory in rats. Behavioural pharmacology. 1999; 10. Publisher: LWW:675–80

256. Malysz J, Anderson DJ, Grønlien JH, Ji J, Bunnelle WH, Håkerud M, Thorin-Hagene K, Ween H, Helfrich R, Hu M, et al. In vitro pharmacological characterization of a novel selective α7 neuronal nicotinic acetylcholine receptor agonist ABT-107. Journal of Pharmacology and Experimental Therapeutics. 2010; 334. Publisher: ASPET:863–74

257. Prickaerts J, Goethem NP van, Chesworth R, Shapiro G, Boess FG, Methfessel C, Reneerkens OA, Flood DG, Hilt D, Gawryl M, et al. EVP-6124, a novel and selective α7 nicotinic acetylcholine receptor partial agonist, improves memory performance by potentiating the acetylcholine response of α7 nicotinic acetylcholine receptors. Neuropharmacology. 2012; 62. Publisher: Elsevier:1099–110

258. Horenstein NA, Leonik FM, and Papke RL. Multiple pharmacophores for the selective activation of nicotinic α7-type acetylcholine receptors. Molecular pharmacology. 2008; 74. Publisher: ASPET:1496–511

259. Leonik FM, Papke RL, and Horenstein NA. Quinuclidines as selective agonists for alpha-7 nicotinic acetylcholine receptors. Bioorganic & medicinal chemistry letters. 2007; 17. Publisher: Elsevier:1520–2

260. Yang T, Xiao T, Sun Q, and Wang K. The current agonists and positive allosteric modulators of α7 nAChR for CNS indications in clinical trials. Acta Pharmaceutica Sinica B. 2017 Nov 1; 7:611–22. DOI: 10.1016/j.apsb.2017.09.001

261. Nielsen BE, Minguez T, Bermudez I, and Bouzat C. Molecular function of the novel α7β2 nicotinic receptor. Cellular and Molecular Life Sciences. 2018; 75. Publisher: Springer:2457–71

262. Berman HM, Westbrook J, Feng Z, Gilliland G, Bhat TN, Weissig H, Shindyalov IN, and Bourne PE. The Protein Data Bank. Nucleic Acids Research. 2000 Jan 1; 28:235–42. DOI: 10.1093/nar/28.1.235

263. Delano WL. The PyMOL molecular graphics system. http://wwwpymolorg/. 2002. Publisher: DeLano Scientific

264. Hanwell MD, Curtis DE, Lonie DC, Vandermeersch T, Zurek E, and Hutchison GR. Avogadro: an advanced semantic chemical editor, visualization, and analysis platform. Journal of Cheminformatics. 2012 Dec; 4:17. DOI: 10.1186/1758-2946-4-17

265. Morris GM, Huey R, Lindstrom W, Sanner MF, Belew RK, Goodsell DS, and Olson AJ. AutoDock4 and AutoDockTools4: Automated docking with selective receptor flexibility. Journal of computational chemistry. 2009; 30. Publisher: Wiley Online Library:2785–91

266. Trott O and Olson AJ. AutoDock Vina: Improving the speed and accuracy of docking with a new scoring function, efficient optimization, and multithreading. Journal of Computational Chemistry. 2010; 31:455–61. DOI: 10.1002/jcc.21334

267. Daura X, Gademann K, Jaun B, Seebach D, Gunsteren WF van, and Mark AE. Peptide Folding: When Simulation Meets Experiment. Angewandte Chemie International Edition. 1999; 38:236–40. DOI: 10.1002/(SICI)1521-3773(19990115)38:1/2<236::AID-ANIE236>3.0.CO;2-M

268. Jo S, Kim T, Iyer VG, and Im W. CHARMM-GUI: a web-based graphical user interface for CHARMM. Journal of computational chemistry. 2008; 29. Publisher: Wiley Online Library:1859–65

269. Maier JA, Martinez C, Kasavajhala K, Wickstrom L, Hauser KE, and Simmerling C. ff14SB: improving the accuracy of protein side chain and backbone parameters from ff99SB. Journal of chemical theory and computation. 2015; 11. Publisher: ACS Publications:3696–713

270. Gould I, Skjevik A, Dickson C, Madej B, and Walker R. Lipid17: A comprehensive AMBER force field for the simulation of zwitterionic and anionic lipids. Manuscript in preparation. 2018

271. Case DA, Belfon K, Ben-Shalom I, Berryman J, Brozell S, Cerutti D, Cheatham T, Cisneros G, Cruzeiro V, Darden T, et al. Amber2022. San Francisco: University of California. 2022

272. Wang J, Wolf RM, Caldwell JW, Kollman PA, and Case DA. Development and testing of a general amber force field. Journal of Computational Chemistry. 2004 Jul 15; 25:1157–74. DOI: 10.1002/jcc.20035

273. Jorgensen WL, Chandrasekhar J, Madura JD, Impey RW, and Klein ML. Comparison of simple potential functions for simulating liquid water. The Journal of Chemical Physics. 1983 Jul 15; 79:926–35. DOI: 10.1063/1.445869

274. Abraham MJ, Murtola T, Schulz R, Páll S, Smith JC, Hess B, and Lindahl E. GROMACS: High performance molecular simulations through multi-level parallelism from laptops to supercomputers. SoftwareX. 2015 Sep; 1-2:19–25. DOI: 10.1016/j.softx.2015.06.001

275. Tribello GA, Bonomi M, Branduardi D, Camilloni C, and Bussi G. PLUMED 2: New feathers for an old bird. Computer Physics Communications. 2014 Feb; 185:604–13. DOI: 10.1016/j.cpc.2013.09.018

276. Michaud-Agrawal N, Denning EJ, Woolf TB, and Beckstein O. MDAnalysis: A toolkit for the analysis of molecular dynamics simulations. Journal of Computational Chemistry. 2011 Jul 30; 32:2319–27. DOI: 10.1002/jcc.21787

277. Campello HR, Del Villar SG, Honraedt A, Minguez T, Oliveira ASF, Ranaghan KE, Shoemark DK, Bermudez I, Gotti C, Sessions RB, et al. Unlocking nicotinic selectivity via direct C–H functionalization of (-)-cytisine. Chem. 2018; 4. Publisher: Elsevier:1710–25

278. Andersen ND, Nielsen BE, Corradi J, Tolosa MF, Feuerbach D, Arias HR, and Bouzat C. Exploring the positive allosteric modulation of human α7 nicotinic receptors from a single-channel perspective. Neuropharmacology. 2016; 107. Publisher: Elsevier:189–200

279. Lasala M, Fabiani C, Corradi J, Antollini S, and Bouzat C. Molecular modulation of human α7 nicotinic receptor by amyloid-β peptides. Frontiers in cellular neuroscience. 2019; 13. Publisher: Frontiers Media SA:37

280. Young GT, Zwart R, Walker AS, Sher E, and Millar NS. Potentiation of α7 nicotinic acetylcholine receptors via an allosteric transmembrane site. Proceedings of the National Academy of Sciences. 2008; 105. Publisher: National Acad Sciences:14686–91

281. Bondarenko V, Chen Q, Singewald K, Haloi N, Tillman TS, Howard RJ, Lindahl E, Xu Y, and Tang P. Structural Elucidation of Ivermectin binding to α7nAChR and the induced channel desensitization. ACS Chemical Neuroscience. 2023; 14. Publisher: ACS Publications:1156–65

282. Xiao Y, Hammond PS, Mazurov AA, and Yohannes D. Multiple interaction regions in the orthosteric ligand binding domain of the α7 neuronal nicotinic acetylcholine receptor. Journal of chemical information and modeling. 2012; 52. Publisher: ACS Publications:3064–73

283. Friis S, Mathes C, Sunesen M, Bowlby MR, and Dunlop J. Characterization of compounds on nicotinic acetylcholine receptor alpha7 channels using higher throughput electrophysiology. Journal of Neuroscience Methods. 2009 Feb 15; 177:142–8. DOI: 10.1016/j.jneumeth.2008.10.007

284. Nielsen BE, Stabile S, Vitale C, and Bouzat C. Design, synthesis, and functional evaluation of a novel series of phosphonate-functionalized 1, 2, 3-triazoles as positive allosteric modulators of α7 nicotinic acetylcholine receptors. ACS Chemical Neuroscience. 2020; 11. Publisher: ACS Publications:2688–704

285. Appiani R, Viscarra F, Biggin PC, Bermudez I, Giraudo A, Pallavicini M, and Bolchi C. Selective Potentiation of the (α4)3(β2)2 Nicotinic Acetylcholine Receptor Response by NS9283 Analogues. ACS chemical neuroscience. 2024 Apr 3; 15:1501–14. DOI: 10.1021/acschemneuro.3c00797

286. Grupe M, Grunnet M, Bastlund JF, and Jensen AA. Targeting α4β2 Nicotinic Acetylcholine Receptors in Central Nervous System Disorders: Perspectives on Positive Allosteric Modulation as a Therapeutic Approach. Basic & Clinical Pharmacology & Toxicology. 2015 Mar; 116:187–200. DOI: 10.1111/bcpt.12361

287. Mohler EG, Franklin SR, and Rueter LE. Discriminative-stimulus effects of NS9283, a nicotinic α4β2* positive allosteric modulator, in nicotine-discriminating rats. Psychopharmacology. 2014 Jan; 231:67–74. DOI: 10.1007/s00213-013-3207-5

288. Zhu CZ, Chin Cl, Rustay NR, Zhong C, Mikusa J, Chandran P, Salyers A, Gomez E, Simler G, Lewis LG, Gauvin D, Baker S, Pai M, Tovcimak A, Brown J, Komater V, Fox GB, Decker MW, Jacobson PB, Gopalakrishnan M, Lee CH, and Honore P. Potentiation of analgesic efficacy but not side effects: Co-administration of an α4β2 neuronal nicotinic acetylcholine receptor agonist and its positive allosteric modulator in experimental models of pain in rats. Biochemical Pharmacology. 2011 Oct; 82:967–76. DOI: 10.1016/j.bcp.2011.05.007

289. Grupe M, Jensen A, Ahring P, Christensen J, and Grunnet M. Unravelling the mechanism of action of NS9283, a positive allosteric modulator of (α4)3(β2)2

nicotinic ACh receptors. British Journal of Pharmacology. 2013; 168:2000–10. DOI: 10.1111/bph.12095

290. Olsen JA, Kastrup JS, Peters D, Gajhede M, Balle T, and Ahring PK. Two Distinct Allosteric Binding Sites at α4β2 Nicotinic Acetylcholine Receptors Revealed by NS206 and NS9283 Give Unique Insights to Binding Activity-associated Linkage at Cys-loop Receptors. The Journal of Biological Chemistry. 2013 Dec 13; 288:35997–6006. DOI: 10.1074/jbc.M113.498618
291. Mazzaferro S, Bermudez I, and Sine SM. Potentiation of a neuronal nicotinic receptor via pseudo-agonist site. Cellular and Molecular Life Sciences. 2019 Mar; 76:1151–67. DOI: 10.1007/s00018-018-2993-7
292. Jin Z, Khan P, Shin Y, Wang J, Lin L, Cameron MD, Lindstrom JM, Kenny PJ, and Kamenecka TM. Synthesis and activity of substituted heteroaromatics as positive allosteric modulators for α4β2α5 nicotinic acetylcholine receptors. Bioorganic & Medicinal Chemistry Letters. 2014 Jan 15; 24:674–8. DOI: 10.1016/j.bmcl.2013.11.049
293. Landrum G, Tosco P, Kelley B, Rodriguez R, Cosgrove D, Vianello R, sriniker, gedeck, Jones G, NadineSchneider, Kawashima E, Nealschneider D, Dalke A, Swain M, Cole B, Turk S, Savelev A, Vaucher A, Wójcikowski M, Take I, Scalfani VF, Walker R, Ujihara K, Probst D, g godin guillaume, Pahl A, tadhurst-cdd, Lehtivarjo J, Berenger F, and jasondbiggs. RDKit: Open-source cheminformatics. https://www.rdkit.org. 2023. DOI: 10.5281/zenodo.591637
294. Hornak V, Abel R, Okur A, Strockbine B, Roitberg A, and Simmerling C. Comparison of multiple Amber force fields and development of improved protein backbone parameters. Proteins: Structure, Function, and Bioinformatics. 2006 Nov 15; 65:712–25. DOI: 10.1002/prot.21123
295. Bauer D. WHAM - An efficient weighted histogram analysis implementation written in Rust. Version v1.1.3. 2021 Jul 22. DOI: 10.5281/zenodo.5121486

296. Viscarra F, Vinas TM, Bermudez I, and Biggin PC. BPS2025 - Is TC2559 an allosteric super-agonist at high-sensitivity (a4)2(b2)3 nicotinic acetylcholine receptors? Biophysical Journal. 2025 Feb 13; 124. Publisher: Elsevier:458a. DOI: 10.1016/j.bpj.2024.11.2432

297. Zwart R, Carbone AL, Moroni M, Bermudez I, Mogg AJ, Folly EA, Broad LM, Williams AC, Zhang D, Ding C, Heinz BA, and Sher E. Sazetidine-A Is a Potent and Selective Agonist at Native and Recombinant α4β2 Nicotinic Acetylcholine Receptors. Molecular Pharmacology. 2008 Jun 1; 73. Publisher: American Society for Pharmacology and Experimental Therapeutics Section: Article:1838–43. DOI: 10.1124/mol.108.045104

298. Damle VN and Karlin A. Effects of agonists and antagonists on the reactivity of the binding site disulfide in acetylcholine receptor from Torpedo californica. Biochemistry. 1980 Aug 19; 19:3924–32. DOI: 10.1021/bi00558a006

299. Lee HS, Seok C, and Im W. Potential Application of Alchemical Free Energy Simulations to Discriminate GPCR Ligand Efficacy. Journal of Chemical Theory and Computation. 2015 Mar 10; 11. Publisher: American Chemical Society:1255–66. DOI: 10.1021/ct5008907

300. Oshima H, Re S, and Sugita Y. Prediction of Protein–Ligand Binding Pose and Affinity Using the gREST+FEP Method. Journal of Chemical Information and Modeling. 2020 Nov 23; 60. Publisher: American Chemical Society:5382–94. DOI: 10.1021/acs.jcim.0c00338

301. Yao X, Song F, Chen F, Zhang Y, Gu J, Liu S, and Liu Z. Amino acids within loops D, E and F of insect nicotinic acetylcholine receptor β subunits influence neonicotinoid selectivity. Insect Biochemistry and Molecular Biology. 2008 Sep 1; 38:834–40. DOI: 10.1016/j.ibmb.2008.05.009

302. Basak S, Gicheru Y, Samanta A, Molugu SK, Huang W, Fuente Mld, Hughes T, Taylor DJ, Nieman MT, Moiseenkova-Bell V, and Chakrapani S. Cryo-EM

structure of 5-HT3A receptor in its resting conformation. Nature Communications. 2018 Feb 6; 9. Publisher: Nature Publishing Group:514. DOI: 10.1038/s41467-018-02997-4

303. Oliveira ASF, Shoemark DK, Campello HR, Wonnacott S, Gallagher T, Sessions RB, and Mulholland AJ. Identification of the Initial Steps in Signal Transduction in the α4β2 Nicotinic Receptor: Insights from Equilibrium and Nonequilibrium Simulations. Structure. 2019 Jul 2; 27:1171–1183.e3. DOI: 10.1016/j.str.2019.04.008

304. Kim JJ, Gharpure A, Teng J, Zhuang Y, Howard RJ, Zhu S, Noviello CM, Walsh RM, Lindahl E, and Hibbs RE. Shared structural mechanisms of general anaesthetics and benzodiazepines. Nature. 2020 Sep; 585. Publisher: Nature Publishing Group:303–8. DOI: 10.1038/s41586-020-2654-5

305. Miller PS and Aricescu AR. Crystal structure of a human GABAA receptor. Nature. 2014 Aug; 512. Publisher: Nature Publishing Group:270–5. DOI: 10.1038/nature13293

306. Moody OA and Jenkins A. The role of loops B and C in determining the potentiation of GABA receptors by midazolam. Pharmacology Research & Perspectives. 2018; 6. _eprint: https://onlinelibrary.wiley.com/doi/pdf/10.1002/prp2.433:e00433. DOI: 10.1002/prp2.433

307. Morlock EV and Czajkowski C. Different Residues in the $GABA_A$ Receptor Benzodiazepine Binding Pocket Mediate Benzodiazepine Efficacy and Binding. Molecular Pharmacology. 2011 Jul; 80:14–22. DOI: 10.1124/mol.110.069542

308. Amin J, Brooks-Kayal A, and Weiss DS. Two Tyrosine Residues on the α Subunit Are Crucial for Benzodiazepine Binding and Allosteric Modulation of -Aminobutyric $Acid_A$ Receptors. Molecular Pharmacology. 1997 May 1; 51:833–41. DOI: 10.1124/mol.51.5.833

309. Padgett CL and Lummis SCR. The F-loop of the GABAA Receptor 2 Subunit Contributes to Benzodiazepine Modulation *. Journal of Biological Chemistry. 2008 Feb 1; 283. Publisher: Elsevier:2702–8. DOI: 10.1074/jbc.M705699200

310. daCosta CJB and Baenziger JE. Gating of pentameric ligand-gated ion channels: structural insights and ambiguities. Structure (London, England: 1993). 2013 Aug 6; 21:1271–83. DOI: 10.1016/j.str.2013.06.019

311. Rucktooa P, Smit AB, and Sixma TK. Insight in nAChR subtype selectivity from AChBP crystal structures. Biochemical Pharmacology. Nicotinic Receptor-Based Therapeutics: Emerging Frontiers in Basic Research & Clinical Science 2009 Oct 1; 78:777–87. DOI: 10.1016/j.bcp.2009.06.098

312. Smit AB, Syed NI, Schaap D, Minnen J van, Klumperman J, Kits KS, Lodder H, Schors RC van der, Elk R van, Sorgedrager B, Brejc K, Sixma TK, and Geraerts WP. A glia-derived acetylcholine-binding protein that modulates synaptic transmission. Nature. 2001 May 17; 411:261–8. DOI: 10.1038/35077000

313. Sine SM. The nicotinic receptor ligand binding domain. Journal of Neurobiology. 2002 Dec; 53:431–46. DOI: 10.1002/neu.10139

314. Parker HP, Dawson A, Jones MJ, Yan R, Ouyang J, Hong R, and Hunter WN. Delineating the activity of the potent nicotinic acetylcholine receptor agonists (+)-anatoxin-a and (-)-hosieine-A. Acta Crystallographica Section F, Structural Biology Communications. 2022 Sep 1; 78(Pt 9):313–23. DOI: 10.1107/S2053230X22007762

315. Bocquet N, Prado de Carvalho L, Cartaud J, Neyton J, Le Poupon C, Taly A, Grutter T, Changeux JP, and Corringer PJ. A prokaryotic proton-gated ion channel from the nicotinic acetylcholine receptor family. Nature. 2007 Jan 4; 445:116–9. DOI: 10.1038/nature05371

316. Tasneem A, Iyer LM, Jakobsson E, and Aravind L. Identification of the prokaryotic ligand-gated ion channels and their implications for the mechanisms and origins

of animal Cys-loop ion channels. Genome Biology. 2004 Dec 20; 6:R4. DOI: 10.1186/gb-2004-6-1-r4

317. Cecchini M, Corringer PJ, and Changeux JP. The Nicotinic Acetylcholine Receptor and its Pentameric Homologs: Toward an Allosteric Mechanism of Signal Transduction at the Atomic Level. Annual Review of Biochemistry. 2024 Feb 12. DOI: 10.1146/annurev-biochem-030122-033116

318. Administration UF
bibinitperiodD. Determination That CHANTIX (Varenicline Tartrate) Tablets, 0.5 Milligram and 1 Milligram, Has Not Been Withdrawn From Sale for Reasons of Safety or Effectiveness. Federal Register. 2023 Feb 27

319. Dalal V, Arcario MJ, Petroff JT, Tan BK, Dietzen NM, Rau MJ, Fitzpatrick JAJ, Brannigan G, and Cheng WWL. Lipid nanodisc scaffold and size alter the structure of a pentameric ligand-gated ion channel. Nature Communications. 2024 Jan 2; 15:25. DOI: 10.1038/s41467-023-44366-w

320. Gielen M, Barilone N, and Corringer PJ. The desensitization pathway of GABAA receptors, one subunit at a time. Nature Communications. 2020 Oct 23; 11:5369. DOI: 10.1038/s41467-020-19218-6

321. Shi S, Lefebvre SN, Peverini L, Cerdan AH, Milán Rodríguez P, Gielen M, Changeux JP, Cecchini M, and Corringer PJ. Illumination of a progressive allosteric mechanism mediating the glycine receptor activation. Nature Communications. 2023 Feb 13; 14:795. DOI: 10.1038/s41467-023-36471-7

322. Kindig K, Gibbs E, Seiferth D, Biggin PC, and Chakrapani S. Mechanisms underlying modulation of human GlyRα3 by Zn2+ and pH. Science Advances. 2024 Dec 18; 10. Publisher: American Association for the Advancement of Science:eadr5920. DOI: 10.1126/sciadv.adr5920